AQUEOUS CORROSION OF MAGNESIUM AND MAGNOX

A Thesis submitted for the Degree of

Doctor of Philosophy

at the University of Southampton

by

Paul Rimmer Harvey

October 1987

Department of Chemistry

To Adrianne

To my Parents

UNIVERSITY OF SOUTHAMPTON

ABSTRACT

FACULTY OF SCIENCE

CHEMISTRY

Doctor of Philosophy

AQUEOUS CORROSION OF MAGNESIUM AND MAGNOX

by Paul Rimmer Harvey

The early stages of film growth on magnesium and Magnox alloy have been investigated *in situ* using an automatic nulling ellipsometer coupled with potential control of the specimens. SIMS and scanning Auger spectroscopy in conjunction with ion beam milling have been used where possible to confirm the ellipsometric results.

Initial results obtained in 0.01 mol/dm^3 NaOH indicated that substrate dissolution was leading to a roughening of the film/substrate interface. This was attributed to carbon dioxide absorption in the air-saturated solutions causing a reduction in pH to values below 11.5 with a consequent breakdown in passivity. This led to further experiments under various conditions of solution composition and pH. The proposal of a rough surface was investigated initially by computer simulations whereby the rough surface was treated as an effective film containing both the substrate and the overlying film. Confirmation of these theoretical models was sought by the use of ellipsometry at a different angle of incidence and by scanning electron microscopy.

Maintaining the pH near 12 prevented the breakdown of passivity in Magnox. This enabled a more detailed study of the corrosion processes to be made. The behaviour of Mg under these conditions was still anomalous and was attributed to the more porous film present on Mg compared to Magnox. This could cause a channelling of the corrosion attack leading to a roughened substrate.

The results obtained for Magnox in neutral and strongly alkaline solutions (1 mol/dm^3 NaOH) could not be explained either by a single layer or rough layer model. The results could, however, be explained if it was assumed that the optical constants of the substrate were changing. This could occur if there was segregation of the alloy components near the metal surface.

ACKNOWLEDGEMENTS

I would like to express my sincere thanks to Dr. Bob Greef for his help and guidance during the last five years. I am also indebted to Dr. Stewart Tyfield for his help and many fruitful discussions during my periods at B.N.L. I would also like to thank Dr. Tyfield's colleagues at B.N.L., Dr. G.C. Allen and Dr. R. Wild for their help with surface analysis.

I am particularly indebted to Adrianne Parkinson for her endless patience during the final stages of my write-up and for help in producing the diagrams. I would also like to express my gratitude to Alice Roberts for working long unsociable hours to enable my thesis to be typed quickly.

I would also like to acknowledge the financial support of the S.E.R.C. and the C.E.G.B.

CONTENTS

Page No.

CHAPTER 1 INTRODUCTION

1.1 A brief history of Magnox A180

Magnox A180 is a high magnesium alloy, containing typically 0.8% wt Al and 0.005% wt Beryllium, which is widely used as a cladding material for gas-cooled nuclear reactors using natural uranium as fuel. The reason for this is due primarily to the very low cross-section for absorption of thermal neutrons by Mg and its alloys,[1] necessary for economical operation using non-enriched uranium. Magnox also has excellent compatibility with uranium unlike otherwise suitable materials such as aluminium and beryllium.[1] Although this type of reactor has been superseded by the advanced gas-cooled reactor (A.G.R.) and the pressurized water reactor (P.W.R.) over half the world's nuclear power had been generated by Mg alloy clad uranium fuels up to 1972[2] and it is expected that reprocessing of Magnox will be necessary in the U.K. until the early years of the next century.[3]

The development of Magnox as a canning material for uranium and its subsequent use together with various metallurgical properties has been discussed by several authors.[1,2,4,5,6] Originally, pure Mg was the preferred material but was found to be not resistant to oxidation at high temperatures in wet CO_2, and it was decided[4] that an oxidation resistant alloy should be used. This resulted in the development of the Magnox (MAGnesium No OXidation) alloys which contained small quantities of beryllium, to increase oxidation resistance, and aluminium to facilitate Be introduction and to increase strength at operating temperatures.

On removal from the reactor the fuel elements are stored in station ponds for a period of about one hundred days which allows time for the short-lived radioactive products, principally radioactive iodine, to decay and for the decay heat output to fall to a suitable level for transport off site for reprocessing.[5] During this period corrosion control of the Magnox is essential to ensure the integrity of the fuel elements during storage as penetration would result in the release of uranium fission products, having high activity, into the ponds. Penetration will mainly occur as a result of localized corrosion but there is also a requirement for the general corrosion to be as low as possible. This is because impurities in the Magnox cladding such as zinc become activated in the core and lead to problems with effluent disposal.

1.2 The aqueous corrosion of magnesium and Magnox

1.2.1 The anomalous electrochemistry of magnesium

Relatively few studies have considered the aqueous corrosion of magnesium and its alloys in alkaline environments over the last few decades, particularly in the absence of aggressive anions such as halides and thiocyanates. Several papers have been published however referring to battery applications,[7-14] sacrificial anodes,[15-19] and to the anomalous electrochemical behaviour of Mg.[20-38] The latter is characterized by the negative difference effect,[20-36] the delay effect,[8,9,12,13] and by the experimentally measured behaviour of the open circuit or corrosion potential, E_{corr}.[12-14,34,37,38]

The negative difference effect is an increase in the magnitude of the hydrogen evolution current from its value at open circuit as the potential is taken more positive.[26] This has a practical significance insomuch as it results in a loss of anodic current efficiency, defined as the ratio of the actual Coulombs passed to the theoretical Coulombs obtainable from an anode for a given weight loss.[22] Several theories have been proposed to explain this phenomenon, e.g. formation of monovalent magnesium ions,[30,36] anodic disintegration or the 'chunk' effect[24,28] and formation of magnesium hydride.[31,39]

Another characteristic of the electrochemistry of Mg is the large difference between the theoretical reversible potential for the Mg/Mg^{2+} couple and E_{corr}. The standard potentials in acid and alkaline environments are:[40]

$$Mg^{2+} + 2e = Mg \qquad E^{o} = -2.36 \text{ V nhe} \qquad .....(1.1)$$

$$Mg(OH)_2 + 2e = Mg + 2OH^{-} \qquad E^{o} = -2.69 \text{ V nhe} \qquad .....(1.2)$$

Experimentally determined values for E_{corr} however are in general 1V more noble.[34,39]

The most active potentials (~ -2.0 V nhe) are recorded in acid solutions and it has been suggested[23,39] that in this region there is a mixed potential between Mg dissolution and hydrogen evolution. It is also suggested[39] that there is cathodic control, the controlling reaction being proton diffusion to the metal surface.[41] In alkaline and neutral media there is a shift to more noble potentials of several hundred mV.[39] There is less agreement as to the probable corrosion mechanisms in this region but it is generally recognized that film formation is probably important.[16,22,23,33,39,42] The third anomalous characteristic, the delay effect, is a sudden sharp rise in the anode potential when there is an increase in the anodic current drawn from the cell which is followed by a return to more active potentials after a few seconds, (fig. 1.1). This phenomenon is observed in neutral and alkaline environments and results in a temporary power loss in battery applications. It has been explained as being due to hydride formation,[31,39] or resulting from a breakdown of passivation due to hydrolysis within pits.[12]

1.2.2 The structure of the corrosion film formed on Mg and Magnox in alkaline environments

According to the Pourbaix diagram, fig. 1.2,[43] Mg is in the passive state above a pH of about 11.3 due to the formation of $Mg(OH)_2$. The fall in the corrosion rate has been experimentally verified for both Mg[16,44] and Magnox[6] with a reduction in the corrosion rate of Magnox from ~0.07 g m^{-2} day^{-1} to 0.005 g m^{-2} day^{-1} between pH 10.5 and 11.5. It has also been widely accepted[16,23,39,43-53] that the bulk corrosion film formed on Mg in alkaline media is $Mg(OH)_2$ and this has been unequivocally determined to be the case for Magnox corroding in degassed sodium hydroxide solution.[49] It has been suggested[50] however that there may be a thin film or barrier layer between the $Mg(OH)_2$ film and the underlying substrate (fig. 1.3), with mass transport processes through this thin film controlling the corrosion rate.

Friskney _et al._[50] have put forward the proposal, based on the position of thermodynamic equilibria at 50°C, that this barrier layer may be an oxide, MgO. Vermilyea[48] also suggests the idea of a layer of MgO underneath the $Mg(OH)_2$ film due to the similarity of the rate of dissolution of MgO and Mg in inhibitor-free solutions. Friskney _et al._[50] also consider the possibility of a three-layered corrosion film with an MgH_2 layer between the Mg substrate and the MgO layer with a film of $Mg(OH)_2$ as the topmost layer, (fig. 1.4). This would be expected to occur if the hydrogen chemical potential at the metal film interface was sufficiently high, which is possible as it is known that the corrosion film grows at the metal film interface.[49]

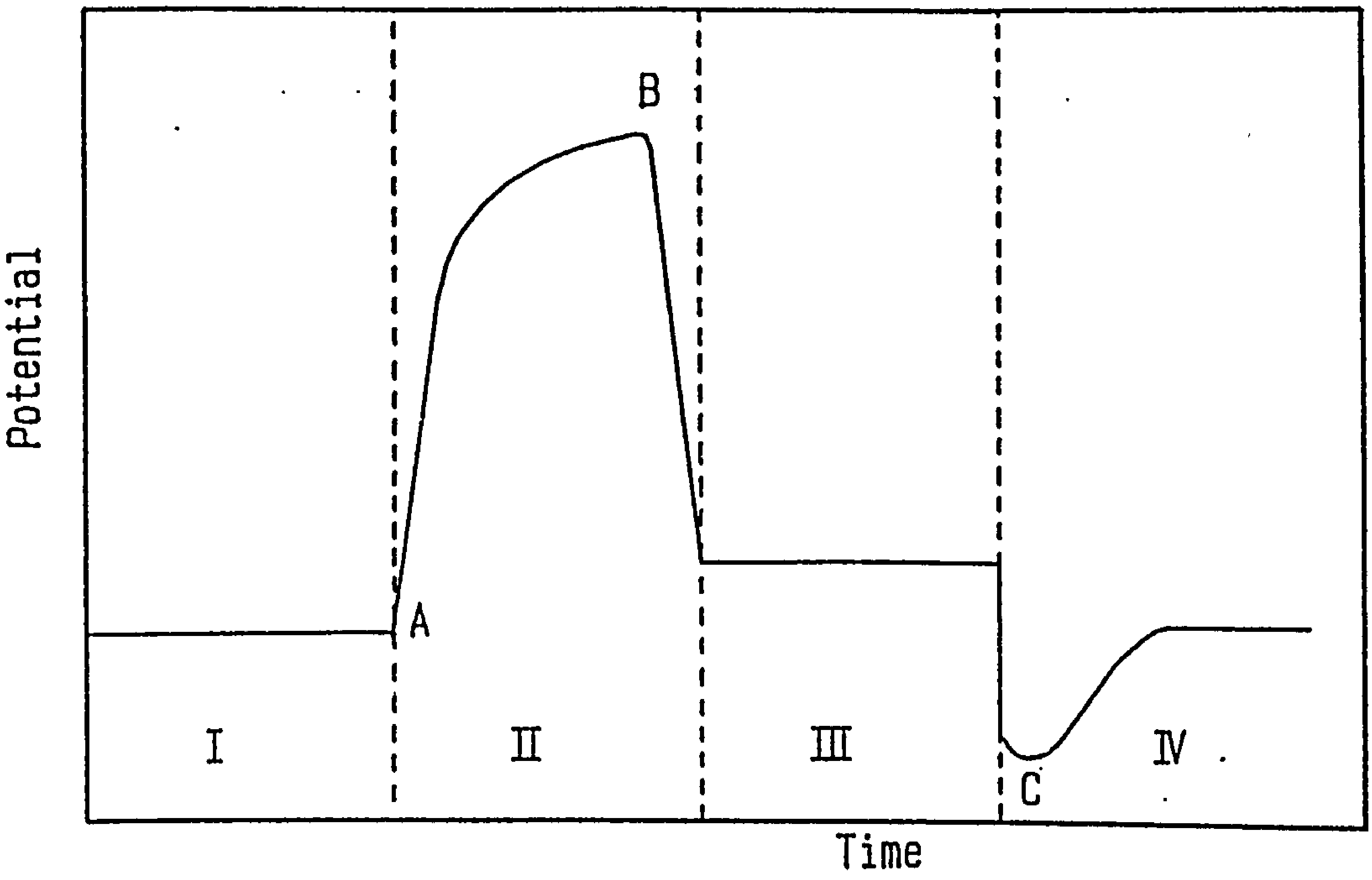

I. Behaviour at the rest potential

II. Polarization current switched on at A followed by a sudden sharp rise in the electrode potential

III. Activation of electrode at point C

IV. Polarization of electrode stopped at C electrode potential becomes more negative before slowly recovering to original rest potential

Fig. 1.1 The delay effect[12]

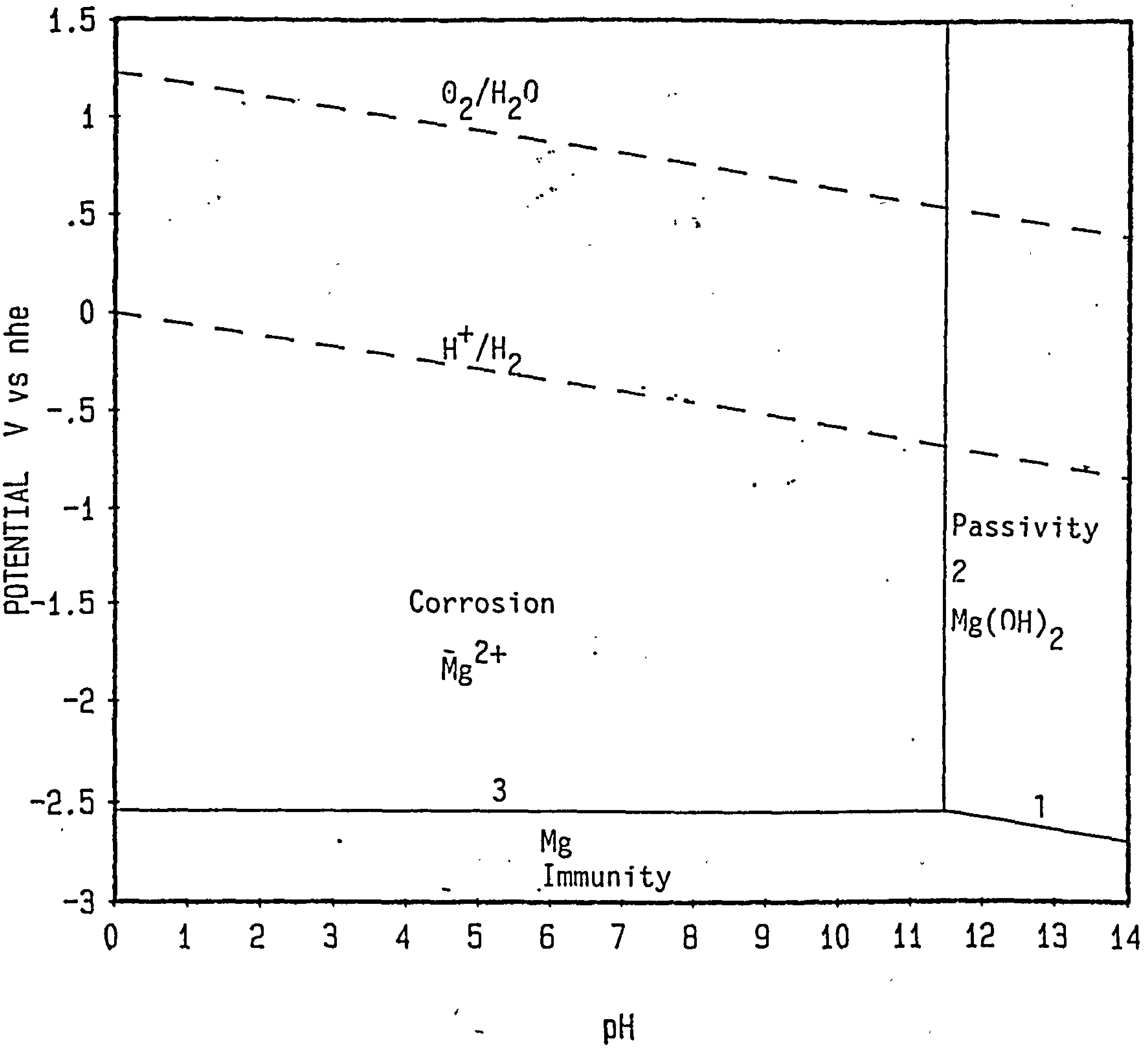

1. $Mg(OH)_2 + 2H^+ + 2e^- = Mg + 2H_2O$

   $E^\circ = -1.862 - 0.0591\ pH$

2. $Mg(OH)_2 = Mg^{2+} + 2OH^-$

   $\log(Mg^{2+}) = 16.93 - 2\ pH$

3. $Mg^{2+} + 2e = Mg$

   $E^\circ = -2.363 + 0.0295\ \log(Mg^{2+})$

Fig. 1.2 Pourbaix diagram for Magnesium[43]

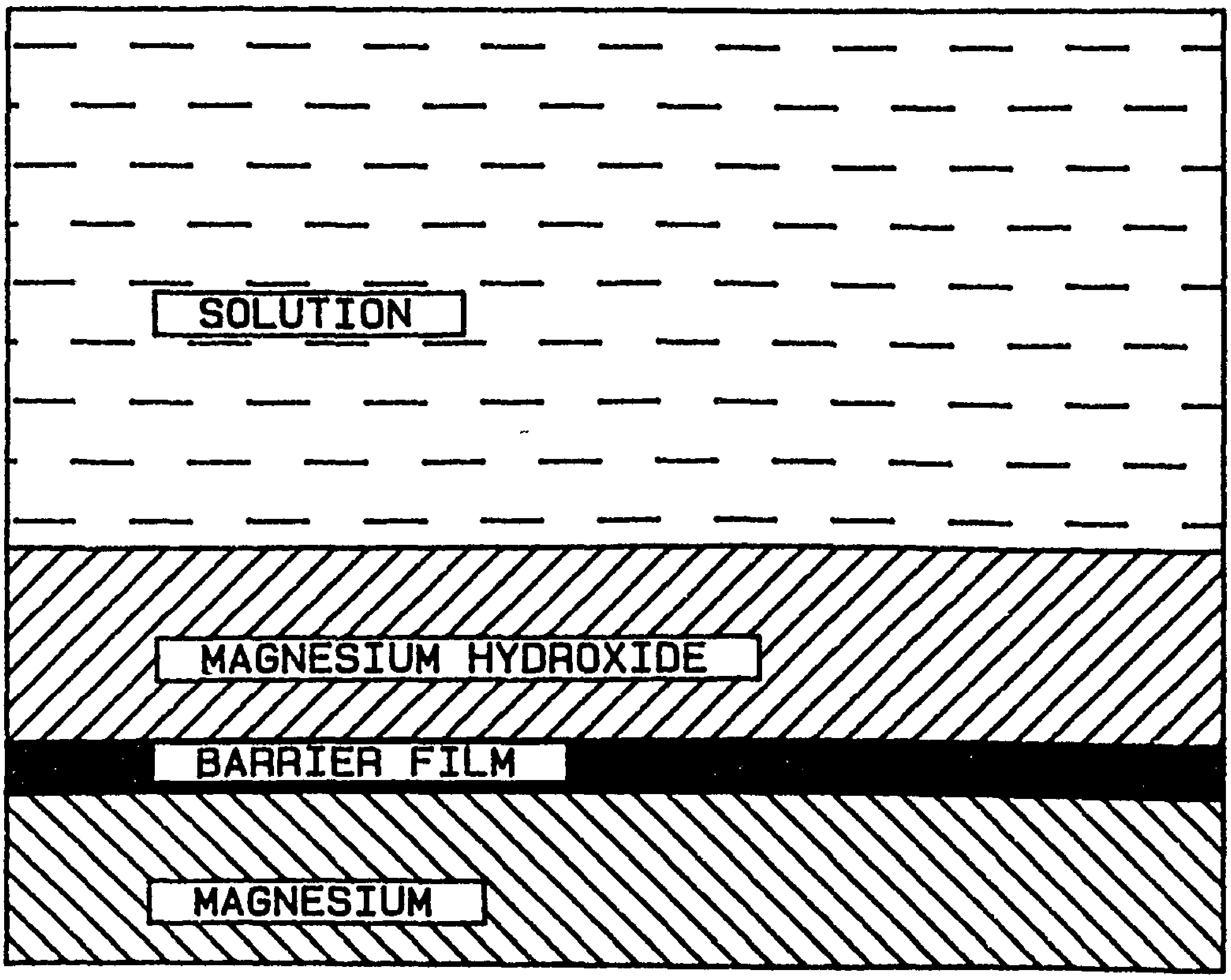

Fig. 1.3 Model of proposed barrier film for the corrosion of magnesium in aqueous solution

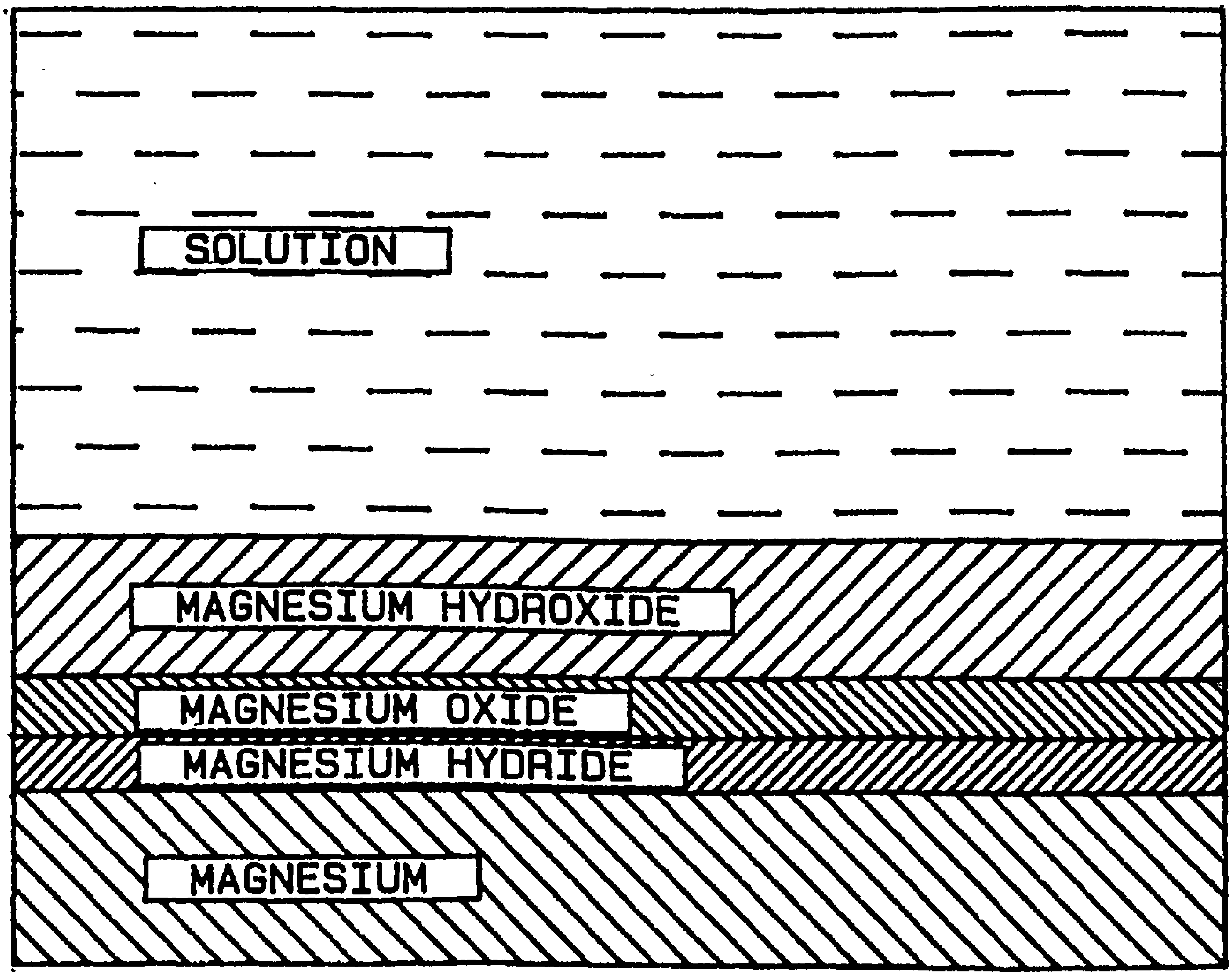

Fig. 1.4 Model of proposed bi-layer barrier film for the corrosion of magnesium in aqueous solution

Perrault[31,37-39,52,53] has also suggested the presence of an MgH_2 layer based upon his modified Pourbaix diagram (fig. 1.5). This was obtained from an analysis of the relevant thermodynamic equilibria for Mg. However it was stated[52] that the oxides of Mg were not considered in the calculations, instead of which the hydroxides were used. According to his results a layer of MgH_2 forms on Mg in neutral and alkaline environments providing that the overpotential for the hydrogen evolution reaction is of the order of, or greater than about 1 V:

$$Mg + 2H^+ + 2e^- \rightarrow MgH_2 \qquad .....(1.3)$$

The hydride is then oxidized to the hydroxide:

$$MgH_2 + 2OH^- \rightarrow Mg(OH)_2 + H_2 + 2e^- \qquad .....(1.4)$$

The presence of either an MgO or an MgH_2 layer on Magnox corroding in neutral and alkaline environments was not detected by ion beam studies[49] with a resolution depth of 100 nm. The presence of MgH_2 has been detected however in corrosion tests carried out in water vapour.[50] As mentioned above magnesium hydride formation has however been used to account for the negative difference effect, the delay effect and the value of E_{corr}.[39] The existence of an MgH_2 layer may also explain the phenomenon of breakaway corrosion whereby the corrosion rate of Magnox in alkaline solution increases steeply after a period of several hundred days, (fig. 1.6).[50] The time to breakaway depends upon the surface pre-treatment, temperature and solution composition and it is thought that it may be due to stress causing the rupture of the proposed barrier layer.

1.2.3 The effect of oxygen on the corrosion of Mg and Magnox

The very electronegative potential for the oxidation of Mg implies that it may corrode in aqueous electrolytes even in the absence of oxygen. Blanchet *et al.*[54] and Schneider[12] found that dissolved oxygen had very little effect on the corrosion of Magnox and Mg. Perrault however found no corrosion for Mg immersed in alkaline solution with a pH near 10 to 12 at very low partial pressures of oxygen.[39] Fabjan *et al.*[56] also report the presence of an oxygen reduction reaction in 1 molar KOH containing KCl.

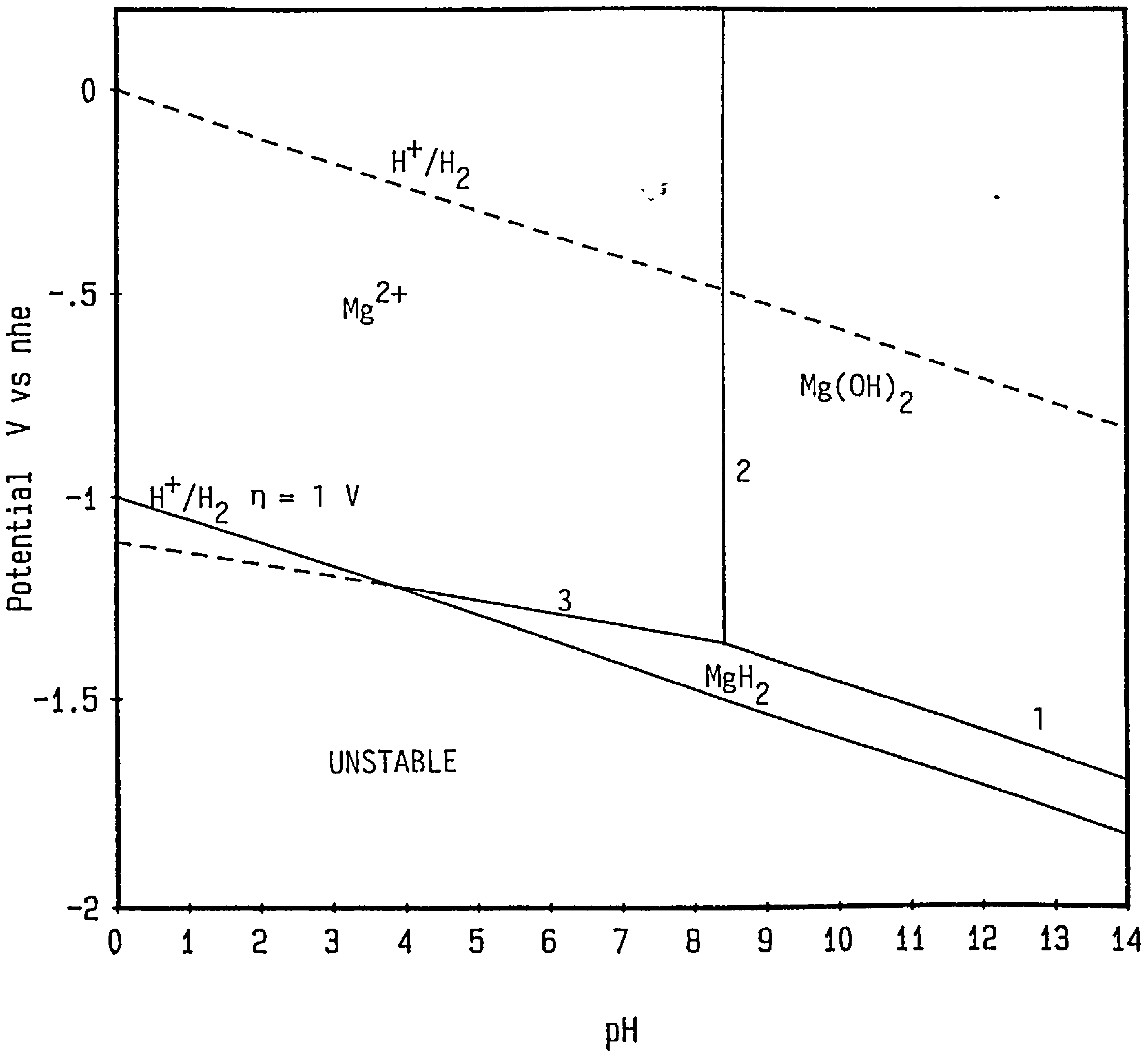

1. $Mg(OH)_2 + H^+ + 2e^- = MgH_2 + 2OH^-$

$E° = -2.501 \text{ V} - 0.0591 \text{ pH}$

2. $Mg(OH)_2 = Mg^{2+} + 2OH^-$

$\log(Mg^{2+}) = 16.93 - 2 \text{ pH}$

3. $Mg^{2+} + H_2 + 2e^- = MgH_2$

$E° = -2.176 \text{ V}$

Fig. 1.5 Modified potential - pH diagram for Mg for overpotential of the hydrogen evolution reaction equal to 1 V.[52]

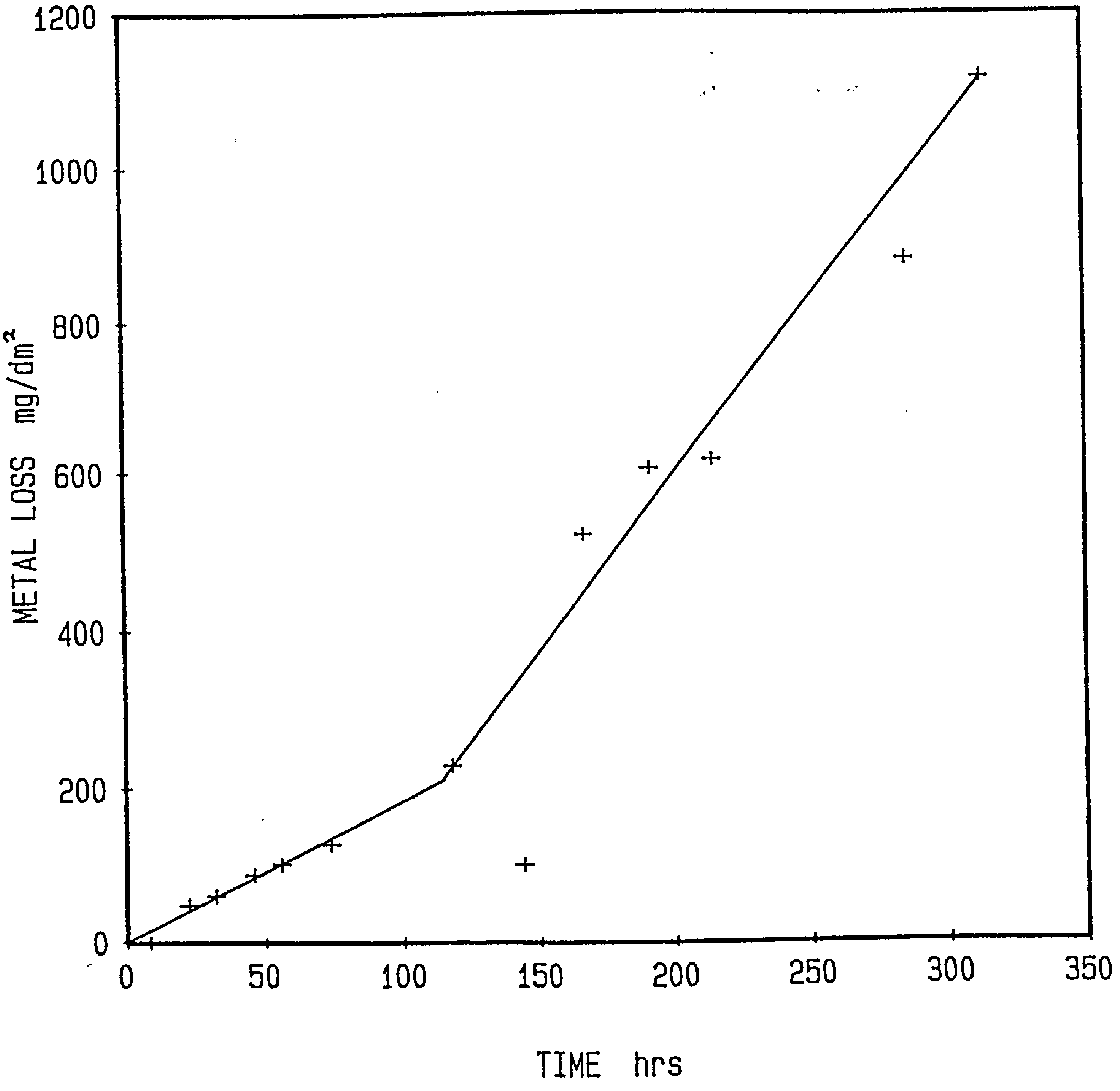

Corrosion rate increases sharply after 120 hours.

Fig. 1.6 Corrosion of etched Magnox Al-80 at 373 K in sodium hydroxide solution[50]

1.2.4 Inhibition of the corrosion of Mg and Magnox

Both phosphate and chromate are reported as inhibiting the corrosion rate of Mg over a wide range of pH values.[9,46] Perrault attributes their action as being due to the formation of an insoluble compact-oxide film on the metal surface.[39] Vermilyea[47,48] has studied the inhibition of MgO and $Mg(OH)_2$ dissolution and found that periodate, germanate, tellurate, vanadate and tellurite ions retarded the dissolution of MgO and commercial $Mg(OH)_2$ in alkaline solutions. He suggested that this was due to incorporation of these ions into the $Mg(OH)_2$ structure and the formation of strong hydrogen bonds with the surface layers. The same ions also inhibit MgO dissolution, as this first reacts with water to form $Mg(OH)_2$ with the overall dissolution rate being controlled by $Mg(OH)_2$ dissolution. He also found that sodium dodecyl sulphate was an inhibitor for MgO and $Mg(OH)_2$ in acid solutions which he proposed was due to the high positive charge of the $Mg(OH)_2$ particles at low pH values and the repulsion between water and the aliphatic hydrocarbon portion of the inhibitor.

Fluoride is reported as inhibiting both the corrosion of Mg[44] and Magnox[50] and also increasing the resistance of Magnox to localized attack by chloride ions. The presence of fluoride ions is effective at very low levels and it has been suggested[50] that it reduces the corrosion rate by modifying the mechanical properties of the proposed barrier layer and mass transport through this layer.

1.2.5 Breakdown of passivation of Mg and Magnox by certain anions

Chlorides, bromides, iodides, sulphates, persulphates, chlorates, hypochlorites and salts of heavy metals displaced by Mg all have a deleterious effect on the corrosion of Mg in aqueous environments.[55] The effect of chloride in particular has been well characterized in the past[16,20,22,34,44,50,51] with high concentrations of Cl^- causing pitting initially, leading to exfoliation and spalling. The exact mechanism of breakdown is not known, but the breakdown potential (pitting potential) becomes more negative with increasing chloride content[34,57] and it is possible that the initiation of pitting corresponds to a critical potential where the adsorption of chloride ions is preferred to the adsorption of oxygen atoms or water molecules, as has been suggested for aluminium.[58] Richardson and Wood[59] have suggested that in the case of aluminium the aggressive anions only propagate small pores already present in the surface layer. Once the bare metal is exposed cathodic evolution of hydrogen takes place within the pits and an activated pit may be formed with a lower pH than that in the bulk solution. A similar mechanism is stated to occur during the corrosion of Mg in alkaline solutions containing perchlorate ions.[12]

Beck and Chan[60] have postulated the formation of a magnesium chloride salt film on magnesium in high concentrations of magnesium chloride at high anodic potentials (> 2 V sce). This film acts as a diffusion barrier for water and prevents repassivation by an oxide film.

The deleterious effect of silicate on the corrosion rate of Magnox in alkaline solutions above 60°C has been reported.[61] The effect is temperature dependent with a negligible increase in corrosion rate at 60°C on exposure to 100 ppm silicate compared to a four-fold increase in rate at 121°C for similar silicate concentrations. The silicate was observed in the corrosion film particularly at grain boundaries even at 60°C probably in the form of hydrated magnesium aluminium silicate.

1.3 Ellipsometry in corrosion testing: the work in this thesis

Although control of Magnox corrosion can be effectively achieved,[50] as attested by many years experience in the C.E.G.B., by storage in sodium hydroxide solution (pH > 11.5) with strict control of aggressive anions, there remain several outstanding scientific questions concerning the corrosion in aqueous environments. Many workers support the idea of a thin barrier-type layer controlling the corrosion but there has been little direct evidence for this film. As well as doubt as to its function in controlling corrosion there is also uncertainty as to its nature and thickness.[49,50]

The early stages of corrosion of materials which exhibit passivity, such as Magnox in alkaline solution, are crucial, as it is during these stages that the character of this film is established. The properties of this film will have a marked effect on both its long-term stability due to such factors as internal stresses and on its resistance to breakdown due to external factors such as penetration of the film by depassivating ions, e.g. chloride.

Previous published studies relating to the corrosion of Magnox have consisted of either in vacuo surface studies using techniques such as Rutherford backscattering, E.S.C.A., S.I.M.S. and Auger spectroscopy[49] or weight gain and hydrogen pressure measurements.[6,49,50] These techniques are not ideally suited to study the early stages of film growth on Mg and Magnox, either because of their lack of sensitivity, or of the need to examine in vacuo - which may alter the film. Ellipsometry however provides a highly sensitive, non-destructive technique which can be used to investigate the initial corrosion processes in situ.[62,63] It is capable in principle of accurately measuring the optical constants and thickness of single and multi-layered films provided that the optical constants of the film-free surface are known or can be measured. It is also ideally suited to coupling with electrochemical corrosion techniques such as d.c. polarization and cyclic voltammetry enabling a thorough study of the dynamic characteristics of the corrosion processes.

The major use of ellipsometry has traditionally been in the study of passivation[64-70] for which thin films and smooth substrates are generally present. It has also however been widely used in the study of general corrosion phenomena[71-75] and recent advances have been made in the use of spectroscopic ellipsometry in conjunction with regression analysis.[76] This enables much more accurate and rapid data aquisition and analysis. Interest has also been shown in the last fifteen years in the use of ellipsometry to study localized corrosion processes such as pitting and stress corrosion cracking.[77,78] The development of more sophisticated and effective methods for characterizing rough surfaces and inhomogeneous films will probably increase the scope for ellipsometry in this field.

General reviews of the use of ellipsometry in corrosion are given by Hayfield[63,74] and Kruger.[73] Petit and Dabosi[77] review the use of ellipsometry in the investigation of localized corrosion processes up to 1980. For more general information concerning the use and application of ellipsometry the proceedings of five international conferences[79-83] are available together with several reviews.[84-86]

The aims of this research were to obtain a deeper insight into the corrosion mechanisms of Mg and Magnox in neutral and alkaline media from an investigation of the early stages of film growth and to relate changes observed in different environments during these early stages to the long term behaviour. It was hoped that this may suggest ways of reducing the long term corrosion rate and enable Magnox fuel elements to be stored for longer periods.

Most of the work was undertaken using an automatic nulling ellipsometer coupled with potential control of the corroding metal. Initial results obtained in a regime similar to that used by the C.E.G.B. for the storage of Magnox fuel elements (0.01 mol/dm^3 sodium hydroxide in the absence of chloride ions) indicated that substrate roughening was occurring. This resulted in a marked deviation in the ellipsometric results from theoretical predictions based on a smooth substrate model. A deeper understanding of this was sought - initially through theoretical methods of handling the roughness using computer simulations. Confirmation of this proposal of surface roughening was sought by the use of additional techniques - scanning electron microscopy and secondary ion mass spectrometry, the latter in conjunction with ion beam milling.

The initial results were partly attributed to a reduction in pH which caused the breakdown of the passive film formed on Magnox. This led to other ellipsometric studies under different solution conditions, by the presence of other ions and changes in pH. Maintaining the pH above 11.5 and below 14 prevented the breakdown of the passive film formed on Magnox and permitted easier analysis of the results using less complicated theories. Confirmation of these results was again sought by the use of secondary ion mass spectrometry and also scanning Auger spectroscopy, both in conjunction with ion beam milling. The results for Mg under similar conditions were anomalous however. This was originally postulated as being due to epitaxial film growth but similar results obtained using a single crystal of Mg made this unlikely.

CHAPTER 2 THEORY

2.1 Polarized light

2.1.1 Linear, circular and elliptical polarization

A light beam can be represented by two transverse waves, electric and magnetic, which are orthogonal to each other and to the propagation direction, fig. 2.1. In dealing with nonmagnetic media it is the usual practice to consider only the electric vector and to ignore the magnetic vector due to the weak interaction of matter with the magnetic field of the light wave.[85] This allows a monochromatic light beam to be completely described by its frequency, propagation direction, phase, amplitude and orientation of the electric vector.

In ellipsometry the electric wave is decomposed into two orthogonal components which are defined with respect to a plane of incidence. This plane refers to reflection of light from a plane surface and contains the incident, reflected and refracted waves, fig. 2.2. The component of the electric vector parallel to the plane of incidence is referred to as the p vector and the perpendicular component as the s vector.

These two vectors representing a transverse wave can be described mathematically by:

$$E_p = |E_p| \cos(\omega t + \delta_p) \qquad \text{.....(2.1)}$$

$$E_s = |E_s| \cos(\omega t + \delta_s) \qquad \text{.....(2.2)}$$

where E_p and E_s are the instantaneous values of the p and s vectors, $|E_p|$ and $|E_s|$ are the electric field amplitudes in each direction and δ_p and δ_s are the respective time-independent phase of each component.

Depending on the phase difference between the p and s components and their relative amplitudes various polarization states are produced, (fig. 2.3). It can be seen that linear polarization is produced for the condition that $\delta_p - \delta_s = n\pi$ where $n = \pm1, \pm2, \pm3, \ldots$ and circular polarization results from the case where the phase change is $\pm\pi/2$. The direction of circularly polarized light is defined in optics as being right-handed if on looking into the beam the direction of rotation of the electric vector appears clockwise and left-handed if the rotation appears anti-clockwise.[87]

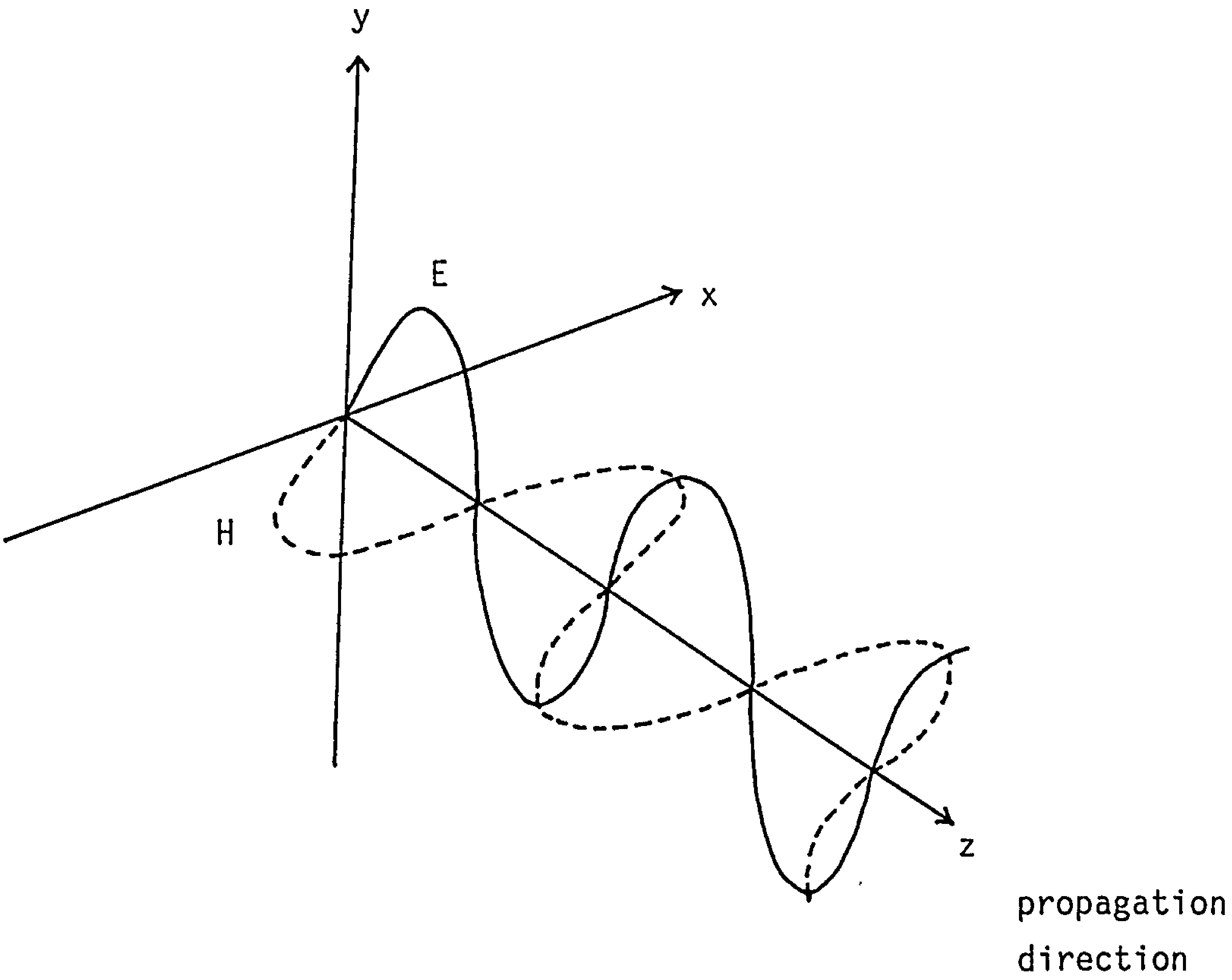

Fig. 2.1 Vector representation of a light beam

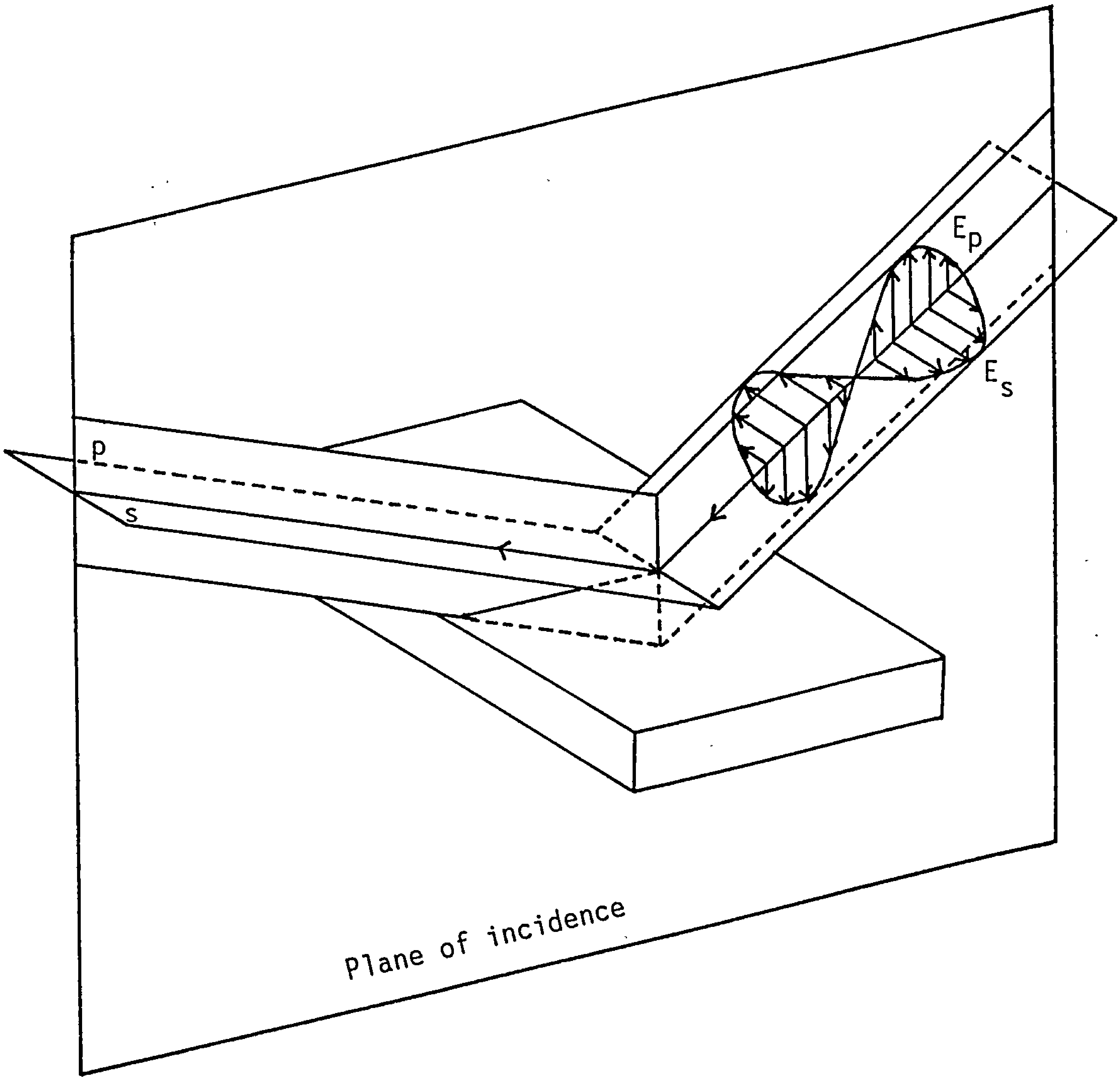

Fig. 2.2 Reflection of polarized light. The s and p components have electric vectors normal and parallel to the plane of incidence respectively.

Fig. 2.3 Polarization states produced by phase difference between p and s compounds

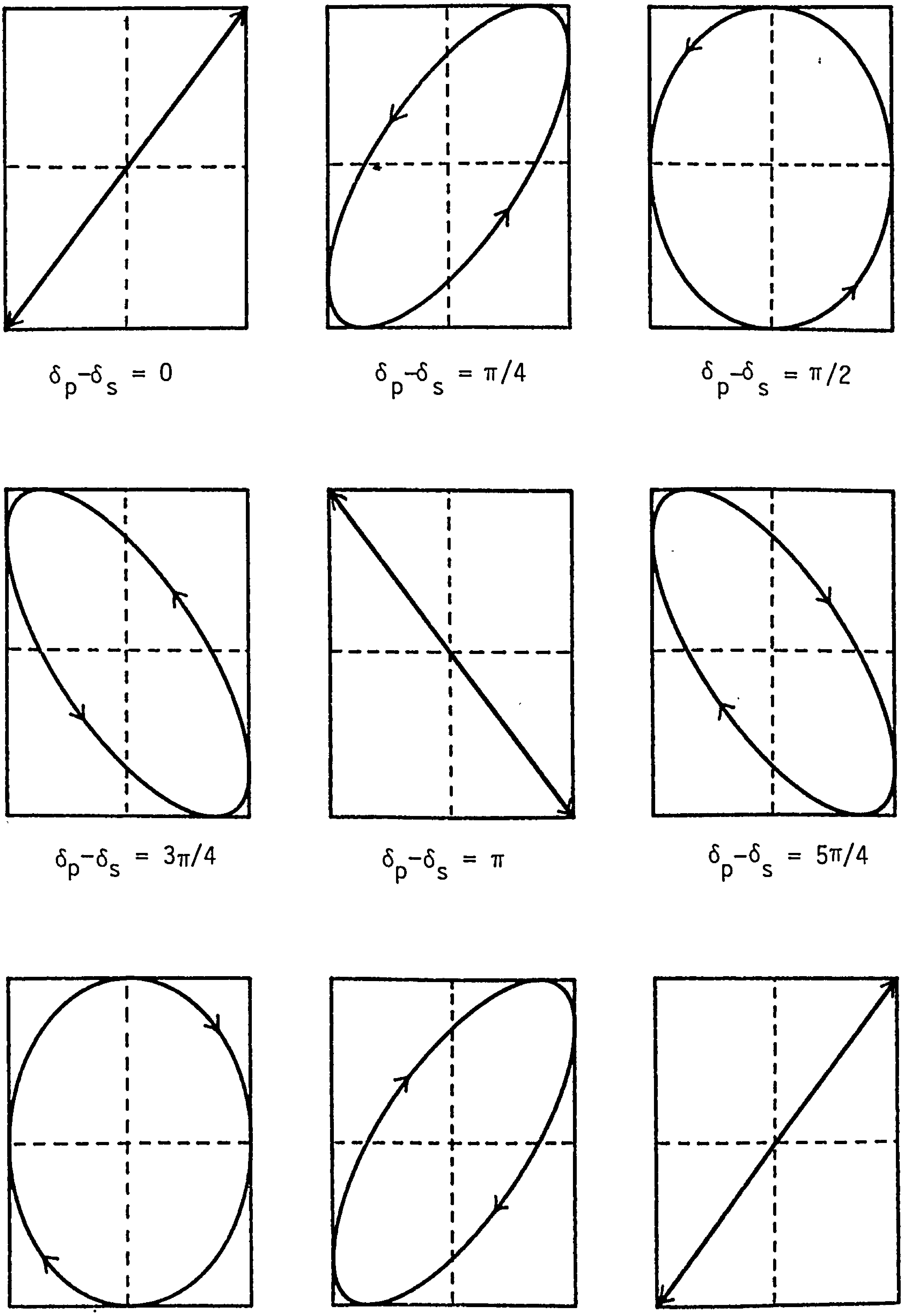

$\delta_p-\delta_s = 0$ $\delta_p-\delta_s = \pi/4$ $\delta_p-\delta_s = \pi/2$

$\delta_p-\delta_s = 3\pi/4$ $\delta_p-\delta_s = \pi$ $\delta_p-\delta_s = 5\pi/4$

$\delta_p-\delta_s = 3\pi/2$ $\delta_p-\delta_s = 7\pi/4$ $\delta_p-\delta_s = 2\pi$

There are a number of conventions used to describe the ellipse, which is the general form of polarized light. The ellipse can, for instance, be defined by two angles, one being the azimuth of the ellipse with respect to the positive x axis and the other being the tangent of the length ratio of minor axis to major axis. The most useful of these with regard to ellipsometry is to define the physical parameters Δ and Ψ:

$$\tan \Psi = \frac{|E_p|}{|E_s|} \qquad .....(2.3)$$

$$\Delta = \delta_p - \delta_s \qquad .....(2.4)$$

where:

$$0 \leqq \Psi \leqq 90°$$

$$0 \leqq \Delta \leqq 360°$$

These parameters are illustrated in fig. 2.4. Tan Ψ is a measure of the ratio of the amplitudes of the p and s components and Δ is the phase difference between them. The above definitions for Δ and Ψ are those decided upon by participants at the International Conference on Ellipsometry in 1968[88] and are convenient when using a nulling ellipsometer which measures Δ and Ψ directly. Other ellipsometers such as intensity measuring types do not directly measure Δ and Ψ and use different conventions.

2.1.2 Phasor notation

Nowadays phasor notation is used to describe monochromatic light as it enables easy mathematical manipulation of light phenomena to be undertaken without recourse to lengthy trigonometric calculations. This involves the use of complex exponential notation whereby equations (2.1) and (2.2) become:

$$E_x = |E_x| \, e^{i\delta_x} \qquad .....(2.5)$$

$$E_y = |E_y| \, e^{i\delta_y} \qquad .....(2.6)$$

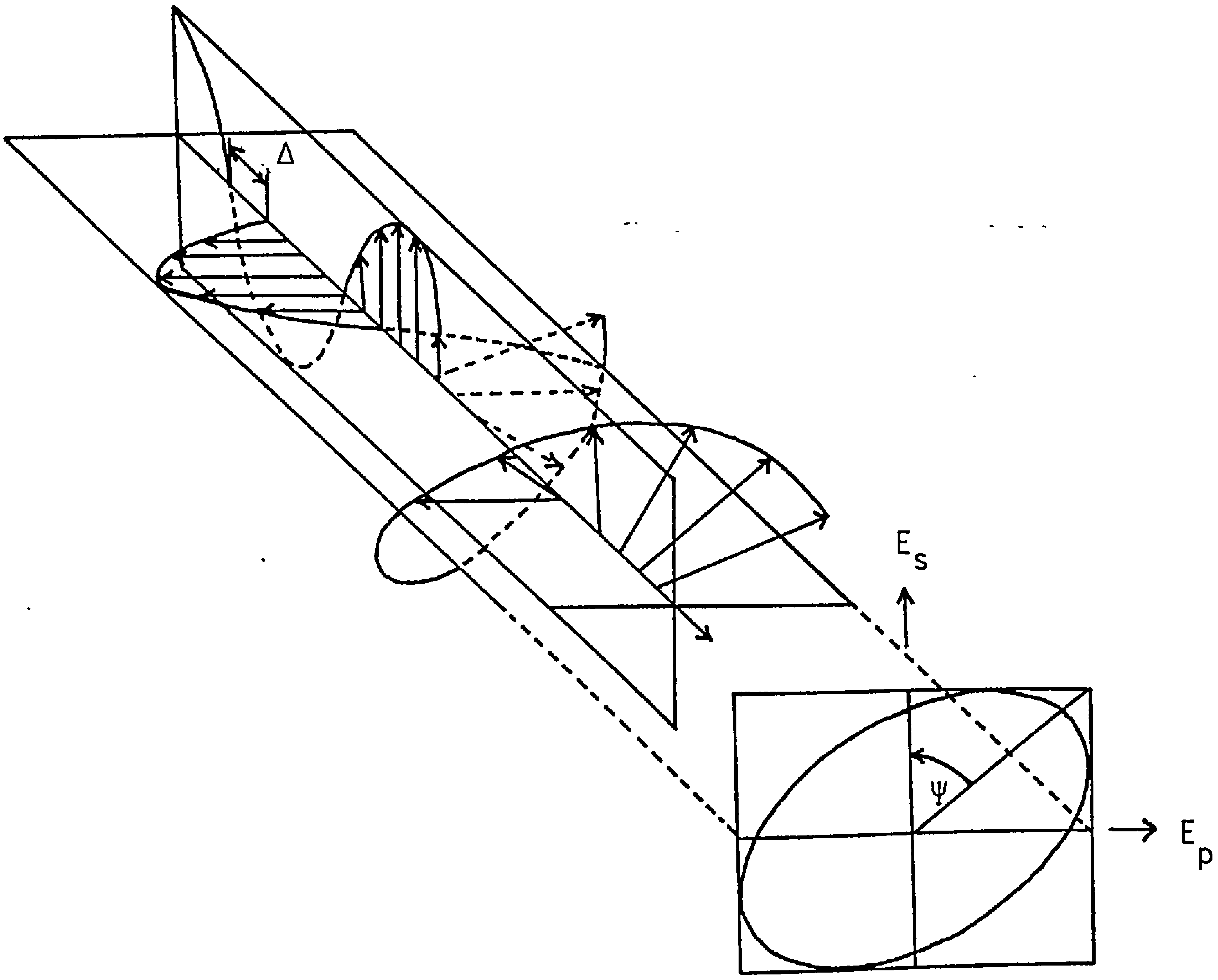

Fig. 2.4 Elliptical polarization resulting from the superposition of two orthogonal linear polarized states.

where x and y represent the two orthogonal vectors describing the light wave. This notation arises from the use of the Gauss equation:

$$e^{ix} = \cos x + i\sin x \qquad .....(2.7)$$

with the real part of the expansion representing the oscillation of the light wave. This is a convention to remove the time dependent ωt term as it is assumed for monochromatic light that ω is known and invariant.

2.1.3 Jones and Stokes vectors

The above equations, (2.5) and (2.6), can be conveniently expressed by means of Jones vectors which have the form of a 1 x 2 matrix. The upper element indicates the amplitude and phase of the x component and the lower the same parameters for the y component:

$$E = \begin{pmatrix} E_x\, e^{i\delta_x} \\ \\ E_y\, e^{i\delta_y} \end{pmatrix} \qquad .....(2.8)$$

The vectors are usually simplified by normalizing so the sum of the squares of the elements equals unity. They enable pure states of polarized light to be specified in a simple and compact form, some examples of which are shown in table 2.1.[89]

Jones vectors have the advantages that they are compact and can be used in the addition of coherent beams, i.e. beams which when superimposed produce an interference pattern. They cannot however be used with unpolarized or partially polarized light for which a different representation is used, the Stokes vectors. These again are column vectors but contain 4 rather than 2 elements:

$$\begin{bmatrix} I \\ M \\ C \\ S \end{bmatrix}$$

Table 2.1

Standard Normalized Jones Vectors for Various Forms of Polarized Light[89]

Polarization state	Standard normalized Jones vector
Linear horizontally polarized	$\begin{vmatrix} 1 \\ 0 \end{vmatrix}$
Linear polarization at -45°	$\frac{\sqrt{2}}{2} \begin{vmatrix} 1 \\ -1 \end{vmatrix}$
Right circularly polarized	$\frac{\sqrt{2}}{2} \begin{vmatrix} -i \\ 1 \end{vmatrix}$

I is the intensity of the beam, usually unity for the incident beam. M is the horizontal preference, C the preference for +45° inclination and S is the preference for right circular polarization. e.g. a horizontally polarized beam of unit intensity would have the following Stokes vector, (1,1,0,0). Other examples of Stokes vectors are given in table 2.2. Jones and Stokes vectors have the great advantage of simplicity in calculating the effect of various optical devices on a light beam. These calculations are performed by the Mueller calculus for Stokes vectors and the Jones calculus for Jones vectors, the former calculus being necessary if there are scattering devices present or partially polarized or unpolarized light. Table 2.3 gives examples of both Mueller and Jones vectors for various optical devices.

2.1.4 Jones and Mueller calculus

Both methods use matrix algebra whereby the normal rules of matrix multiplication are used to determine the effect of an optical device in the light wave. This can be illustrated by considering the effect of an ideal linear polarizer [M] with a transmission axis at -45° (see table 2.3) on an incident beam $[V_i]$ which is partially and left elliptically polarized (see table 2.2). The vector of the emerging beam $[V_e]$ is then calculated using the Mueller calculus:

$$[V_e] = [M][V_i] \qquad \text{.....(2.9)}$$

$$\therefore \quad [V_e] = \begin{bmatrix} .5 & 0 & -.5 & 0 \\ 0 & 0 & 0 & 0 \\ -.5 & 0 & -.5 & 0 \\ 0 & 0 & 0 & 0 \end{bmatrix} \begin{bmatrix} 6 \\ 3 \\ 2 \\ -1 \end{bmatrix} = \begin{bmatrix} 2 \\ 0 \\ -2 \\ 0 \end{bmatrix} \qquad \text{.....(2.10)}$$

$[V_e]$ can be seen to be 100% linearly polarized at -45°.

A series or train of optical devices can be represented by a series of matrix multiplications, e.g. for an incident beam, $[V_i]$ passing through devices $[M_A]$, $[M_B]$, and $[M_C]$ the emergent beam $[V_e]$ is given by:

$$[V_e] = [M_C][M_B][M_A][V_i] \qquad \text{.....(2.11)}$$

Table 2.2

Stokes Vectors for Various Forms of Polarized Light[89]

Polarization state	Normalized Stokes Vector [I,M,C,S]
Horizontally polarized unit intensity	[1,1,0,0]
Vertically polarized unit intensity	[1,-1,0,0]
Left circularly polarized unit intensity	[1,0,0,-1]

Table 2.3

Mueller Matrices of Basic Optical Devices[85]

Device	Mueller Matrix
Linear retarder (retardation δ)	$\begin{bmatrix} 1 & 0 & 0 & 0 \\ 0 & 1 & - & - \\ 0 & 0 & \cos\delta & \sin\delta \\ 0 & 0 & -\sin\delta & \cos\delta \end{bmatrix}$
Rotator (angle of rotation α)	$\begin{bmatrix} 1 & 0 & 0 & 0 \\ 0 & \cos2\alpha & \sin2\alpha & 0 \\ 0 & -\sin2\alpha & \cos2\alpha & 0 \\ 0 & 0 & 0 & 1 \end{bmatrix}$
Ideal polarizer (orientation θ)	$\frac{1}{2}\begin{bmatrix} 1 & \cos2\theta & \sin2\theta & 0 \\ \cos2\theta & \cos^2 2\theta & \sin2\theta\cos2\theta & 0 \\ \sin2\theta & \sin2\theta\cos2\theta & \sin^2 2\theta & 0 \\ 0 & 0 & 0 & 0 \end{bmatrix}$

The train of optical devices can be represented by a single overall 4 x 4 matrix, $[M_t]$, or Mueller matrix which is obtained by multiplying the matrices of all the optical devices. In the previous case $[M_t]$ is given by:

$$[M_t] = [M_C][M_B][M_A] \qquad .....(2.12)$$

A similar procedure is followed in the Jones calculus which is more compact but which cannot be used for depolarizing systems.

An alternative method of describing polarized light is to use the Poincare sphere which can be considered as a 3-dimensional Stokes vector whereby each polarization state is represented by its position on the sphere. The poles of the sphere represent circularly polarized light with points on the equator representing linear polarization. Other points on the sphere indicate elliptical polarization. Its main use has been in describing the effect of a retarder on a polarized beam in which the retarder is represented by an arc whose length is dependent on the retardance. The incident beam is at one end of the arc and then the other end represents the polarization of the emerging beam.

2.2 Reflection from bare surfaces

2.2.1 Reflection from a bare non-absorbing surface

The fact that the polarization of light changes on reflection was discovered in 1808 by E.L. Malus and in 1823 Fresnel developed equations to describe the reflection of light incident on the boundary between two isotropic dielectric media, fig.2.5. Although his theory of light was incorrect the equations have been proved correct experimentally and can be theoretically derived using Maxwell's equations.[90]

The Fresnel amplitude coefficients, r_p and r_s, describing the ratio of amplitudes of incident and reflected waves for the p and s components are:

$$r_{p_{1,2}} = \frac{E'_p}{E_p} \qquad .....(2.13)$$

$$r_{s_{1,2}} = \frac{E'_s}{E_s} \qquad .....(2.14)$$

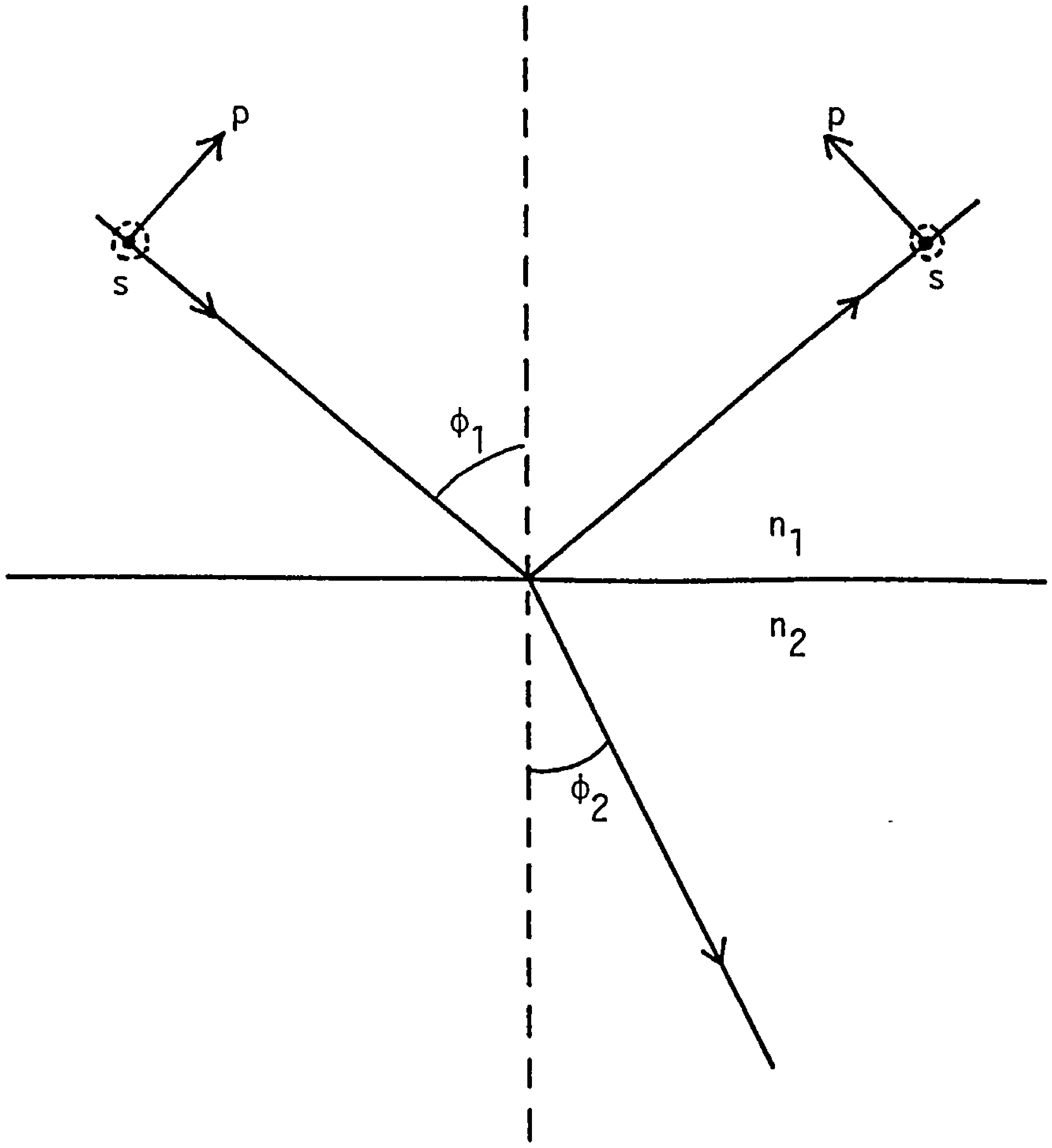

Fig. 2.5 Reflection and refraction at a dielectric interface

Symbols ϕ_1 and ϕ_2 are the angles of incidence and refraction respectively.

n_1 and n_2 are the refractive indices of mediums 1 and 2.

p and s are the components of the electric field vector (parallel (arrows) and perpendicular (circles)).

where a single prime refers to the reflected wave and unprimed to the incident wave.

Using his elastic theory of light Fresnel related these reflection coefficients to the angles of incidence and refraction and to the refractive indices of the media:

$$r_{p_{1,2}} = \frac{n_2\cos\phi_1 - n_1\cos\phi_2}{n_2\cos\phi_1 + n_1\cos\phi_2} \qquad .....(2.15)$$

$$r_{s_{1,2}} = \frac{n_1\cos\phi_1 - n_2\cos\phi_2}{n_1\cos\phi_1 + n_2\cos\phi_2} \qquad .....(2.16)$$

n_1 = refractive index of incident medium
n_2 = refractive index of second medium
ϕ_1 = angle of incidence
ϕ_2 = angle of refraction

Equations (2.15) and (2.16) can be rewritten using Snell's law:

$$n_1\sin\phi_1 = n_2\sin\phi_2 \qquad .....(2.17)$$

to give:

$$r_{p_{1,2}} = \frac{\tan(\phi_1 - \phi_2)}{\tan(\phi_1 + \phi_2)} \qquad .....(2.18)$$

$$r_{s_{1,2}} = \frac{-\sin(\phi_1 - \phi_2)}{\sin(\phi_1 + \phi_2)} \qquad .....(2.19)$$

2.2.2 Propagation of light in non-absorbing media

The optical constant n defined in equations (2.15)-(2.17) is a fundamental constant of the material.[91] It depends upon the interaction of the material with an electromagnetic wave oscillating at optical frequencies which for a non-absorbing medium can be shown by the time dependent solution of Maxwell's equations to be:

$$\underline{E} = \underline{E}_o \exp[i(\omega t - \frac{2\pi n}{\lambda} \underline{s}.\underline{r}.)] \qquad .....(2.20)$$

$\underline{E}_o$ is the wave amplitude, $\underline{E}$ the instantaneous value of the electric field vector, $\underline{r}$ a position vector in an arbitrary co-ordinate system, $\underline{s}$ a unit vector in the propagation direction, λ the vacuum wavelength and ω the frequency of radiation.

The index of refraction, n, of the medium is defined by:

$$n = \frac{c}{v} = \sqrt{\frac{\varepsilon\mu}{\varepsilon_o\mu_o}} \qquad .....(2.21)$$

where c is the velocity of light in vacuo, v is the phase velocity of the wave in the medium, ε is the dielectric constant or permittivity of the medium, ε_o the permittivity of free space, μ and μ_o the permeability of the medium and free space respectively. For most non-magnetic materials the ratio μ/μ_o is approximately unity so that equation (2.21) can be simplified to:

$$n = \sqrt{\frac{\varepsilon}{\varepsilon_o}} \qquad .....(2.22)$$

The above equation is known as Maxwell's relation.

2.2.3 Propagation of light in absorbing media

For a wave travelling in an absorbing medium equation (2.20) becomes:

$$\underline{E} = \underline{E}_o[i(\omega t \frac{-2\pi n}{\lambda} \underline{s}.\underline{r}.)] \exp[\frac{-2\pi k}{\lambda} \underline{s}.\underline{r}.] \qquad .....(2.23)$$

The additional terms represent the attenuation of the wave due to the damping effect of the conduction electrons as the wave passes through the medium. This gives rise to a complex refractive index, $\hat{n}$, where:

$$\hat{n} = n - ik \qquad .....(2.24)$$

n is the real part of the refractive index and k the extinction coefficient.

The reduction in intensity of the wave as it propagates into the medium is given by the reduction in the square of the amplitude:

$$I = I_o \exp^{-\alpha Z} \qquad .....(2.25)$$

where Z is increasing distance normal to the surface and α is the linear absorption coefficient, given by:

$$\alpha = \frac{4\pi k}{\lambda} \qquad .....(2.26)$$

The value of Z at which the intensity of the wave decreases by a factor e^{-1} is known as the penetration depth and is dependent on k and λ:

$$Z = \frac{\lambda}{4\pi k} \qquad .....(2.27)$$

For a material to be transparent the penetration depth must be large compared to its thickness. For most metals however the penetration depth is very small, e.g. for Cu it is about 0.6 nm in the ultra-violet.[92]

The need for a complex refractive index also results in the dielectric constant being complex:

$$\frac{\hat{\varepsilon}}{\varepsilon_o} = \varepsilon' - i\,\varepsilon'' \qquad .....(2.28)$$

ε' represents the real part of the dielectric constant and ε'' the imaginary part.

Using equations (2.22), (2.24) and (2.28), ε' and ε'' can be related to n and k:

$$\varepsilon' = n^2 - k^2 \qquad .....(2.29)$$

$$\varepsilon'' = 2nk \qquad .....(2.30)$$

2.2.4 Reflection from a film-free metallic surface

The need to use a complex refractive index means that Snell's law, equation (2.17), will require that the angle of refraction and the Fresnel reflection coefficients are complex.

The Fresnel reflection coefficients, $\hat{r}_p$ and $\hat{r}_s$, are usually expressed in phasor notation:

$$\hat{r}_p = \frac{|E'_p|}{|E_p|} e^{i(\zeta'_p - \zeta_p)} \quad .....(2.31)$$

$$\hat{r}_s = \frac{|E'_s|}{|E_s|} e^{i(\zeta'_s - \zeta_s)} \quad .....(2.32)$$

ζ_p and ζ_s are the absolute phase of the p and s components of the incident beam and ζ'_p and ζ'_s are the absolute phases of the p and s components for the reflected beam. $|E_p|$ and $|E_s|$ are the amplitudes of the incident beam components and $|E'_p|$ and $|E'_s|$ the amplitudes for the reflected beam.

Equations (2.31) and (2.32) can be rewritten as:

$$\hat{r}_p = |r_p| e^{i\delta_p} \quad .....(2.33)$$

$$\hat{r}_s = |r_s| e^{i\delta_s} \quad .....(2.34)$$

where $|r_p|$ and $|r_s|$ are the ratio of amplitude of the reflected and incident components and δ_p and δ_s are the phase change of the p and s components on reflection.

In ellipsometry the most useful parameter is ρ, the ratio of the complex Fresnel reflection coefficients:

$$\rho \doteq \frac{\hat{r}_p}{\hat{r}_s} = \frac{|r_p|}{|r_s|} e^{i(\delta_p - \delta_s)} \quad .....(2.35)$$

From equations (2.3) and (2.4):

$$\rho = \tan\Psi\, e^{i\Delta} \qquad .....(2.36)$$

This is known as the fundamental equation of ellipsometry. Ditchburn[93] has developed trigonometric equations for Δ and Ψ avoiding the use of complex notation:

$$n^2 - k^2 - \sin^2\phi = \frac{t^2\,(\cos 2\Psi - \sin^2 2\Psi \sin^2\Delta)}{(1 + \sin 2\Psi \cos\Delta)^2} \qquad .....(2.37)$$

$$2nk = \frac{t^2 \sin 4\Psi \sin\Delta}{(1 + \sin 2\Psi \cos\Delta)^2} \qquad .....(2.38)$$

$$t = \sin\phi\, \tan\phi \qquad .....(2.39)$$

ϕ is the angle of incidence.

Alternative trigonometric equations have been developed by Koenig.[94]

2.3 Characterization of bare surfaces using ellipsometry

2.3.1 Factors affecting the values of Δ and Ψ measured for a bare surface

Determining the optical constants of a bare surface has both theoretical and practical importance and can in principle be easily performed using ellipsometry. The parameters Δ and Ψ measured for a bare surface have been defined previously, equations (2.3), (2.4) and (2.36). These values depend upon a number of factors:

1. The optical constants of the incident medium, usually air, vacuum or a transparent solution in which case n is not complex.

2. The optical constants of the substrate, usually complex, i.e. $\hat{n} = n - ik$.

3. The angle of incidence.

4. The wavelength of light used.

In nulling ellipsometry the normal procedure is to fix the angle of incidence and wavelength of light. As n for the medium is known or can be easily obtained, e.g. by an Abbe refractometer, then n and k for the substrate can be obtained. There are several equations whereby this calculation can be performed, one of which is:

$$n_1 = n_0 \tan\phi \left[1 - \frac{4\rho}{(1+\rho)^2} \sin^2\phi\right]^{\frac{1}{2}} \qquad \text{.....(2.40)}$$

n_1 and n_0 are the refractive indices of the substrate and incident medium respectively. ϕ is the angle of incidence and ρ has been defined in equation (2.36). The use of complex notation can be avoided by the use of either Ditchburn's equations[93] (equations (2.37)-(2.39)) or by those of Koenig.[94]

If the angle of incidence, wavelength of light and incident medium remain constant then there is a one-to-one relationship between n and k of the substrate and Δ and Ψ for the bare surface. This can clearly be seen in the n,k nomogram in fig. 2.6. The areas into which metals, semiconductors and insulators fall are found in distinct regions as illustrated by fig. 2.7. Insulators are found either along the $\Delta = 0$ or $\Delta = 180°$ axis which is a result of the differences in phase shifts, r_p and r_s being either 0 or π. The angle of incidence at which the change occurs from 0 to π radians is known as the Brewster angle and is dependent upon the refractive index of the dielectric and the incident medium. This is considered in more detail in section 2.3.3.

Semiconductors have frequency-dependent optical constants usually with very low k values providing that the frequency of incident radiation is not at a band transition frequency. The low k values arise from the dependence of n and k on the conductivity:

$$2nk = \frac{\sigma}{\omega} \qquad \text{.....(2.41)}$$

where σ = conductivity and ω = frequency.
At the wavelength of light used in figs. 2.6 and 2.7 (632.8 nm) semiconductors have a very low conductivity and as n typically lies in the range 2.5 to 4.5 k is very small.

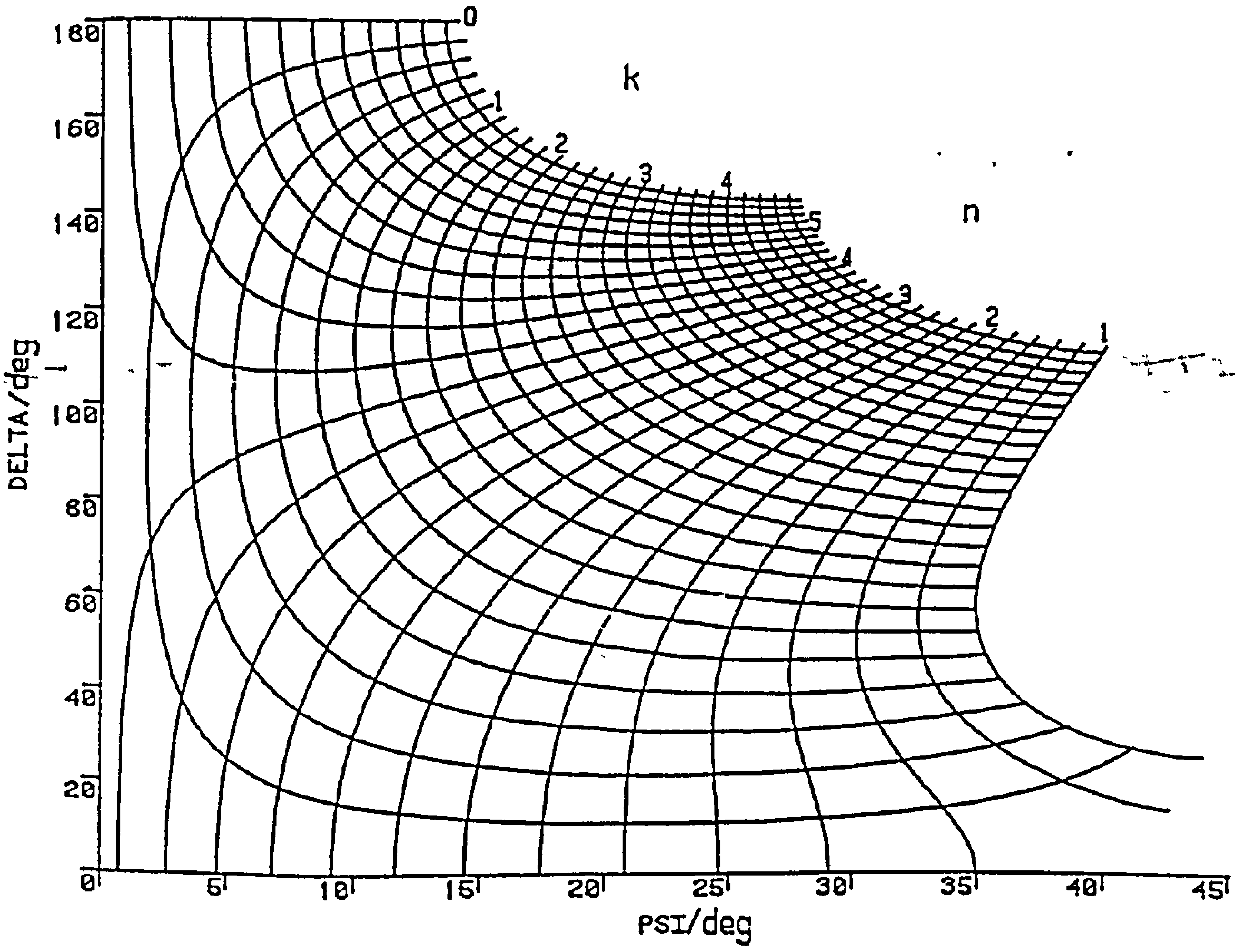

$\phi = 70°$, $\lambda = 632.8$ nm, n(medium) = 1.334

Fig. 2.6 n,k nomogram showing one to one relationship between Δ and Ψ and the optical constants

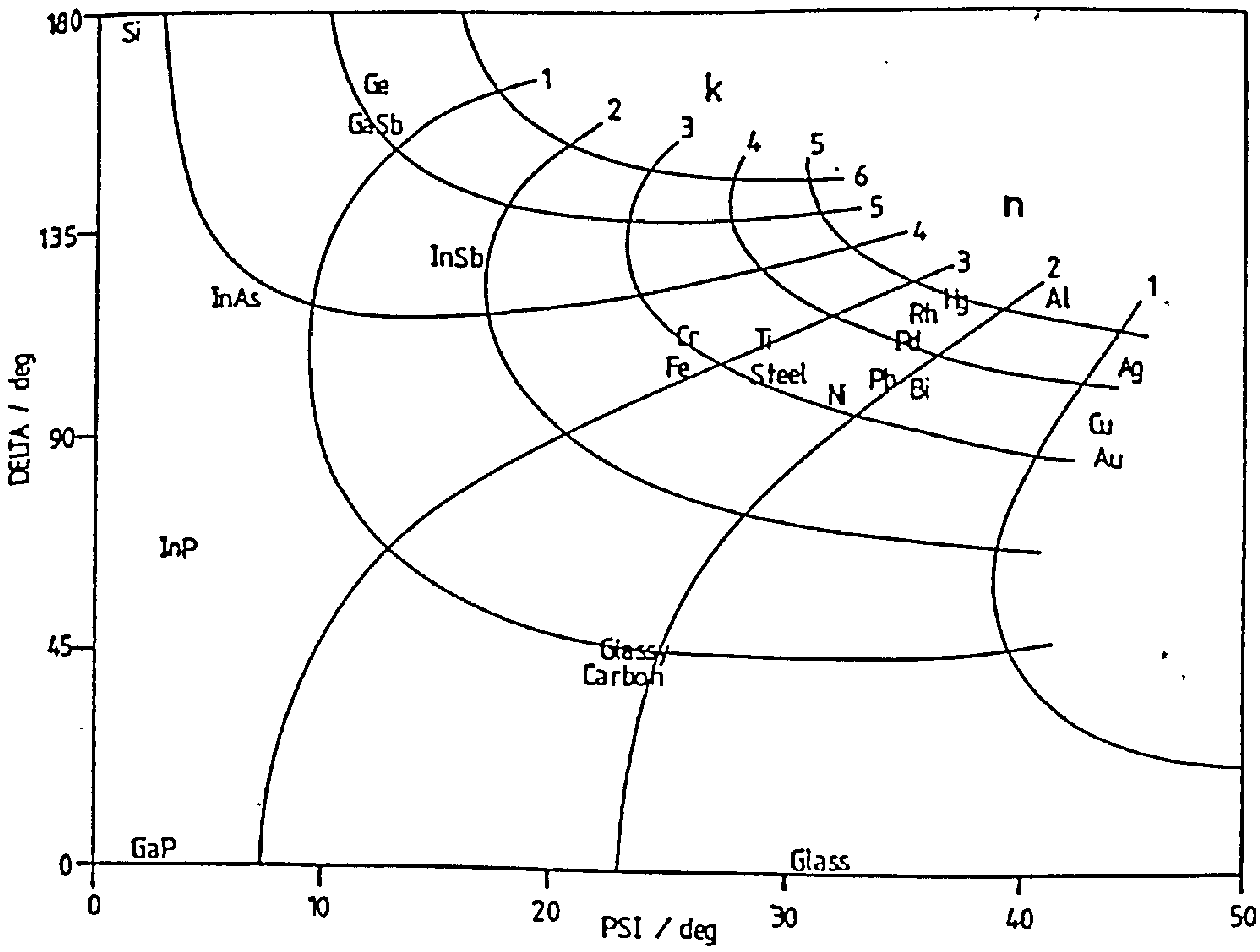

Fig. 2.7 A simplified nomogram illustrating the position of some metals, semi-conductors and insulators

Metals have much higher conductivities and widely varying n and k values. Their optical behaviour can be described using a theory proposed by Drude. This is described in the next section.

2.3.2 Frequency dependence of the optical constants

The frequency dependence of the dielectric constant arises from the effect of the oscillating electromagnetic field on the distortion of the electron distribution and molecular geometry of the material. The latter effect is known as polarization and is related to the dielectric constant by:

$$P = \frac{\varepsilon - 1}{4\pi} E \qquad \text{.....(2.42)}$$

E = electric field
P = electronic polarization

At optical frequencies the only contribution to the polarization is from the effect of the electron cloud. At these high frequencies the molecules cannot orientate themselves sufficiently rapidly for the polarization of permanent dipoles to contribute, and the atomic nuclei are too sluggish to follow the oscillations for the polarization of bonds in polar molecules to be important.

Classically the effect of frequency at these wavelengths on the polarization of insulators was treated by Lorentz. His model is of an electron bound to an infinitely heavy nucleus by an elastic force analogous to a small mass bound to a much heavier mass by springs. Drude[95] considered the case of dispersion for metals using a free electron model, by equating the restoring force in Lorentz's model to zero. He arrived at an equation relating ε' and ε" to frequency (ω):

$$\varepsilon' = 1 - \frac{4\pi Ne^2}{m} \frac{1}{\omega^2 + \Gamma^2} \qquad \text{.....(2.43)}$$

$$\varepsilon'' = \frac{4\pi Ne^2}{m} \frac{\Gamma}{\omega(\omega^2 + \Gamma^2)} \qquad \text{.....(2.44)}$$

e and m are the electronic charge and mass respectively, $\mathcal{N}$ the total number of atoms per unit volume. Γ is the damping constant in the Lorentz model which is related to the mean free time between collisions. The natural frequency with which the free electrons and positive ions, or plasma, within a metal vibrate is known as the plasma frequency, ω_p. At frequencies below this critical value the metal behaves as if it were a strongly absorbing material with a reflectivity near unity and a complex refractive index. This results in the intensity of the penetrating wave falling off exponentially as it propagates into the metal. At frequencies higher than ω_p the material behaves as if it were transparent with a real n and a rapidly decreasing reflectivity as the frequency increases.

The Drude model can successfully explain the optical behaviour of some metals such as Mg[96] and Al[97] both of which exhibit a marked reduction in reflectance at the plasma frequency. The reflectance of other metals such as Cu however does not show a sharp transition but rather a series of absorption bands, and for other metals such as Ag a high reflectivity can be seen at frequencies above ω_p.

2.3.3 The effect of angle of incidence on Δ and Ψ

In addition to being dependent on the optical constants of the surrounding media and substrate and the wavelength, Δ and Ψ are also dependent on the angle of incidence. By considering the Fresnel equations for an insulator, equations (2.18) and (2.19), and Snell's law, equation (2.17), it can be seen that for the case of $n_2 > n_1$ then $\phi_1 > \phi_2$ and r_s will be negative for all values of ϕ_1 whereas r_p is positive from 0° decreasing to zero at the Brewster angle, ϕ_p, where $\phi_1 + \phi_2 = 90°$. Then as ϕ_1 continues to increase r_p becomes negative. When either r_p or r_s are negative then there will be a phase change of π radians on reflection. For metals $\hat{n}$ is complex and there is no angle of incidence for which r_p disappears. This is illustrated in fig. 2.8 in which the change in r_p and r_s is shown for some dielectrics and metals.

The n, k nomogram in fig. 2.6 is for an angle of incidence of 70°, a commonly used value in ellipsometry as it gives large changes in Δ and Ψ for a given increment in film thickness and gives a large separation in the $\Delta\Psi$ plane for the optical constants of two bare

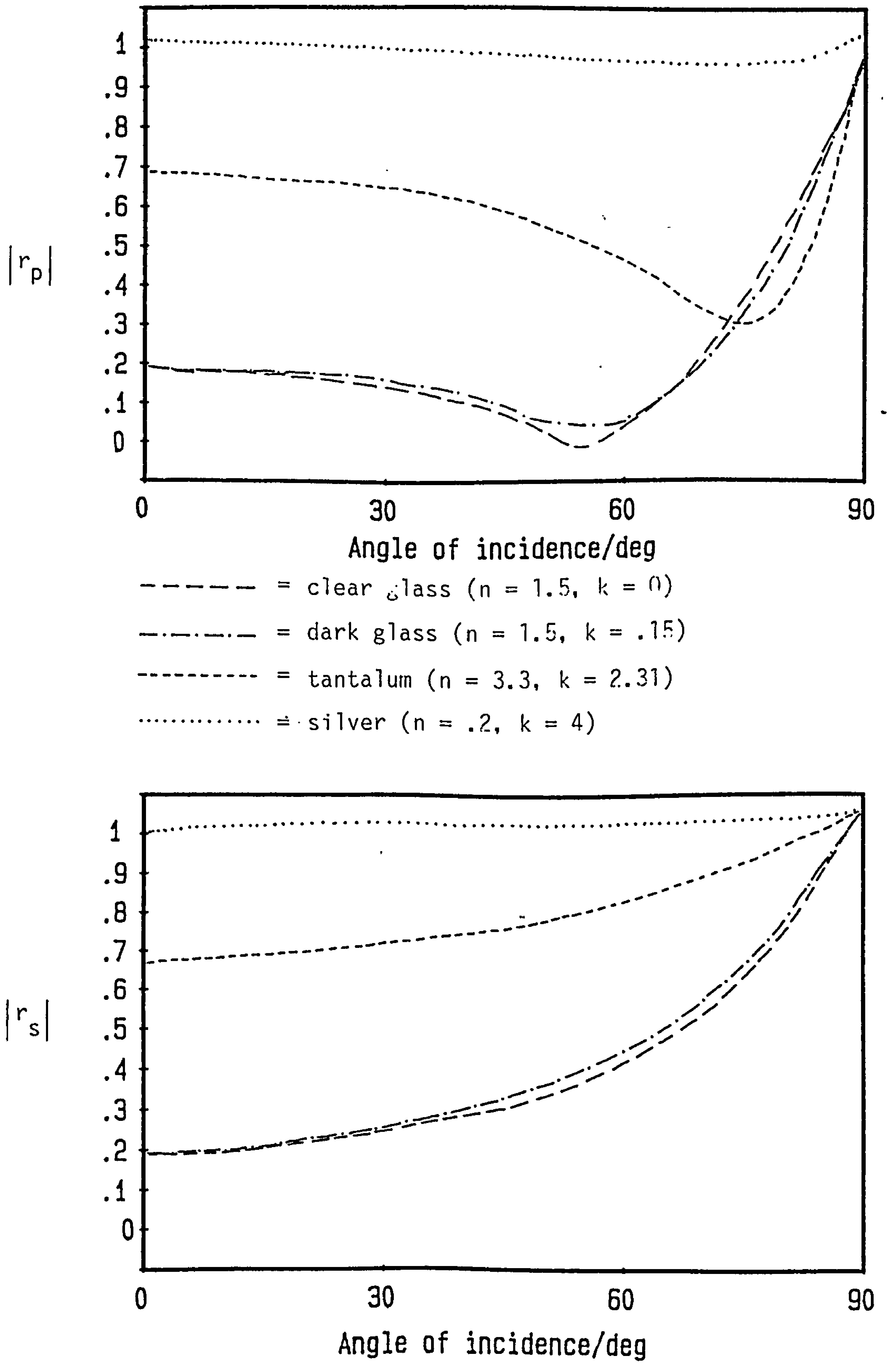

Fig. 2.8 Variation of reflection coefficients with angle of incidence

metallic substrates. This latter point can be illustrated by examination of the nomograms for other angles of incidence, figs. 2.9-2.11. At 70°, fig. 2.6, the lines on the nk net are well separated whereas on moving to higher or lower angles of incidence the lines are compressed into a much smaller region reducing sensitivity and making determination of theoretical constants from Δ and Ψ values more difficult.

2.4 Reflection from a smooth isotropic film covered surface

This situation was considered by Drude in 1889 for a perfectly flat surface on which there is a completely uniform film whose outer surface is flat and parallel to the substrate. When a light beam is incident on a film-covered surface the beam becomes divided into a number of beams, fig. 2.12, by multiple reflections within the film. The overall effect can be calculated by summing all the reflections for both the p and s components from both the film/medium interface and the substrate/film interface. This gives rise to an overall complex reflection coefficient, $\hat{R}$, for the p and s component:

$$\hat{R}_{p,s} = \frac{\hat{r}_{12\,p,s} + \hat{r}_{23\,p,s}\exp(-iD)}{1 + \hat{r}_{12\,p,s}\,\hat{r}_{23\,p,s}\,\exp(-iD)} \qquad .....(2.45)$$

D is the phase delay due to traversal of the film and is given by:

$$D = \frac{2\pi d n_2 \cos\phi_2}{\lambda_o} \qquad .....(2.46)$$

where d is the film thickness, n_2 the refractive index of the film, ϕ_2 the complex angle of refraction of the film and λ_o the vacuum wavelength of light.

The Fresnel reflection coefficients in equation (2.45) are:

$$r_{12\,p} = \frac{\tan(\phi_1 - \phi_2)}{\tan(\phi_1 + \phi_2)} \qquad .....(2.47a)$$

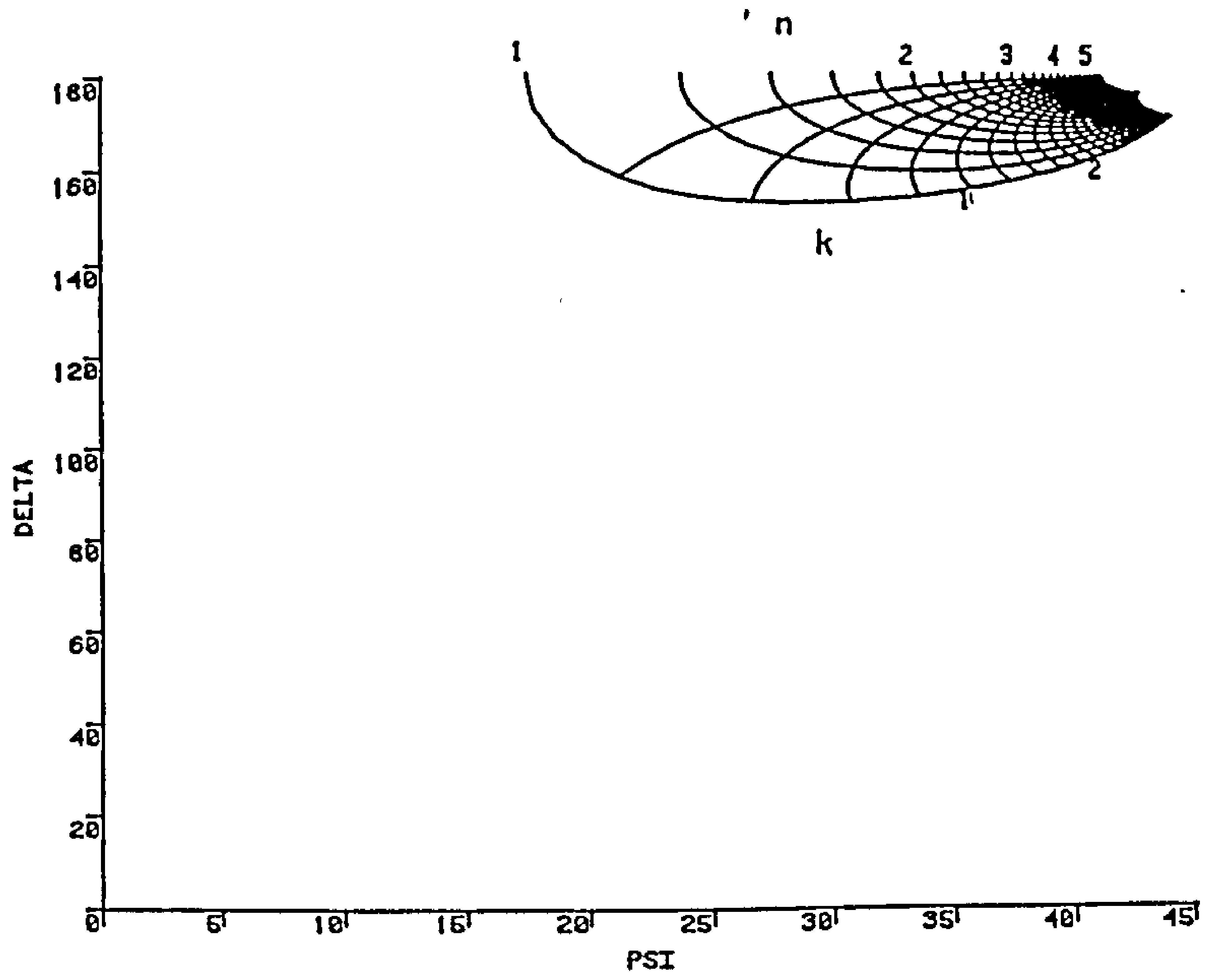

Fig. 2.9
n, k nomogram angle
of incidence = 30°

Fig. 2.10
n, k nomogram angle
of incidence = 85°

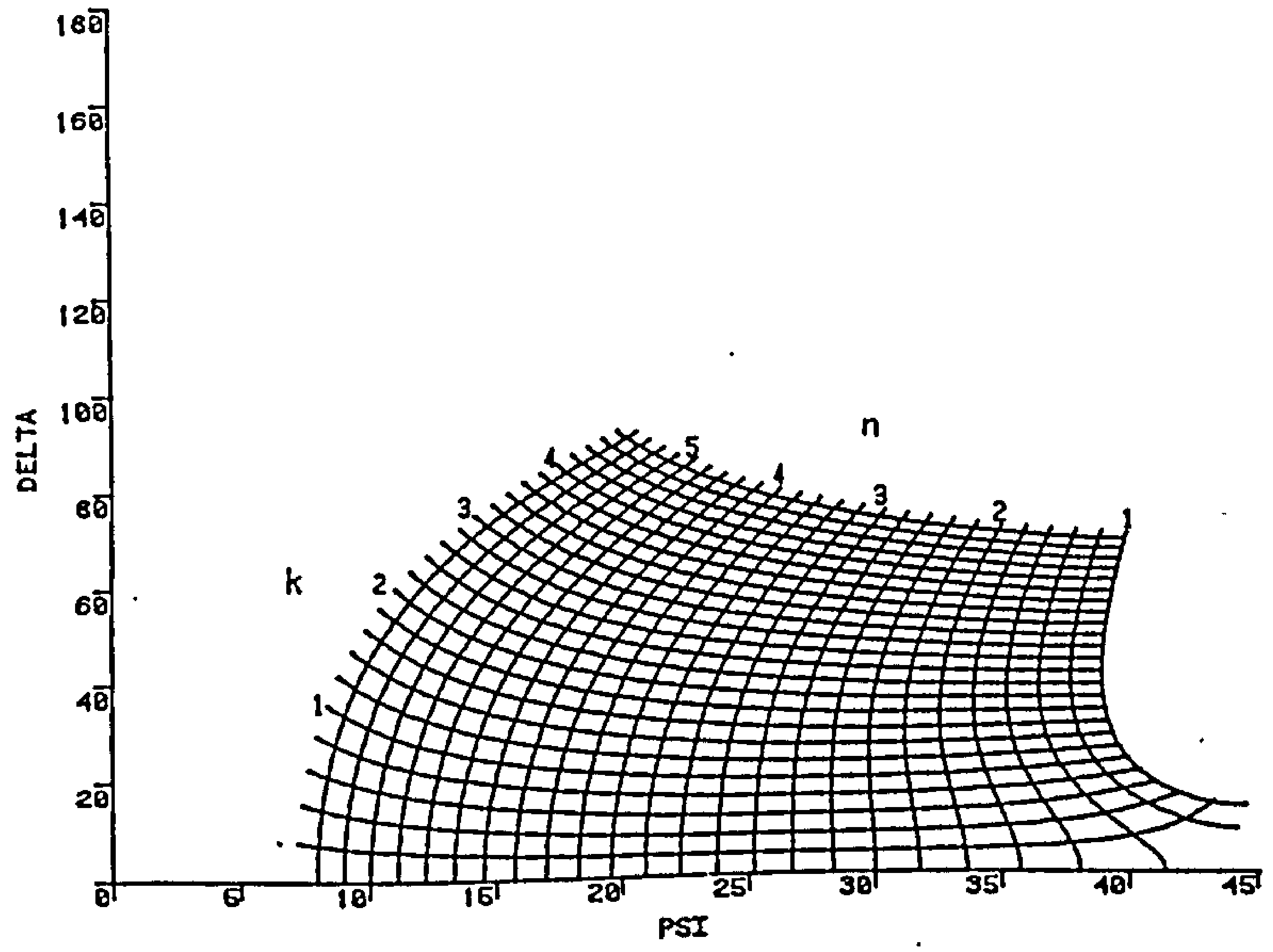

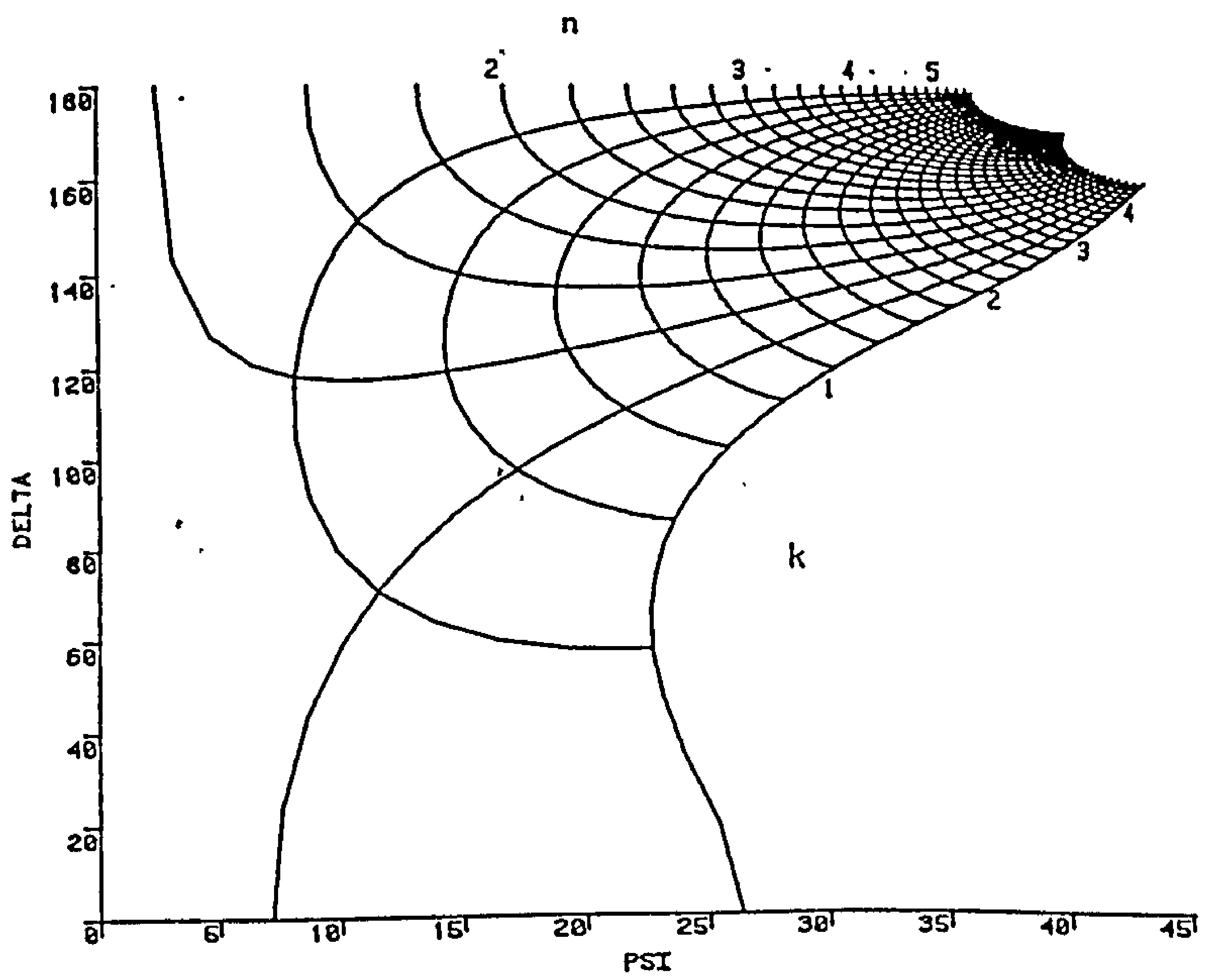

Fig. 2.11
n, k nomogram angle
of incidence = 45°

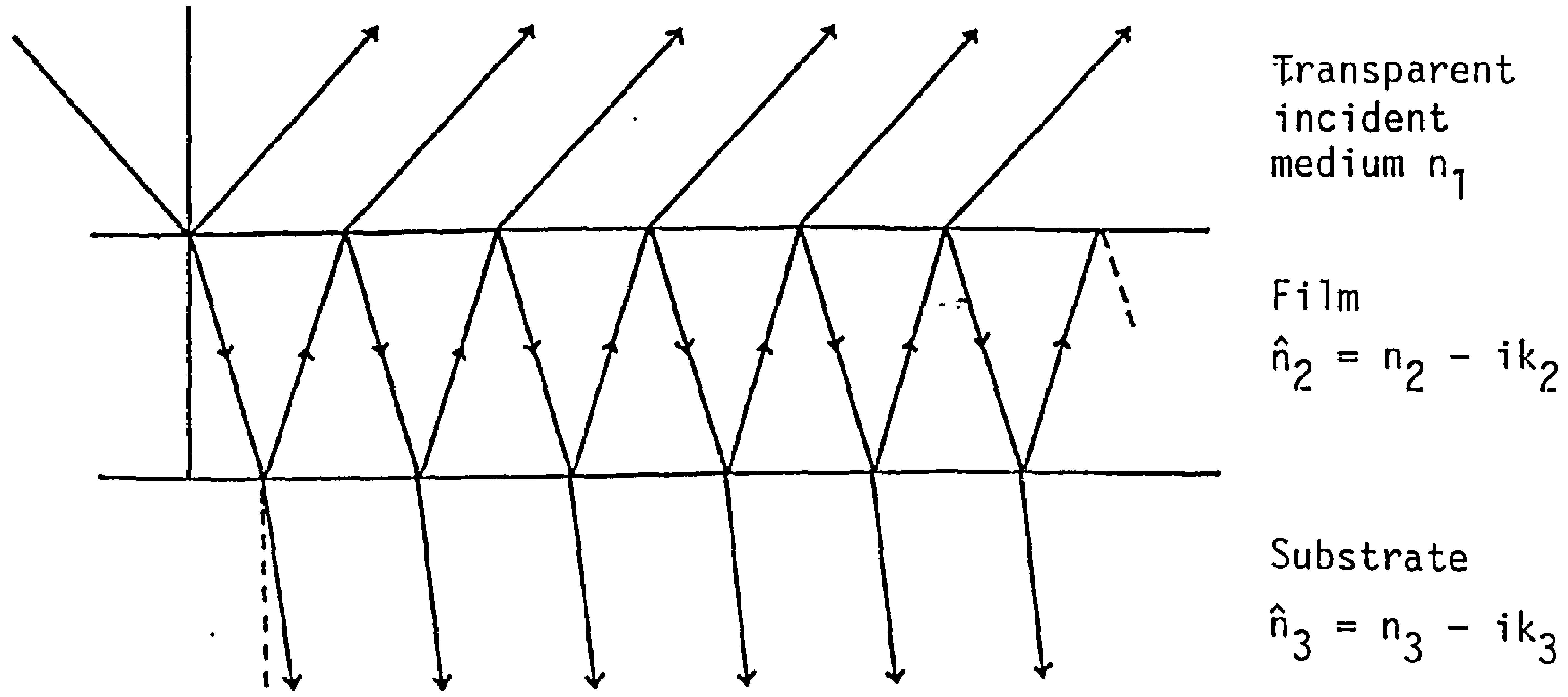

Fig. 2.12 Multiple beam reflecting from an idealised film covered surface

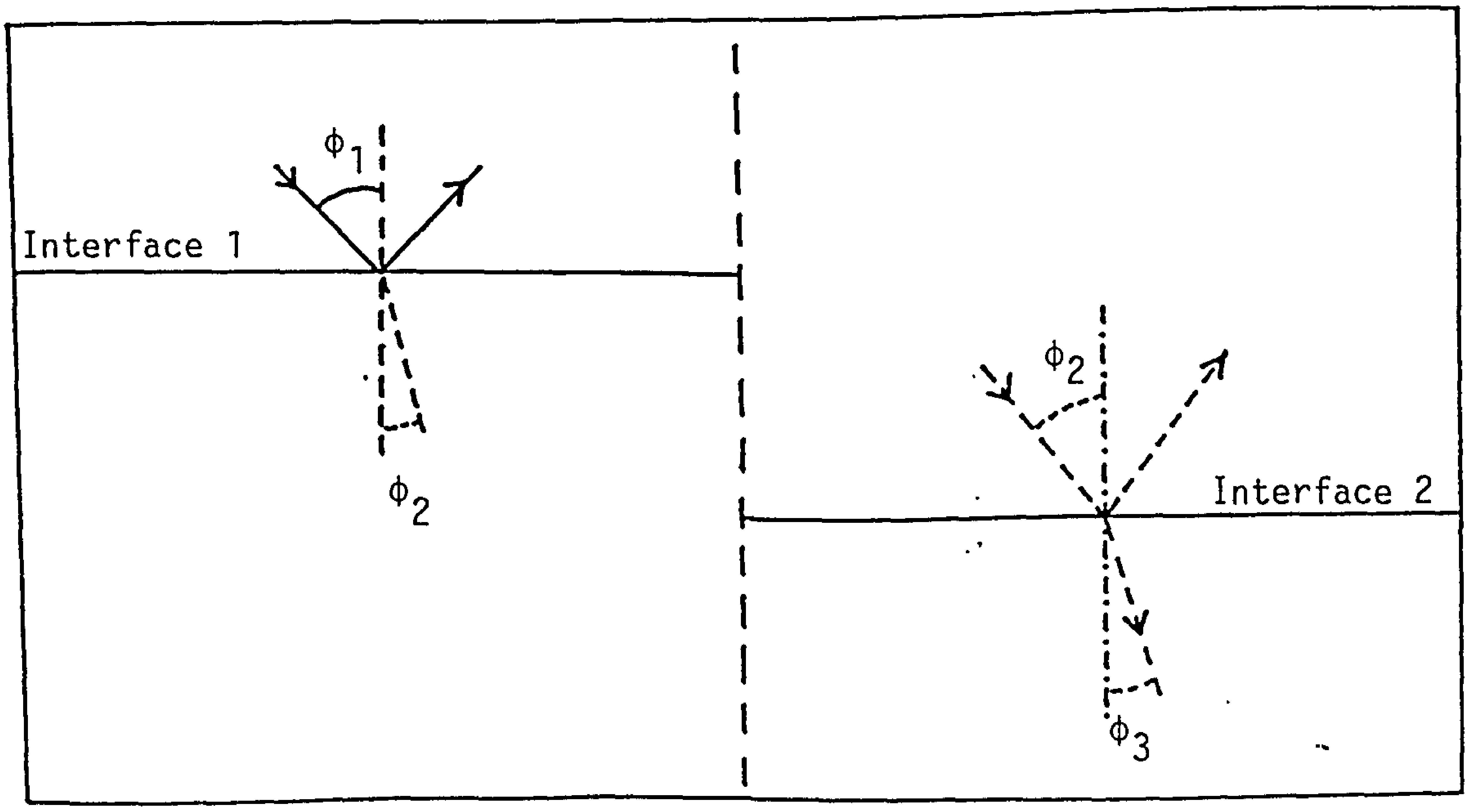

Fig. 2.13 Reflection from a film covered surface

$$r_{12\,s} = \frac{-\sin(\phi_1 - \phi_2)}{\sin(\phi_1 + \phi_2)} \quad \text{.....(2.47b)}$$

$$r_{23\,p} = \frac{\tan(\phi_2 - \phi_3)}{\tan(\phi_2 + \phi_3)} \quad \text{.....(2.47c)}$$

$$r_{23\,s} = \frac{-\sin(\phi_2 - \phi_3)}{\sin(\phi_2 + \phi_3)} \quad \text{.....(2.47d)}$$

where $\phi_{1,2,3}$ are indicated in fig. 2.13.

The three angles are related by Snell's law:

$$n_1\sin\phi_1 = n_2\sin\phi_2 = n_3\sin\phi_3 \quad \text{.....(2.48)}$$

Again the ratio ρ of the reflection coefficients is determined:

$$\rho = \frac{\hat{R}_p}{\hat{R}_s} \quad \text{.....(2.49)}$$

$$\rho = \frac{[\hat{r}_{p12} + \hat{r}_{p23}\exp(-2iD)][1 + \hat{r}_{s12}\,\hat{r}_{s23}\exp(-2iD)]}{[\hat{r}_{s12} + \hat{r}_{s23}\exp(-2iD)][1 + \hat{r}_{p12}\,\hat{r}_{p23}\exp(-2iD)]} \quad \text{...(2.50)}$$

$$= \tan\Psi\, e^{i\Delta} \quad \text{.....(2.36)}$$

The ellipsometric parameters Δ and Ψ can thus be related to the optical properties of a three-phase system. The use of the above equations in modelling single and multilayered films by computer methods is described in chapter 3.

2.5 Other experimental optical methods for characterizing surfaces

Although ellipsometry has traditionally been used to determine optical constants[98] and is considered to be the most precise method it suffers from either being slow or expensive if sophisticated fully automated instruments are used. This has led to the use of reflectance methods whereby the reflectivity, R, is determined rather than

Δ and Ψ. The reflectivity is related to the Fresnel reflection coefficients by:

$$R = |r_{12}|^2 = r_{12}.r_{12}^* \qquad .....(2.51)$$

r_{12}^* is the complex conjugate of r_{12}.

By analogy with the Δ and Ψ nomogram, fig. 2.14 shows the relationship between n and k and the reflectivity at normal incidence. In this case however an experimental value for the reflectivity at a fixed wavelength and angle of incidence gives rise to an infinite number of solutions of n and k. Reflectance measurements can and have been widely used to calculate optical constants of bare surfaces and for films grown on the surface although the data requires more manipulation than in ellipsometry due to the more complicated nature of the equations.

The methodsby which the optical constants of a bare metal surface can be obtained by measurements of the reflectivity of light polarized parallel to and perpendicular to the plane of incidence at various angles of incidence are discussed by McIntyre.[99] Alternatively the relative phase information which can be obtained directly from ellipsometry can be obtained indirectly in reflectance measurements by means of the Kramers-Kronig analysis.[100] This method uses the Kramers-Kronig dispersion relations whereby the overall absorption spectrum of a material can be related to a dispersion property such as refractive index. In practice knowing the reflectivity over the whole frequency range is impossible but at lower frequencies the reflectivity is frequency independent and at higher frequencies extrapolation methods can be used. Hageman _et_ _al_.[96] use this method in determining the optical constants of various metals including Mg.

Reflectance methods have also been widely used in the analysis of film-covered surfaces although again data manipulation is far more complicated than in ellipsometry. For a three-phase system the reflectivity is given by equations (2.45) and (2.49):

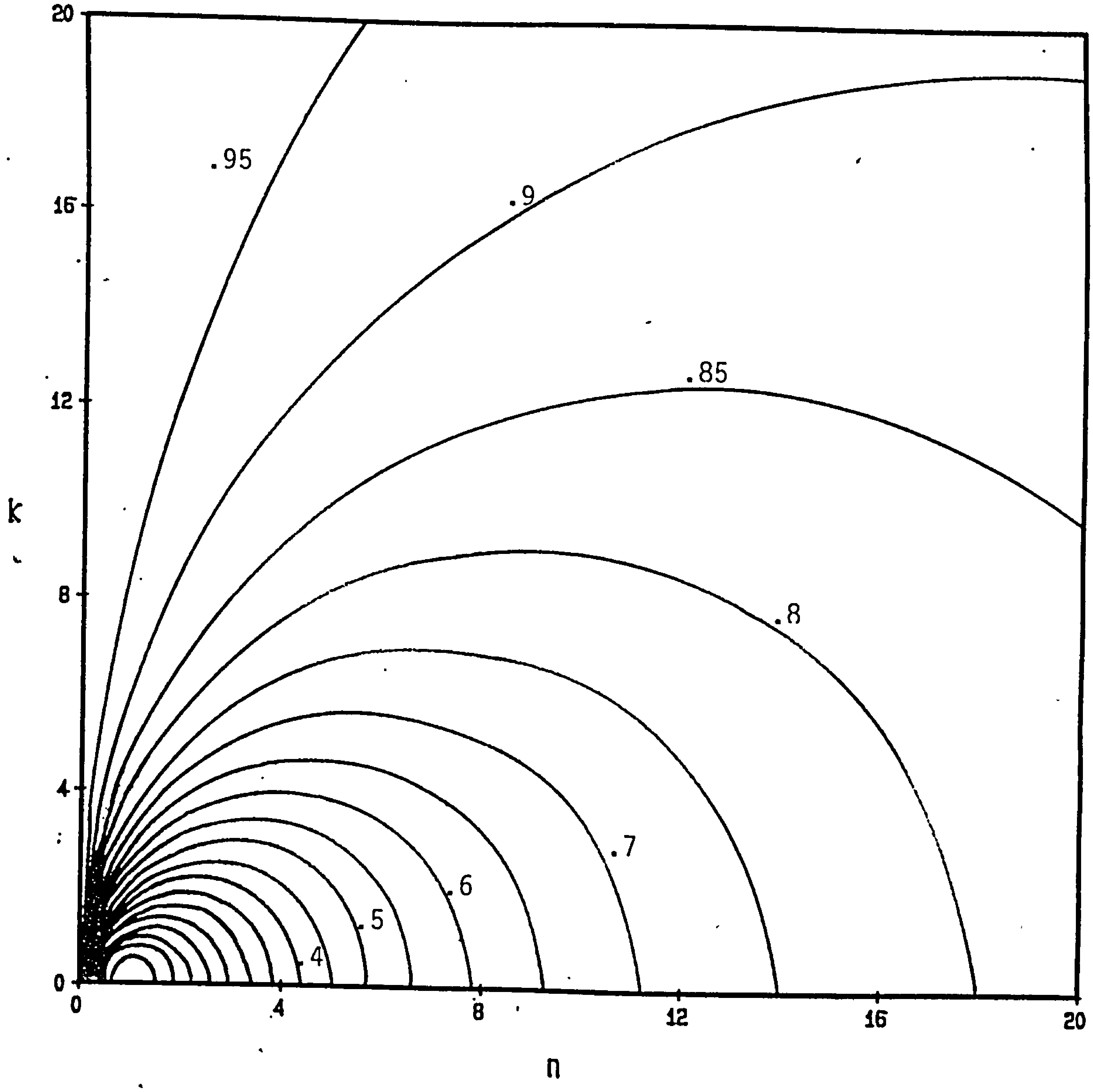

Fig. 2.14 Relation between normal incidence reflectivity and optical constants

$$R = \frac{R_{12} + R_{23}\,\exp^{(-2iD)} + 2(R_{12})^{\frac{1}{2}}\,(R_{23})^{\frac{1}{2}}\,e^{-iD}}{1 + R_{12}\,R_{23}\,\exp^{(-2iD)} + 2(R_{12})^{\frac{1}{2}}\,(R_{23})^{\frac{1}{2}}\,e^{-iD}} \qquad \text{.....(2.52)}$$

for both the p and s components.

The reflectivity of a film-free two phase system, R_{13}, will be identical to that of a three phase system with d = 0, hence:

$$R_{13} = R(o) \qquad \text{.....(2.53)}$$

$$R_{123} = R(d) \qquad \text{.....(2.54)}$$

Absolute measurements of R(o) and R(d) are experimentally difficult which has resulted in the normalized reflectivity being the quantity usually measured:

$$\frac{\Delta R}{R} = \frac{R(d) - R(o)}{R(o)} \qquad \text{.....(2.55)}$$

This has the effect of cancelling out various optical system errors such as electrolyte absorption and scattering which will be common to both measurements. The exact equations for R(o) and R(d) are however both too complicated to permit the precise analysis of the effect of the dielectric constant and film thickness on the reflectivity. This has led to the development of the linear approximation theory[101] which is valid for films with a thickness very much less than the wavelength of light used in the measurement. It has been derived by expanding the equation for the Fresnel reflection coefficients, equation (2.45), and ignoring any terms higher than 1st order to give:

$$\left(\frac{\Delta R}{R}\right)_p = \frac{8\pi d n_1 \cos\phi_1}{\lambda}\ \mathrm{Im}\left(\frac{\hat{\varepsilon}_2-\hat{\varepsilon}_3}{\varepsilon_1-\hat{\varepsilon}_3}\right)\left[\frac{1-(\varepsilon_1/\hat{\varepsilon}_2\hat{\varepsilon}_3)(\hat{\varepsilon}_2+\hat{\varepsilon}_3)\sin^2\phi_1}{1-(1/\hat{\varepsilon}_3)(\hat{\varepsilon}_1+\hat{\varepsilon}_3)\sin^2\phi_1}\right] \qquad \text{.....(2.56)}$$

$$\left(\frac{\Delta R}{R}\right)_s = \frac{8\pi d n_1 \cos\phi_1}{\lambda}\ \mathrm{Im}\left(\frac{\hat{\varepsilon}_2-\hat{\varepsilon}_3}{\varepsilon_1-\hat{\varepsilon}_3}\right) \qquad \text{.....(2.57)}$$

At normal incidence these further reduce to:

$$\frac{\Delta R}{R} = \frac{8\pi d n_1}{\lambda}\ \mathrm{Im}\left[\frac{\hat{\varepsilon}_2-\hat{\varepsilon}_3}{\varepsilon_1-\hat{\varepsilon}_3}\right] = \frac{-8\pi d n_1}{\lambda}\ \mathrm{Im}\left[\frac{\varepsilon_1-\hat{\varepsilon}_2}{\varepsilon_1-\hat{\varepsilon}_3}\right] \qquad .....(2.58)$$

2.6 Reflection from rough and inhomogeneous surfaces

2.6.1 Rough surfaces

The previous treatment for reflection from bare and film covered surfaces using the Fresnel equations has assumed that the interfacial regions are separated by a well defined sharp boundary with all surfaces being completely flat. This is rarely the case with "real" surfaces which are subject to polishing and machining marks. In the field of corrosion substrate dissolution processes such as pitting can occur leading to gross surface roughness. In the latter case very marked deviations from results predicted for a smooth surface are seen. The effect of surface roughness has created considerable interest in the field of optics and ellipsometry in the last thirty years with many theories having been proposed to predict the polarization changes that result on reflection of a light beam from rough surfaces.[102-125]

Surface roughness can be defined by two parameters - the root mean square of the height irregularities above a mean plane, σ, and the correlation lenth, ℓ, defined as being the distance between adjoining peaks or troughs. These parameters are illustrated in fig. 2.15 together with the angle, tan β, which is the ratio of σ and ℓ. Microscopic roughness is characterized by values of σ being very much less than the wavelength of light, λ, and giving specular reflection. As the value of σ approaches and exceeds λ, as for macroscopically rough surfaces, scattering of the light occurs reducing the intensity of the specularly reflected beam, and depolarization of the reflected beam can happen.

There are two broad classes of treatment for microscopic roughness: highly complex theoretical derivations based upon diffraction or vector perturbation theories or more phenomelogical methods based upon treating the roughness as a separate film with its own optical properties. The diffraction theories are applicable for undulating roughness with $\ell \gg \lambda$

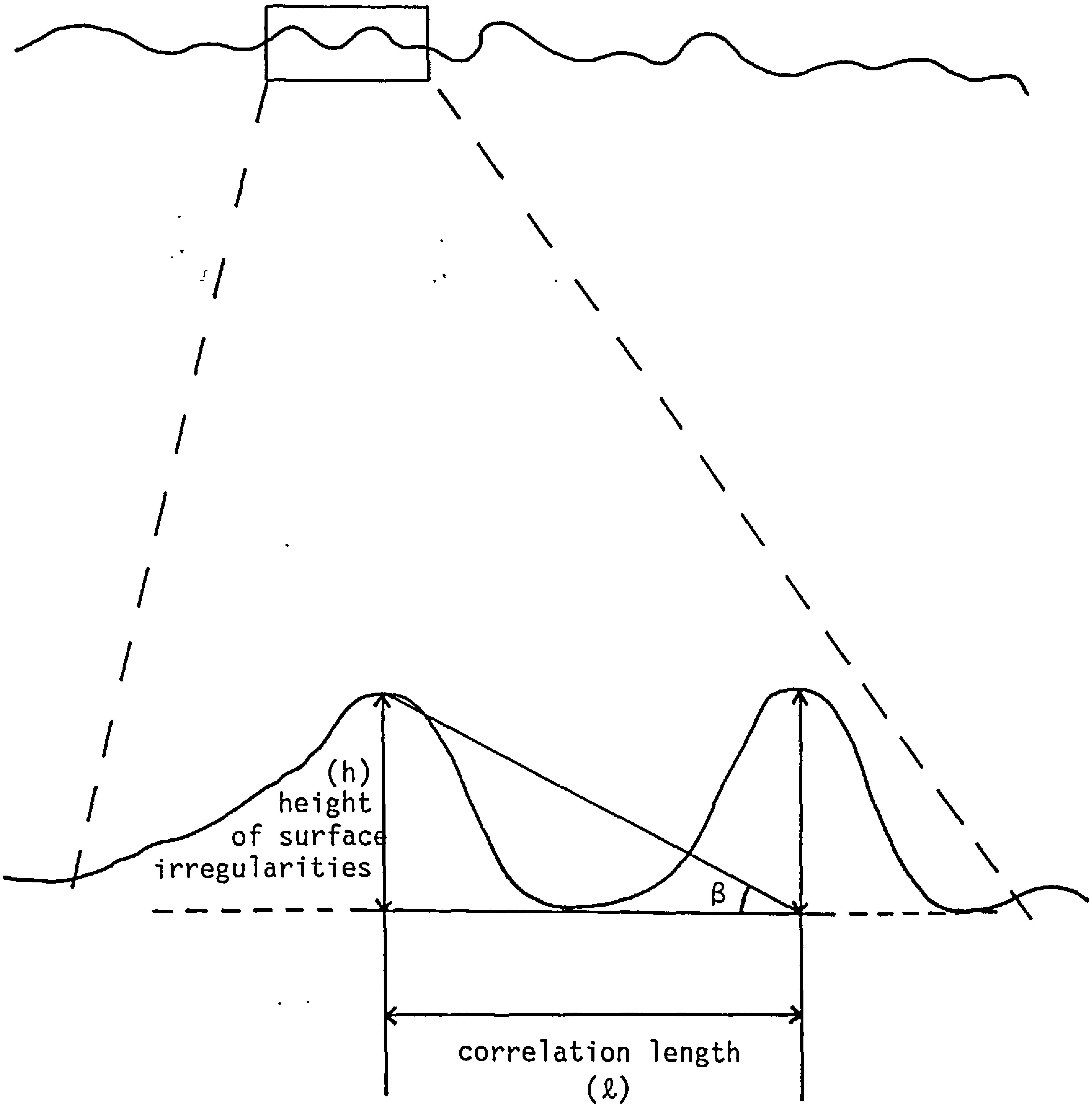

tan β = ratio of mean height of surface irregularities to the correlation length

Fig. 2.15 Diagrammatic representation of a rough surface whereas the effective film theories have been generally applied for values of $\ell << \lambda$. All these theories however are for small scale irregularities and there has been little published work concerning the effect of macroscopic roughness.

2.6.2 Diffraction theories

This approach is typified by Ohlidal and Lukes[118] who initially applied the Kirchoff scalor theory of diffraction to a simplified model of a rough surface. They assumed that the surface was uniformly rough with the slopes of the height irregularities (tan β_o in fig. 2.15) less than 0.01. This constraint on tan β_o enables the local field in the surface to be treated as if it were part of an infinitely flat plane - the tangent plane approximation. Another assumption is that there is a maximum of intensity in the direction of specular reflectance. The distant electric field was obtained by considering the integration of the diffracted and specularly reflected beams in the direction of specular reflectance using the Helmholtz-Kirchoff (H-K) integral. In a later paper[119] the same authors used a similar treatment but used the Stratton-Chu-Silver integral (S-C-S) rather than the H-K integral and arrived at a similar result but one which was more general. Azzam and Bashara[120] and also Vorburger[121] and Ludema have also used this type of approach in calculating Δ and Ψ for rough surfaces.

Wind and Vlieger[122,123] point out inconsistencies in Ohlidal and Lukes's calculations and derive expressions for surface roughness by using a fictitious layer separating the two media. This treatment gives the same result as that for the tangent plane approximation approach using the S-C-S and H-K integrals. However if Ohlidal and Lukes's calculations are altered to include the correct second order field terms then their calculations give the same results as those from Wind and Vleiger's calculations. These second order field terms arise from the curvature of the substrate and are ignored in the tangent plane approximation. The result in fig. 2.16 has been obtained from a computer program originally written by P. Bobbert, illustrate the differences between Wind and Vleiger's theory and Ohlidal and Lukes's calculations using both the S-C-S and H-K integrals for a rough, film free Mg substrate (n = 0.85, k = 5.75) immersed in a non-absorbing solution (n = 1.334, k = 0). The results calculated using the S-C-S and H-K integrals are similar with both Δ and Ψ decreasing

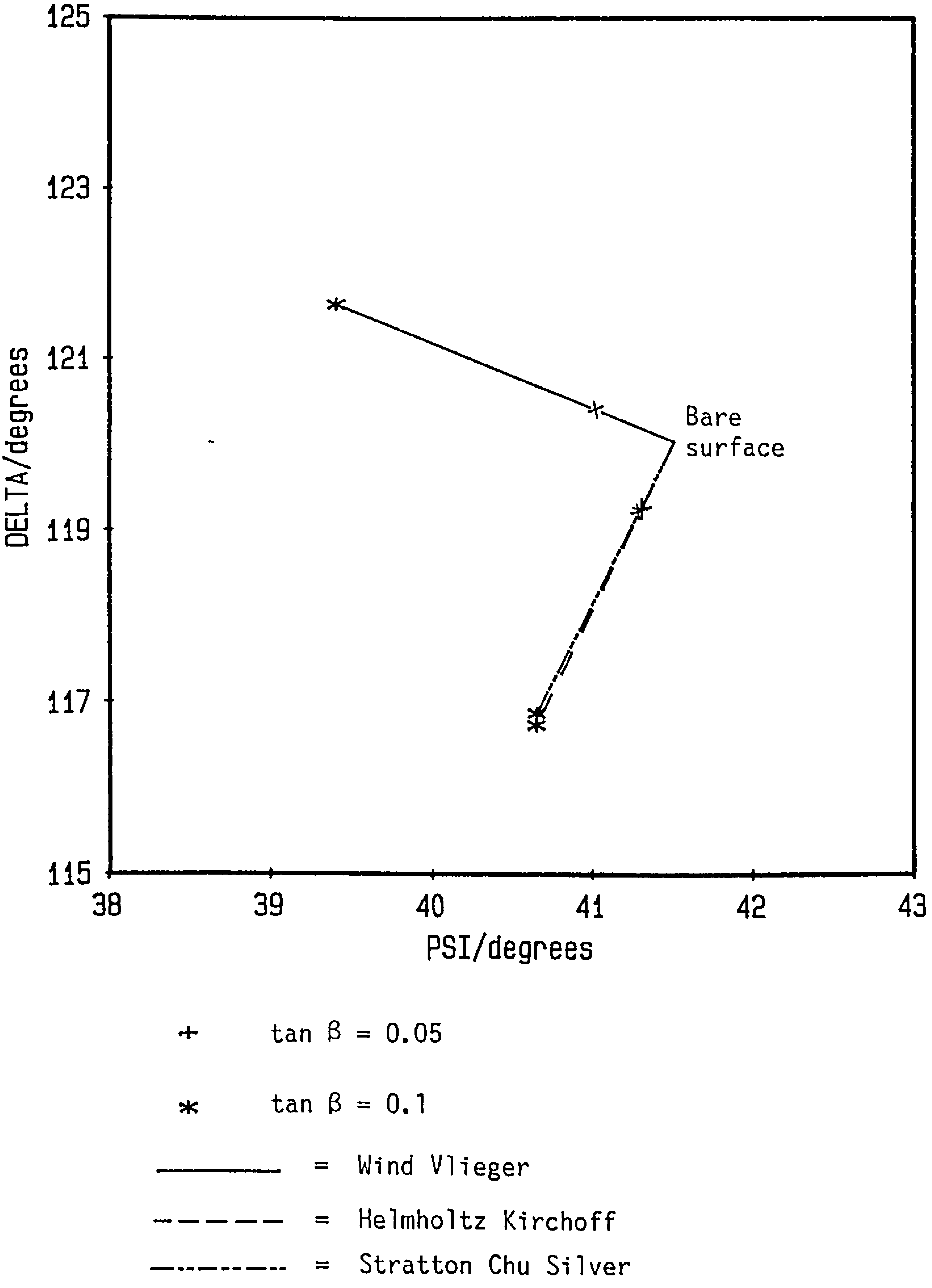

Fig. 2.16 The effect of increasing surface roughness of a film-free substrate (n = 0.85, k = 5.75) using the Wind Vlieger, H-K, and S-C-S models

as tan β increases. Wind and Vleiger's calculations however predict that Ψ will decrease and Δ increase slightly as tan β increases. The effect of growing a non-absorbing film (n = 1.47) on a rough surface for two values of tan β using the above theories can be seen in Figs. 2.17a and 2.17b. There are very marked differences in the Δ,Ψ curve using predictions based upon Wind and Vleiger's theory and those based upon Ohlidal and Lukes's calculations. This is due to the large changes that occur in the Δ,Ψ curves with slight changes of n and k for the bare surface near values of Ψ = 45°.

An alternative scattering theory to those of Wind and Vleiger and Ohlidal and Lukes is given by Church and Zavada.[124] They did a perturbation calculation using the Rayleigh Rice formulation to calculate the effect on Δ and Ψ of slightly rough surfaces. Their calculations however only predicted small corrections for Δ and Ψ from smooth surface values unless the correlation length, ℓ, was of the same order as the wavelength of light and the theory was only applicable to very small height irregularities.

2.6.3 Effective medium theories

The most widely used method to calculate the effect of surface roughness in ellipsometry has been to treat the rough surface as a separate layer or effective medium having optical properties dependent on the surrounding media. A simple volume averaging of the refractive indices of the two components of a mixture has been used.[125]

$$\hat{\varepsilon}_m = f_a\hat{\varepsilon}_a + (1-f_a)\,\hat{\varepsilon}_b \qquad .....(2.59)$$

$\hat{\varepsilon}_m$, $\hat{\varepsilon}_a$, $\hat{\varepsilon}_b$ are the dielectric constants of the effective medium and the media a and b respectively. f_a is the volume fraction of a in the effective medium. This approach is not theoretically valid in general however. Although the molecules in a dense medium see an average electric field, E, their interactions result in a local field, E_i, at any given molecule so that the total field, E_t, is:

$$E_t = E + E_i \qquad .....(2.60)$$

In a mixture of dielectrics the effect of interactions between molecules on their polarization and hence dielectric constant must be considered.

(a) tan β = 0.02

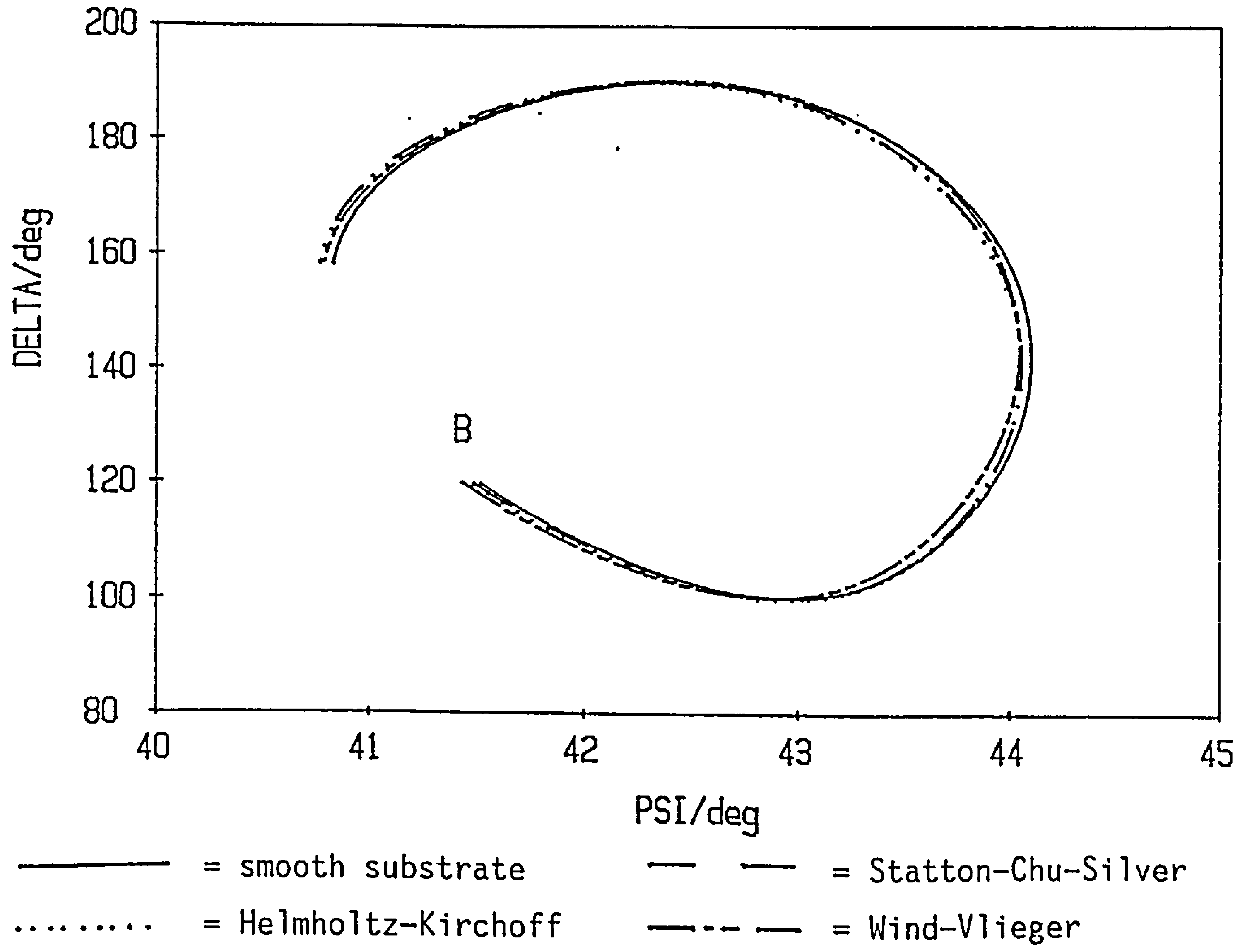

(b) tan β = 0.1

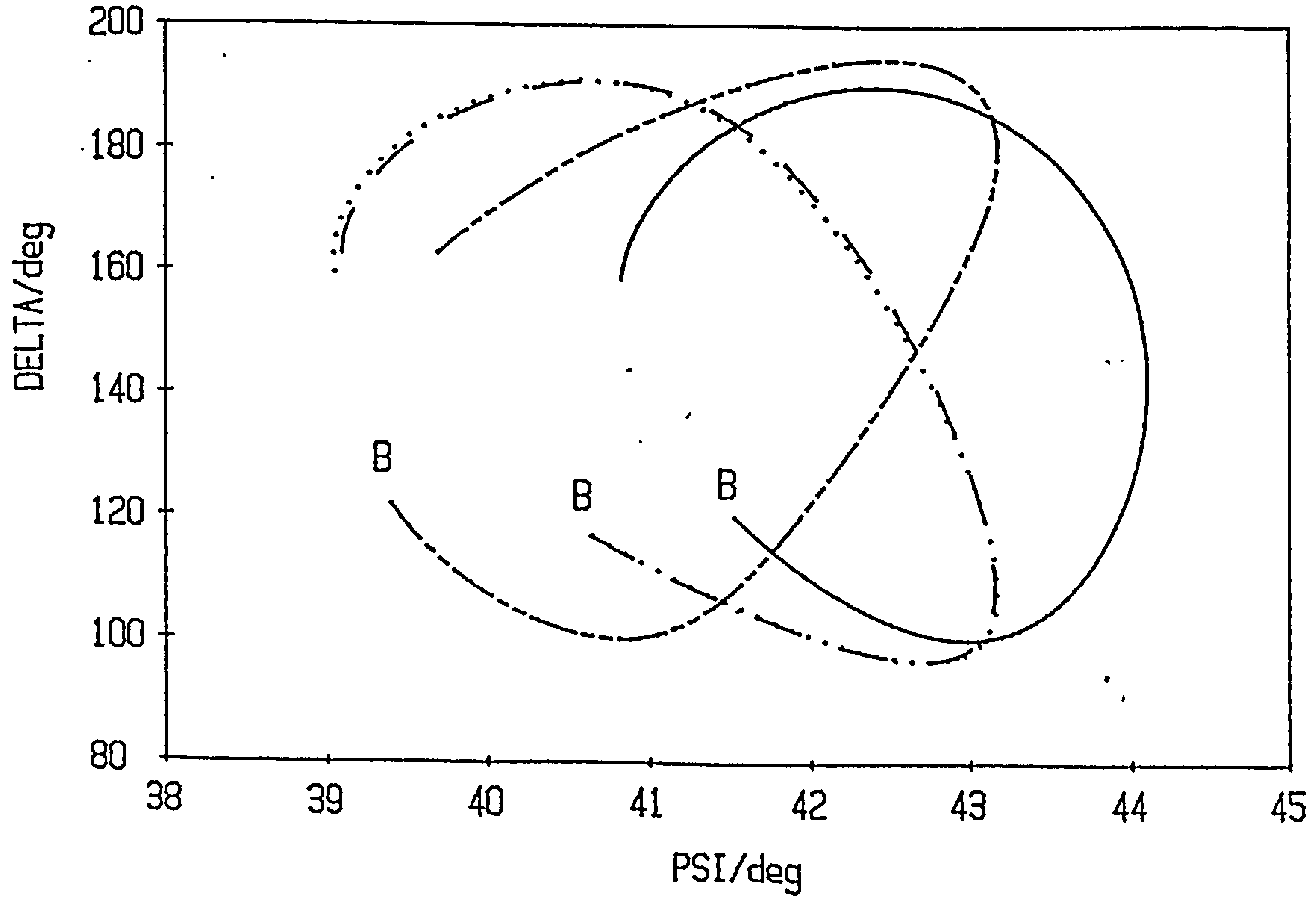

Fig. 2.17 The effect of growing a 350 nm film ($n = 1.47$, $k = 0$) on a rough magnesium substrate using the Wind-Vlieger, S-C-S and H-K theories

Clausius Mosotti equation

To determine the dielectric constant exactly for a given microstructure would involve obtaining the local electric field and dipole moment per unit volume at every point in space and averaging these values to obtain the uniform macroscopic electric field and the polarization per unit volume. As this is impossible different approaches have to be used. Classically this problem was treated by Lorentz[126] who calculated the internal field due to interactions between neighbouring molecules by constructing a sphere around the molecule in question, fig. 2.18. The internal field, E', due to the external charges is:

$$E' = \frac{4\pi P}{3} \qquad \text{.....(2.61)}$$

P is the polarization per unit volume.

There is also another field, E", the local field, due to material within the sphere. For a cubic array or random distribution of dipoles however this field is zero. The total field at 0 then is due to the surface charge and the average dielectric field, E :

$$E_t = E + \frac{4\pi P}{3} \qquad \text{.....(2.62)}$$

An identical result is obtained using the solve-average approach of Aspnes.[127]

The polarization is related to E by the molecular polarizability α:

$$P = n\alpha E \quad \text{for n molecules} \qquad \text{.....(2.63)}$$

$$= n\alpha \left[E + \frac{4\pi P}{3}\right] \qquad \text{.....(2.64)}$$

The dielectric constant ε is related to the polarization P by:

$$\varepsilon E = E + 4\pi P \qquad \text{.....(2.65)}$$

so from (2.64)

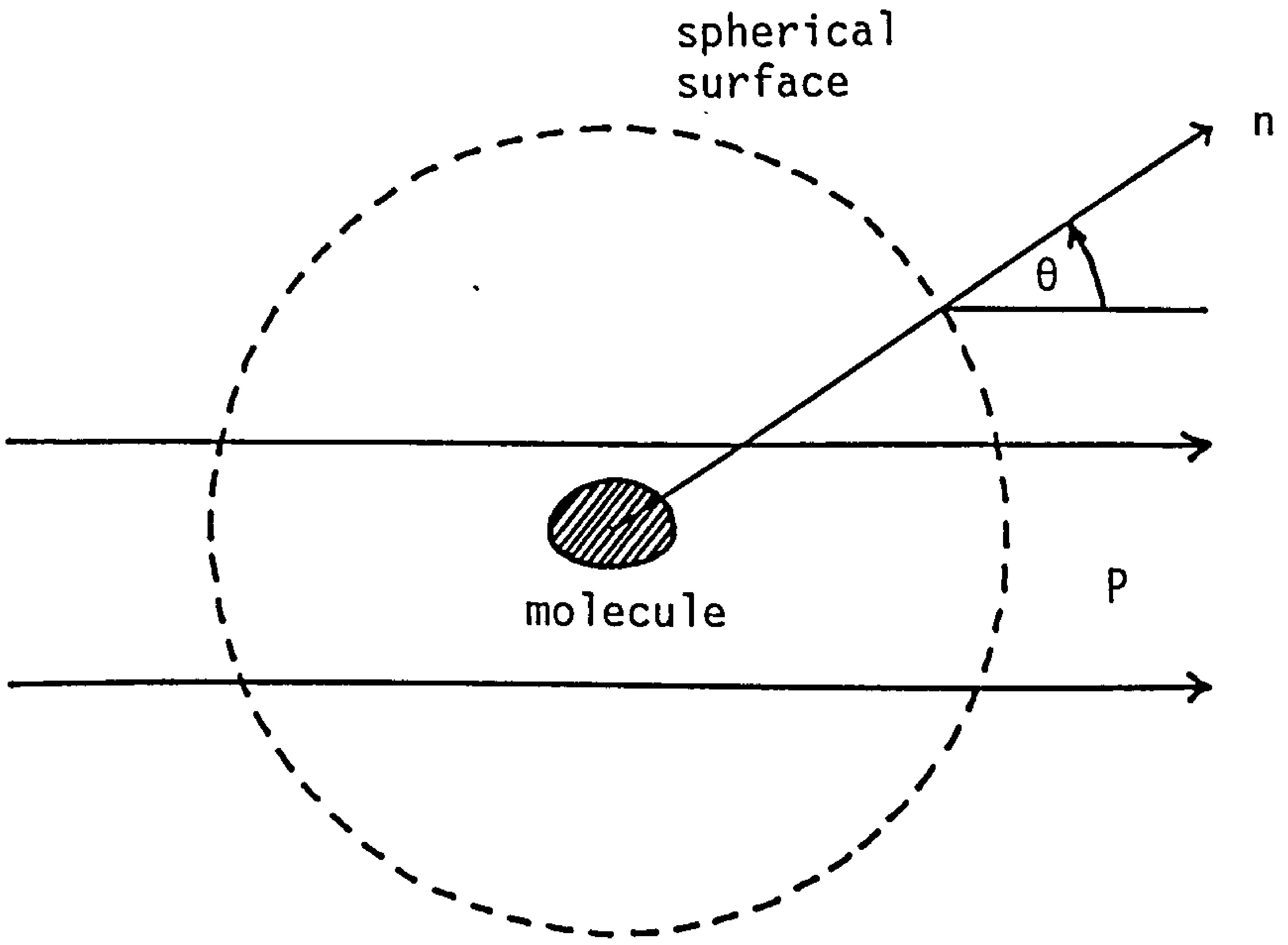

n is outward normal from spherical surface

P is polarization field

Fig. 2.18 Pictorial representation of the model used in calculating the internal field contribution from distant molecules

$$(\varepsilon-1) = \frac{4\pi P}{E} = \frac{4\pi n\alpha}{1-4/3\pi n\alpha} \qquad .....(2.66)$$

and

$$(\varepsilon+2) = \frac{3}{1-4/3\pi n\alpha} \qquad .....(2.67)$$

Dividing equation (2.66) by equation (2.67) leads to the Clausius Mosotti equation:

$$\frac{(\varepsilon-1)}{(\varepsilon+2)} = \frac{4\pi n\alpha}{3} \qquad .....(2.68)$$

This only holds for dilute gases and cubic lattices however.

Lorentz Lorenz expression

Two separate phases with their own polarizabilities α_a and α_b mixed on an atomic scale will have a composite dielectric constant given by equation (2.68):

$$\frac{(\varepsilon-1)}{(\varepsilon+2)} = \frac{4\pi}{3}(n_a\alpha_a + n_b\alpha_b) \qquad .....(2.69)$$

Alternatively

$$\frac{(\varepsilon-1)}{(\varepsilon+2)} = f_a \frac{(\varepsilon_a-1)}{(\varepsilon_a+2)} + f_b \frac{(\varepsilon_b-1)}{(\varepsilon_b+2)} \qquad .....(2.70)$$

where ε_a and ε_b are the dielectric constants for a and b and f_a and f_b are the volume fractions of the phases a and b.

The Lorentz Lorenz (LL) expression assumes that the host medium is a vacuum (ε=1) with dilute inclusions but in the case of surface roughness in ellipsometry each of the separate phases are considered to have their own dielectric identity and other expressions are used, as follows.

Maxwell Garnet equation

In the Maxwell Garnet (MG) expression the host medium is defined as being the less dilute phase, e.g. if the dilute phase is represented by the subscript b then:

$$\frac{(\varepsilon-\varepsilon_a)}{(\varepsilon+2\varepsilon_a)} = f_b\,\frac{(\varepsilon_b-\varepsilon_a)}{(\varepsilon_b+2\varepsilon_a)} \qquad \text{.....(2.71)}$$

and vice versa for a being the dilute phase.

It has been pointed out[128] however that this equation is not self consistent and different values of the effective medium are obtained if the host and inclusions are interchanged.

Bruggeman's effective medium approximation

The EMA approximation was developed by Bruggeman to be self consistent. The effective medium itself acts as the host medium:

$$f_a\left[\frac{\varepsilon_a-\varepsilon}{\varepsilon_a+2\varepsilon}\right] + f_b\left[\frac{\varepsilon_b-\varepsilon}{\varepsilon_b+2\varepsilon}\right] = 0 \qquad \text{.....(2.72)}$$

The EMA and MG expressions describe different microstructures with the MG theory describing a separated-grain structure (fig. 2.19) and the EMA expression a random mixture microstructure (fig. 2.20). There have been several modifications of these basic effective medium theories, a good review of which is given by Tinga and Voss.[129]

Comparison of effective medium theories

A comparison of the real and imaginary parts of the dielectric constant for Mg is shown in figs. 2.21 and 2.22 using a simple volume average of the refractive indices and for the results predicted using the MG and EMA expressions. It can be seen that the values predicted for the MG and EMA theory are similar at low volume fractions of inclusions but differ widely at the higher values for which there is a greater similarity between the simple averaging of the optical constants and the EMA theory. Grandqvist and Hunderi[130] have performed similar calculations between Bruggeman's EMA equation and other modifications of the MG equation by Polder and Van Santens and Hunderi. Identical results were seen in the limit of vanishing volume fraction of inclusions but for the range $0.2 = f \leq 0.8$ only Bruggeman's EMA theory was found to be applicable. Aspnes, Theeton and Hottier[131] have compared the LL, MG and EMA theories and have found that the EMA

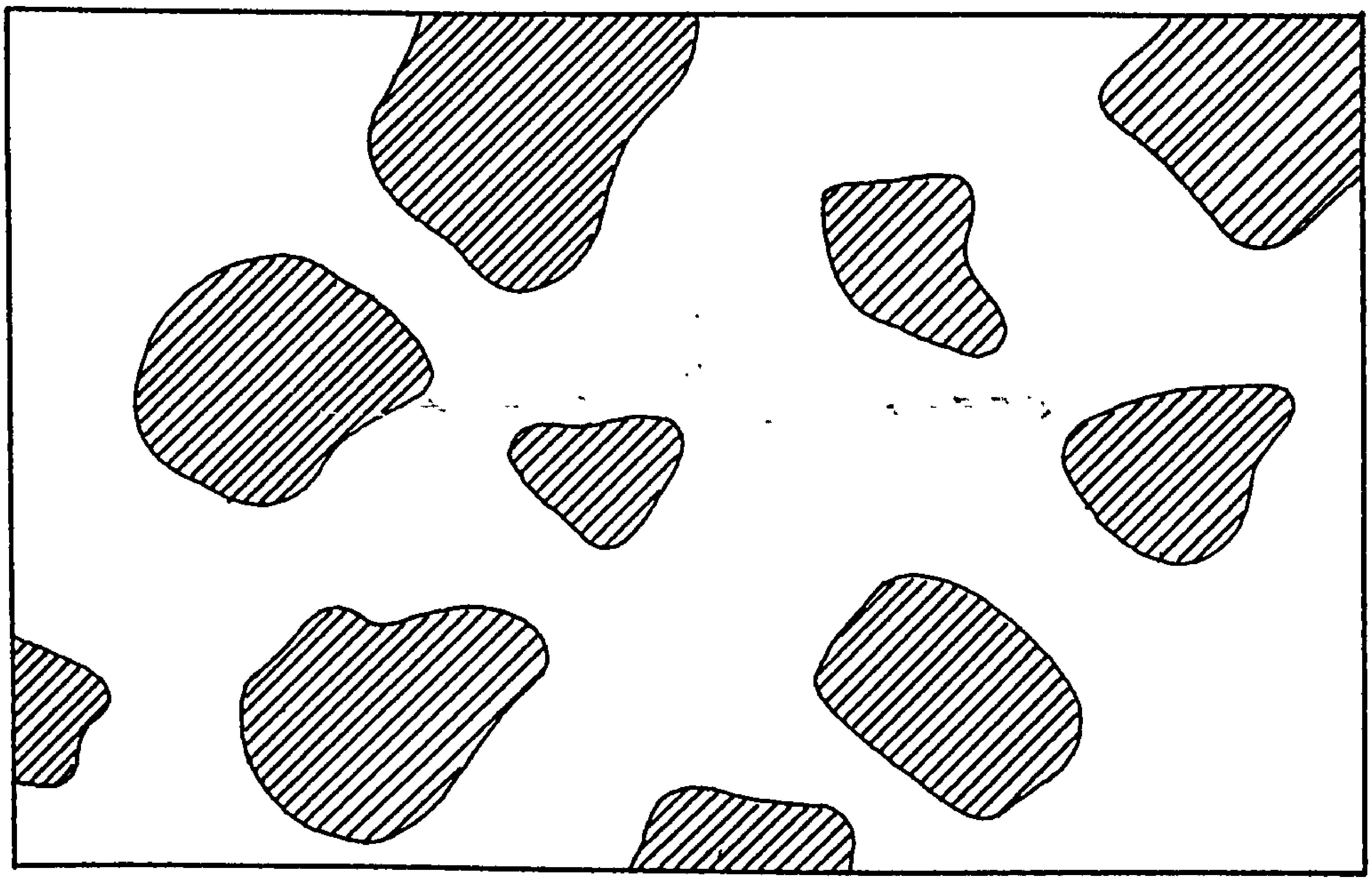

Fig. 2.19 Separated grain structure representing MG microstructure

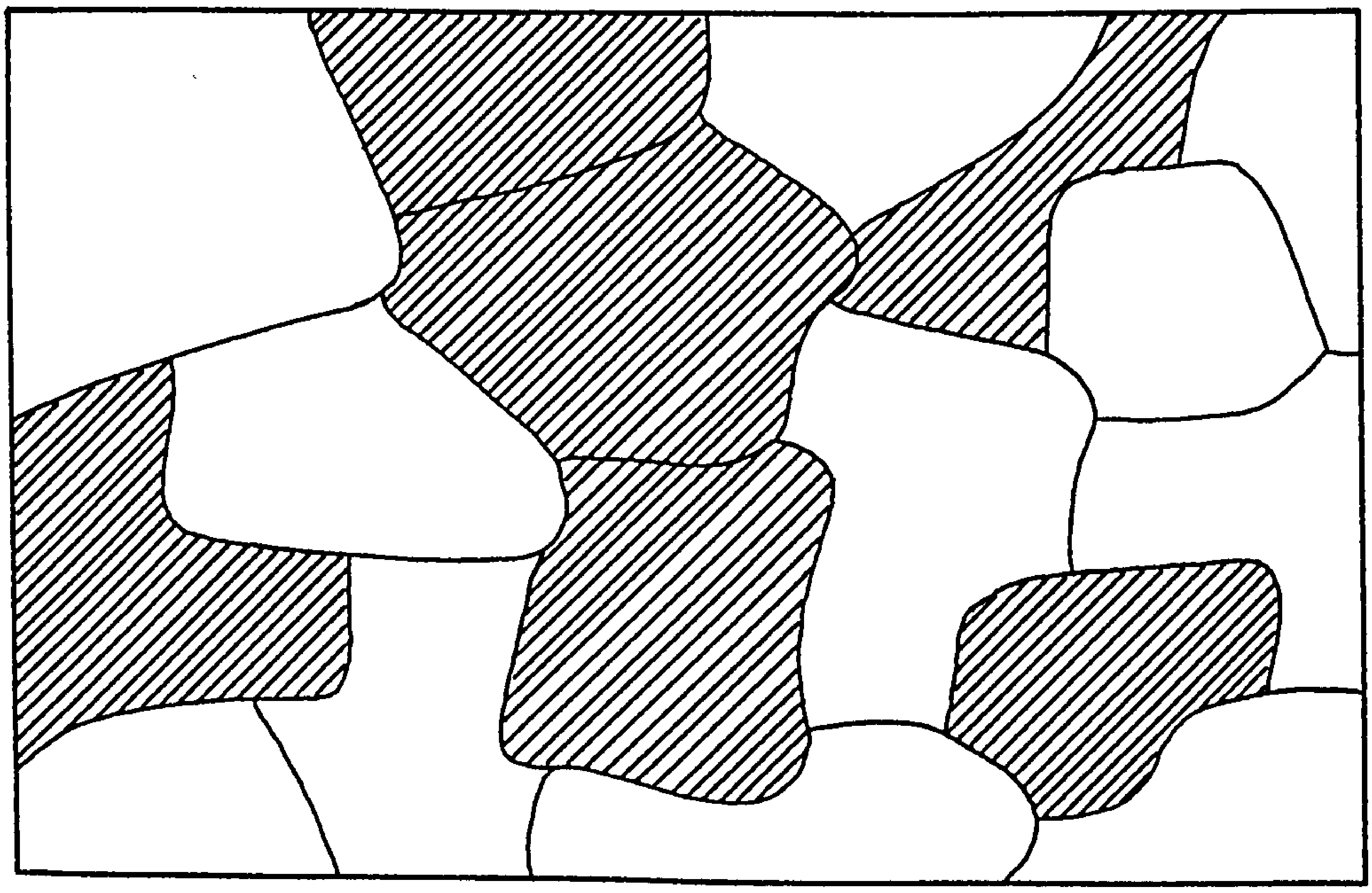

Fig. 2.20 Random mixture structure representing EMA microstructure

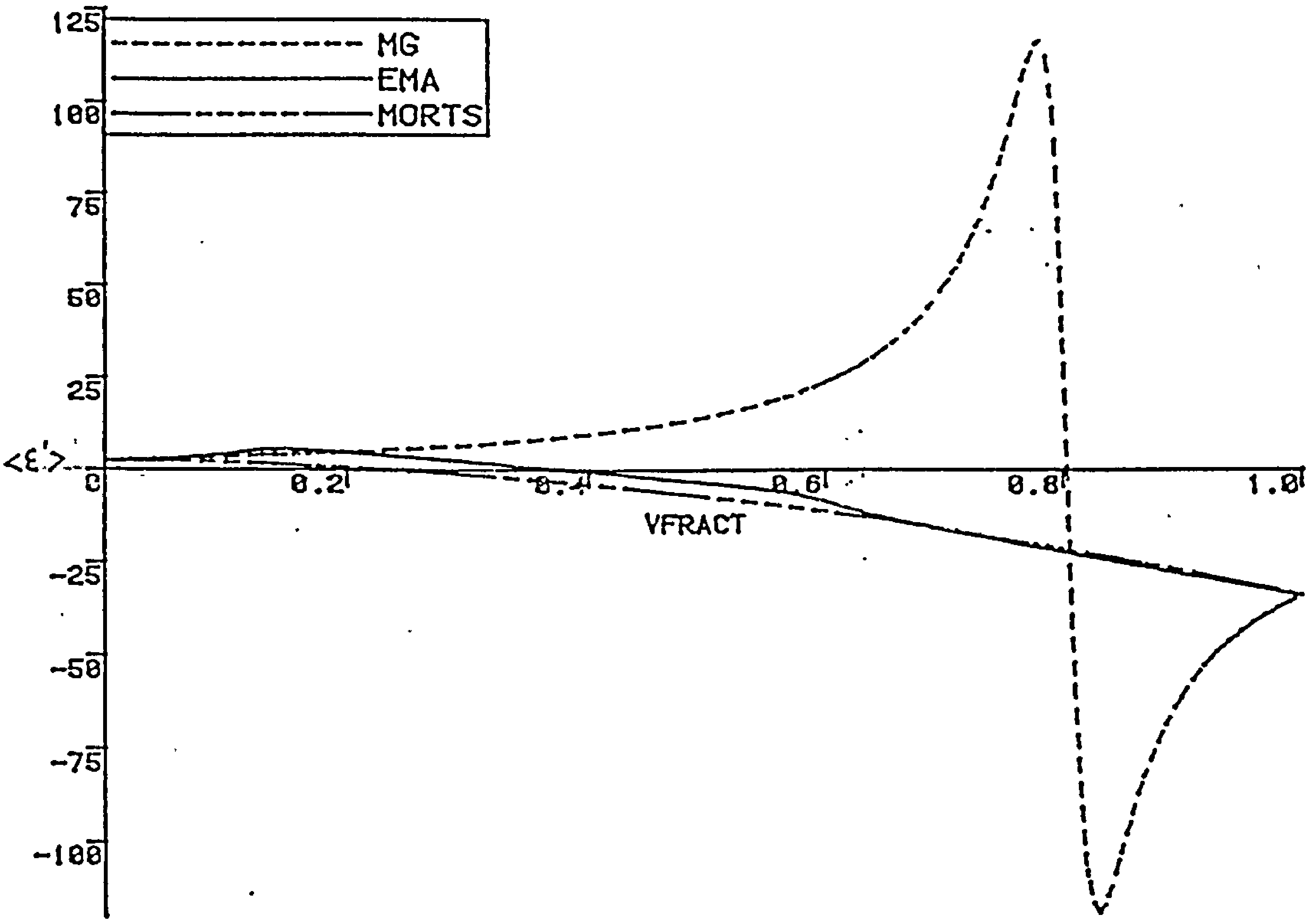

Fig. 2.21 Variation of the real part of the dielectric constant with volume fraction of inclusions using the MG, EMA theories and a simple volume average (MORTS)

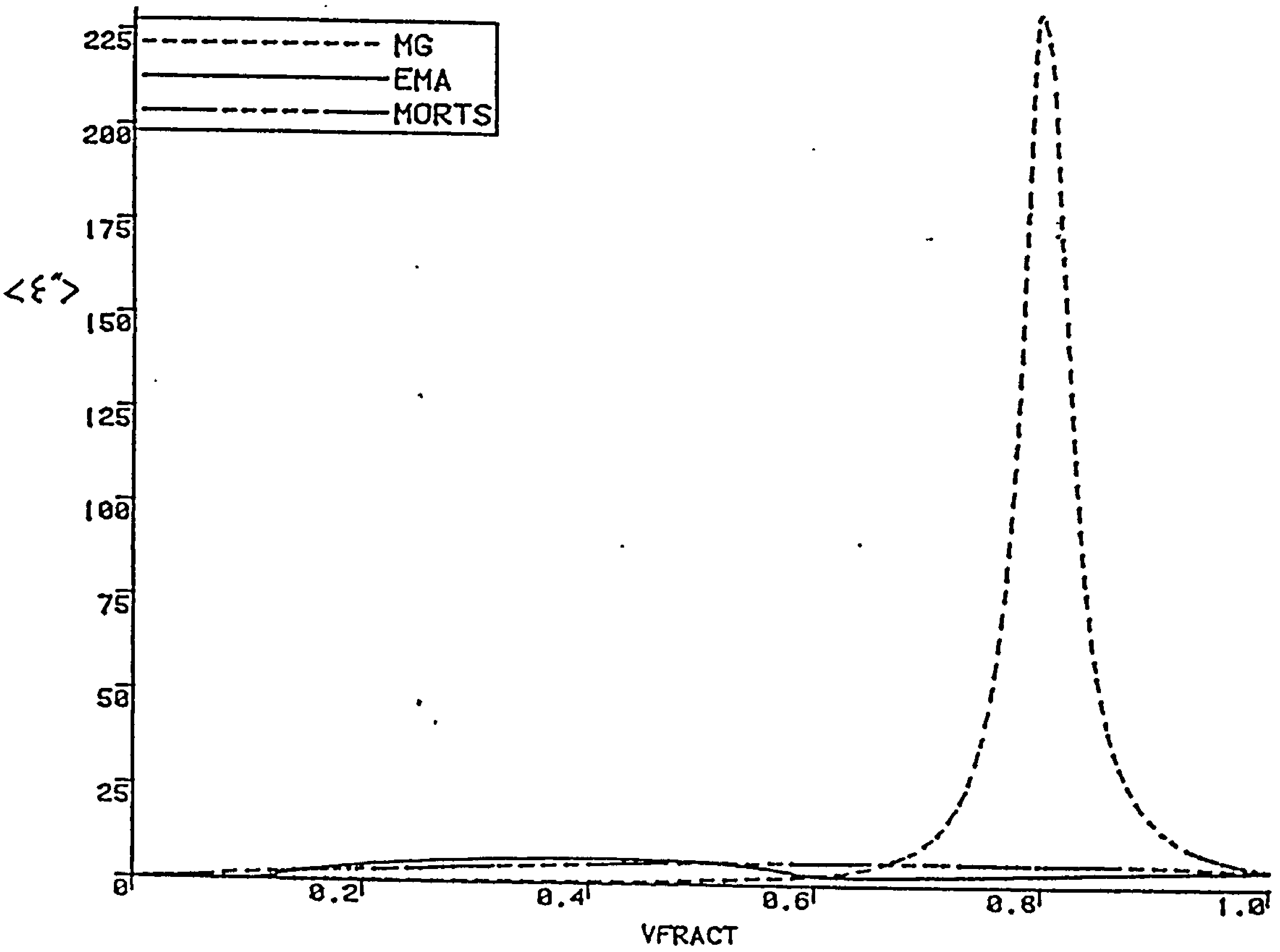

Fig. 2.22 Variation of the imaginary part of the dielectric constant with volume fraction of inclusions using the MG, EMA theories and a simple volume average (MORTS)

theory gave reasonable agreement with experimental data for rough Si films.

The use of roughness theories in theoretically modelling the experimental data from rough films is described in chapter six.

2.6.4 Gross roughness

The previous theories have all been for relatively small scale roughness with the mean height of irregularities being less than the wavelength of light. In certain ellipsometric applications such as corrosion however there is a possibility of gross surface roughness occurring. There has been very little work to date concerning the effect of this on Δ and Ψ, but T. Smith[132] has published a series of ad hoc equations for ridges, pits and bumps. He calculated the fraction of light reflected from the top and bottom of surface irregularities allowing for the effect of shadowing, fig. 2.23, and used these values in conjunction with various microscopic roughness theories to account for experimentally observed values of Δ and Ψ for macroscopically rough surfaces. He found poor agreement between the experimental results and his theory in conjunction with microscopic roughness theories based on vector perturbation or Kirchoff scalor diffraction theories. Much better agreement was found on combining his theory with more phenomenological theories.

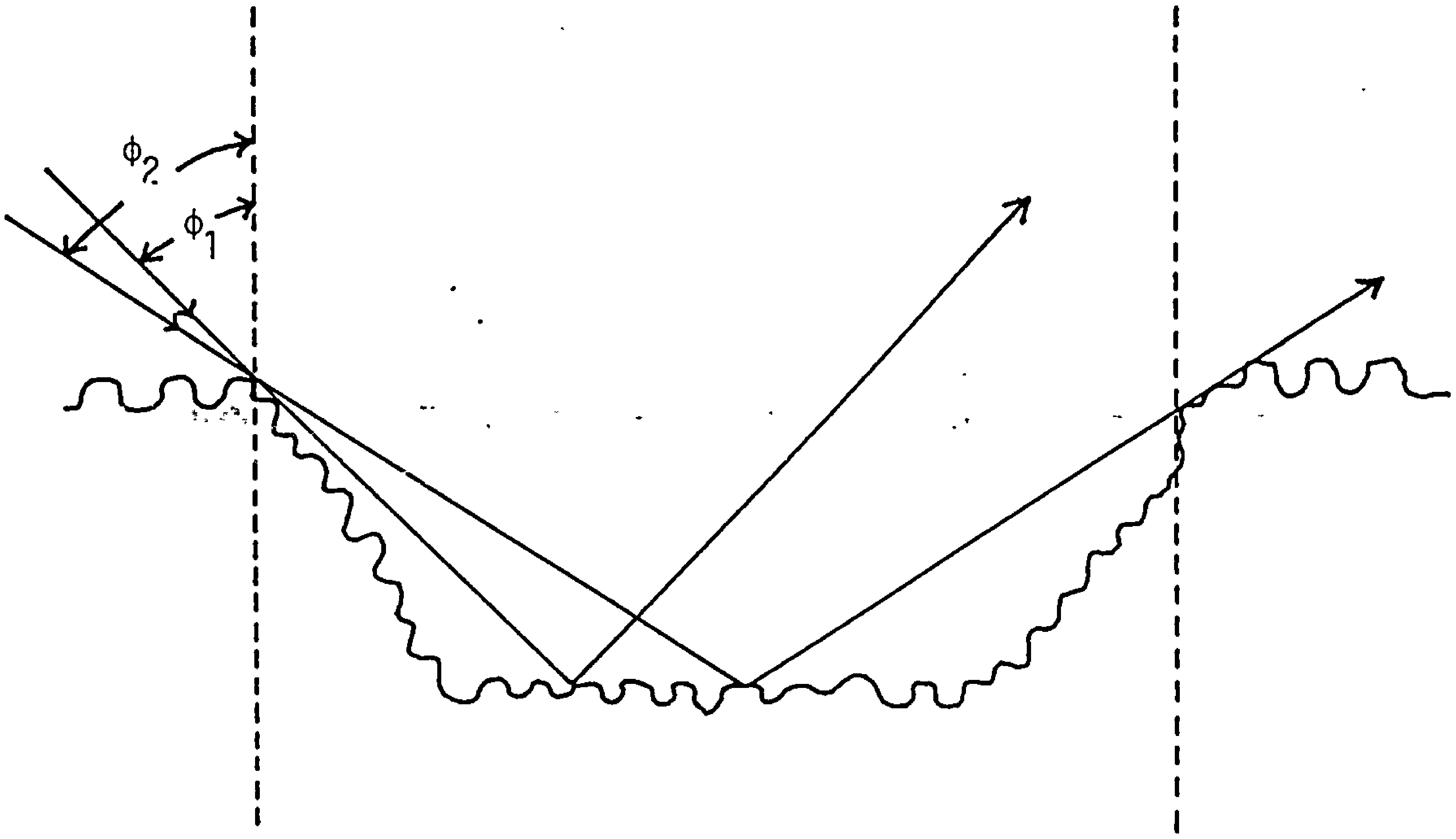

Angle of incidence = ϕ

$\phi < \phi_1$	No shadowing occurs, reflection is a function of whole surface area
$\phi_1 < \phi < \phi_2$	Shadowing does occur, reflection is a function of angle of incidence and rough surface geometry
$\phi > \phi_2$	Shadowing is complete, only reflections from top surface detected

<u>Fig. 2.23</u> Reflection from a pit illustrating shadowing that occurs from gross surface roughness

CHAPTER 3 INSTRUMENTAL

3.1 Introduction

The main features of a generalized ellipsometer are shown in fig. 3.1. These are a source of radiation, S, production of a known polarization state, interaction with a sample and detection of the subsequent polarization state. It is also necessary to determine the change in polarization between the two states and to relate this change to the physical state of the sample. Hauge[133] describes the various instruments available for doing this up to 1979 in his review and classifies them according to the number of elements of the Mueller matrix of the system that are measured.

Some recent advances since that review include the development of microellipsometry by Sugimoto and Matsuda to study the film growth in individual grains[134] in steel and in pits[135] and the use of angle of incidence derivative ellipsometry (AIDER).[136,137] The latter technique uses a small rotational oscillation of the angle of incidence to provide an increase in the number of experimentally measured parameters.

The instrument used in this study was a nulling ellipsometer built by I.B.M. at Southampton. It has been fully automated by the use of Faraday modulation and compensation in association with phase sensitive detection, a method described by A.S. Winterbottom[138] and H.P. Leyer.[139] The polarization range of the polarizer and analyser however has been increased to 360° by mechanical means as described by Ord by the addition of servo operated Rochon prisms coupled with moire angle encoders. The instrument is capable of wavelength scanning over the range ca. 250-650 nm with angle of incidence being variable between 90° and 25°, This design gives rise to a very versatile, sensitive (angles of 1 second of arc in 360° can be resolved on the polarizing prisms), accurate (see table 3.1) instrument capable of responding to changes in null angles typically within 0.1s.[140] It does however suffer from the inherent problem of nulling ellipsometers of being able to be used only for non-polarizing systems[86] as it only produces half of the sixteen elements in the Mueller matrix of the system.

Two previous authors have described this instrument. A.C. Lowe[141] gives a brief description of the optical, mechanical, electronic aspects and a detailed analysis of the limits of its accuracy. The latter is based on the measured properties and the geometrical and optical

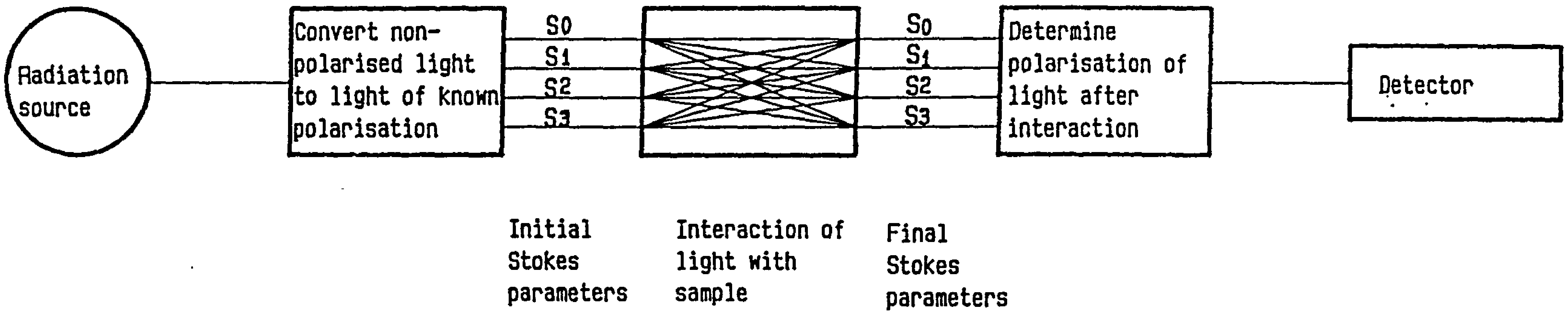

Fig. 3.1 Schematic representation of a generalized ellipsometer

components, a summary of which is shown in table 3.1.

P. Pearson[140] gives a more detailed analysis of the instrumental components and setting up procedures. The major changes since these two reports have been in the use of a Motorola M6809 microprocessor to control data acquisition and manipulation. There have also been several minor modifications such as in the hardware used for obtaining data from the ellipsometer, a change in the fixed wavelength light source and the substitution of solid state flow sensing devices for the cooling water circuit instead of the old electro-mechanical devices.

3.2 Mechanical, optical and electronic components

The instrument is constructed of welded steel and supported on a 1.22 m^2 block of granite standing on three levelling legs. Its size and general layout can be seen from the photograph, fig. 3.2, and the diagram in fig. 3.3. The arms on which the optical devices are mounted are counter-balanced by two weighted steel arms to reduce the load upon the main axis. The ellipsometer electronics are housed in a rack measuring 1.85 m x 0.5 m which contains the microprocessor, data acquisition and nulling circuitry, an oscilloscope for monitoring the null signal and the monochromator drive.

The light source is selected by a sliding totally internally reflecting (T.I.R.) quartz prism to be either a He/Ne laser (Rofin 1.75 mW), $\lambda = 632.8$ nm or a 75 W high pressure Xenon arc (Osram) focused onto a quartz prism monochromator (Schaeffel Instruments QPH 30S). The wavelength for the latter is controlled manually by a micrometer screw or automatically via a computer driven stepper motor (Superior type SS25) over the range 190 nm - 1500 nm. The beam is directed by three T.I.R. quartz prisms to the quartz rochon polarizer (I.C. Optical Services) fig 3.4, which is mounted in a three-armed spider attached by spring clips to steel flanges which are fixed to the arm mounts by bearings. The polarizer is a birefringence type of a high optical quality with a beam deviation of 3.5 seconds of arc (measured by I.B.M.). This type of polarizer gives excellent performance over a wide wavelength range (typically 200 nm to 5000 nm) and introduces very little ellipticity into the emerging beam. The poor separation between the ordinary and extraordinary beams however necessitates the use of stops to remove the unwanted extraordinary beam.

Table 3.1

Azimuthal Accuracy Limits for Ellipsometer[141]

		Error (deg)		
	λ nm	P	Q	A
Worst	250	0.0182	0.0228	0.008
Case	900	0.0117	0.0163	0.008
Best	250	0.0146	0.0154	0.0044
Case	900	0.0081	0.0089	0.0044

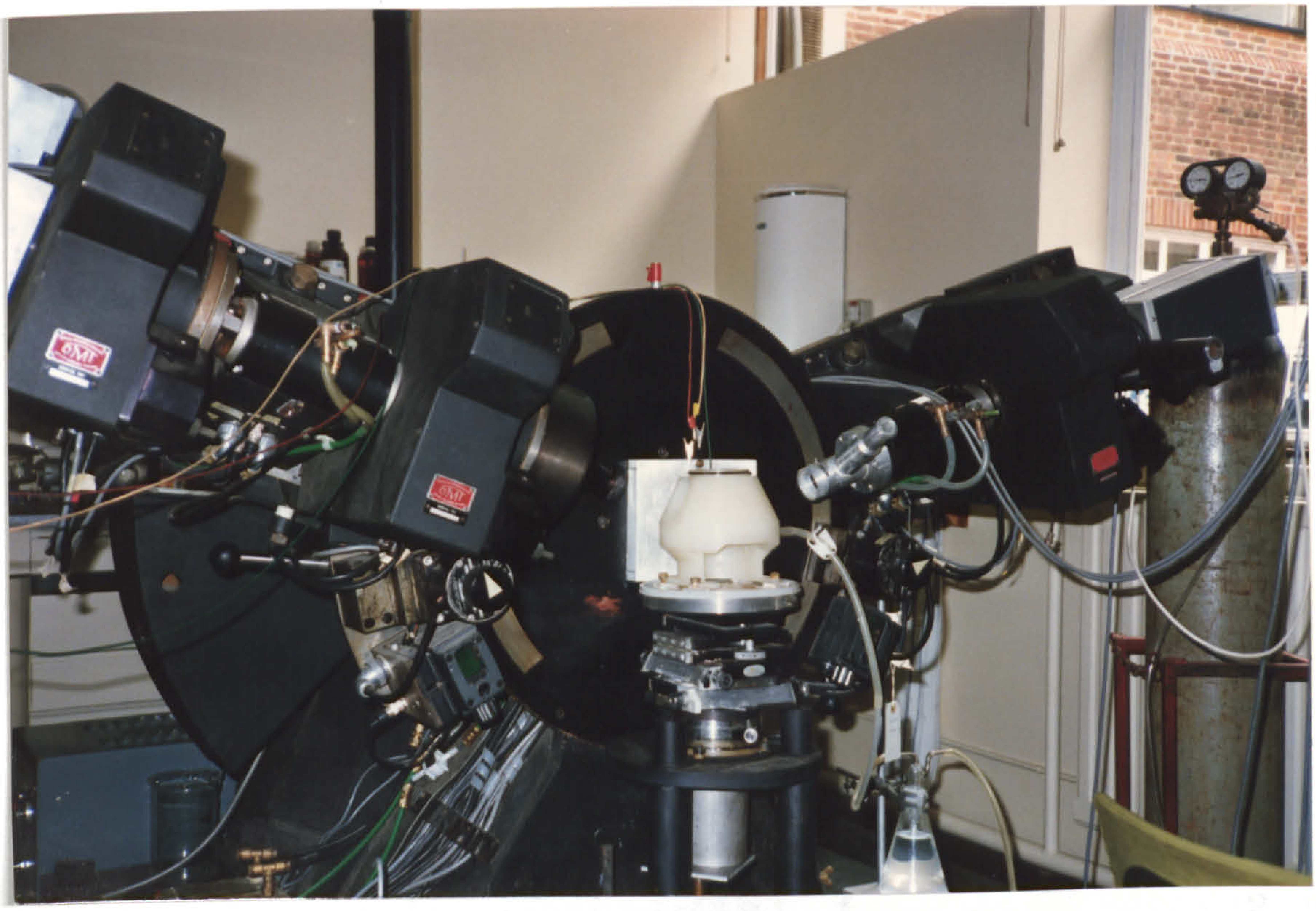

Fig. 3.2 Photograph of the automatic nulling ellipsometer used to obtain data in this thesis

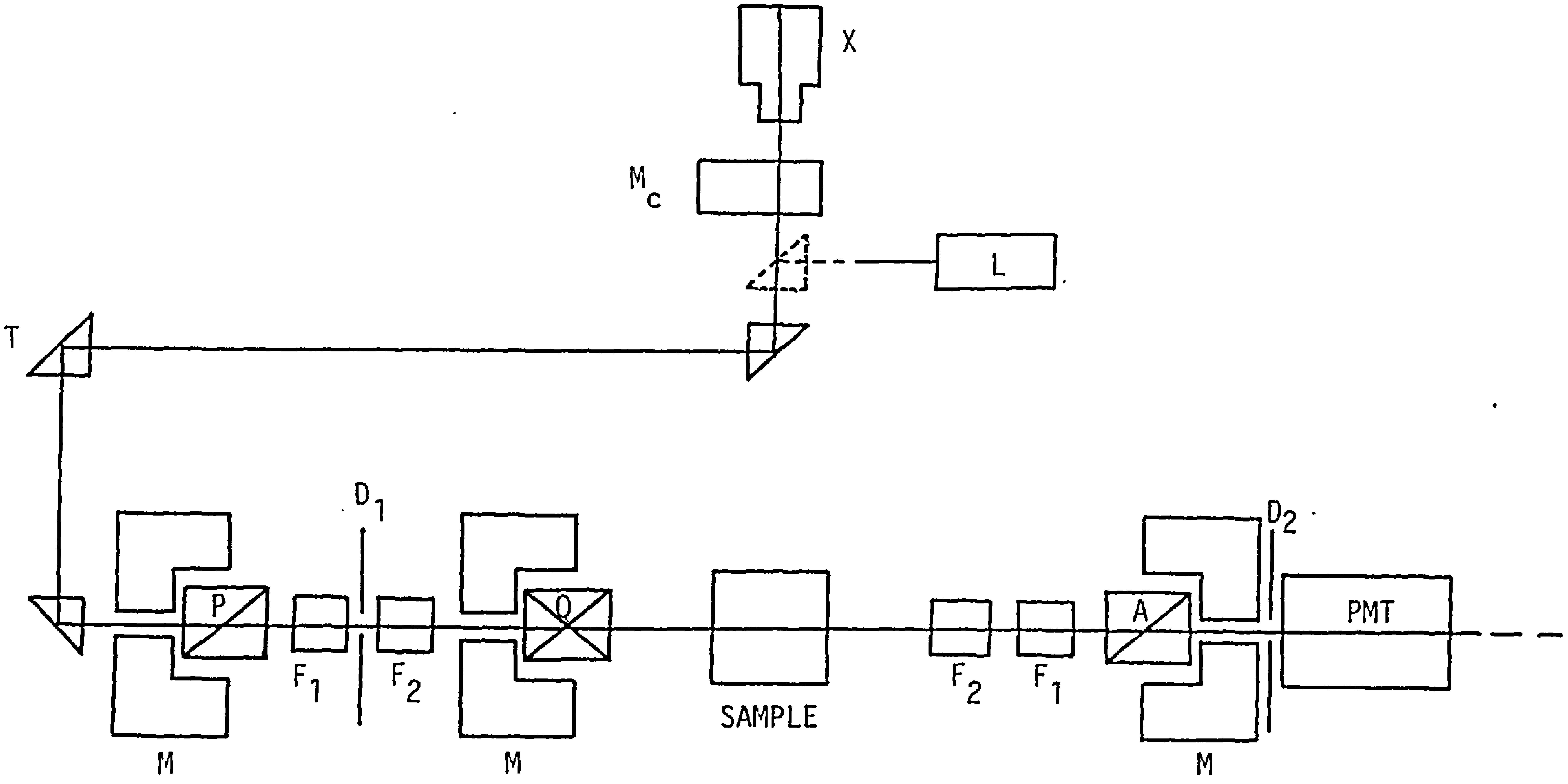

A - Analyser
P - Polarizer
Q - Quarter Wave Plate
M - Moire Encoders
F_1 - Faraday Cores (dc)
F_2 - Faraday Cores (ac)

T - Internal Reflection Mirror
PMT - Photomultiplier
$D_{1,2}$ - Stops to eliminate extraordinary ray
X - Xenon arc lamp
L - Laser (HeNe)
M_c - Monochromator

Fig. 3.3 The optical layout of the ellipsometer

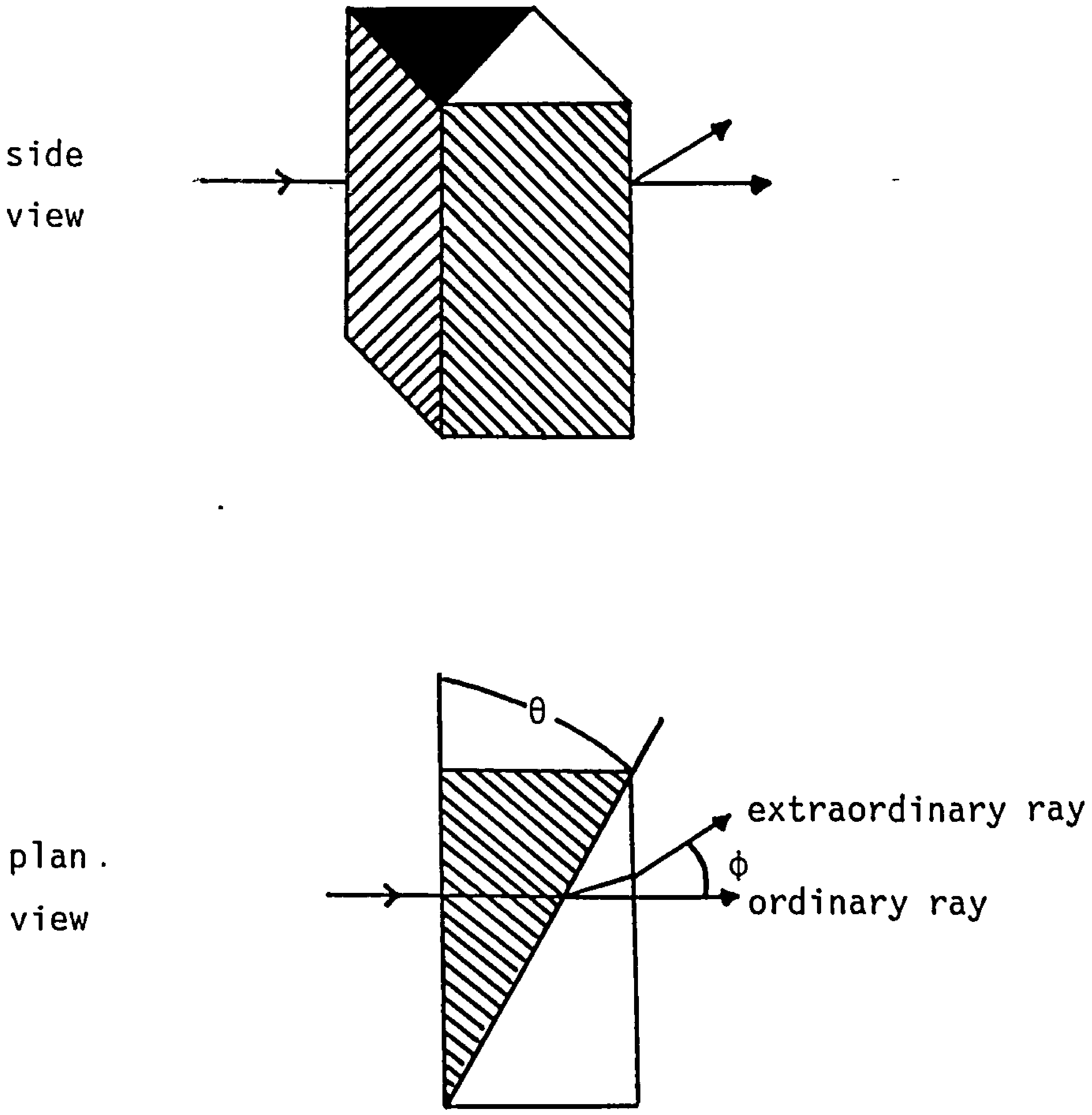

φ depends upon θ

Fig. 3.4 Diagram of a Quartz Rochon Polariser

The polarizer is mounted on the same assembly as the large glass divided circles used to measure the prism azimuths (Optical Measuring Tools Ltd) by means of the Moire fringe effect, fig. 3.5. Photocells detect moire fringes resulting from the movement of lines scribed on the glass circles relative to those present in a fixed grating. This creates a series of pulses which are counted by the angular display unit (Newall Electronics), the number and phase of the fringes giving the angle moved through and the direction of rotation respectively. On switching on the instrument the polarizing circles are rotated until the photocells detect fixed markers on the circle which correspond to an exact known azimuth. Any other azimuth can then be obtained from the pulses counted either side of the marker. This technique provides great accuracy and sensitivity giving a resolution of 1 second of arc in 360°, an overall accuracy of ±2 seconds in 360°. The azimuths are displayed as degrees, minutes and seconds on nixie tubes in the angular display unit and are converted to binary coded decimal (BCD) for subsequent data transfer to the microprocessor.

The light then passes through two Faraday rotation devices which rotate the plane of polarization of the light beam depending on the magnetic flux density in the medium, the length of medium traversed and the wavelength of the light beam.[142] The equation governing the relation is:

$$\theta = V B \ell \qquad \text{.....(3.1)}$$

V = Verdet constant
B = magnetic flux density
ℓ = length of medium traversed

The devices comprise synthetic silica cores manufactured from Spectrosil synthetic silica (Thermal Syndicate) at the National Physical Laboratory. These have end faces parallel to 0.001° giving a beam deviation of about 0.0005°. The cores are surrounded by current carrying coils which are cooled by a Churchill closed loop water circulator, fig. 3.6. The loop for each coil contains a liquid flow sensor (RS Components RS 30431) which generate a pulsed output when the flow is above a certain rate. The output of these sensors is directed to a

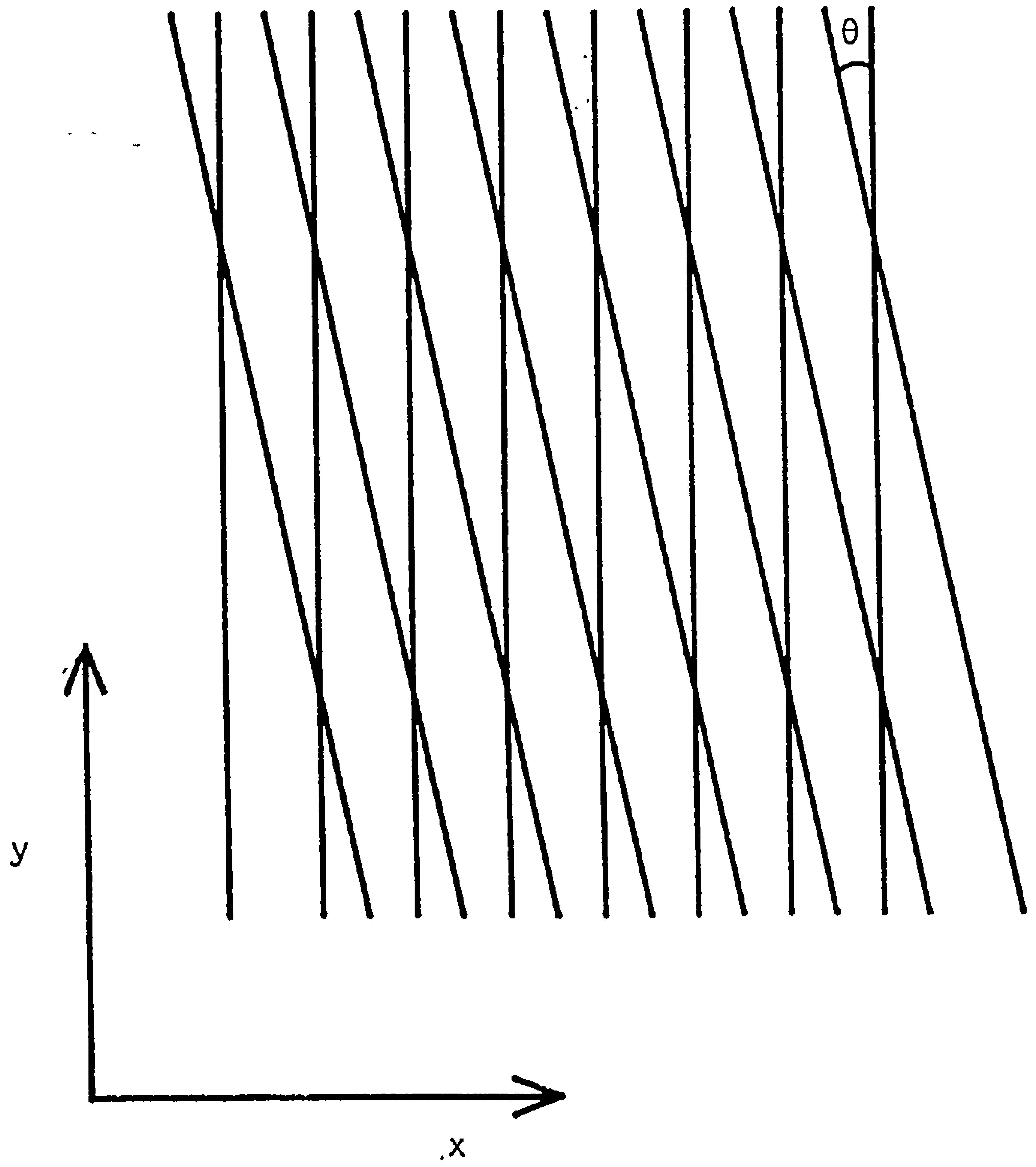

Movement in the x direction produces moire fringes moving in the y direction at a relative speed 100-1000 times that of the x direction depending upon the angle θ. Decreasing θ increases the relative speed of the fringes.

Fig. 3.5 Moire Fringe Effect

Fig. 3.6 Diagram of cut-out device for coolant water loop for Faraday coils

retriggerable monostable, the outputs of which are connected to two high voltage relays wired in series to the Faraday coil power supplies. If the coolant flow should fail or be interrupted for more than a few seconds in either arm the power supply to all the coils is cut off.

The first rotation device is the d.c. Faraday Compensator which provides offset in the plane of polarization of (±13° at $\lambda = 250$ nm or ±1° at $\lambda = 800$ nm). It has a maximum rate of change of slew of 100° s^{-2} at $\lambda = 400$ nm which enables small changes occurring on the surface under study to be followed rapidly without the need to turn the polarizing prisms A and P. The second Faraday rotation device is the a.c. modulator which provides modulation about the null for the phase sensitive detection (p.s.d.) system. This is discussed in Section 3.3. The polarizer and analyser coils operate at different frequencies, 830 hz and 1170 Hz respectively, which have no common harmonics. These frequencies are high enough to provide a rapid response to changes in null, provide a reasonable signal to noise ratio, yet do not require too large a power input. Operating at higher frequencies would improve the signal to noise ratio but would require a higher power input due to the increased impedance of the modulating coils at higher frequencies.

Before the light beam reaches the sample it has a phase shift of $\pi/4$ radians introduced between the p and s components by the quarter wave retarder. This is a King type achromatized three reflection rhomb (Bellingham and Stanley), fig. 3.7, with a stated retardation of 90° to 90.2° for $\lambda = 200$-900 nm. It utilises the fact that for light incident at a phase boundary at angles of incidence greater than the critical angle the light will be totally reflected and a phase shift, δ, introduced between the p and s components depending on the refractive index of the incident medium, n, and the angle of incidence, ϕ:[143]

$$\tan \delta/2 = \frac{\cos\phi(n^2\sin^2\phi - 1)^{\frac{1}{2}}}{n\sin^2\phi} \qquad \text{.....(3.2)}$$

The device in fig. 3.7 utilizes three total internal reflections, two at ~72° and one at 54° to give a total phase change close to 90°. It can be seen from equation (3.2) that the phase change is dependent on n and hence wavelength. By coating one surface with a low refractive index film such as MgF_2 of a suitable thickness (~27.5 nm) the

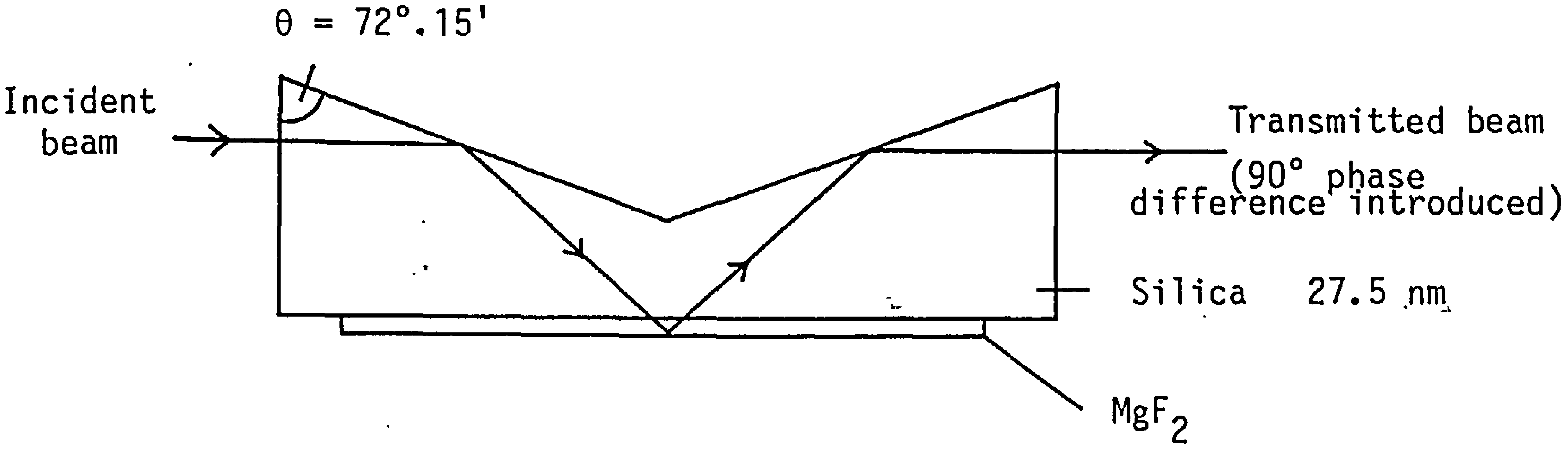

Fig. 3.7 Achromatized 3 reflection rhomb

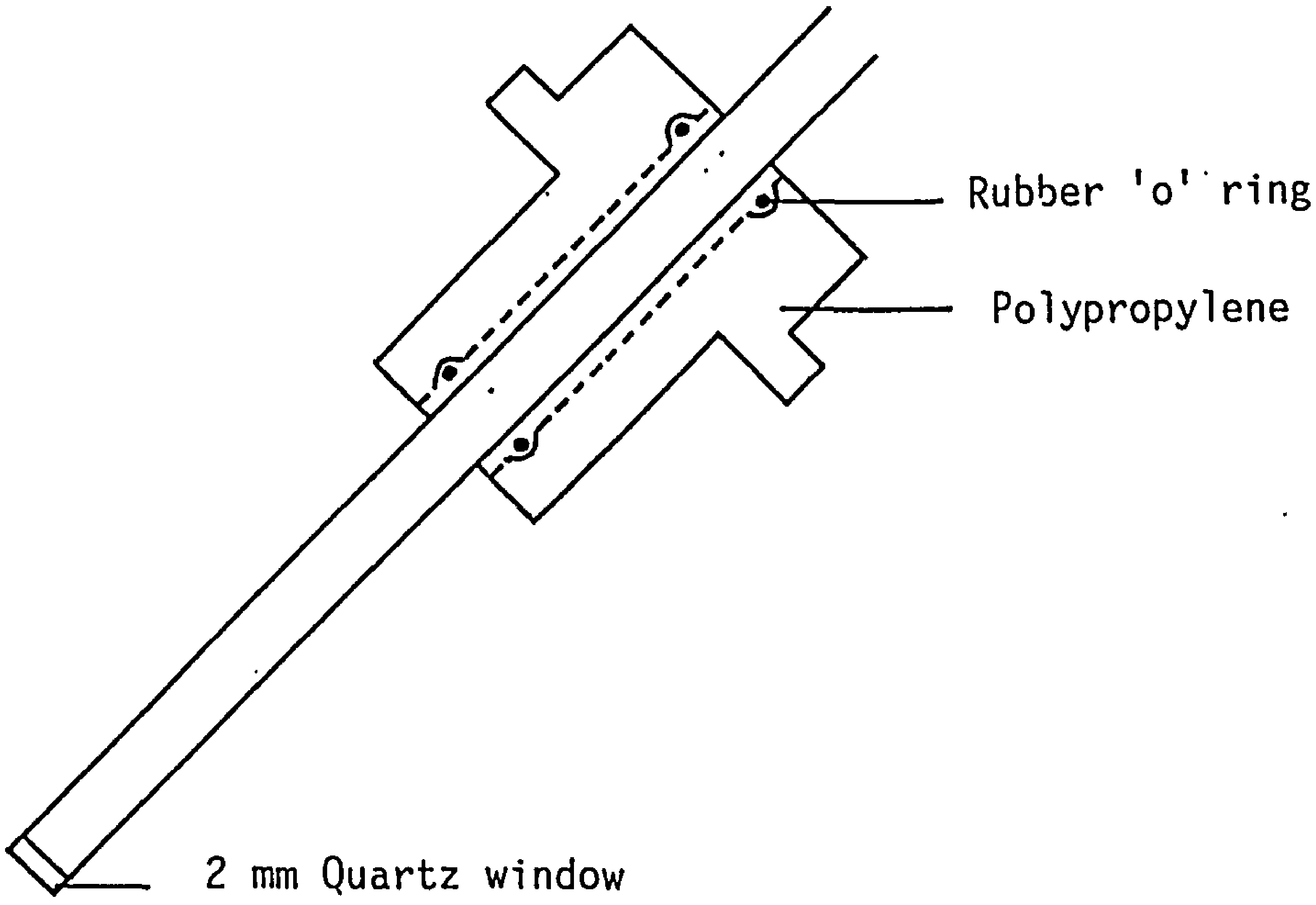

Fig. 3.8 Cell window and holder

reduction in phase difference in the film with decreasing wavelength cancels out the increase in n for silica with decreasing wavelength resulting in a highly achromatic device.

The light beam reaches the sample cell through a 2 mm thick fused quartz window held in position by rubber 'o' rings mounted in a polypropylene holder, fig. 3.8. It is capable of partial extension and retraction into the ellipsometer arms to facilitate positioning of the sample cell. The sample cell rests on a welded steel platform (Microcontrole) which can be raised or lowered by a hydraulic jack. The platform can be translated horizontally in two directions and rotated through 360°. In addition there is limited tilt in two planes to allow the sample surface to be accurately positioned in a horizontal plane. The reflection from the sample can be observed on a matte perspex screen mounted on a sliding tube containing a T.I.R. prism.

On reflection the beam travels through two more Faraday coils, a.c. and d.c. and then through the analyser which is a quartz Rochon type as before utilizing the Moire fringe effect for determination of its azimuth. Light passing through this is detected by a photomultiplier tube (E.M.I. type 9659 Q.A.M.) with an extended S20 photocathode (Centronix 9428359) and quartz window.

Each arm is capable of being independently rotated in the vertical plane from 90° to 0°, although the minimum experimental angle of incidence is 25° due to the large bulk of the arms. The arms are positioned by stepper motors (Superior type SS50) meshing with teeth on a disk coaxial with the axis of rotation. The angle of incidence is obtained to an accuracy of 0.01° by reading two angular measuring tapes (Heidenhain) mounted on the periphery of the toothed disk.

3.3 Obtaining a null

If the ellipsometer is at a null and a.c. modulation is applied to the plane of polarization then the frequency seen at the photomultiplier tube (P.M.T.) will be twice that of the modulating frequency,[138,139] whereas if the system is off null then there will be an additional fundamental frequency component of the form:[140]

$$I = 2AB\sin(\omega t) - \frac{A^2}{2}\cos 2\omega t \qquad .....(3.4)$$

ω = frequency of modulation
t = time
B = offset from null
A = peak rotation of the polarization of the a.c. modulator

The effect of null errors on the a.c. component of the P.M.T. output and the P.S.D. output is shown in fig. 3.9 for the polarizer circuit for signals at, close to and far from null. The P.S.D. multiplies successive ½ cycles by +1 and −1 and integrates the result over a certain time period. This generates a zero, positive or negative signal of varying magnitudes depending on the offset from null and whether it is negative or positive.

An electronically identical circuit is used for the analyser at a different frequency, the outputs from both a.c. signals being combined and displayed on an oscilloscope. This produces a characteristic signal, fig. 3.10, depending on the distance from null.

The time averaged P.S.D. output is amplified and directed to the d.c. compensator. If the magnitude of this signal is outside a predetermined positive or negative limit (approx. ±0.5°) then a pulse is generated by a d.c. coupled monostable which is amplified and used to drive the respective prisms in such a way as to maintain the system close to null, fig. 3.11. If a series of pulses are sent to the prism drives and no pulses are received from the Moire fringe encoders then an audible alarm is triggered. This alarm provides a warning that action must be taken to prevent damage to the motor drives.

3.4 Microprocessor and interfacing details

The microprocessor used is the Motorola M6809 C.P.U. connected to various peripherals via eight ports, four input and four output. Fig. 3.12 shows the general layout of the electronics. The information required from the ellipsometer electronics is the P, Q and A circle azimuths, originally in digital form, and the four analogue channels measuring cell voltage and current and the d.c. Faraday compensator voltages. Multiplexed information containing either the circle

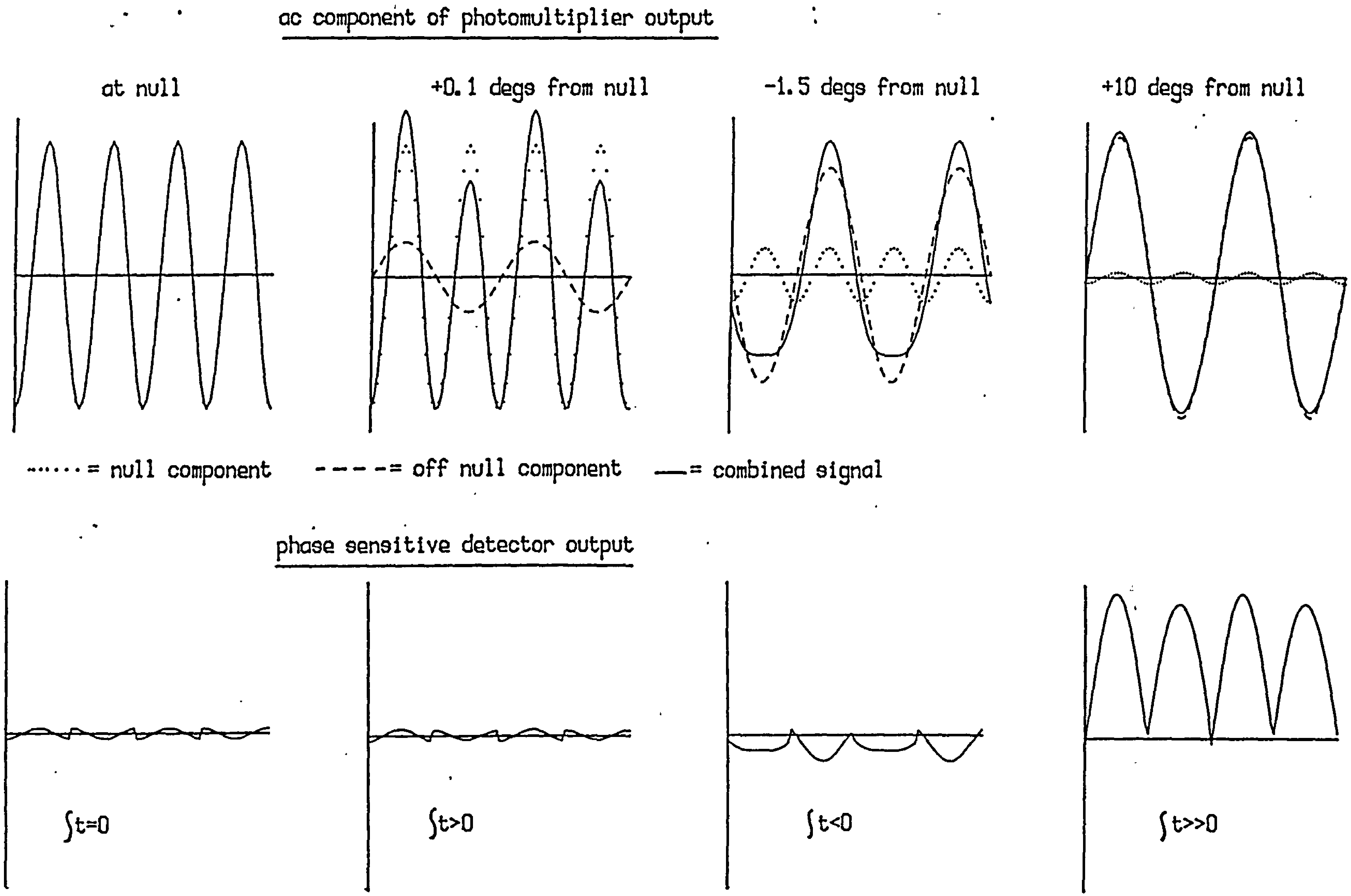

Fig. 3.9 ac component of photomultiplier output and phase sensitive detector output for the polarizer circuit

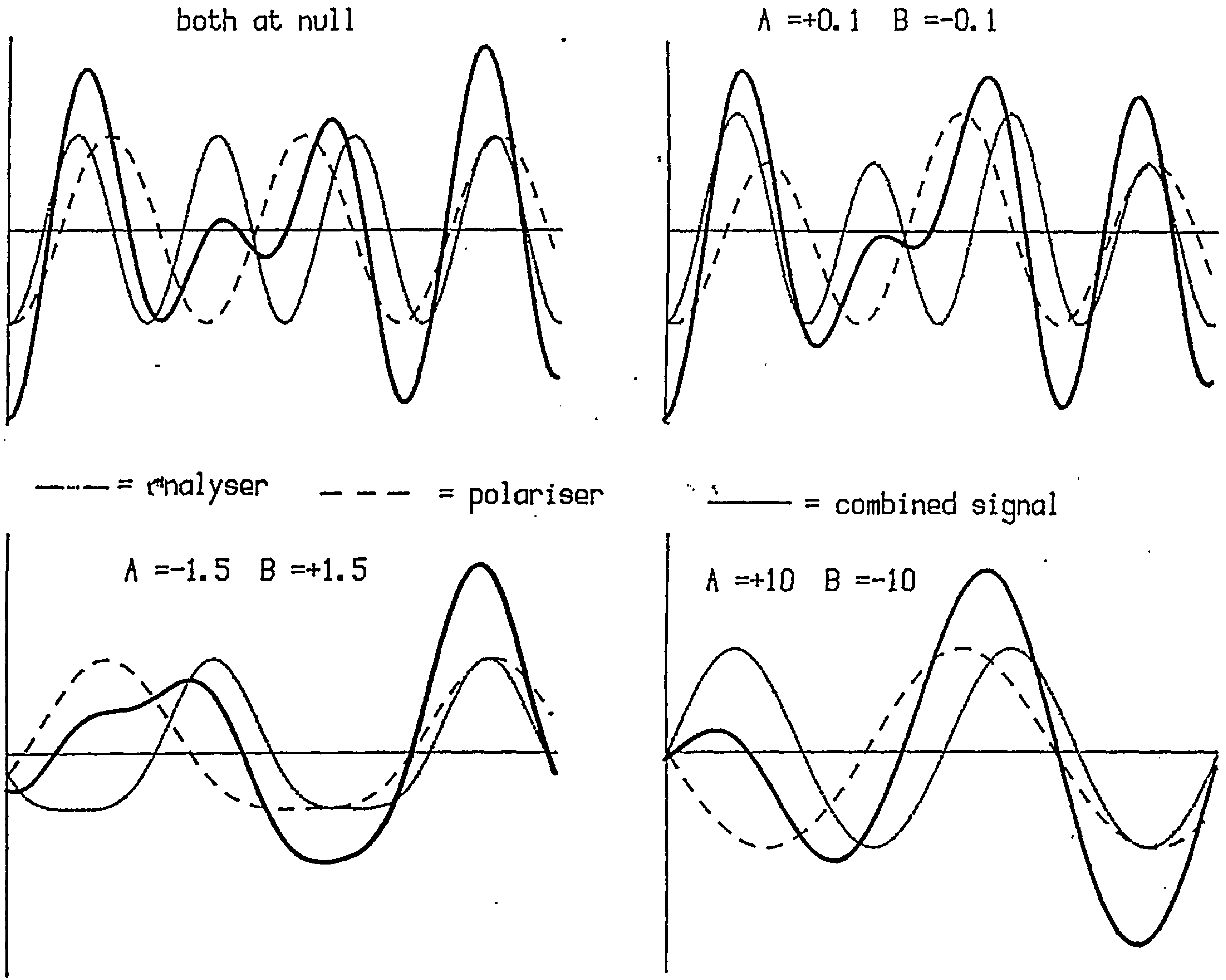

Fig. 3.10 Characteristic signal produced by null errors from combination of analyser and polarizer signals

Fig. 3.11 Analyser servo loop

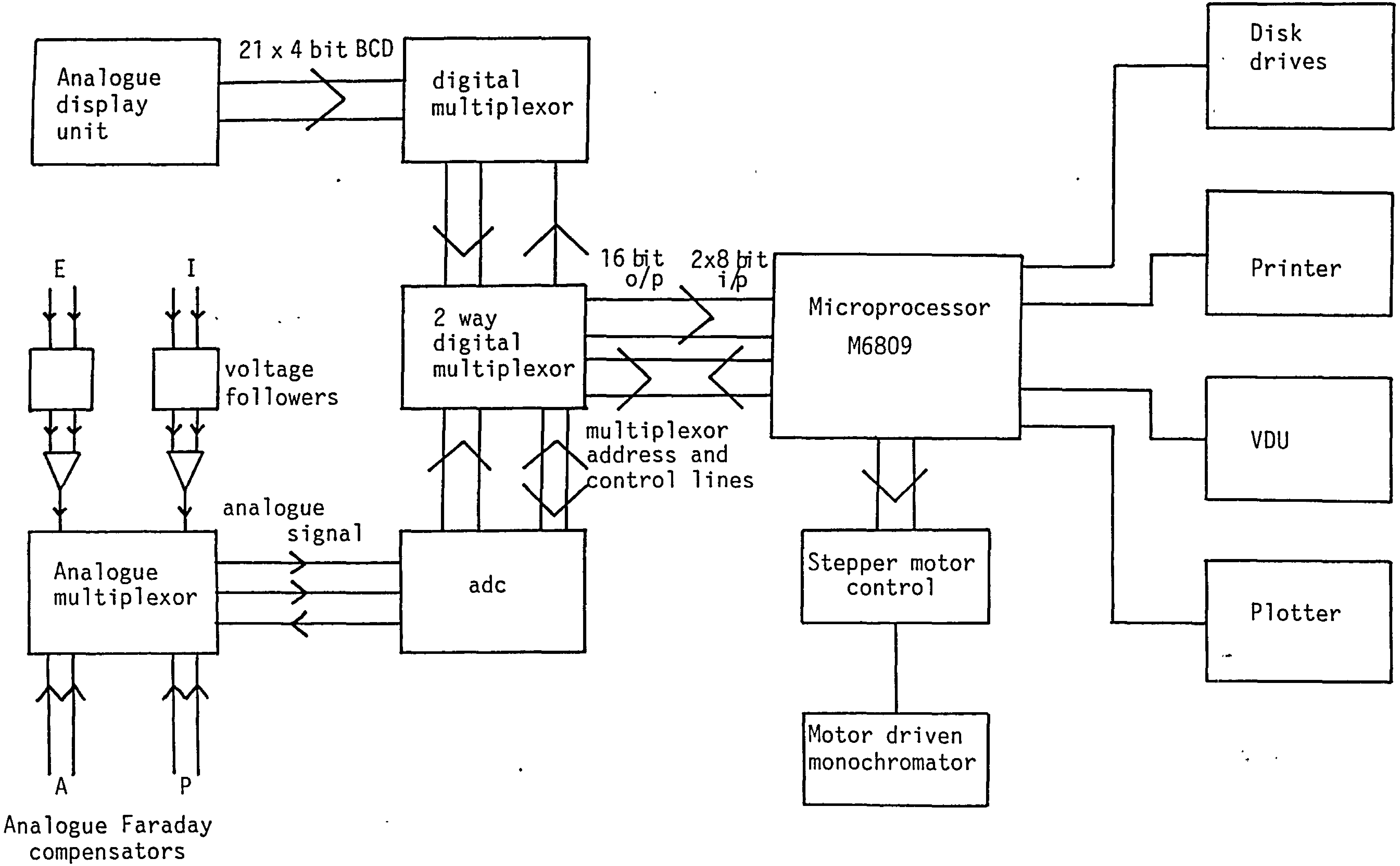

Fig. 3.12 General layout of ellipsometer electronics

azimuths or one of the analogue channels is obtained by selecting the correct address on the address bus using a 4 bit word, table 3.2. The most significant bit (msb) is used by the 2-way digital multiplexor (75257) to select whether the data required is analogue in origin (msb = 1) or digital (msb = 0) and then one of two further multiplexors selects the particular analogue or digital channel required. Data from the circles is originally in the form of 21 x 4 bit binary coded decimal (bcd) digits. When requested, this data is sent to the two-way multiplexor in the form of 2 16-bit words. The analogue signal is converted to a 12 bit 2's complement binary number by an analogue to digital (adc) convertor situated between the analogue multiplexor and 2-way digital multiplexor. The data is sent from the 2-way digital multiplexor to the C.P.U. in the form of 2 x 8 bit words. Analogue channels 1 and 2 (cell voltage and current) are buffered by the use of voltage followers (TC084) and in addition the cell current is amplified by a factor of 10 prior to being multiplexed.

Apart from visual display of the data (Newbury 4008 VDU) a hard copy can be obtained from a dot matrix line printer (NEC PC8023D-C) and the data can be stored on-line using one of two floppy disk drives. There is also a graphics plotter (Hewlett Packard HP7470A) for plotting out the data in graphical form either during or after an experimental run.

The system contains an S-Bug-E monitor program (S.W.T.P.) stored in read only memory (ROM) for communication between the VDU and CPU, for machine code development and for initial loading of the disk operating system (DOS). The latter is FLEX 2-7-3 (Technical Systems Consultants Inc.) and comprises a file management system, DOS and utility command set. The high level language used for data acquisition and manipulation is extended basic, X-BASIC (Technical Systems Consultants Inc.) which is stored in random access memory (RAM) together with stored data and the machine code program used to access data and drive the monochromator.

Two timers are interfaced to the CPU to provide interrupts for time delays during experimental runs. A date-time chip has been installed to enable the data and time elapsed between points to be recorded. A hardware arithmetic chip (AM9511) has also been installed to speed up the calculation of trigonometric functions for theoretical calculations.

Table 3.2

Data Selection and Structure

MUX address binary	"HICIRC" $E00A		"LOCIRC" $E008		Memory location hex
		Data in binary coded decimal			
0001	–	A° hundreds	A° tens	A° units	F7FE–F7FF
0010	A' tens	A' units	A" tens	A" units	F7FC–F7FD
0011	–	P° hundreds	P° tens	P° units	F7FE–F7FF
0100	P' tens	P' units	P" tens	P" units	F7FC–F7FD
0101	–	Q° hundreds	Q° tens	Q° units	F7FE–F7FF
0110	Q' tens	Q' units	Q" tens	Q" units	F7FC–F7FD
		Data in 12 bit 2's complement			
1000	-	External Channel 1 (Cell Voltage)			F7ED–F7EE
1001	-	External Channel 2 (Cell Current)			F7ED–F7EC
1010	-	P Faraday Compensator			F7E9–F7EA
1011	-	A Faraday Compensator			F7E7–F7E8

3.5 Data acquisition and software

3.5.1 Data acquisition

Two computer programs are used for obtaining ellipsometric data, a basic program for communicating with the user and a machine code program for communicating with the ellipsometer electronics via the peripheral interface adapters, PIA's. Transfer of information between these two programs is by means of user routines whereby a 16 bit argument is passed to the machine code program which then uses this information to obtain the required data from the ellipsometer electronics and store it in RAM. At the end of this process the data can be obtained in the BASIC program by using PEEK statements.

3.5.2 Basic program

The main basic program used for data acquisition is GETPLT which will obtain an infinite number of data prints with varying time intervals. It processes the data during the experimental run and obtains Δ and Ψ from the circle azimuths and d.c. compensator readings which it files and/or plots together with cell voltage (V) and current (I) and time elapsed since the start of the experiment. The full program is in Appendix A1.

The first part of the program initialises the plotter, draws and labels plotter axes and sets various flags depending on the output wanted. The machine code program sub routine (mcp s/r) 'INIT' is called to configure the PIA's and the time interval between the points is set using the mcp s/r 'TINT'. The azimuth of the quarter wave retarder is obtained and the program temporarily stopped if it is not 45° or 135° within ±0.001°. The program then waits for an operator generated start, and gets the real time to within 0.1s from the date time chip using the mcp s/r 'TINIT'. The azimuth and analogue data are obtained using the mcp s/r 'CIRC' and 'ANALOG' and a 50 cycle loop instigated if the cell current is to be averaged, i.e. if it is particularly noisy. The azimuth data is obtained in the form of degrees, minutes and seconds and is converted to a decimal value in degrees. The analogue data is converted from 2's complement to decimal values. A correction factor is applied to the analogue data which converts the digitized signal to a value representing the initial voltage.

For the d.c. compensator signals this conversion factor incorporates a term relating the d.c. compensator voltage to the variation of the plane of polarization in degrees from equation (3.1). Δ and Ψ are calculated from the P, Q and A values by dividing the data into groups or zones depending on the value of P, Q and A, table 3.3. Δ and Ψ are then obtained by subtraction using the polarizer and analyser values respectively. For example a value of A = 45°, Q = 45° and P = 90° would give values of $\Delta = 450-2P = 270°$ and $\Psi = 45°$.

The data is then output to the VDU, filed, printed and plotted as required and then the mcp s/r 'TINT' is used for the set time delay. At the end of this interval the time elapsed is obtained. The program then proceeds to find the next data points until it is interrupted by the operator.

Although this program is flexible and provides a real time plot indicating the changes occurring during an experiment, it does have the disadvantage that a time period of about 0.9 seconds is needed to obtain data. If rapid changes are occurring in the data e.g. during fast potential sweeps then a modification of the above program is used - 'GETPLT3'. This obtains raw data from the mcp and stores it in RAM for processing at the end of the experiment. It can obtain one datum point in about 0.02 seconds, but provides no "real time" indication of how an experiment is progressing.

3.5.3 Machine code program

The machine code program used is 'FAST1.BIN' and is listed in Appendix A2. It consists of the following subroutines.

Name	Description
INIT	Initializes PIA's so that circles are inputs and the prism motors, monochromator motor and address bus are outputs.
CIRC	Reads a single value from basic either 1 (A), 2 (P) or 3 (Q) then selects the correct multiplexor address, table 3.2 to read the required circle azimuth.

Name	Description
TINIT	Uses the RS304 548 date time chip which generates a 4 bit BCD value depending on the addbuss value, see table 3.4, after a read data pulse has been sent. The 12 byte output is stored in memory locations \$F7F0-\$F7FB. If the data registers are updated during a read operation then the data bus is set to \$F, the data rejected, and the data bus re-read.
ANALOG	Reads the four analogue channels. It selects the correct multiplexor address for each channel in turn and sends a pulse to the a.d.c. to enable it to digitize the selected analogue signal into a 12 bit 2's complement binary word. The information is stored at \$F7E1-\$F7E6.
STEPIT	Drives the monochromator at 400 steps/second by pulsing the stepper motor with the required number of pulses, called from BASIC. A loop is provided for a time delay between pulses.
TINT	Uses the two timers at port ≠ 3 to generate a time delay between data points. The first timer generates 10 ms ticks which are counted down by the second timer according to a divisor set before the start from BASIC. The routine waits for the flag from the second timer to be set before exiting from the s/r.

3.5.4 Plotting data

Data obtained from the previous two programs is filed on disk as a 3 column (Δ, Ψ and time interval between points) or a 5 column (Δ, Ψ, t, cell voltage and cell current) data file. Various basic programs have been written to read and plot these files on the graphic plotter. Routines in the program automatically scale the data, find the maximum and minimum points and allow for overlay of several graphs. The program 'PLOTV' in Appendix A3 contains these routines and can in addition provide plots in a variety of formats together with different line types and symbols for data points. It also contains a routine for annotating the finished diagram.

Table 3.3

Calculation of Δ and Ψ from P, Q and A Readings

Analyser* degrees	Quarter wave Retarder degrees	Polariser* degrees	Δ degrees	Ψ degrees
0-90	45	0-45	90-2P	A
		45-180	450-2P	A
0-90	135	0-45	630-2P	A
		45-180	2P-90	A
90-180	45	0-135	270-2P	180-A
		135-180	630-2P	180-A
90-180	135	0-135	90-2P	180-A
		135-180	2P-270	180-A

* If A or P are outside the range 0-180° then 180° is added for negative values or 180° subtracted for values greater than 180°.

Table 3.4

Selection of Data for Date/Time

Address Register BCD	Data Selected	Memory Location Hex
0001	Tenths of sec	F7F0
0010	Units of secs	F7F1
0011	Tens of secs	F7F2
0100	Units of mins	F7F3
0101	Tens of mins	F7F4
0110	Units of hours	F7F5
0111	Tens of hours	F7F6
1000	Units of days	F7F7
1001	Tens of days	F7F8
1010	Day of week	F7F9
1011	Units of months	F7FA
1100	Tens of months	F7FB
1101	Years	-
1110	Stop/Start	-
1111	Interrupt and status	-

CHAPTER 4 EXPERIMENTAL

4.1 Reagents

All electrolytes were prepared from analytical grade reagents using singly distilled water. In most cases the electrolytes were air-saturated but for some experimental runs they were deoxygenated with white spot nitrogen for two hours prior to use. All the alkaline solutions were stored in plastic containers to avoid the leaching of silica, the deleterious effect of which has been discussed in Chapter One.

4.2 Electrochemical equipment

Electrode potentials were monitored and controlled by a Wenking potentiostat (70 TS1) coupled to a voltage scan generator (Wenking VSG 72) capable of scanning over the range ±10V. A platinum foil counter electrode (~30 mm^2) was used, and either a saturated calomel (Radiometer K401) or a reversible hydrogen reference electrode. The latter comprised a strip of platinized platinum foil (~3 mm x 15 mm) contained in an open ended tube, half of which was in an atmosphere of cathodically generated hydrogen with the remainder immersed in the test solution, fig. 4.1. This produced a reference electrode which had a stable potential over a period of weeks. It also has the advantage that it did not contaminate the sample solution with e.g. chloride ions which are well known for their depassivating effect on Mg and Magnox as was discussed in Chapter One. The potential of the reversible hydrogen electrode was periodically checked by comparison with the potential obtained from a saturated calomel reference electrode. If found to be significantly different from the thermodynamic value for the $H_2/2H^+$ couple at the pH of the solution then the electrode was cleaned, replatinized and recharged with hydrogen.

The cell current and voltage could be recorded in analogue form using a chart recorder (Farnell DW 212 A) or digitally using the ellipsometer data acquisition routine via two buffered analogue inputs as described in Chapter Three.

4.3 Spectroscopic apparatus

Most of the surface analysis was carried out at B.N.L. using a V.G. Scientific Secondary Ion Mass Spectrometry (SIMS) instrument.

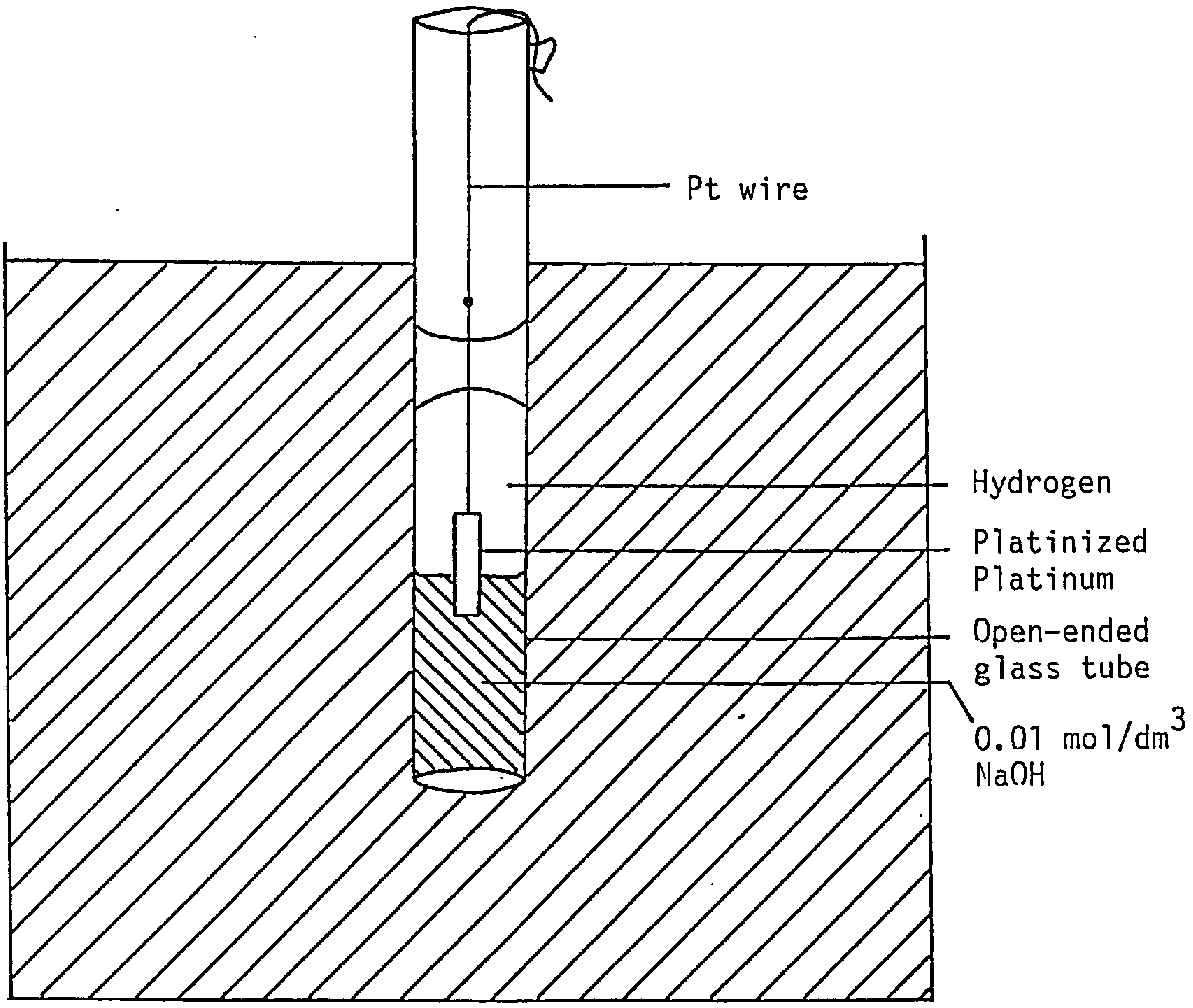

Fig. 4.1 Reversible hydrogen reference electrode

An AG 61 argon ion gun with a maximum voltage of 5 KeV and a beam current varying from 20-100 nA was used with the products being analysed by an SQ 300 quadropole mass spectrometer. A vacuum of less than 10^{-9} mbar was maintained inside the u.h.v. chamber using an Edwards oil diffusion pump and two rotary pumps. Scanning Auger analysis was undertaken by R. Wild using a Perkin Elmer S95 instrument.

4.4 Sample cell

The sample cell, fig. 4.2, consists of a machined polypropylene block open at the top. It has an aperture at the bottom for the sample holder and large oval apertures at the sides for the cell windows. The latter are necessarily large compared to the diameter of the cell windows to permit the angle of incidence to be varied from 30° to 80°. This arrangement exposes the solution, contained in the cell, to air and if deoxygenation of this solution is required then the cell is modified. A tight fitting clear perspex lid is used to seal the top of the cell whilst permitting observation of the sample during experiments. This lid is perforated by four tapered holes to allow reference and working electrodes and a gas distribution tube, for deoxygenation, to be inserted. The cell window apertures can be sealed using silicone rubber gaskets which have however the disadvantage of restricting the angle of incidence to 70° and also making sample alignment difficult. If very low levels of oxygen and/or carbon dioxide are not required an alternative system is therefore used: polythene bags are attached to the sample cell and cell windows by elastic bands and a suitable pressure of the deoxygenating gas is used to maintain an inert blanket above the deoxygenated solution. A deoxygenated solution can be admitted to the cell after sample etching whilst maintaining an "oxygen free" atmosphere by the use of a reservoir placed above the cell. This system, fig. 4.3, was necessary as deoxygenation _in situ_ prior to the insertion of the electrode was impossible as the electrode is inserted into the base of the cell holder. The experimental solution was deoxygenated in the reservoir for a period of about 2 hours before use using a gas distribution tube with a No.2 porosity sintered end. No stirring of the reservoir solution was undertaken as it was thought that agitation of the solution by the incoming gas would be sufficient to ensure uniform deoxygenation given the small volume of solution used (<200 cm^3).

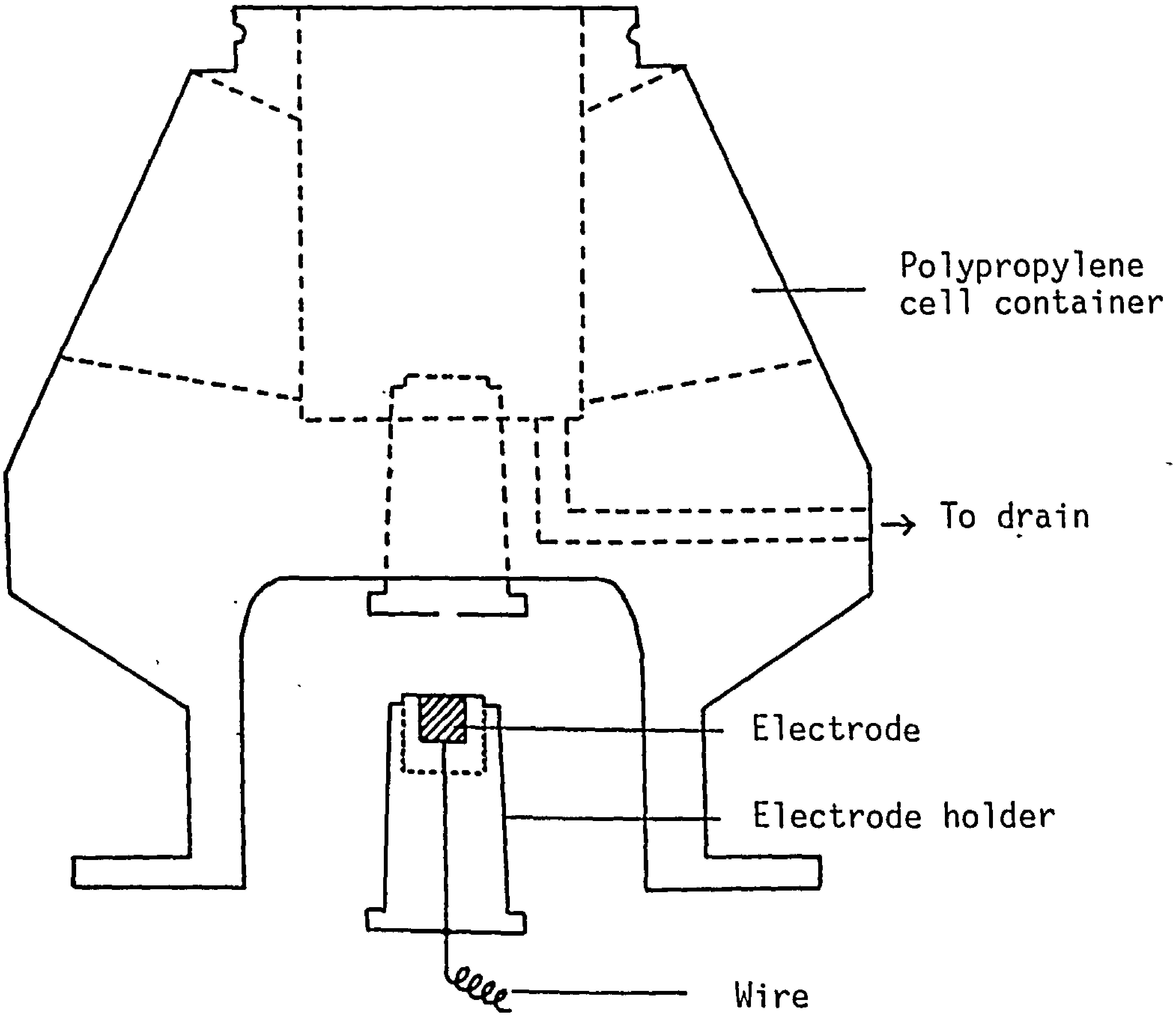

Fig. 4.2 Sample cell and cell holder

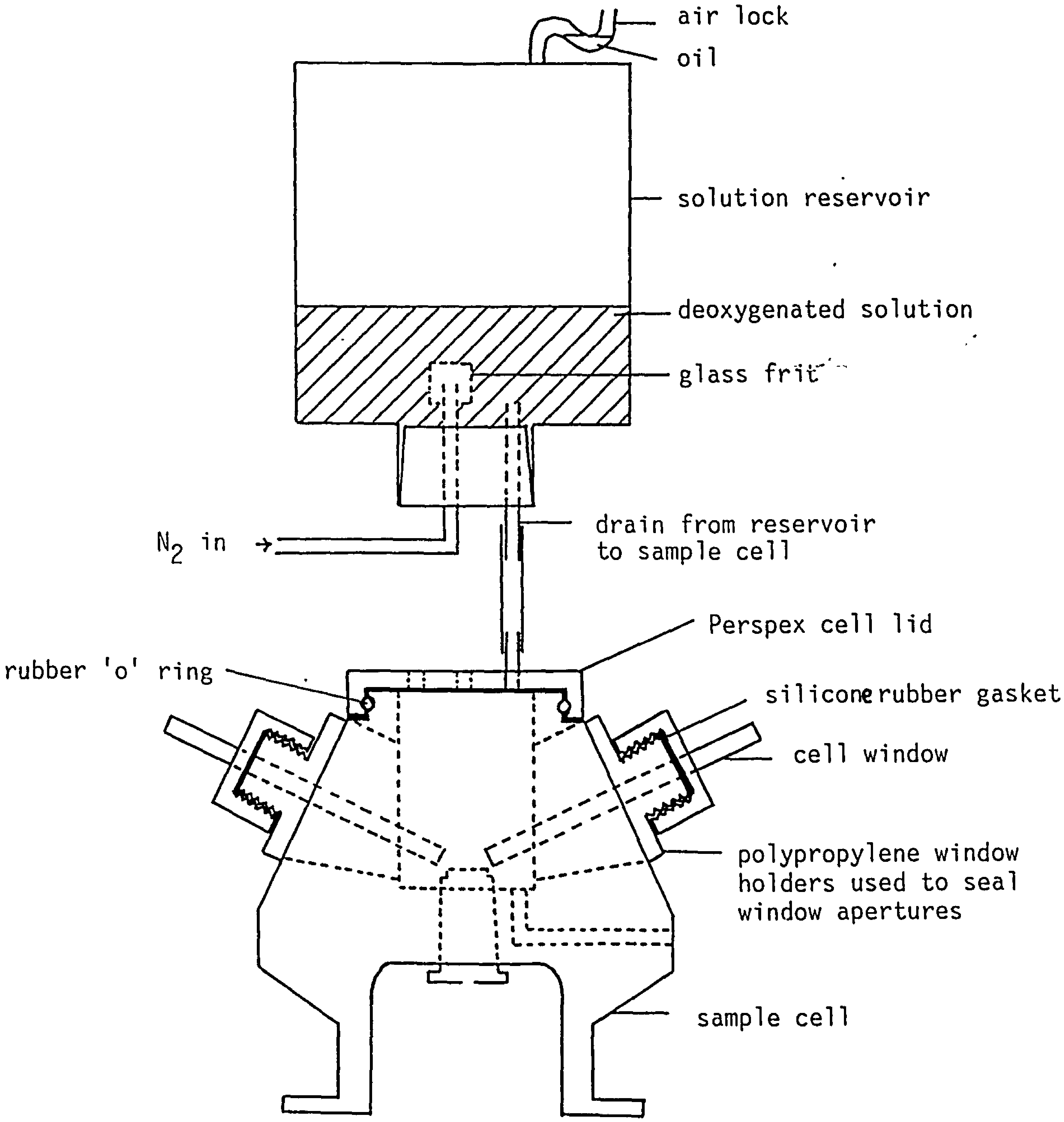

Fig. 4.3 Diagram of sample cell and reservoir used for experiments undertaken in deoxygenated solutions

The level of dissolved oxygen in the sample solution was not measured as the equipment for doing this in situ was not available and it is not claimed that very low oxygen levels (<10 ppb) were obtained. This would not be possible without considerable modification of the cell and the aim was rather to investigate the gross effect of oxygen on the corrosion behaviour.

Due to the rapid oxidation in air of magnesium and Magnox i.e. after chemical etching, as evinced by the experimental results, it is imperative to reduce the time between removing the etchant and replacing it with the experimental solution as far as possible. This was achieved by the use of a hand-held suction pump to remove the etchant.

4.5 Sample preparation

For the majority of experiments the substrate was either polycrystalline, triple distilled magnesium (99.99% pure) or polycrystalline Magnox alloy of a typical composition as given in table 4.1.[2] In addition a high purity (99.99% pure) magnesium crystal (~12 mm^2) from Goodfellow Metals was used to investigate the possibility of epitaxial film growth. The Mg and Magnox rods, of 12 mm diameter, were cut into discs of approximately 2-3 mm in thickness and then mounted in epoxy resin to produce a sample with a diameter of 19 mm and a height of about 10 mm. Electrical contact was maintained by an insulated wire bound to the back of the electrode by silver epoxy resin. The same procedure was followed for the single crystal.

The polycrystalline samples were turned flat on a lathe then polished using successively finer grades of alumina mounted on polyester strips (3 M Mylar strips) using dilute Teepol as a lubricant and finished off with 1μ and 0.05μ alumina powder on a soft polishing cloth (Buehlar microcloth). This preparation method produced a surface that was optically flat and free from obvious scratches although polishing marks could be observed under low power magnification in an optical microscope.

The sample could then be mounted in a tapered polypropylene stopper, using P.T.F.E. tape to provide a tight fit, and fitted into the base of the sample cell. The stopper contained a hole in the base through which the wire attached to the electrode could pass. This hole was sealed with silicone rubber before mounting in the cell holder.

Table 4.1

Typical Composition of Magnox Alloy Used[2]

Element	% Composition
Mg	~99.85
Al	0.8
Be	0.006
Mn	0.003
Fe	0.003

4.6 Solution optical constants

The refractive indices of all the solutions were measured using an Abbe -60 refractometer (Bellingham and Stanley) using illumination from a sodium vapour lamp source at a wavelength of 589.3 nm. The refractive indices at 632.8 nm (He/Ne laser) were calculated by assuming that the dispersion correction for these dilute solutions was the same as that for pure water, table 4.2.[144] The dispersion of a substance is related to its refractive index, in general the larger the refractive index the greater the dispersion for normal dispersion.[145] By applying the dispersion correction for a substance with a similar refractive index at 589.3 nm then the refraction index at 632.8 nm can be estimated.

4.7 Corrosion film optical constants

In Chapter One it was stated that the most likely corrosion films formed on Mg and Magnox in aqueous solution are $Mg(OH)_2$, MgO and MgH_2 and possibly MgF_2 in the presence of fluoride. The optical constants for MgO and MgF are available in the literature over a wide range of wavelengths[146] and those for $Mg(OH)_2$[147] and MgH_2[148] at a wavelength of 589.3 nm. The latter two indices can be corrected to values at 632.8 nm by using the same procedure as in section 4.6 whereby the dispersion of a substance with a similar refractive index is used. For $Mg(OH)_2$ it was found that KBr had a very similar refractive index (1.560 for KBr at 589.3 nm[146] c.f. 1.559 for $Mg(OH)_2$) and the dispersion correction for this material was used. It was more difficult to find a suitable material for MgH_2 with a known dispersion but AgCl was thought to be reasonably close (2.066 for AgCl at 589.3 nm[146] c.f. 1.95 for MgH_2). Table 4.3 gives the optical constants and dispersion equations for MgO, MgF_2, $Mg(OH)_2$ and MgH_2 with graphs of the dispersion of these materials and for AgCl and KBr shown in fig. 4.4.

It should be pointed out that all these films are crystalline and optically non-absorbing which may not be the case for corrosion films grown under the experimental conditions used.

Table 4.2

Wavelength Dispersion for Water[144]

Wavelength nm	Refractive index
404.66	1.342742
435.84	1.340210
486.13	1.337123
546.07	1.334466
587.56	1.333041
589.00	1.332988
632.80	1.331745
656.28	1.331151
706.52	1.330020

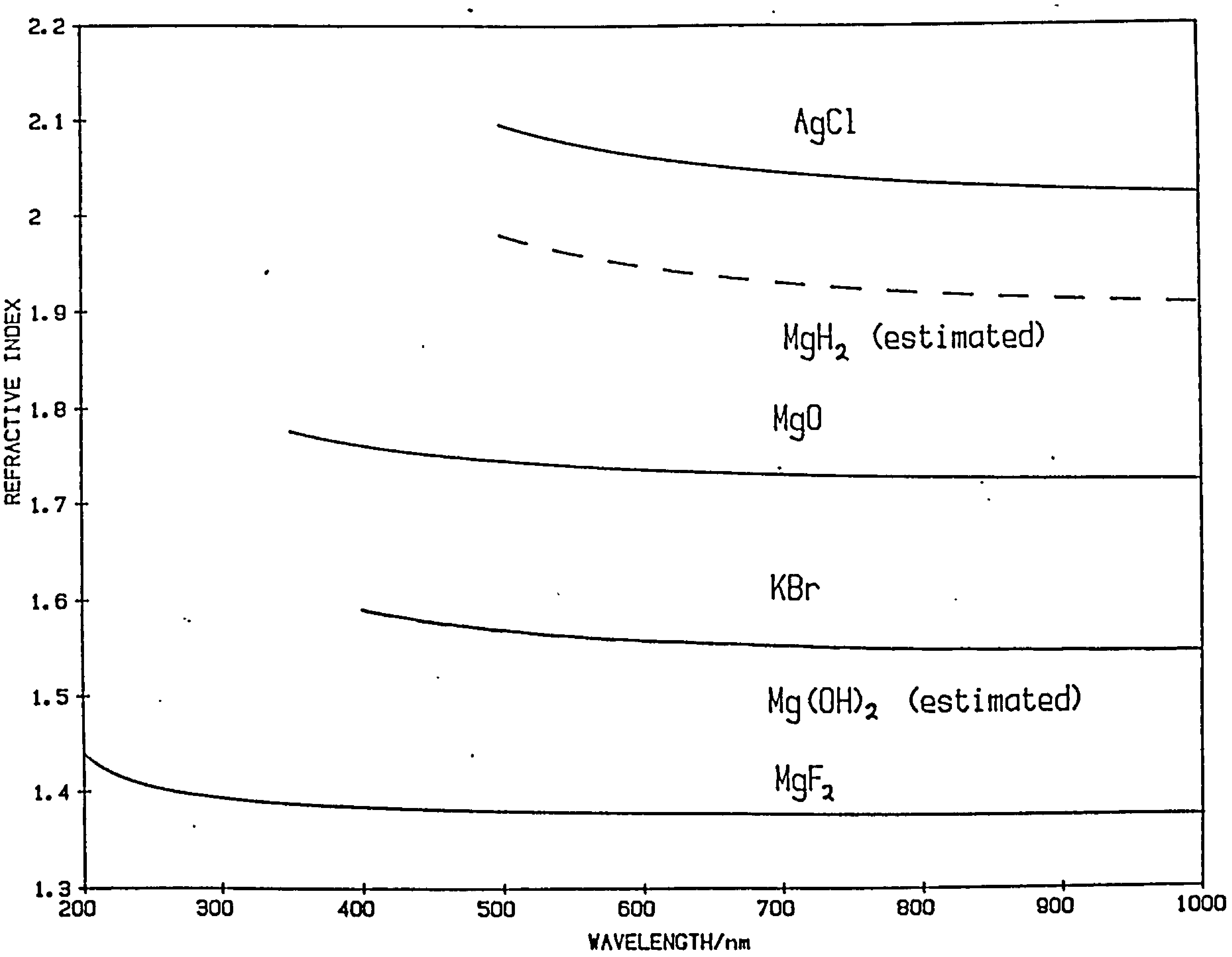

Fig. 4.4 Graphs of the dispersion of refractive index with wavelength for MgO, MgH_2 and $Mg(OH)_2$

Table 4.3

Refractive Indices at 632.8 nm and dispersion equations for MgO, $Mg(OH)_2$, MgF_2 and MgH_2[146,147,148]

Film	n	Dispersion equation used	Ref.
MgO	1.735	MgO	Lange
MgF	1.378	MgF_2	Lange
$Mg(OH)_2$	1.566	KBr	CRC
MgH_2	1.94	AgCl	Ellinger *et al.*

Dispersion equations

MgO

$$n^2 = 2.956362 - 0.0162387\,\lambda^2 - 2.04968 \times 10^{-5}\,\lambda^4 + \frac{0.02145770}{\lambda^2 - 0.01428322}$$

λ in µm

MgF_2

$$n^2 = 1.36957 + \frac{35.821}{\lambda - 1492.5}$$

λ in nm x 10^{-1}

$$n^2 = \left[2.361323 - 3.11497 \times 10^{-4}\,\lambda^2 - 5.8613 \times 10^{-8}\,\lambda^4 + \frac{0.007676}{\lambda^2} + \frac{0.0156564}{\lambda^2 - 0.0324}\right| - Y$$

λ in µm

where $Y = 0.001$ = difference in n between KBr and $Mg(OH)_2$ at 589.3 nm.

MgH_2

$$n^2 = \left[4.00804 - 8.5111 \times 10^{-3}\,\lambda^2 - 1.9762 \times 10^{-7}\,\lambda^4 + \frac{0.079086}{\lambda^2 - 0.04584}\right| - Y$$

λ in µm

where $Y = 0.116$ = difference in n between AgCl and MgH_2 at 589.3 nm.

4.8 Substrate optical constants

4.8.1 Literature optical constants

There are several references[96,149-157] in the literature for the optical constants of magnesium as its high reflectance in the visible and ultraviolet make it a useful metal for mirror coatings. Drude[156] in 1890 obtained the optical constants at a single wavelength of 589.3 nm for bulk Mg and in 1936 O'Bryan[157] published data for n and k over the wavelength range 405-578 nm for evaporated Mg films at a pressure of 10^{-6} mmHg. More recently H.J. Hagemann et al.[96] have published optical data from the far infrared to the X-ray region based on their own data and the published results of other workers. For the visible region n and k were obtained from Kramer's Kronig analysis using extrapolation from transmittance data applied to the reflectivity measurements of other workers.

The differences between the optical constants published in the literature, figs. 4.5a and 4.5b, can be attributed to the different methods of sample preparation, the quality of the vacuum obtainable at the time of the experiment and also the measuring technique used. For a very reactive metal such as Mg, tarnishing in air is rapid[158] requiring great care in sample preparation and a vacuum of the order of 10^{-9} mmHg or less for a film free surface.

The most recent results published by D.E.S.Y.[96] are the most comprehensive and would appear to be the most precise due to the care taken in surface preparation, the ultra high vacuum used and the exhaustive analysis carried out on the results. Using these published values for n and k in the wavelength range 250-830 nm, table 4.4, the optical constants at 632.8 nm can be obtained for n by a cubic spline fit, fig. 4.6a, and for k by a straight line plot, fig. 4.6b.

4.8.2 Experimentally determined optical constants

For reliable modelling of film covered surfaces it is necessary to know the optical constants of the bare substrate.[73] The previous section has described the literature values available for Mg but these are either for bulk magnesium in a poor vacuum[156] or for evaporated Mg films in UHV.[96] The former results are unlikely to represent a film-free surface for a very reactive metal such as Mg and the latter

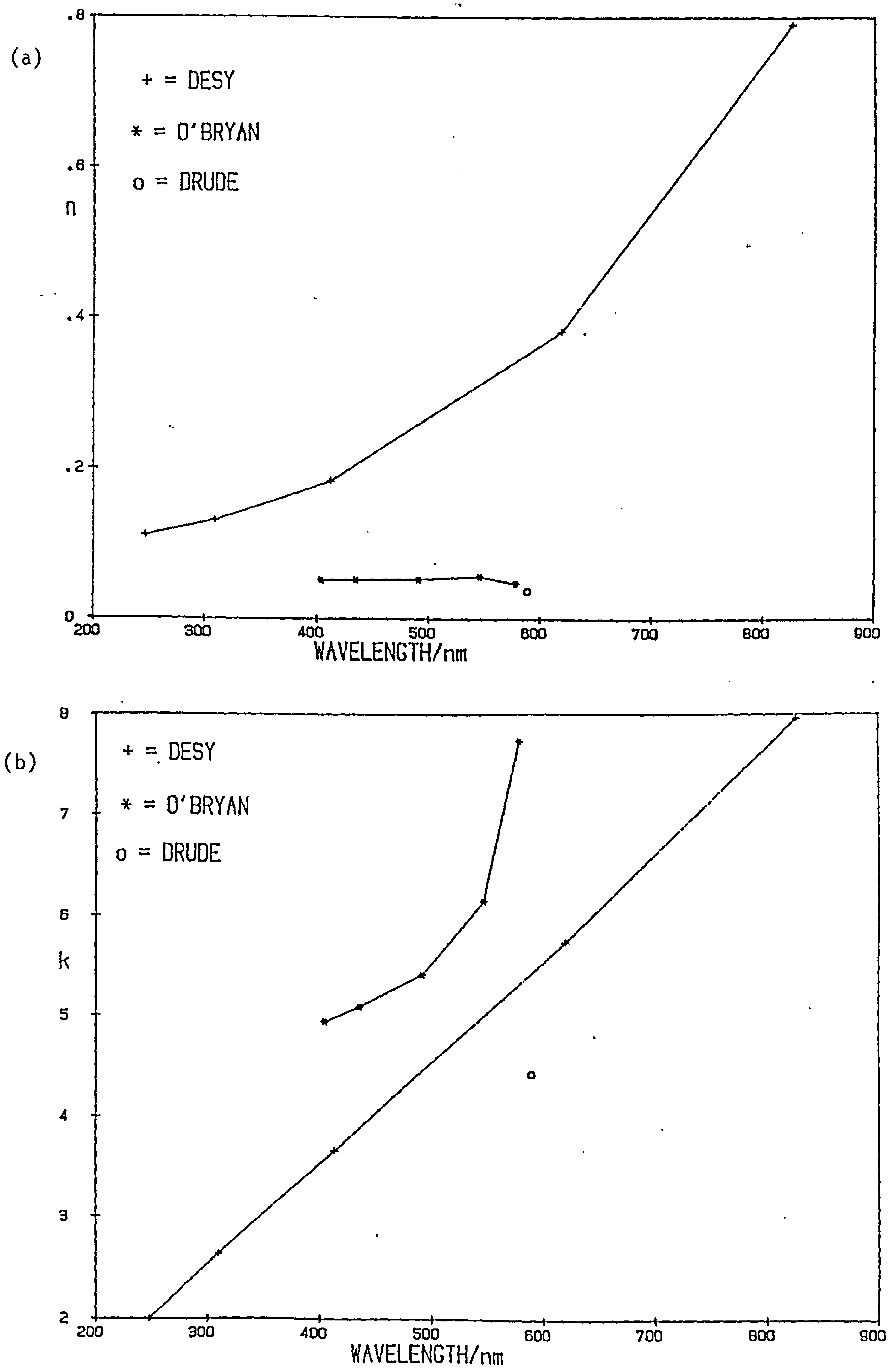

Fig. 4.5 Literature values for the optical constants of Mg[96,156,157]

Table 4.4

Optical Constants for Mg[96].

λ	n	k
247.97	0.111	2.00
304.963	0.132	2.63
413.285	0.184	3.66
619.926	0.382	5.74
826.569	0.791	7.96

632.8	0.392*	5.85†

* calculated from cubic spline of above data.

† calculated from linear plot of above data.

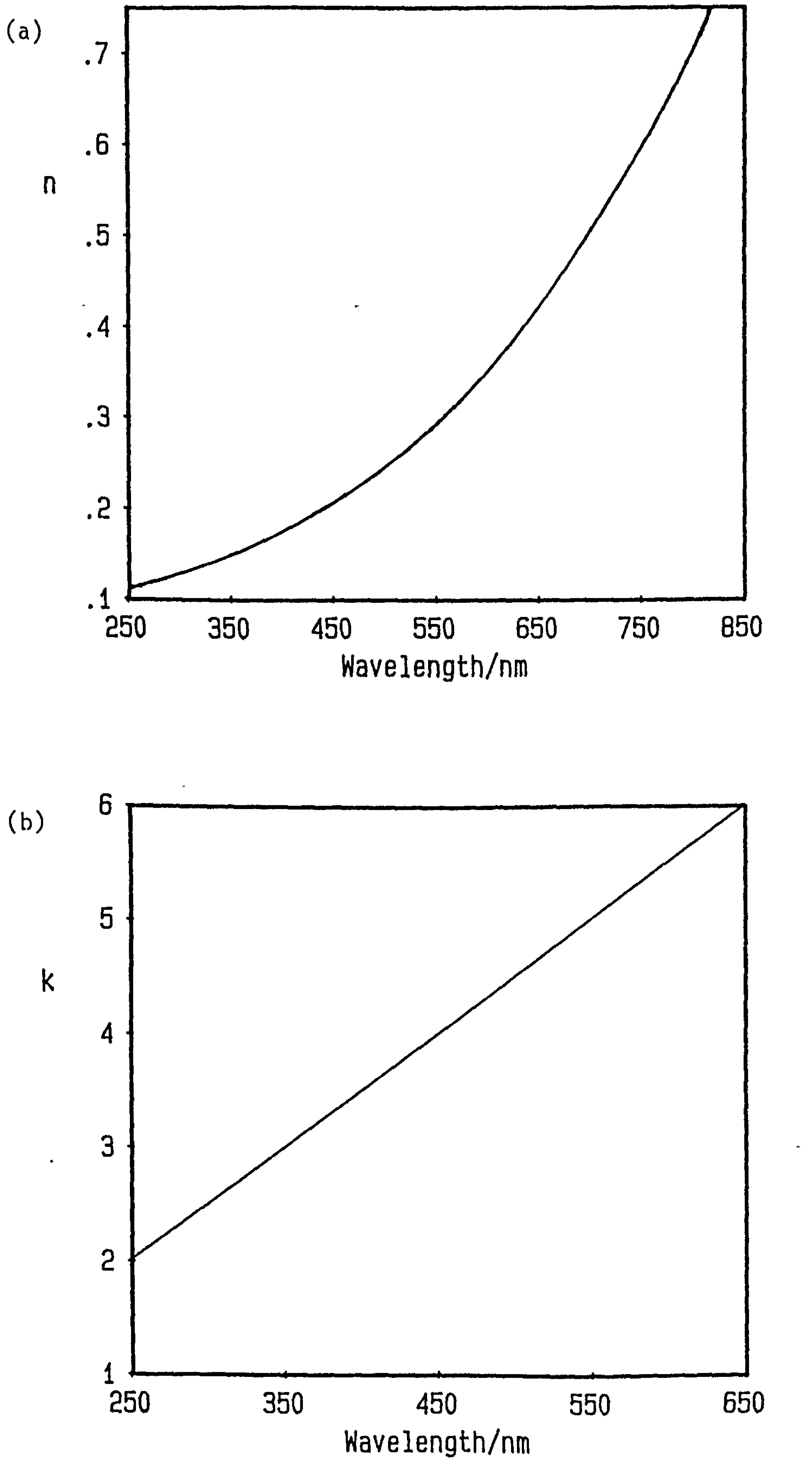

Fig. 4.6 Calculation of n and k for Mg at λ = 632.8 nm from literature values

do not truly represent a mechanically polished surface. In practice these values can only be a guide to the "true" optical constants of the bare Mg and for a high Mg alloy such as Magnox, hence the need for the experimental determination of the optical constants of the specimens under study.

4.8.3 Mechanical polishing

The most convenient method of obtaining an optically flat (i.e. specularly reflecting) and film-free surface necessary for ellipsometric determination of the optical constants is to use mechanical polishing. The results when this was attempted showed a considerable variation both across the surface of individual samples and between different samples for both Magnox, fig. 4.7, and Mg, fig. 4.8. Part of this variation between different samples is due to an imperfect quarter wave plate and can be reduced by zone averaging. This technique is discussed in section 4.10 and has been used to correct subsequent results. Most of the variation in results however is due to the surface pre-treatment which produces a cold worked or Beilby layer containing some of the polishing media and also the oxide film which is expected to be present under the experimental conditions used.[159] The Beilby layer can be reduced by chemical etching and some of the stress relieved by annealing but the latter will result in an increase in thickness of the oxide film. It is this oxide film and the rapidity of its formation that causes the most difficulty in experimentally determining the optical constants of very reactive metals such as Mg but several methods for tackling the problem are available in conjunction with ellipsometry:

1. Chemical etching _in situ_
2. Electrochemical polishing
3. Cathodic reduction
4. Heating in vacuum in the presence of reducing gases
5. Ion bombardment
6. Cleavage
7. Vapour deposition

The latter four methods are vacuum techniques for which the apparatus was not available and cathodic reduction was not feasible due to the very electronegative potential for the oxidation of Mg.

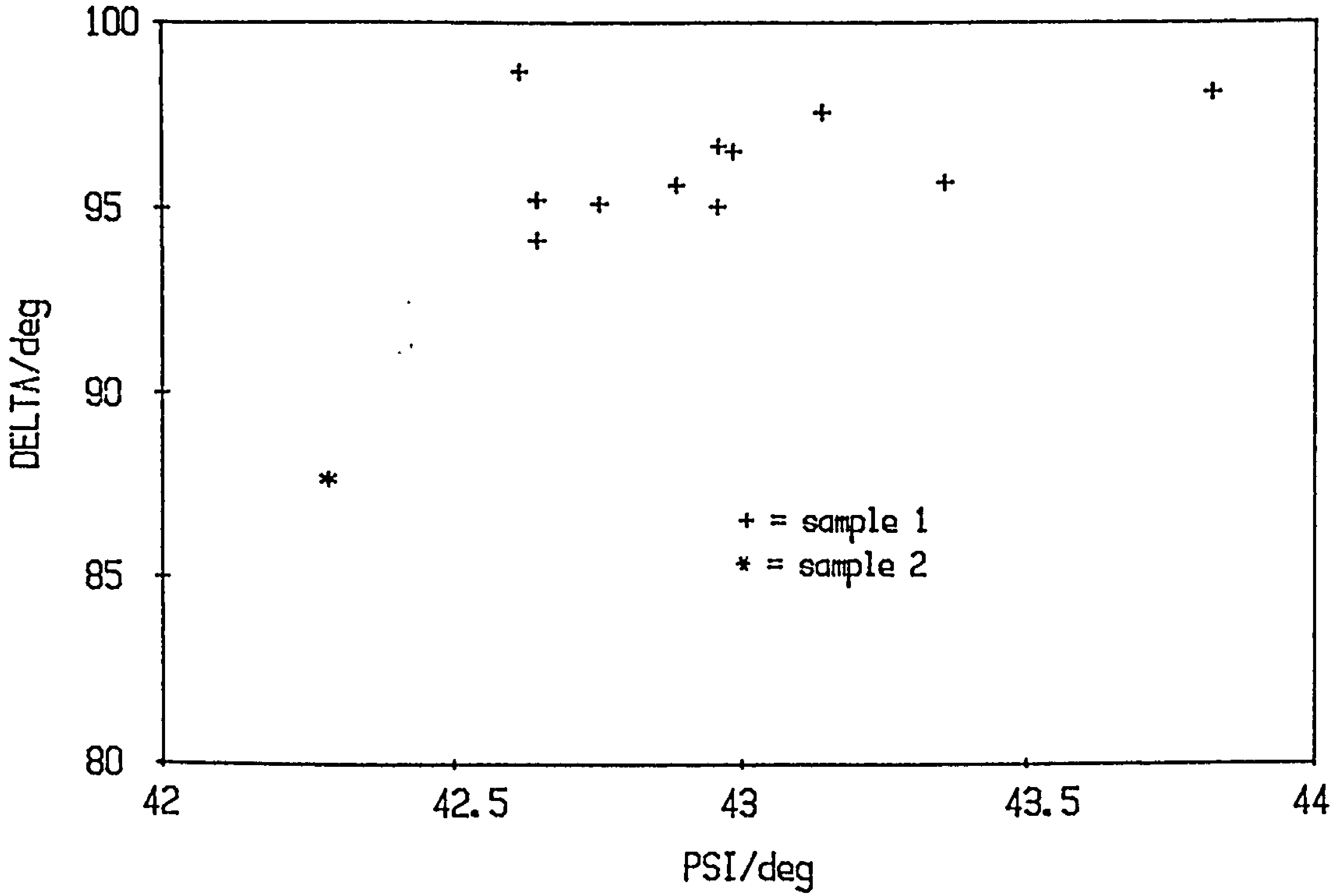

Fig. 4.7 The variation in delta and psi for polished Magnox

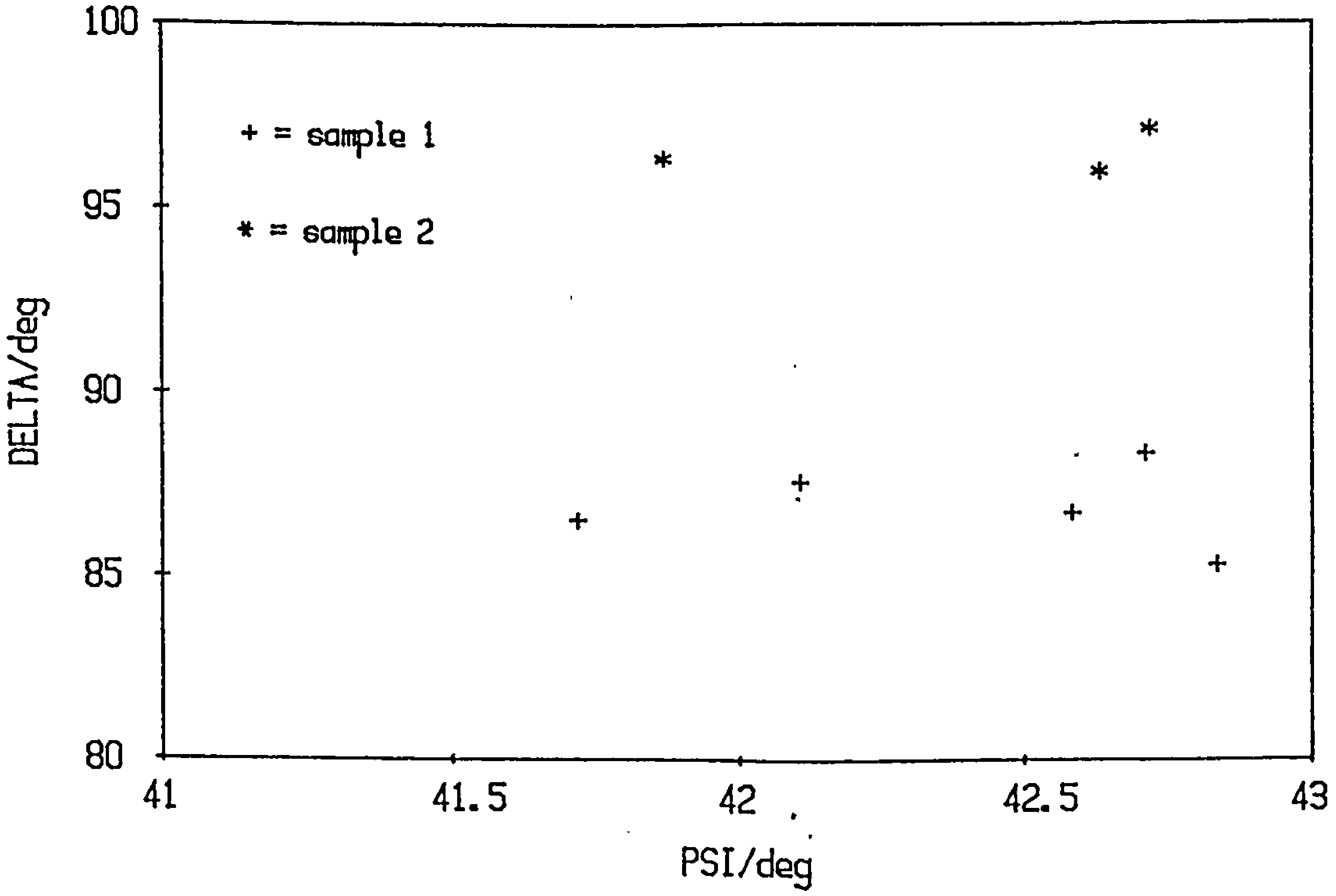

Fig. 4.8 The variation in delta and psi for polished magnesium

There are also indirect ellipsometric methods such as immersion in an ambient medium with a refractive index equal to that of the film. The film will then be eliminated optically and hence the values of Δ and Ψ measured on the filmed surface can be used to obtain n and k for the bare surface. An alternative method has been described by Vedam _et al._[160] whereby a series of measurements of the reflectance at normal incidence and Δ and Ψ values are obtained for a range of values of film thickness. The optical constants of the bare surface are then obtained by relationships derived between the reflectance and the pseudo-optical constants, n' and k' for the metal obtained from Δ and Ψ values assuming that no film was present. These latter two techniques require the refractive index of the film to be known with reasonable accuracy and to be real, i.e. a non-absorbing film. The optical constants of the corrosion film formed on either Mg or Magnox are not known however, which leaves the methods of _in situ_ chemical and electrochemical etching.

4.8.4 Chemical etching

The idea behind this technique is to find a solution which will dissolve the oxide film and the Beilby layer to leave a surface free from stress with no oxide present, and smooth on a macroscopic scale i.e. 1.10μ. Both citric acid and nitric acid solutions have been used as etchants for Magnox[161] and both these acids were tried on Mg and Magnox at various concentrations. Citric acid was found the most suitable at a concentration of 0.2%. The rate of hydrogen evolution at this concentration permitted an ellipsometric signal to be obtained temporarily once any adhering hydrogen bubbles had been removed by pipette. Fig. 4.9 illustrates the effect of this treatment on Δ and Ψ.

This method was improved upon by pumping the etchant across the surface of the sample with a peristaltic pump, fig. 4.10. It was possible to increase the citric acid concentration to 2% and maintain an ellipsometric signal for short periods using this system but the rate of hydrogen evolution in higher concentrations of citric acid was too high to permit determination of Δ and Ψ and after about 20 seconds an 'orange peel' effect was noted on the surface. This made the sample unsuitable for ellipsometric work for which a specularly reflecting surface is needed. The maximum value of Δ obtained using citric acid concentrations of 2% and 0.1% using a pumped flow of

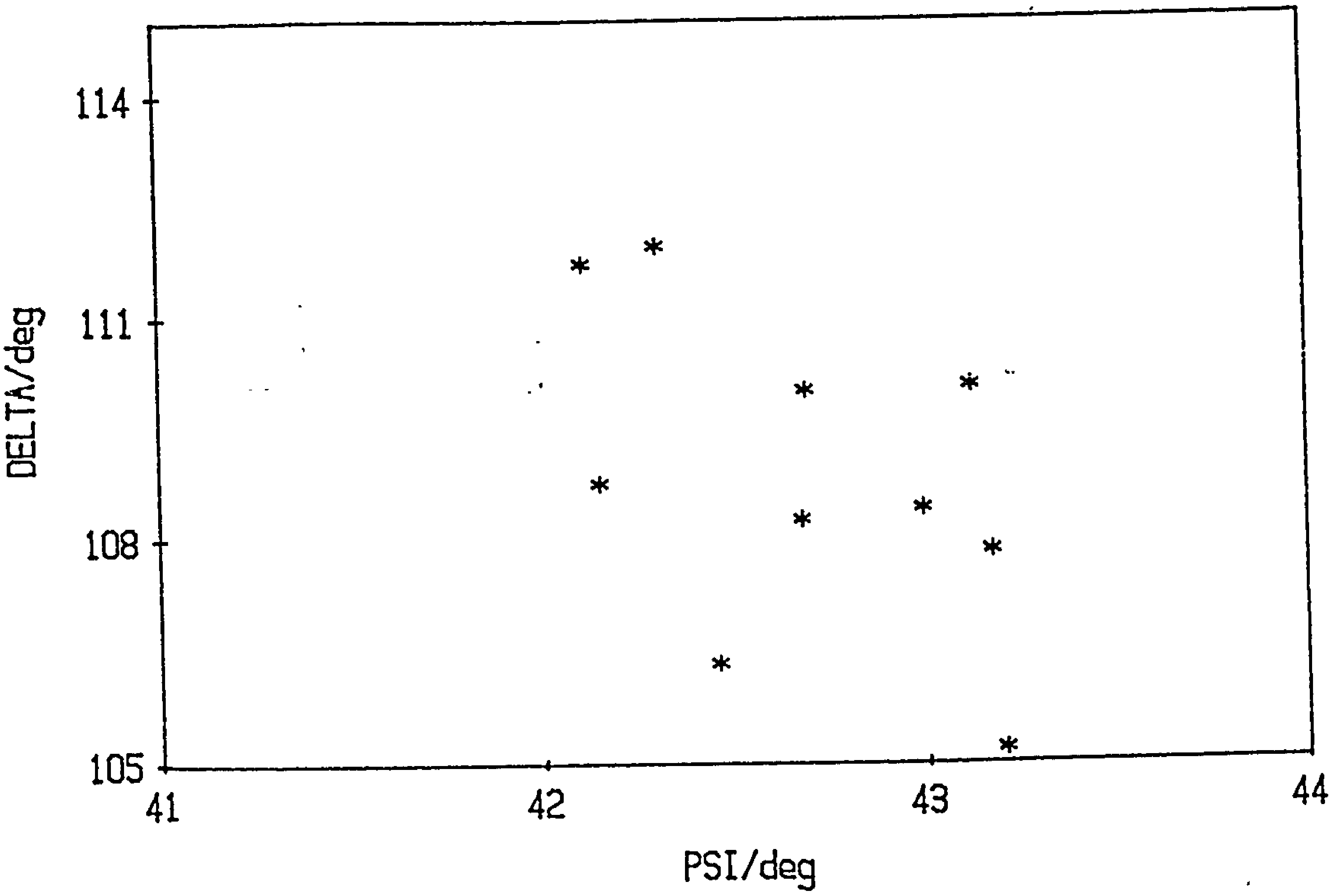

Fig. 4.9 Magnox etched in situ using 0.2% citric acid

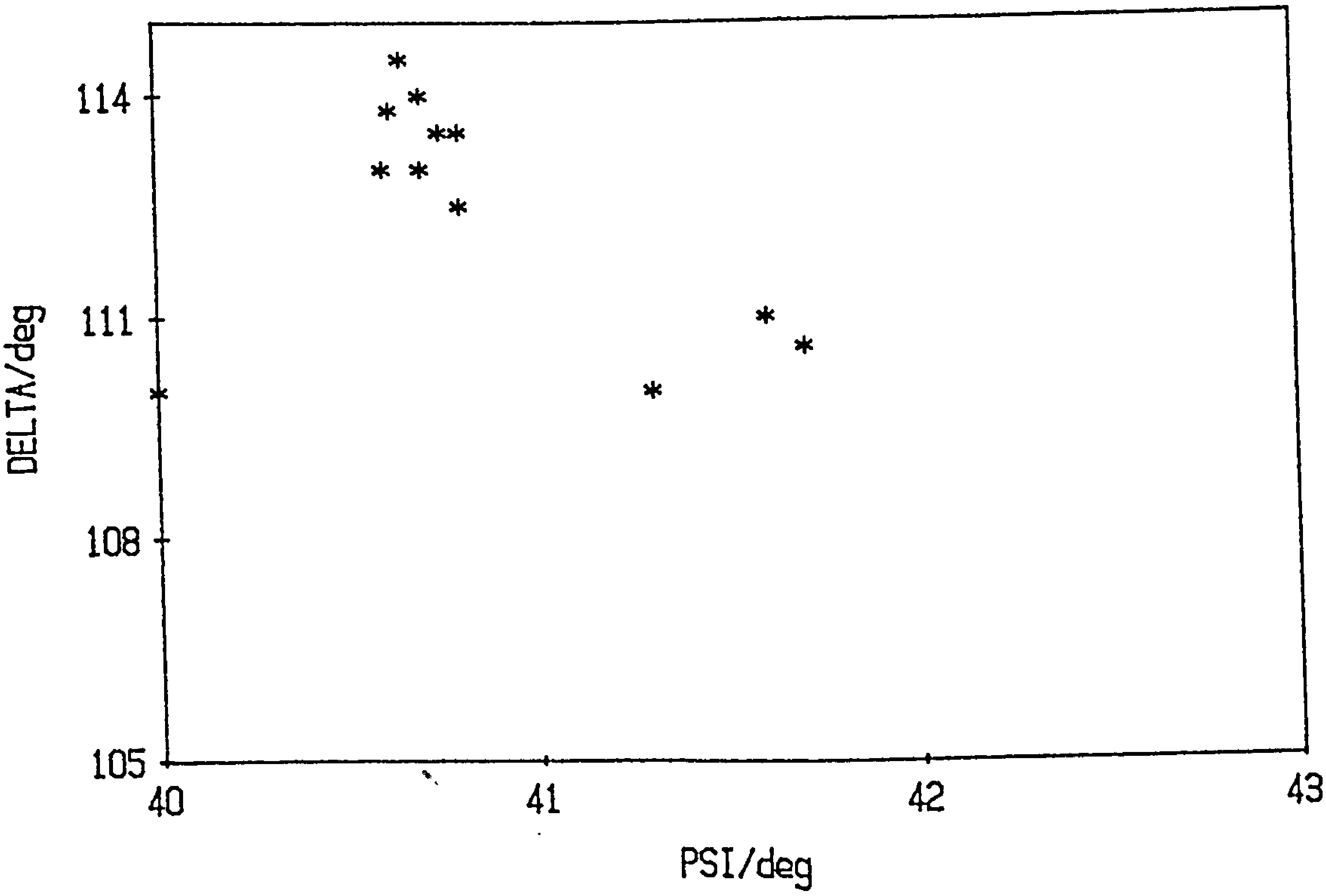

Fig. 4.10 Magnesium etched in situ using pumped 0.1% citric acid

etchant across the surface was about 113° for both Magnox and Mg compared to a value of about 120° expected for Mg based upon results in u.h.v. which indicates that an oxide film may be present after these treatments.

4.8.5 Electrochemical polishing

This technique results in the levelling of the surface due to the establishment of a diffusion or Jacquet layer.[162] This diffusion layer leads to increased dissolution on the peaks of any surface irregularities resulting in a general levelling of the surface. There are various polishing solution compositions given in the literature for Mg[39] some of which are reproduced in table 4.5. It was found experimentally that an electropolishing bath of ethanol and orthophosphoric acid in the ratio 5:3 v/v at room temperature and at a voltage of 1.5 V gave a surface that was bright and apparently free from any surface oxide. Fig. 4.11 and Fig. 4.12 give the values of Δ and Ψ obtained from the *in situ* electropolishing of Mg and Magnox under these conditions. From these results values for n of 0.85 and k of 5.85 are predicted for both Mg and Magnox which are similar to the values given for evaporated Mg film in u.h.v. Unfortunately on removal of the electropolishing solution and rinsing with distilled water or sodium hydroxide solution a white film formed on the surface of the substrate which prevented this technique being used as a pretreatment to remove any oxide film prior to adding the corrodent.

4.9 SIMS analysis of polished and etched Mg and Magnox samples

Surface analysis using SIMS in conjunction with argon ion etching was carried out on Mg and Magnox samples which had been subject to the various surface treatments described previously. This was done primarily with the aim of obtaining the thickness of the oxide present on the surface but it was also hoped to obtain additional information from the depth profile. It was realized that this technique was really only valid for polished samples, as on removal from solution any etched samples would probably oxidize. This in particular applied to the *in situ* electropolished sample. A Magnox sample was also analysed which had been polished then annealed at 390°C and etched in 10% citric acid for a brief period for comparison with previous work.[158]

Table 4.5

Electropolishing Solutions for Mg[39]

Electrolyte	Current and Voltage	Temperature	Cathode	Time
Ethanol (96%) Orthophosphoric acid (d = 1.74) 5:3*	1.5 V 0.01 A/cm^2	24	inox	3-5 min
Ethanol (96%) Orthophosphoric acid (d = 1.74) 5:3*	1.5 V 0.005 A/cm^2	24	inox or Ni	1 hr
2-Ethoxyhexanol HCl 9:1*	50-60 V	2	inox	10-30 s
Ethanol $HClO_4$ H_2O 760:50:140*	0.6-0.9 A/cm^2	24	Ni	60 s
HCl (d = 1.2) 2-Ethoxyhexanol 1:10*	5 V, 1 A/cm^2	30-40	-	-

* All ratios refer to parts by volume.

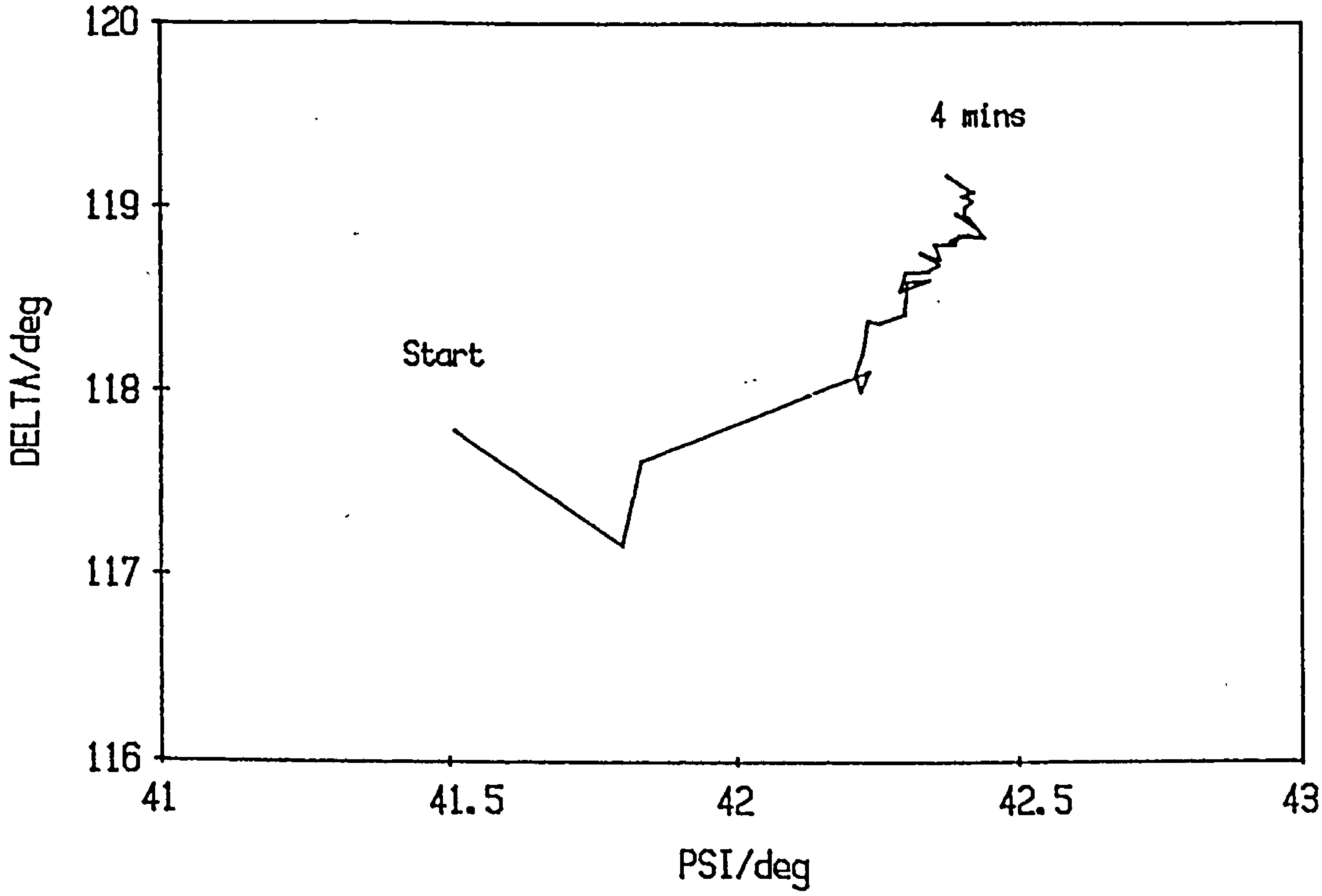

Fig. 4.11 Magnesium electropolished in ethanolic phosphoric acid

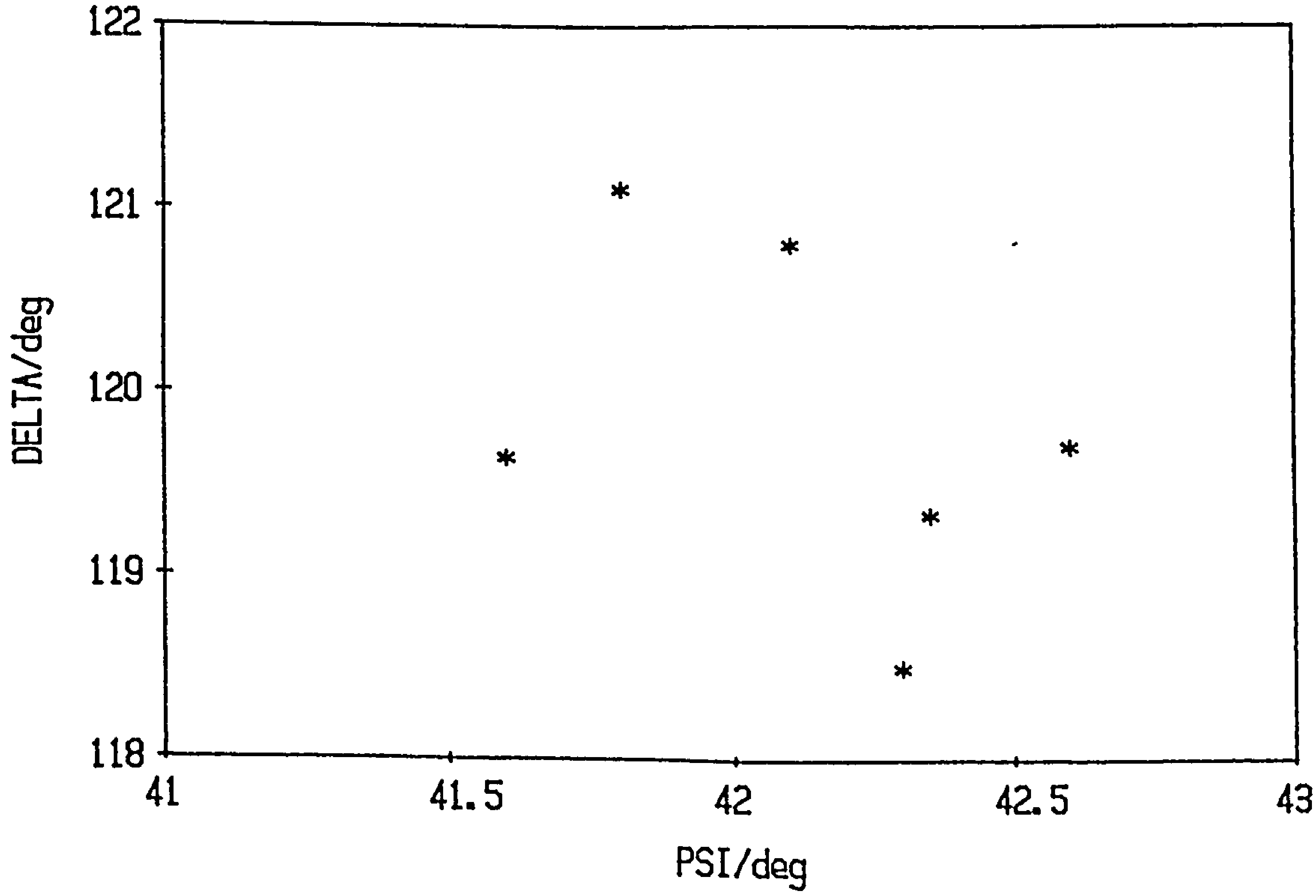

Fig. 4.12 Magnox electropolished in ethanolic phosphoric acid

4.9.1 Errors inherent in depth profiling

There are many errors inherent in this technique and in addition to the matrix effects which SIMS is particularly subject to, whereby the sputter yield is dependent upon the surface matrix, there are also errors associated with argon ion etching. Several authors have discussed these errors both in depth profiling as a general technique[163,164] and separately for SIMS[165] AND AES[166]. A parameter Δz is usually used which is known as the depth resolution and is defined[165] as the layer thickness that must be sputtered away before the signal changes from 5% to 95% (or vice versa) of its maximum value assuming that the element under consideration is distributed in depth according to a step function. The most important of the factors contributing to the depth resolution according to Hofmann and their dependence on the film thickness are given in table 4.6. There is also an error in relating the etching time at a given beam current to sputter depth. Calibration of the etch rate is normally done by obtaining the time taken to sputter through a known thickness of oxide on a metal such as Ta and then assuming that the oxide film on the sample under analysis will be sputtered at the same rate.

4.9.2 Discussion of SIMS of polished and etched Mg and Magnox samples

The spectra for all the Mg and Magnox samples were similar and typical spectra can be seen in figs. 4.13 and 4.14. In the positive ion spectra there are strong Mg peaks at mass no.24 with weaker satellites at 25 and 26. Compound ions are also apparent at mass numbers 40-43 probably corresponding to MgO^+ and $MgOH^+$. The presence of carbon is also indicated throughout the film, as is sodium, particularly in the upper oxide layers. In the negative spectra there are strong peaks at mass numbers 16 and 17 corresponding to O^- and OH^- and weaker peaks due to compound ions at 32 (O_2^-) and 33 (O_2H^-).

The ratio of the Mg/O peaks at mass numbers 24 and 16 respectively was used to give an estimate of the film thickness and the results based on this ratio are given in table 4.7 for Mg and Magnox.
The oxide thickness remaining after polishing and etching varies between 25 and 42 nm whereas the result for the electropolished sample is anomolously high due to a white film which formed on the surface of

Table 4.6

Factors Δz_i contributing to the depth resolution Δz[163]

Factor	Dependence
Instrumental - primary ion beam inhomogeneity	$\Delta z_i = f(z)$
Initial surface roughness	$\Delta z_r = f(z^{\frac{1}{2}})$
Statistical surface erosion model	$\Delta z_s = f(z^{\frac{1}{2}})$
Crystal orientation and imperfections	$\Delta z_c = f(z)$
Information depth	$\Delta z_{\lambda,r} = f(\lambda_i, r_i \ldots)$
Preferential sputtering	$\Delta z_p = f(E_{pi}, m_i/m_{pi})$
Atomic transport	$\Delta z_t = f(D_b, D_s)$

λ = electron escape depth
r = back scattering factor
E_{pi} = energy of primary ions
m_{pi} = mass of primary ions
m_i = mass of ions in sample
D_b = bulk diffusion
D_s = surface diffusion

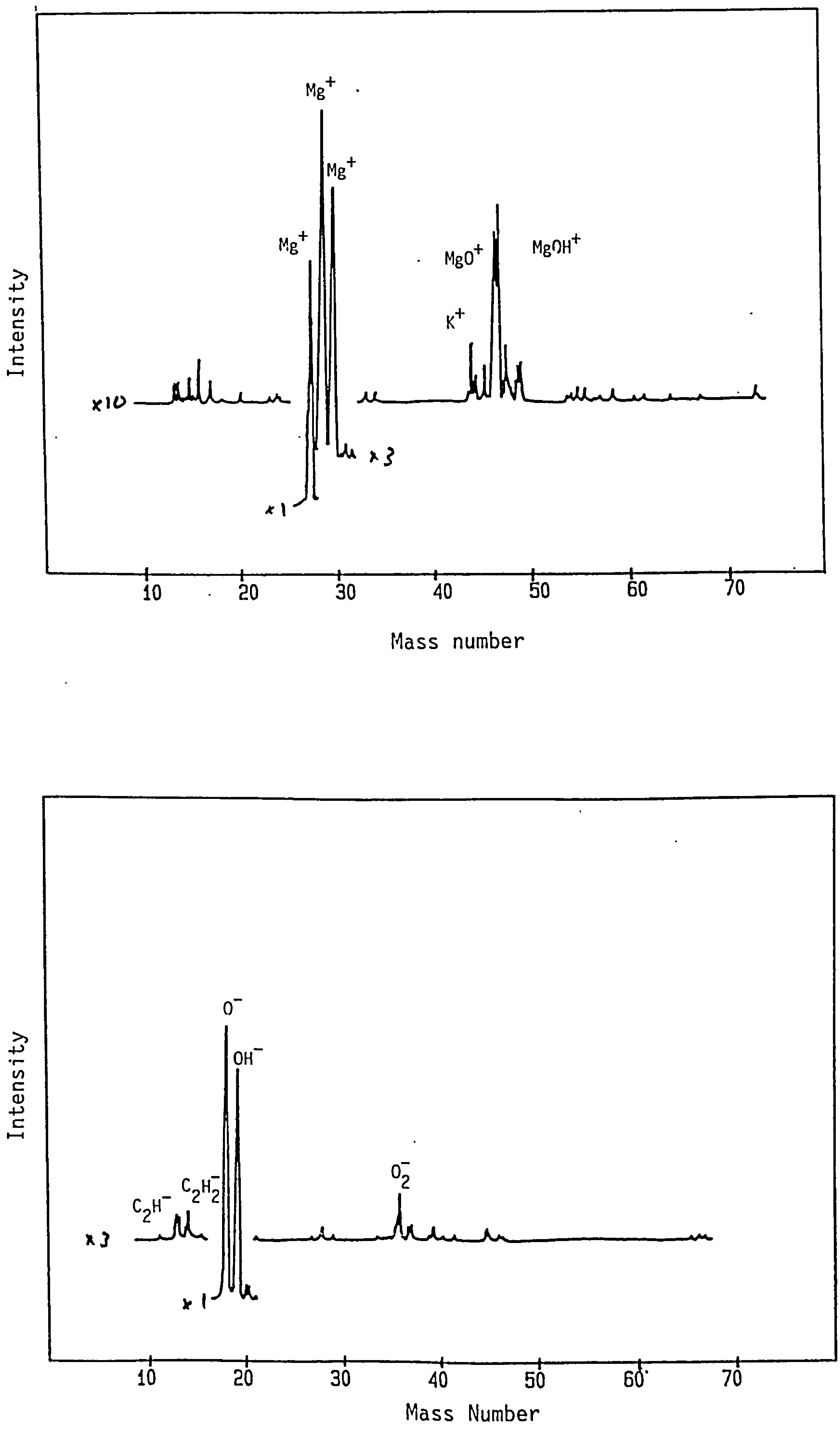

Fig. 4.13 SIMS spectra for a polished and etched Mg specimen after 9 nm of film has been sputtered

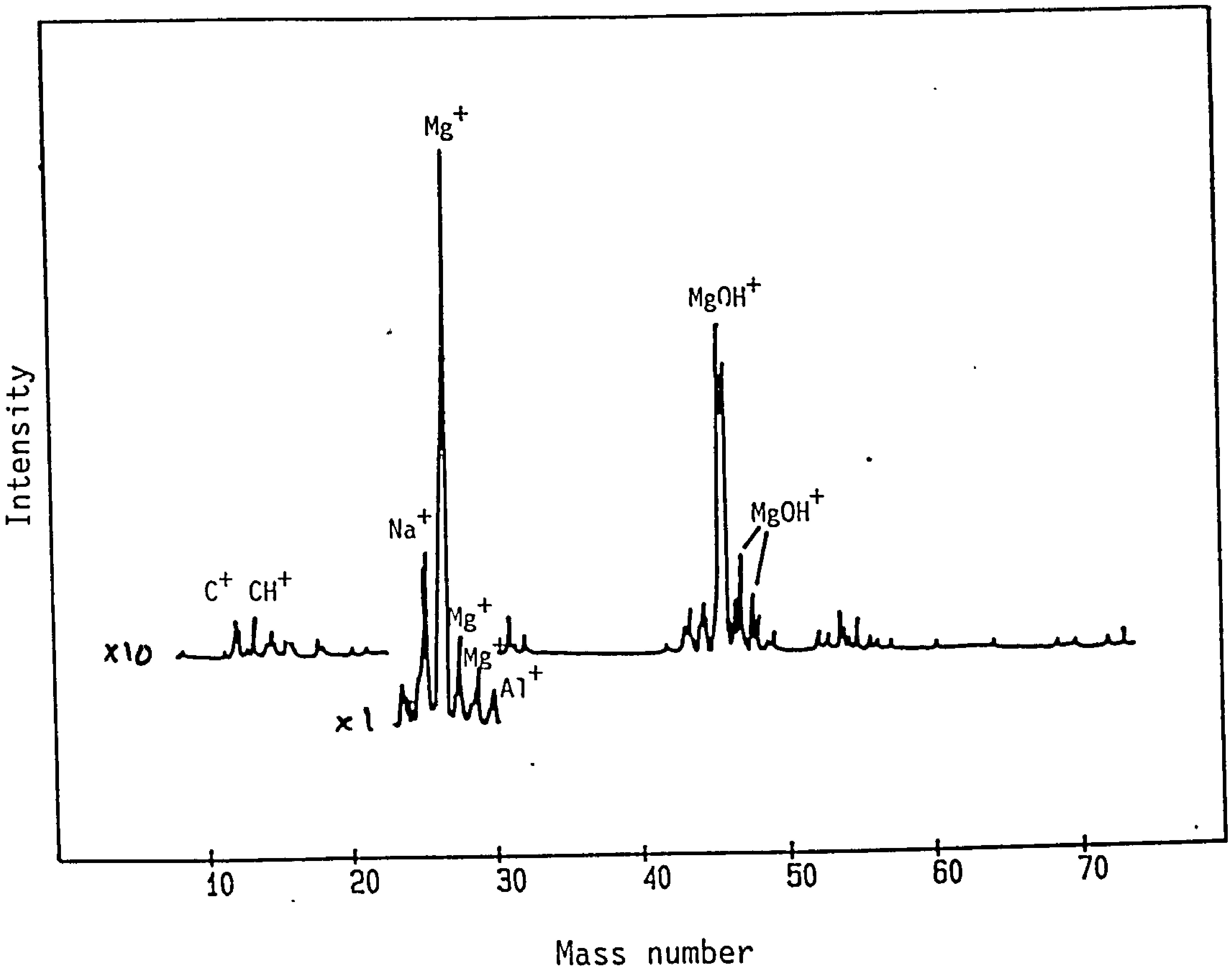

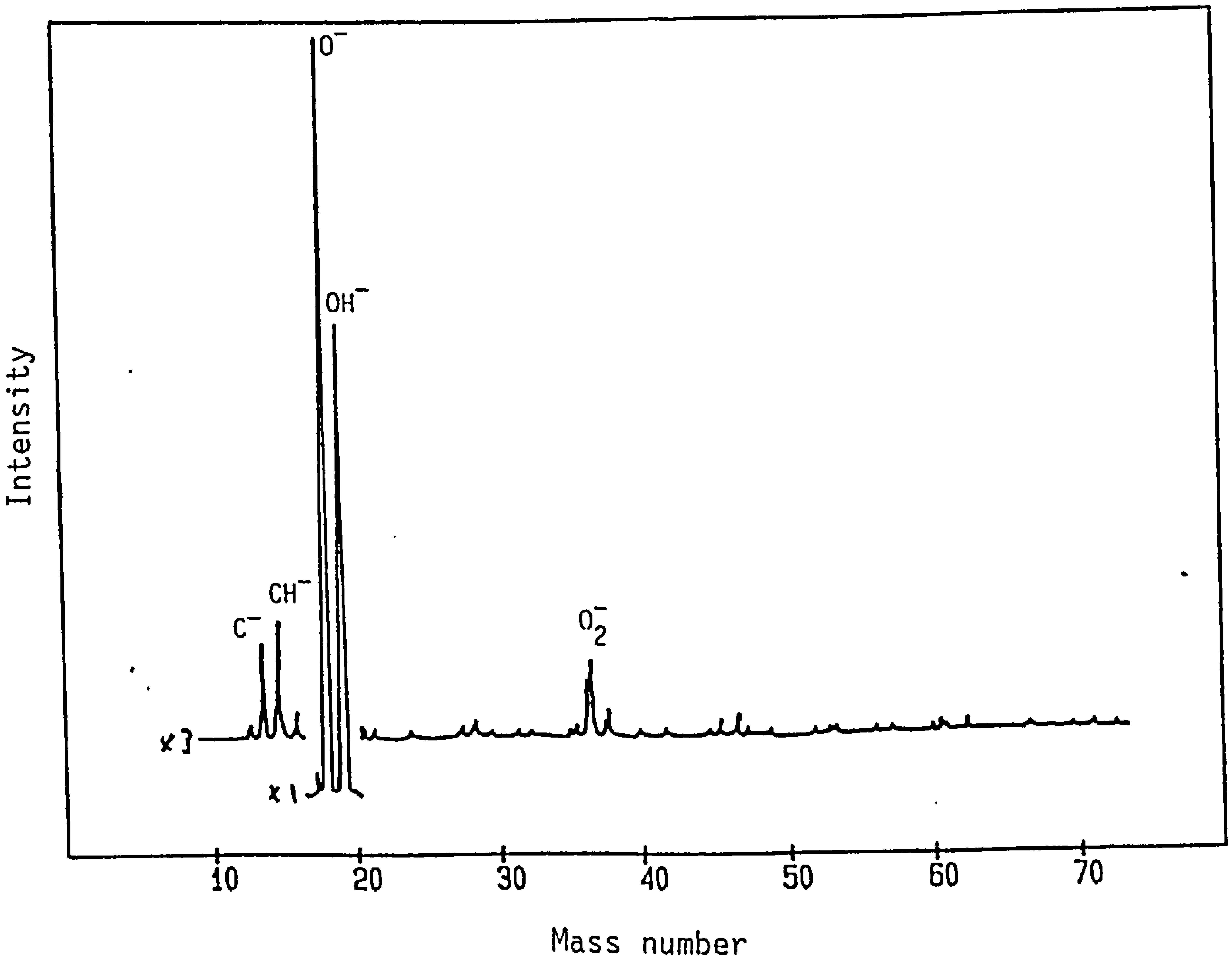

Fig. 4.14 SIMS spectra for a polished and etched Magnox specimen after 7 nm of film has been sputtered

Table 4.7

Estimation of oxide film thickness from SIMS measurements based on the Mg^+/O^- peak height ratio

Sample	Surface treatment	Depth nm
Magnox	polished	30
Magnox	polished and etched 0.2% citric acid	30
Magnox	polished, annealed at 390°C etched 10% citric acid	25
Magnesium	polished	28
Magnesium	polished and etched 0.2% citric acid	42
Magnesium	electropolished	>100

the specimen on removal from the polishing solution. There is not a great variation in oxide thickness between polished and polished-and-etched specimens. The etched Magnox samples have a slightly thinner film than the polished ones, whereas the opposite is true for Mg. These results are in rough agreement with the thickness of the oxide film calculated from the ellipsometric results in figs. 4.7-4.10 for the Mg and Magnox specimens. They are in accord with the thickness of oxide film found in a Magnox specimen annealed at 390°C and etched in 10% citric acid when analysed by SIMS and ion scattering spectroscopy as reported by Allen.[158]

4.10 Zone averaging

It can be shown using either the Poincare sphere[84] or matrix algebra[127] that a given pair of values for Δ and Ψ due to reflection can be obtained from 32 different combinations of polariser, analyser and retarder azimuth settings. This is halved to 16 if all angles are reduced to lie between 0° and 180°. They are grouped into four zones which are identified with quadrants on the equator of the Poincare sphere with each zone having four groups depending on the value of Δ. These zones and the relationship of Δ and Ψ to the azimuths of the polariser, analyser and retarder has been given in table 3.3. If all the ellipsometer components were ideal and perfectly aligned then the values of Δ and Ψ measured for a given surface would be identical in each zone, but in practice the results are significantly different due to component imperfections, azimuth angle errors, beam deviation, surface irregularities and the finite band width of the beam. Azzam and Basharu[167-169] have discussed these various errors in detail and many of them can be reduced or largely eliminated by 2 or 4 zone averaging. It is also possible to obtain a corrected value of Δ and Ψ from measurement in one zone, providing the imperfection parameters describing the devices have been determined.

Fig. 4.15 shows the effect of changing zones for Δ and Ψ for a Magnox sample immersed in 0.01 mol/dm^3 NaOH from which the considerable variation in Ψ of ~1.6° is apparent for measurements in each zone. The change in Δ however is negligible. The values of Δ and Ψ must be known with reasonable accuracy for theoretical modelling of the experimental results and this is especially true for the more sophisticated

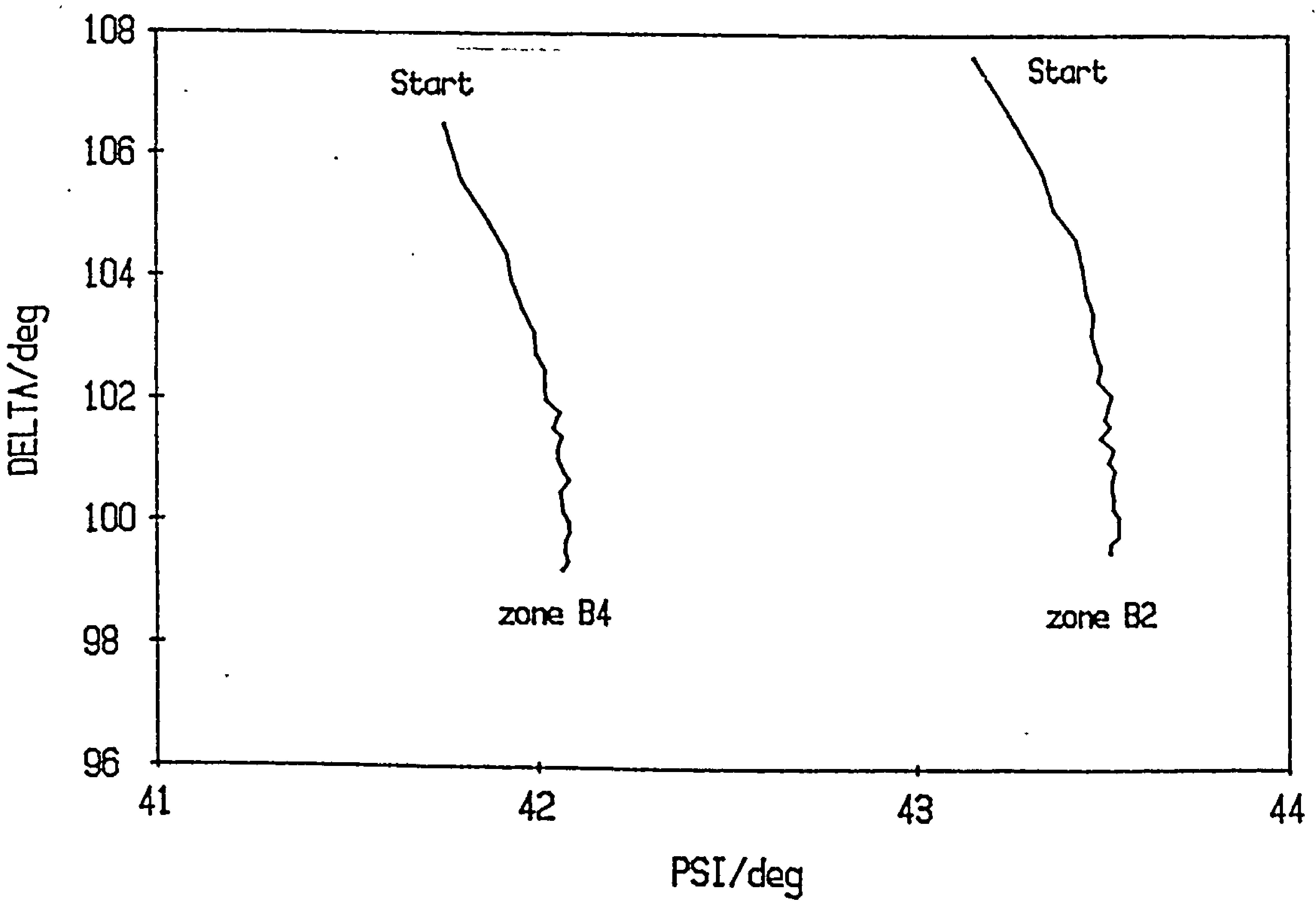

Fig. 4.15 Δ,Ψ curves obtained on taking alternate readings in zones B4 and B2 for Magnox immersed in 0.01 mol/dm^3 sodium hydroxide solution

modelling using rough films in Chapter Six, for which there is a marked difference in the predicted results depending on which value of Ψ is taken.

It was not thought practicable to use either 2 or 4 zone averaging for most of the experimental runs, as some used high rates of data acquisition and others involved nulling a very poor signal from a rough surface. For this reason and from the observation that the variation in Δ between zones was minimal and for Ψ was usually ~1.5° it was decided to correct for this error by adding or subtracting 0.75° to the experimental results. This treatment reduces the errors in Ψ due to the quarter wave plate to values that are small in comparison to differences due to surface irregularities, figs. 4.6 and 4.7.

A more sophisticated treatment could be used by utilizing the CWP routine in McCrackin's program (see section 4.12.3) to determine the error due to the retarder and then using this value in subsequent analysis. The error in the retarder was obtained in this way from 2 sets of P, A and U results the retarder being found to have a retardance of 91.726° at an azimuth of 45° and 90.345° at an azimuth of 135° as opposed to an ideal retardance of 90°. These values were not used to correct the experimental data however as this would have involved laborious and time-consuming operations.

4.11 Experimental procedure

The following steps indicate the general procedure used in obtaining experimental ellipsometric data:

1. The instrument was switched on and allowed to 'warm up' for at least 30 minutes prior to use. During this period the computer program "GETPLT" was run to configure the data acquisition electronics and prepare the plotter.
2. The electrode was prepared and installed in the sample cell as described in section 4.5.
3. The sample was then aligned using height and tilt adjustments until the reflection on the sample from a mirror mounted in the analyser arm coincided with the incident beam. The mirror was then removed and the matte perspex screen in the analyser arm utilized to ensure

that the reflected beam was visible, in the correct position and that the reflected beam was reasonably specular. If there was appreciable scattering of the incident beam from the sample surface then a diffuse image would be observed rather than a small spot of light.

4. The signal was then nulled using the ellipsometer electronics. The p.s.d. output signal was continuously monitored on the oscilloscope to ensure that the signal was satisfactory.
5. The cell windows were inserted on each arm and the beam re-checked by again obtaining a null.
6. The etchant (0.2% citric acid) was added and removed after ~20 seconds by means of a hand-held suction pump.
7. The cell was flushed with the experimental solution which was again removed by suction and then refilled.
8. If necessary the working electrode and reference electrode were placed in the cell and connected along with the sample to the potentiostat.
9. The potentiostat was now switched from standby to the cell position and the data acquisition program started.

The time needed for steps 6 to 9 was less than two minutes.

4.12 Computations

Various computer programs written in both BASIC and FORTRAN were used for data analysis, theoretical modelling and data acquisition. This section describes the computations used in the data analysis and theoretical modelling. The data acquisition routines were discussed in Chapter Three.

4.12.1 Bare surface

The two calculations performed are either to obtain n and k from experimental values for reflection from a bare surface or calculating Δ and Ψ from n and k values. These calculations can both be done in BASIC using Koenig's or Ditchburn's equations[93,94] (2.37)-(2.38) and (2.39). A much shorter and faster computer program written in FORTRAN uses complex notation to perform the same calculation.

The steps for doing this are:

1. Obtain cos (ϕ_1), angle of incidence.
2. Obtain cos (ϕ_2), angle of refraction.

   ϕ_2 is complex for absorbing substrates and is calculated using Snell's law:

$$n_1 \sin\phi_1 = n_2 \sin\phi_2 \qquad \text{.....(2.17)}$$

$$\therefore \quad \cos\phi_2 = \sqrt{1 - \frac{n_1^2}{n_2^2} \sin^2\phi_1} \qquad \text{.....(4.1)}$$

   n_2 is of course complex for a metallic substrate.

3. Obtain the Fresnel reflection coefficients.

$$r_{p_{1,2}} = \frac{n_2\cos\phi_1 - n_1\cos\phi_2}{n_2\cos\phi_1 + n_1\cos\phi_2} \qquad \text{.....(2.15)}$$

$$r_{s_{1,2}} = \frac{n_1\cos\phi_1 - n_2\cos\phi_2}{n_1\cos\phi_1 + n_2\cos\phi_2} \qquad \text{.....(2.16)}$$

4. Evaluate ρ.

$$\rho = \frac{r_{p_{1,2}}}{r_{s_{1,2}}} \qquad \text{.....(2.35)}$$

5. Evaluate Ψ.

$$\tan\Psi = \frac{|r_p|}{|r_s|} \qquad \text{.....(4.2)}$$

6. Evaluate Δ.

$$\rho = \tan\Psi\, e^{i\Delta} \qquad \text{.....(2.36)}$$

but $e^{ix} = \cos x + i\sin x$

$$\therefore \quad \rho = \tan\Psi(\cos\Delta + i\sin\Delta)$$

$$\therefore \quad \rho = \tan\Psi\cos\Delta + i\tan\Psi\sin\Delta$$

$\because$ ρ is complex i.e. $\rho = x + iy$

$$\therefore \quad x + iy = \tan\Psi\cos\Delta + i\tan\Psi\sin\Delta$$

the R.H.S. is now also of the form $x + iy$

$$\therefore \quad \frac{x}{iy} = \frac{\tan\Psi\cos\Delta}{\tan\Psi\sin\Delta}$$

Cancelling tan Ψ and multiplying both sides by i:

$$\frac{x}{y} = \frac{\cos\Delta}{\sin\Delta} = \tan\Delta$$

$$\therefore \quad \Delta = \tan^{-1}(x/y)$$

where x and y are the real and imaginary parts of ρ.

The subroutine DELPSI in the appendix shows the listing for this calculation.

4.12.2 Single isotropic film

Using complex rotation Δ and Ψ can be obtained from equation (2.50):

$$\rho \doteq \frac{[\hat{r}_{p12} + \hat{r}_{p23}\exp(-2iD)][1 + \hat{r}_{s12}\hat{r}_{s23}\exp(-2iD)]}{[\hat{r}_{s12} + \hat{r}_{s23}\exp(-2iD)][1 + \hat{r}_{p12}\hat{r}_{p23}\exp(-2iD)]}$$

where $\hat{r}_{p12}$, $\hat{r}_{p23}$, $\hat{r}_{s12}$, $\hat{r}_{s23}$ are the Fresnel reflection coefficients for the two interfaces given in equations (2.47a)-(2.47d) D is the phase change due to one traversal of the film given in equation (2.46).

Δ and Ψ can also be obtained using non-complex formulae by following a similar process to that above. The steps are:

1. Evaluation of the complex angles of refraction.
2. Calculation of the Fresnel reflection coefficients.
3. Evaluation of the total reflection coefficients.
4. Evaluation of ρ.
5. Calculating Δ and Ψ from ρ.

4.12.3 Multiple and inhomogeneous films

The effect of multiple films is calculated using the FORTRAN computer program written by McCrackin.[169] This was an algorithm whereby the reflection from the bottom-most layer and the substrate is first calculated and then these two layers are treated as the substrate. The reflection is now calculated between this and the next highest layer. Inhomogeneous films are treated by using the effective medium approximation theory to calculate the effective optical constants of a mixed phase from the optical constants of the individual components and their respective volume fractions. This treatment has been more fully discussed in section 2.5.3. The program also contains routines for evaluating and correcting errors due to e.g. an imperfect quarter wave retarder.

CHAPTER 5 EXPERIMENTS UNDERTAKEN IN 0.01 mol/dm^3 SODIUM HYDROXIDE SOLUTION

5.1 Experiments at open circuit and fixed potential undertaken on Magnesium and Magnox in air-saturated 0.01 mol/dm^3 sodium hydroxide

- 5.1.1 Magnox and Magnesium at open circuit during the first thirty minutes
- 5.1.2 Magnox immersed in air-saturated 0.01 mol/dm^3 sodium hydroxide for several hours
- 5.1.3 Magnesium immersed in air-saturated 0.01 mol/dm^3 sodium hydroxide for several hours
- 5.1.4 Discussion of the results for magnesium and Magnox in air-saturated 0.01 mol/dm^3 sodium hydroxide

5.2 Experiments conducted on magnesium and Magnox in air-saturated 0.01 mol/dm^3 sodium hydroxide under a nitrogen blanket

- 5.2.1 The effect of a nitrogen blanket and its removal on Magnox in air-saturated 0.01 mol/dm^3 sodium hydroxide solution
- 5.2.2 Magnox held at -0.5 V vs rhe in air-saturated 0.01 mol/dm^3 sodium hydroxide under a nitrogen blanket
- 5.2.3 Magnesium in air-saturated 0.01 mol/dm^3 sodium hydroxide under a nitrogen blanket
- 5.2.4 Single crystal of magnesium in 0.01 mol/dm^3 sodium hydroxide solution under a nitrogen blanket
- 5.2.5 Discussion of results for magnesium and Magnox specimens immersed in 0.01 mol/dm^3 NaOH under a nitrogen blanket

5.3 Further experiments on Magnox and magnesium at open circuit and fixed potential in 0.01 mol/dm^3 sodium hydroxide

- 5.3.1 The effect of carbonate ions on the passive film formed on Magnox in sodium hydroxide solutions at pH > 11.5
- 5.3.2 The effect of fluoride on the corrosion of Magnox in 0.01 mol/dm^3 NaOH
- 5.3.3 The effect of solution deoxygenation on Magnox and magnesium in 0.01 mol/dm^3 sodium hydroxide
- 5.3.4 Magnox in 0.01 mol/dm^3 sodium hydroxide solution with the addition of 1000 ppm chloride

5.4 Potential sweep experiments undertaken on Mg and Magnox in 0.01 mol/dm^3 sodium hydroxide

5.4.1 Anodic ramp results for magnesium and Magnox

5.4.2 Discussion of the anodic ramp results

5.4.3 Cyclic volammetry of Mg and Magnox in 0.01 mol/dm^3 sodium hydroxide solution

5.4.4 Mg and Magnox in 0.01 mol/dm^3 sodium hydroxide

5.4.5 Discussion of cyclic voltammagrams in 0.01 mol/dm^3 sodium hydroxide

5.4.6 Magnox in 0.01 mol/dm^3 sodium hydroxide with the addition of 1000 ppm fluoride

5.4.7 Magnox and magnesium in 0.01 mol/dm^3 NaOH with the addition of 10, 100 and 1000 ppm Cl$^-$

5. Introduction

The work in this chapter describes the results obtained for Mg and Magnox immersed in 0.01 mol/dm^3 sodium hydroxide. This environment is similar to that used by the C.E.G.B. for the storage of Magnox fuel elements before reprocessing. Experiments have been of both short ($\leq$ 30 minutes) and long (1-12 hours) duration in various electrolytes at open circuit and under potential control.

5.1 Experiments at open circuit and fixed potential undertaken on Magnesium and Magnox in air-saturated 0.01 mol/dm^3 sodium hydroxide

5.1.1 Magnox and Magnesium at open circuit during the first thirty minutes

Initial experiments were undertaken with the electrodes at open circuit in air-saturated 0.01 mol/dm^3 sodium hydroxide solution in the absence of aggressive anions. The duration of these experiments was fairly short as it was thought that the early stages of corrosion, when the passive film is forming, would be the most important. The changes in Δ, Ψ and the open circuit corrosion potential, E_{corr}, during the first thirty minutes for freshly polished and etched Magnox and Mg specimens on exposure to air-saturated 0.01 mol/dm^3 sodium hydroxide solution are shown in figs. 5.1 to 5.4. During this period the appearance of the electrodes becomes slightly dull with a decrease in Δ of several degrees and an overall increase in Ψ of a few tenths of a degree. The small scale irregularities in Ψ, figs. 5.3b and 5.4b, result in the Δ,Ψ curves deviating from the smooth curve which would be the result for the growth of a uniform homogeneous film above a flat, perfectly smooth, substrate, e.g. fig. 5.7.

The changes in E_{corr} (figs. 5.3c and 5.4c) for both substrates are similar, i.e. an initial activation followed by a more gradual ennoblement. Similar behaviour has been observed for stainless steels in magnesium chloride solutions.[171] In that work it was stated that the potential became more active initially due to the magnesium chloride solution attacking the metal through pores and weak points in the air formed oxide film. The potential became more noble as hydroxides precipitated out within the pores, making the film more protective and stifling the corrosion attack.

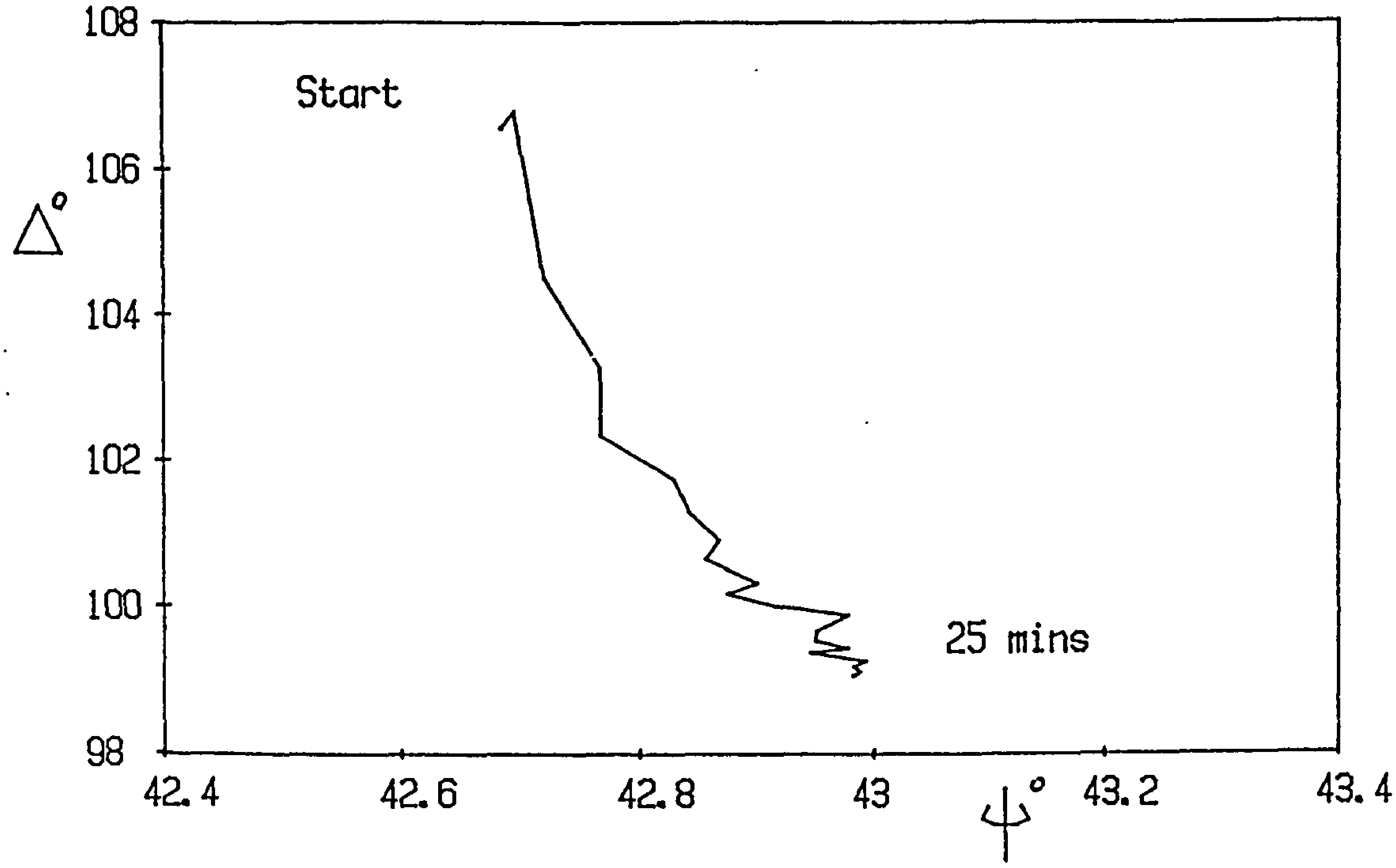

Fig. 5.1 Magnox at Open Circuit in 0.01 mol/dm^3 NaOH

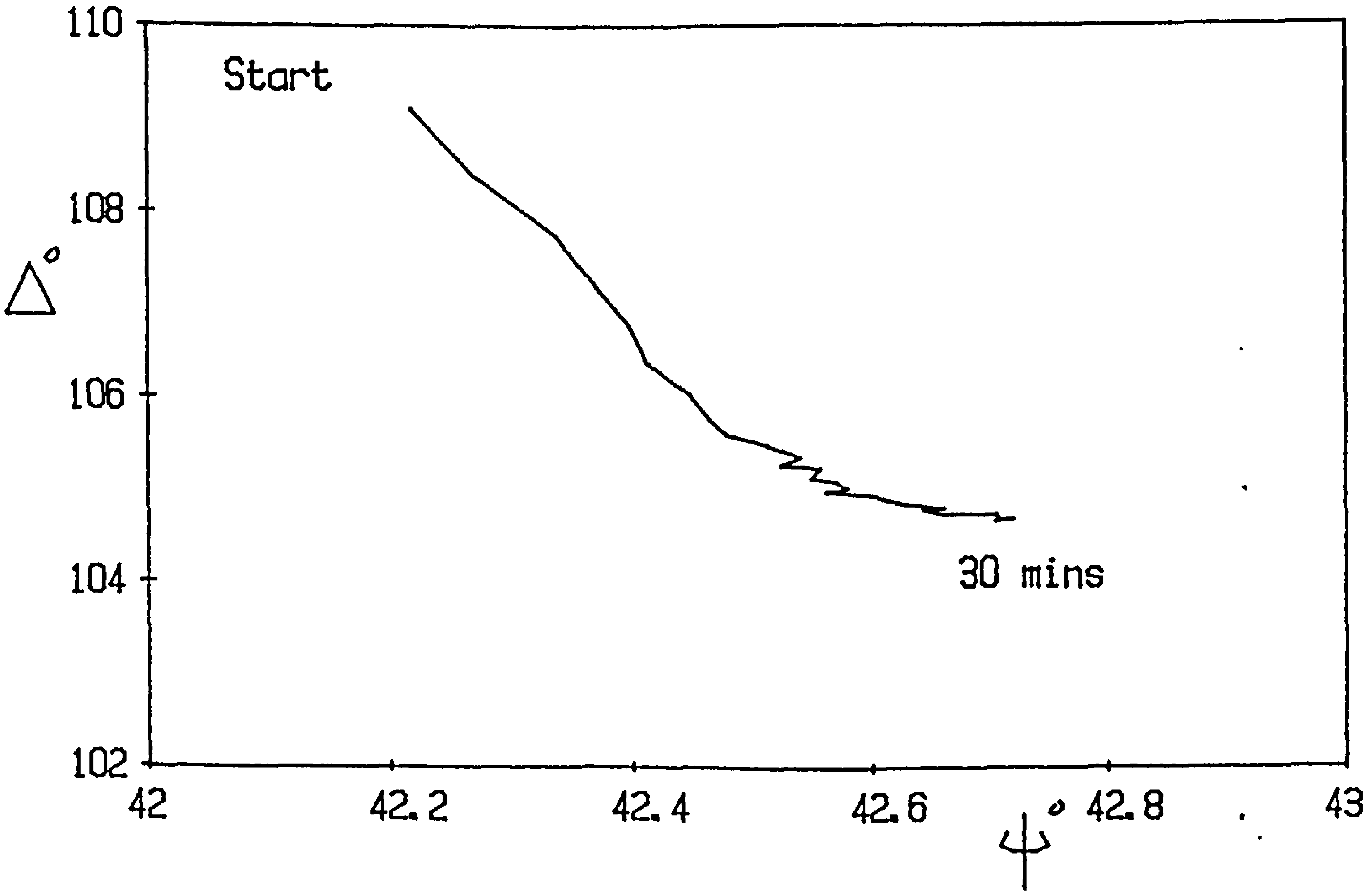

Fig. 5.2 Magnesium at Open Circuit in 0.01 mol/dm^3 NaOH

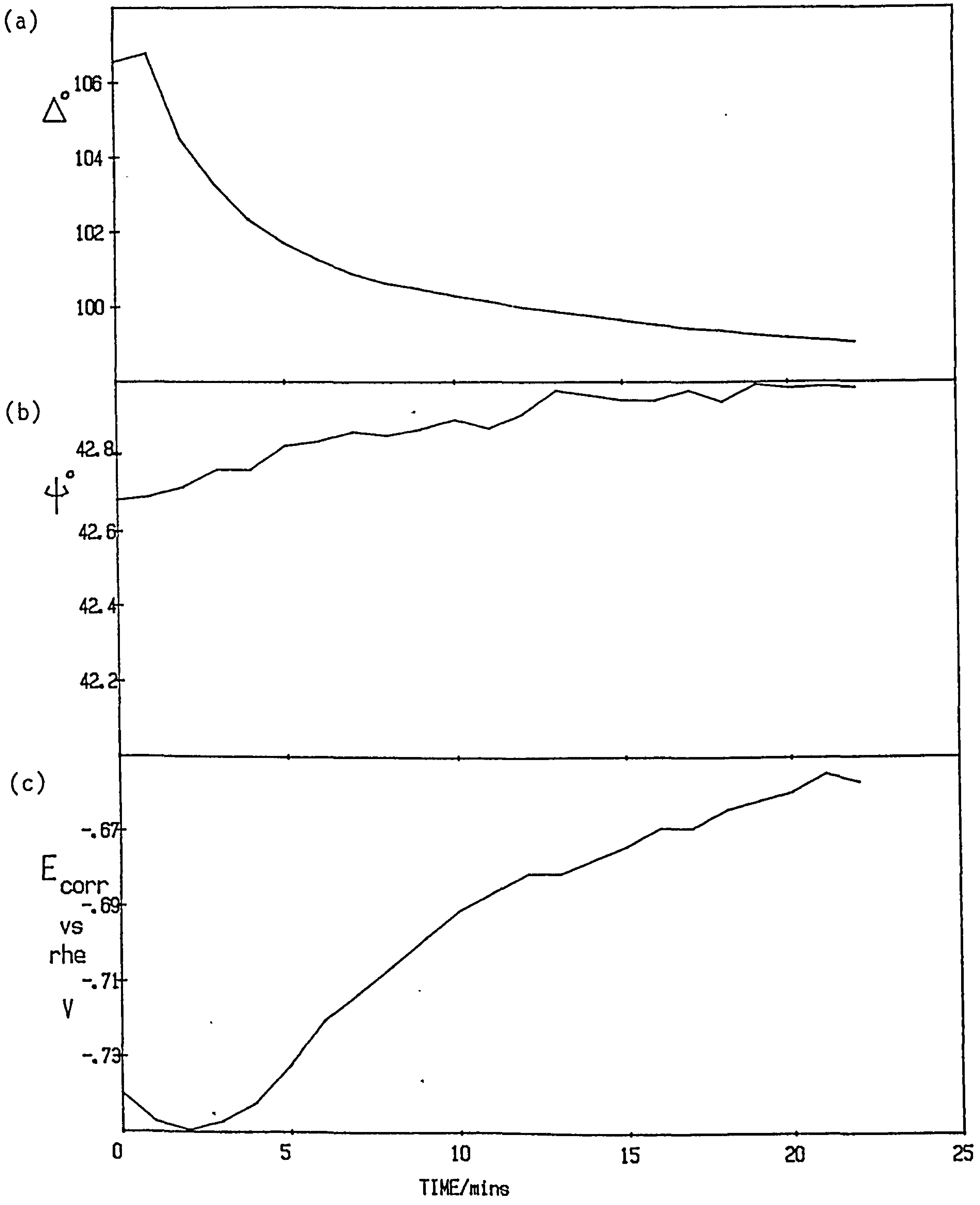

Fig. 5.3 Magnox at Open Circuit in 0.01 mol/dm^3 NaOH

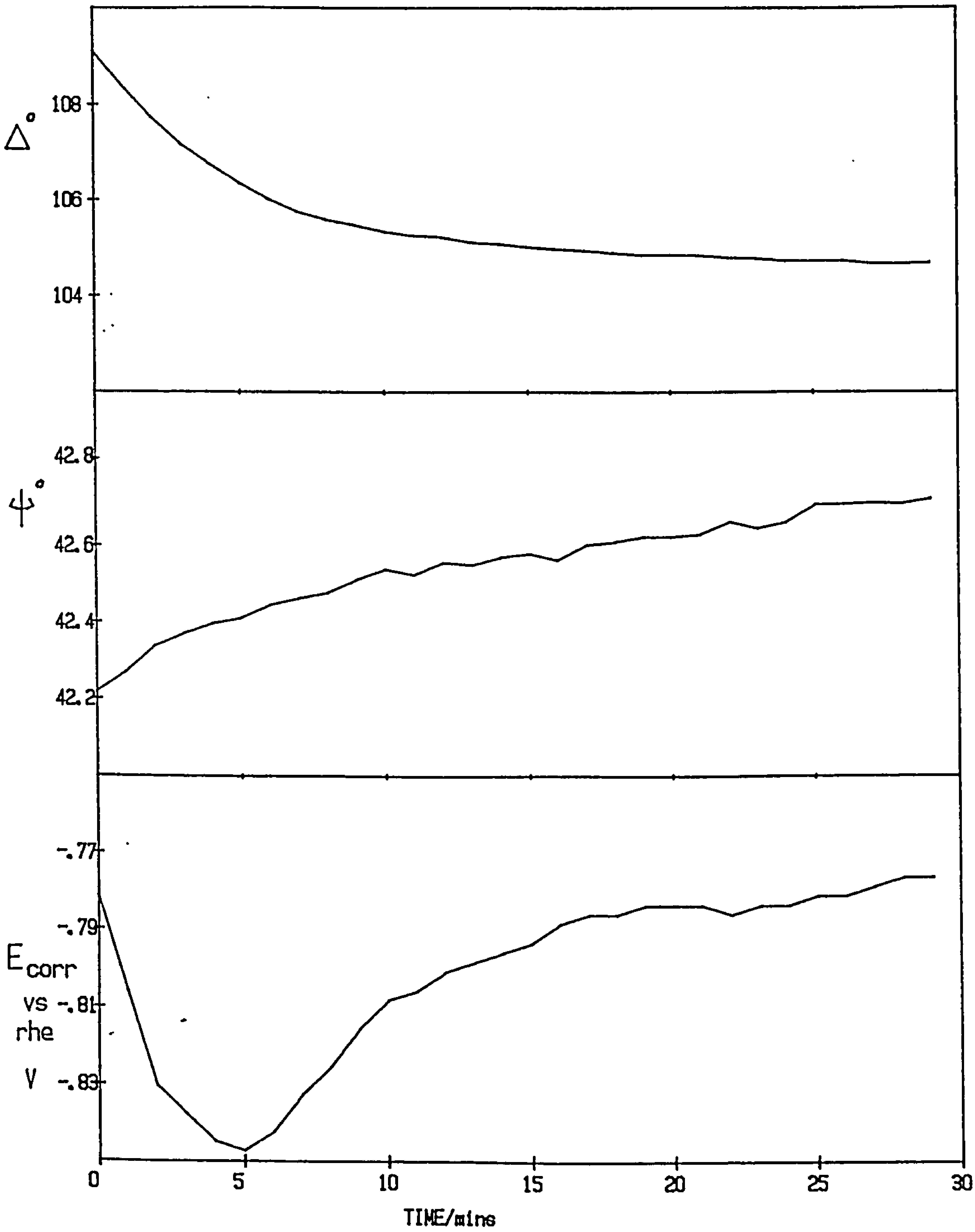

Fig. 5.4 Mg at open circuit in 0.01 mol/dm^3 NaOH

It has already been suggested from the ellipsometric results in Chapter 4 for the bare Magnox and magnesium substrates that there is a fairly thick film present after polishing and etching. If this film is porous then a similar mechanism may be operative here, with penetration of the sodium hydroxide through the film, and its resulting reaction with the substrate forming $Mg(OH)_2$ which blocks the pores as in the case of the stainless steel. This corresponds to a type II passive film, fig. 5.5 using Sato's classification,[172] such as that formed on iron in acid solutions.

An alternative mechanism whereby a more protective layer forms underneath the more porous top layer is also possible, corresponding to a type IV passive film, fig. 5.6, such as crystalline rutile on top of a barrier film of anatase formed on titanium in acid solution.[173] The latter model is in accordance with the proposal that the corrosion of Magnox in alkaline media is controlled by a thin 'barrier' film underneath a more porous top layer.[50]

This behaviour complicates the theoretical modelling of the results, as the simplest theoretical model of a single homogeneous film which will have a constant refractive index throughout is unlikely to represent satisfactorily the experimental result. Useful information however can be obtained by this simple treatment on parameters such as the likely optical constants of the bulk corrosion film and the rate with which its thickness is changing. This has been done using a trial and error method, figs. 5.7 and 5.8, from which it can be seen that slight differences in the optical constants of the bare substrate were found. The optical constants for the film formed on Magnox were found to be identical to brucite, a crystalline form of $Mg(OH)_2$ ($n = 1.56$, $k = 0$) whereas n for the film on magnesium was 1.455 indicating that it may be more porous. It must be stressed however that these predictions are based on a simple single film model and variations in the refractive indices of the films will be obtained if different optical constants for the bare substrate are used. This is particularly pertinent for these results as the small changes in Δ and Ψ over the short time intervals used combined with the experimental variation in the optical constants of the bare surface due to the mechanical polishing preclude any other than an approximate theoretical treatment.

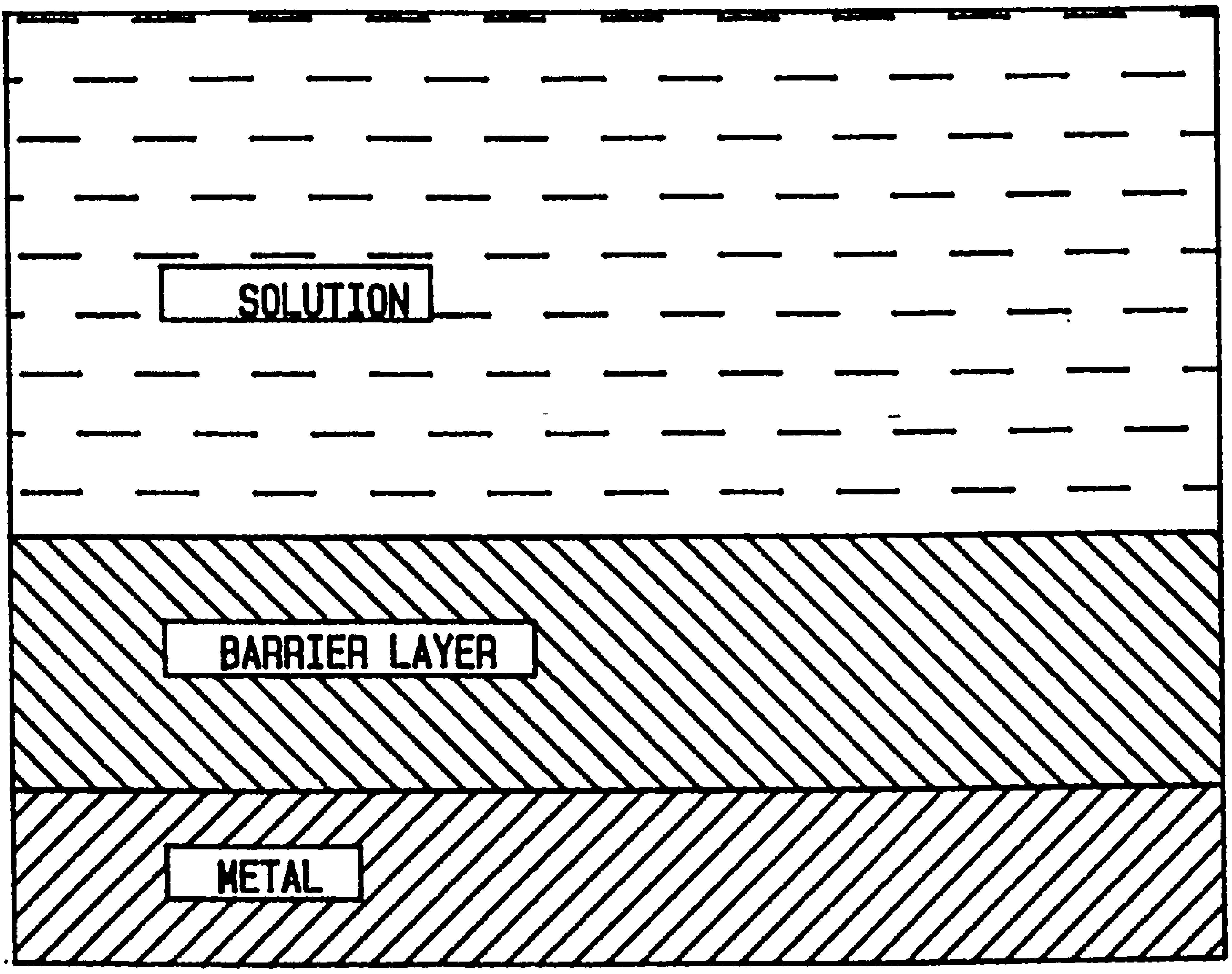

Fig. 5.5   Type II passive film

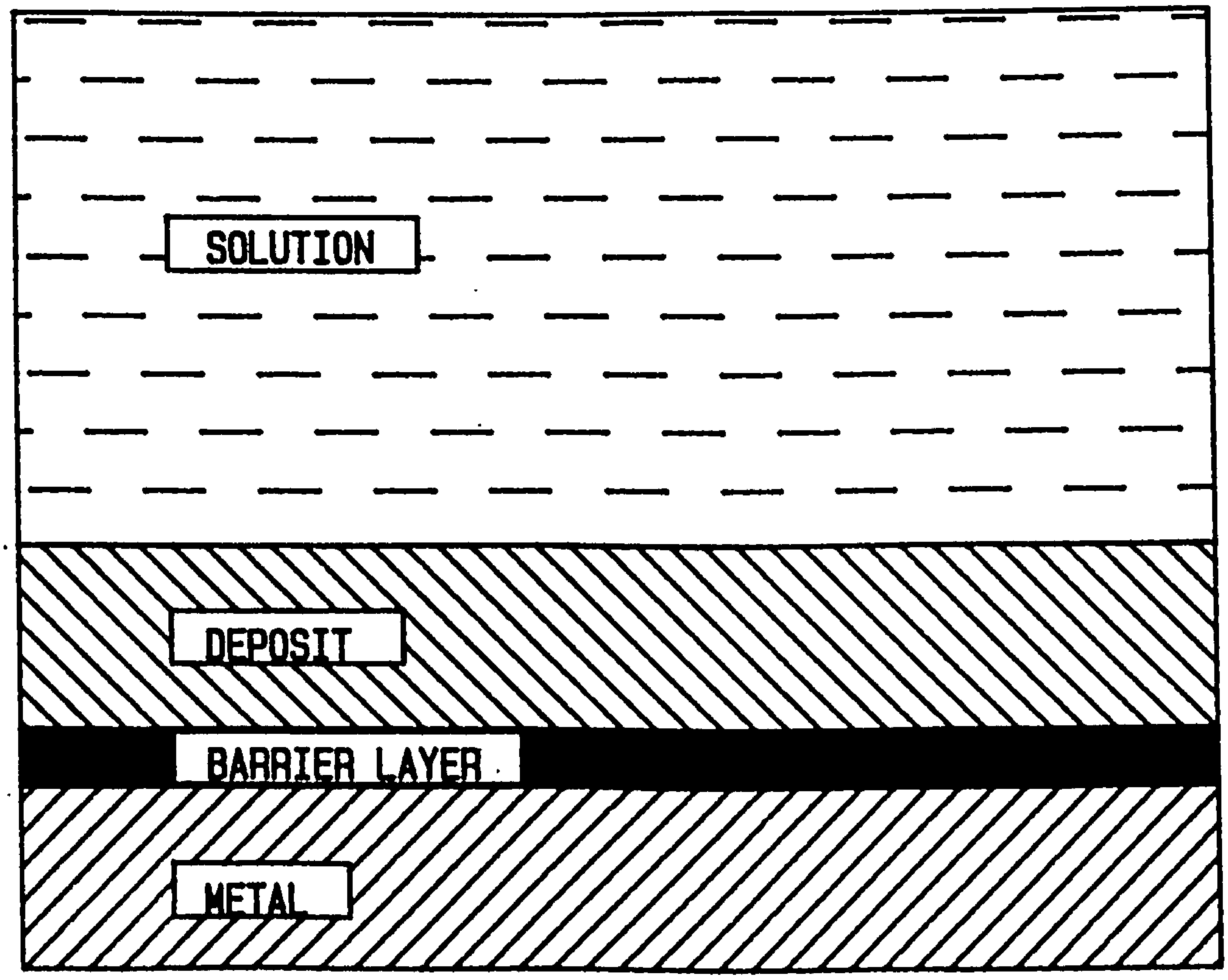

Fig. 5.6   Type IV passive film

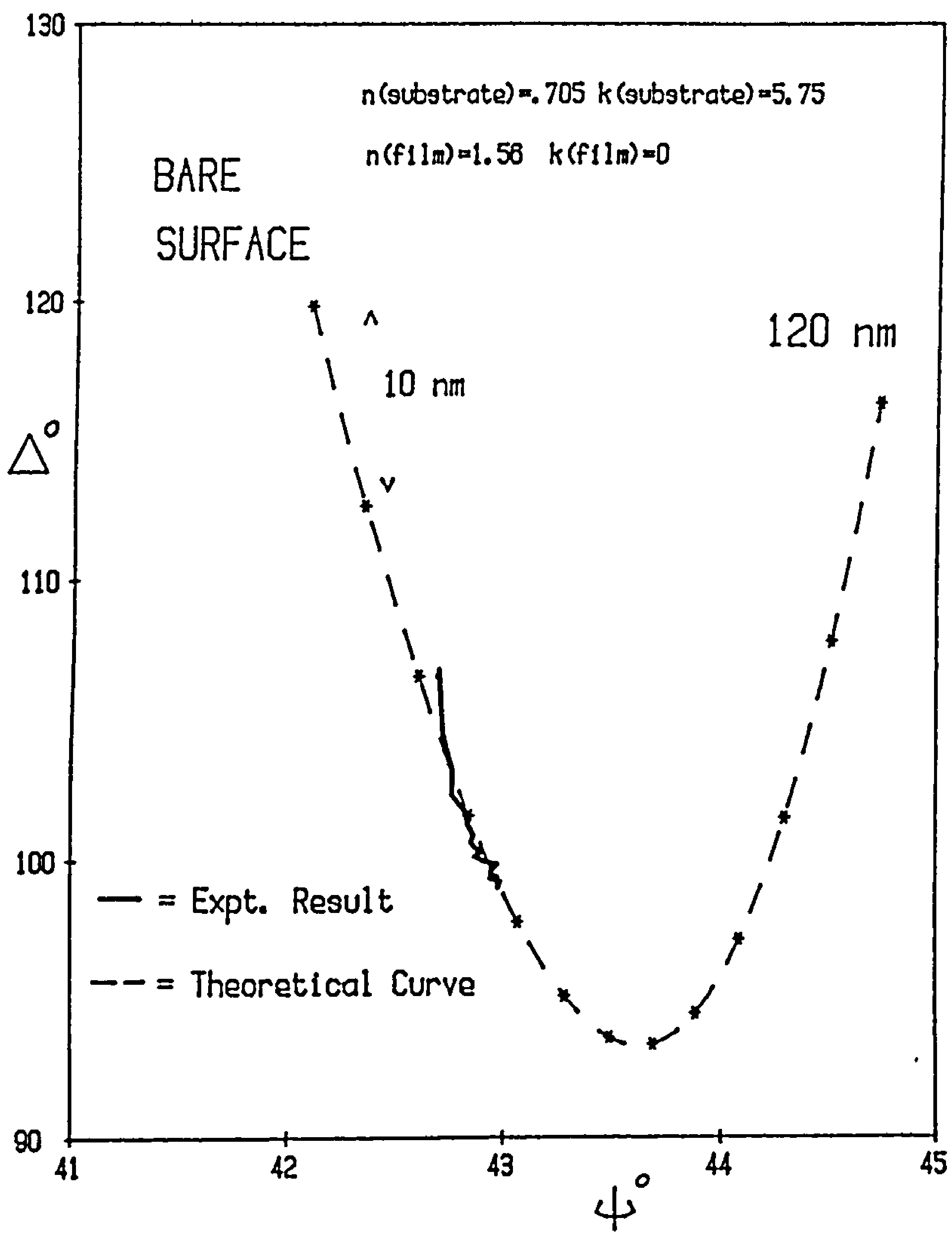

Fig. 5.7 Theoretical modelling of Magnox in 0.01 mol/dm^3 NaOH

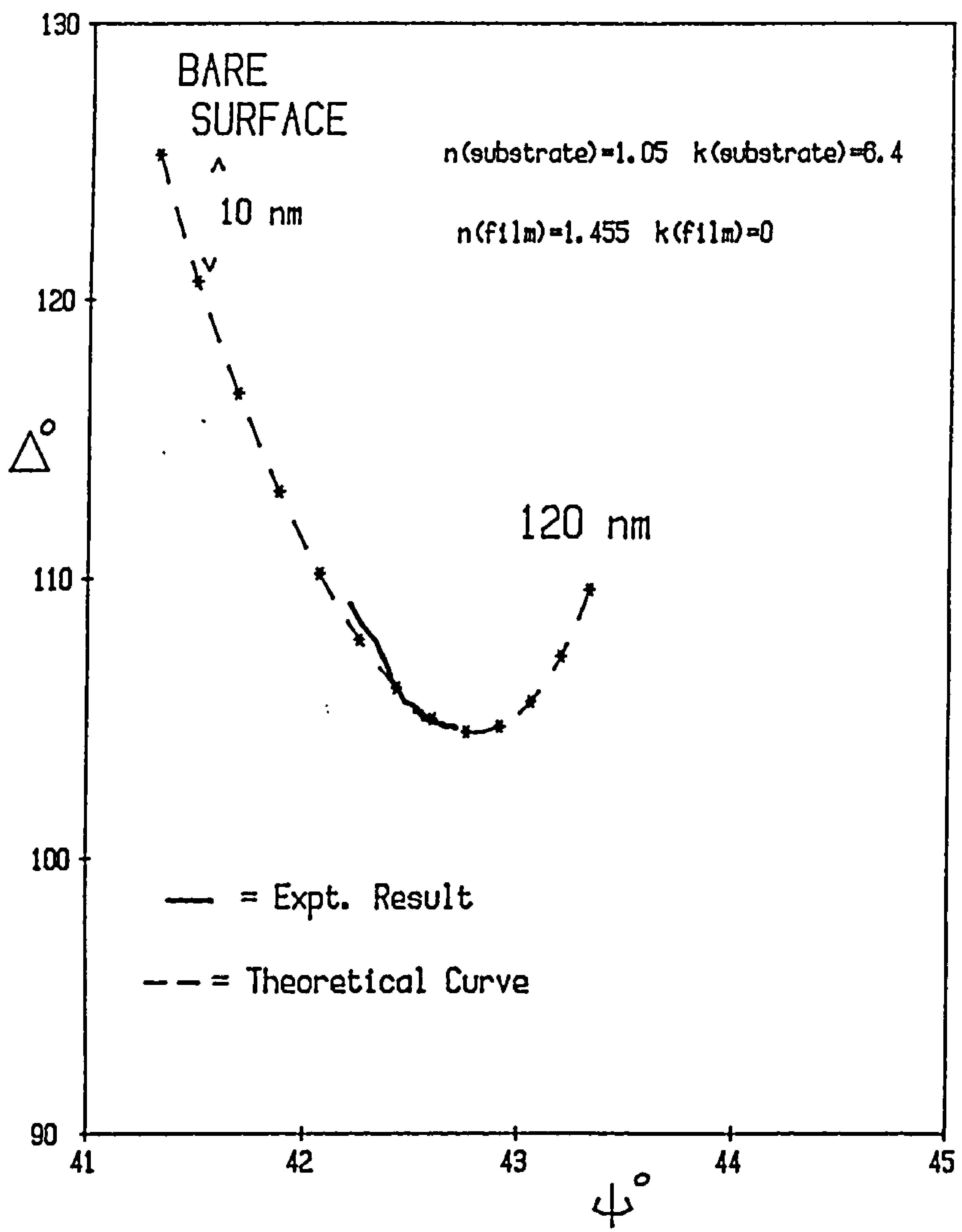

Fig. 5.8 Theoretical modelling of Mg in 0.01 mol/dm^3 NaOH

Using the results in figs. 5.7 and 5.8 the rate of change in film thickness with respect to time, dx/dt, can be obtained (figs. 5.9 and 5.10). It is apparent that film formation is very rapid over the first 15 minutes decreasing to a roughly linear change of film thickness with time thereafter.

5.1.2 Magnox immersed in air-saturated 0.01 mol/dm^3 sodium hydroxide for several hours

In order to obtain further information on the corrosion mechanism and to enable more accurate modelling of the film growth, several experiments were conducted over longer periods. The optical behaviour exhibited by Magnox specimens immersed in air-saturated 0.01 mol/dm^3 sodium hydroxide solutions over several hours in these experiments is unusual (figs. 5.11-5.13). Initial changes in Δ and Ψ are similar to those in fig. 5.1 and characteristic of a transparent film growing on a metallic substrate. The changes after the first hour, although not being highly reproducible have a distinct underlying trend: a decrease in Ψ after a period of 2-3 hours which is initially slow, becoming more rapid after a further hour. The reduction in Ψ is preceded by an activation of E_{corr}, fig. 5.13c, which occurs about 1 hour after immersion. Although the appearance of the electrode does not change during the first few hours, after about 4-6 hours a gradual darkening of the electrode surface is noticeable. After about 8 hours immersion the surface has a patchy light tan colour with small black pits visible near the edge of the sample from which the occasional hydrogen bubble is evolved. A reduction in pH of the test solution was also observed, typically falling from values near pH 12 to values less than pH 10.

It was thought that the changes in pH of the cell solution during the experiment might be affecting the potential of the reference electrode by diffusion of the bulk solution into the open-ended tube of this electrode (fig. 4.1). As the reversible hydrogen electrode is pH dependent, its potential becoming more positive by 59 mV per decrease in pH unit, then a decrease in pH from 12 to 10 would make the potential of this electrode more positive by 118 mV. This would cause an apparent activation of the measured open circuit potential for Magnox (fig. 5.14). To ensure that recorded changes in E_{corr} were due to actual changes in the electrode potential and not to a reduction in pH

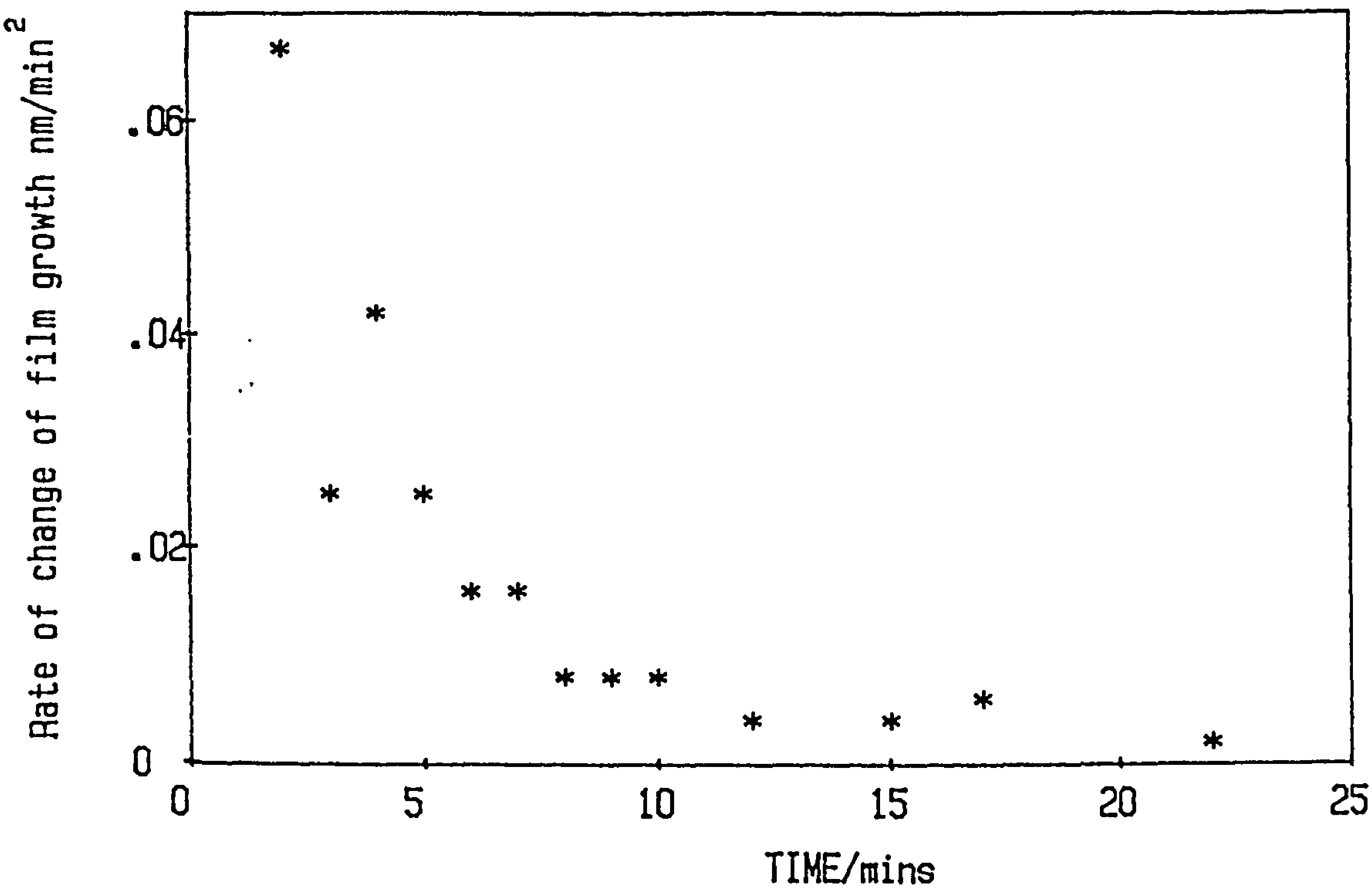

Fig. 5.9 Rate of change of film growth on Magnox in air-saturated 0.01 mol/dm^3 NaOH during the first thirty minutes after immersion

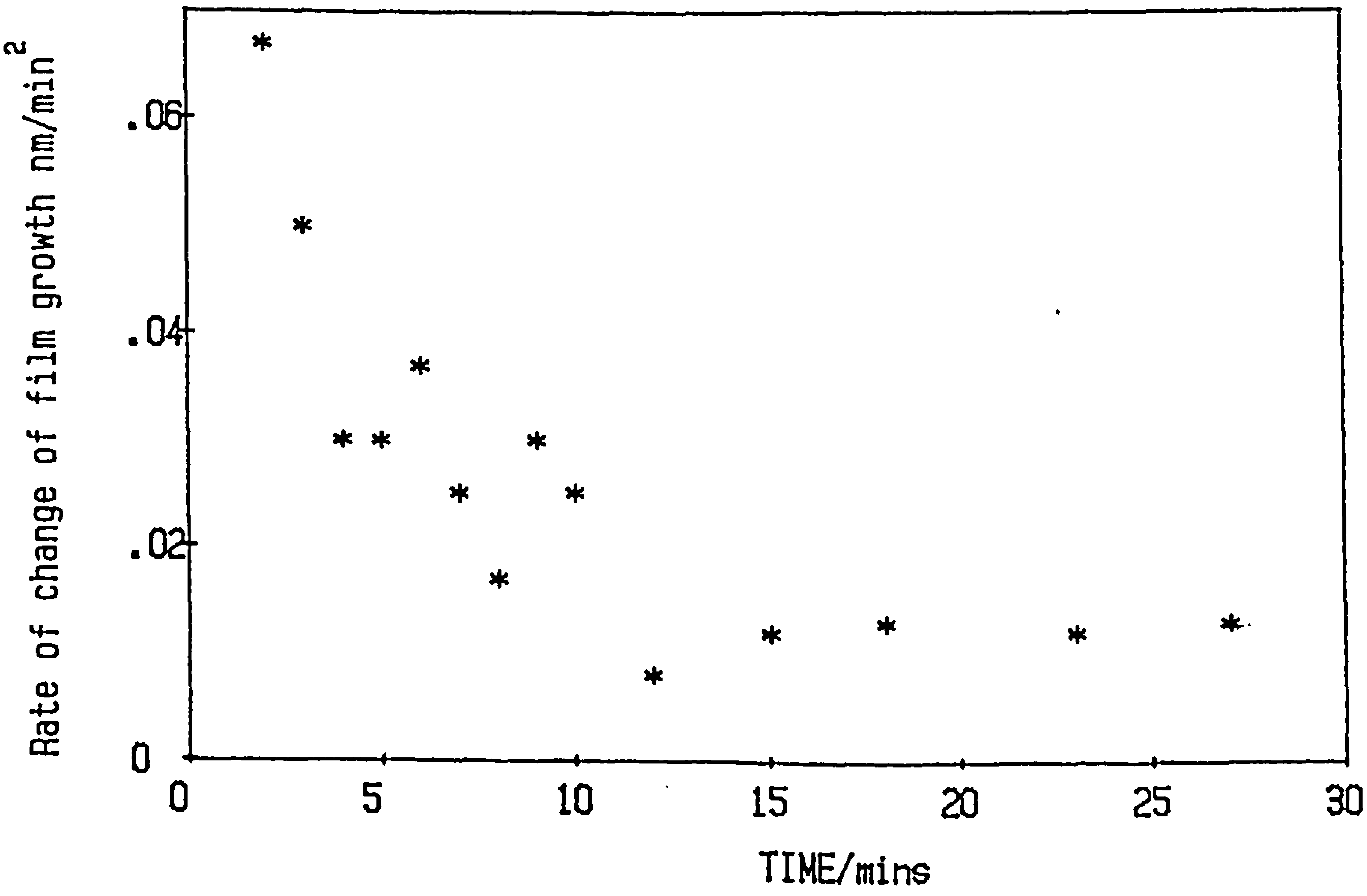

Fig. 5.10 Rate of change of film growth on Mg in air-saturated 0.01 mol/dm^3 NaOH during the first thirty minutes

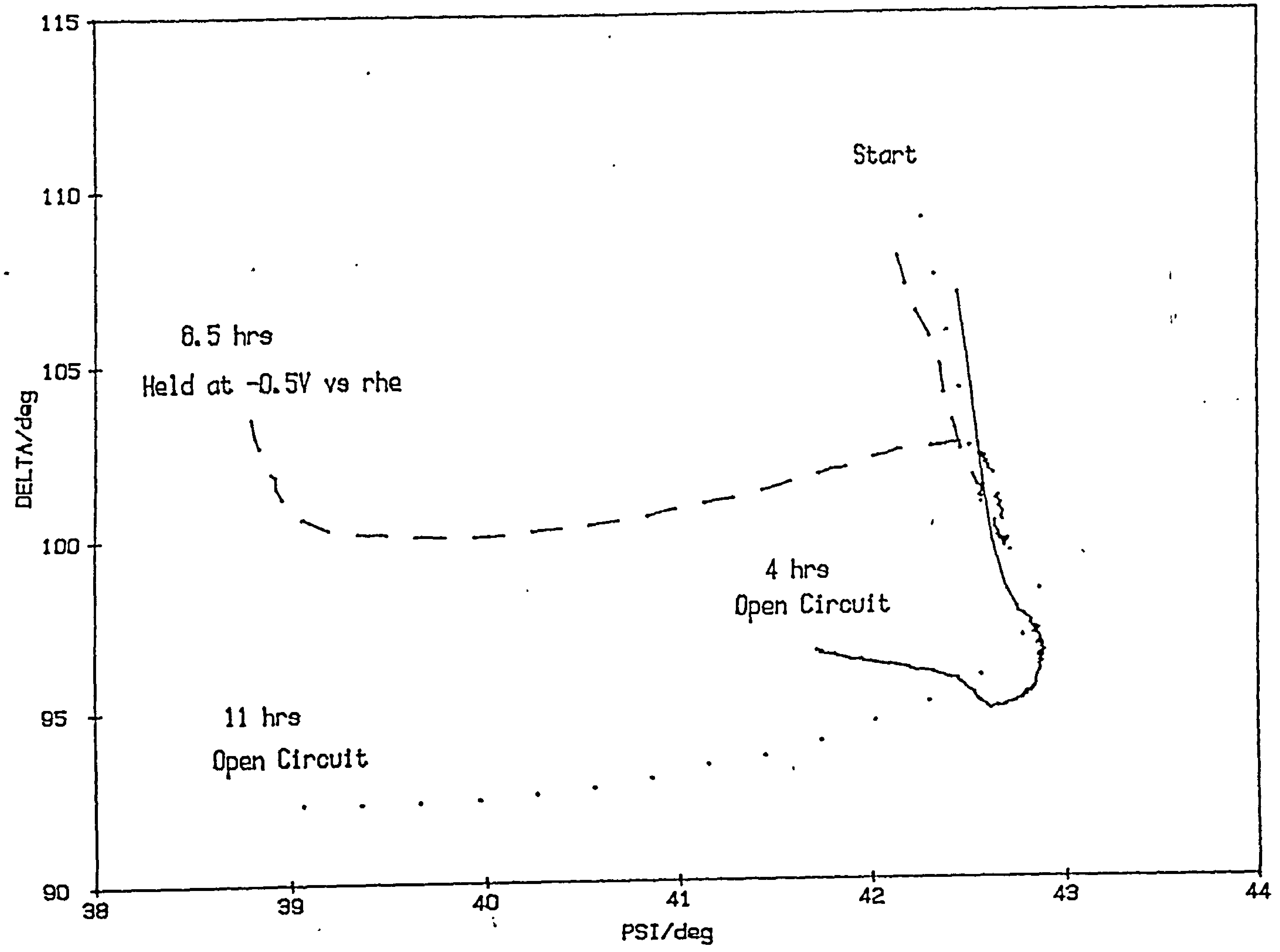

Fig. 5.11 Magnox in air-saturated 0.01 mol/dm^3 NaOH

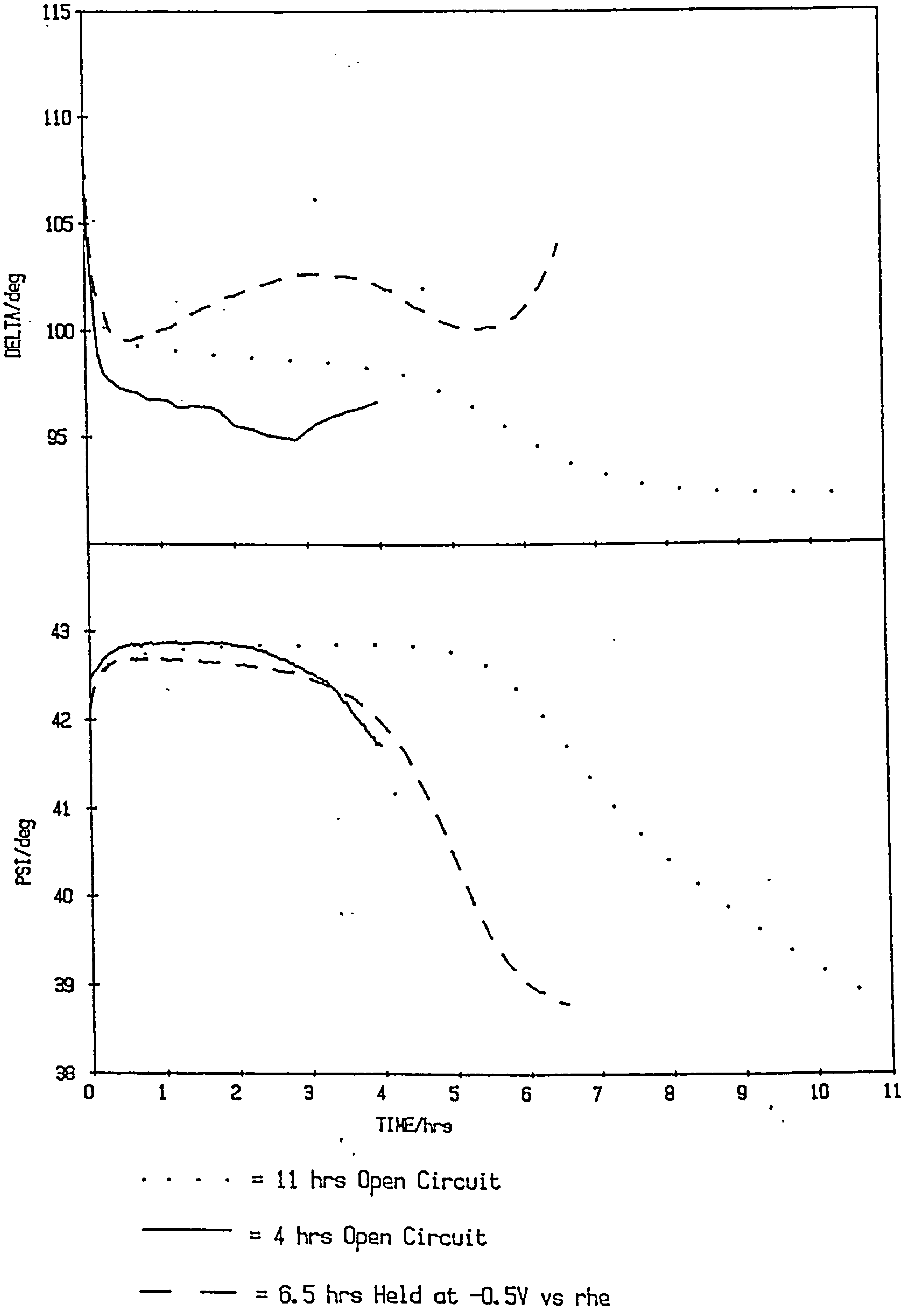

Fig. 5.12 Magnox in air-saturated 0.01 mol/dm3 NaOH

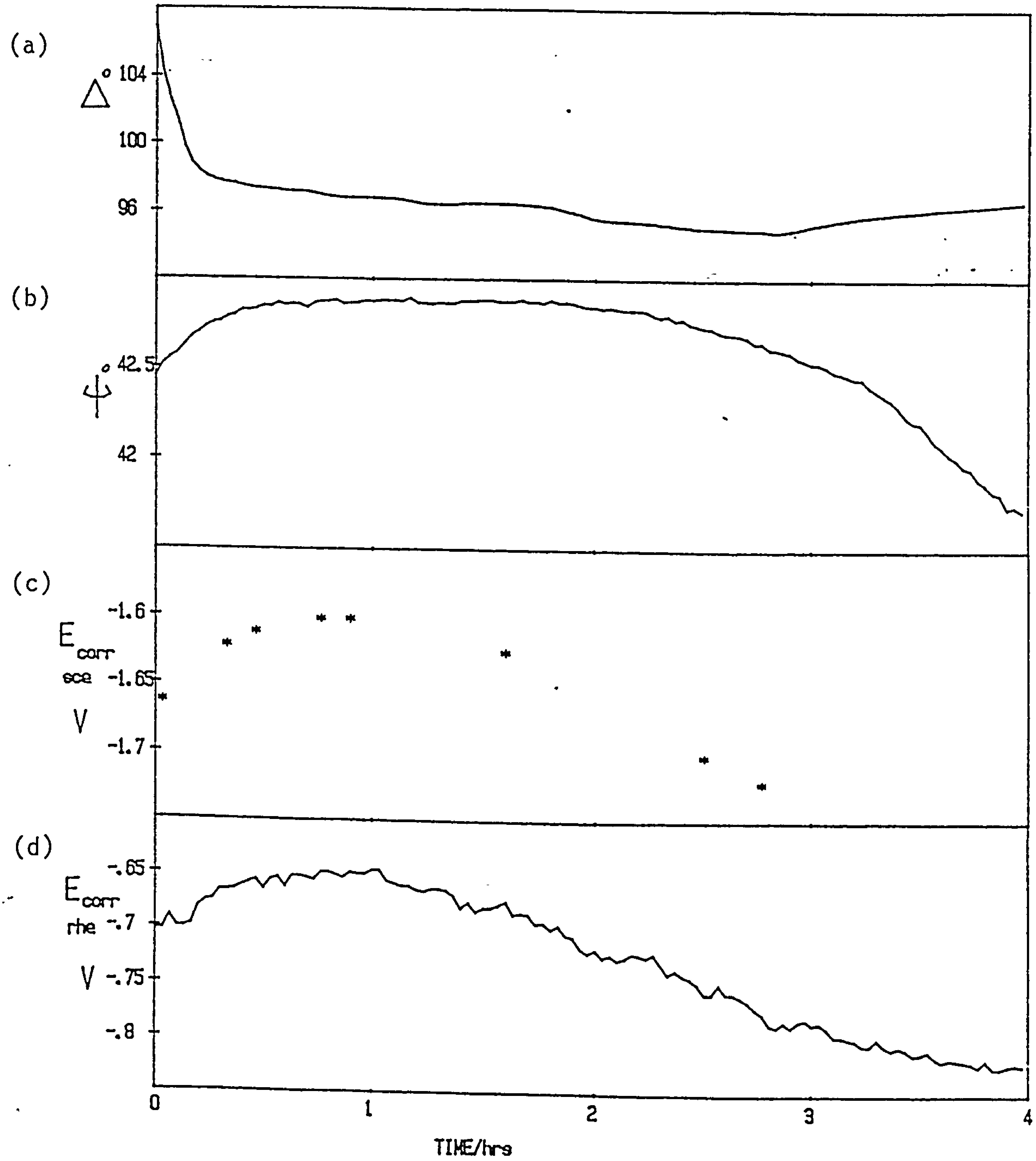

Fig. 5.13 Magnox at open circuit in air-saturated 0.01 mol/dm^3 NaOH

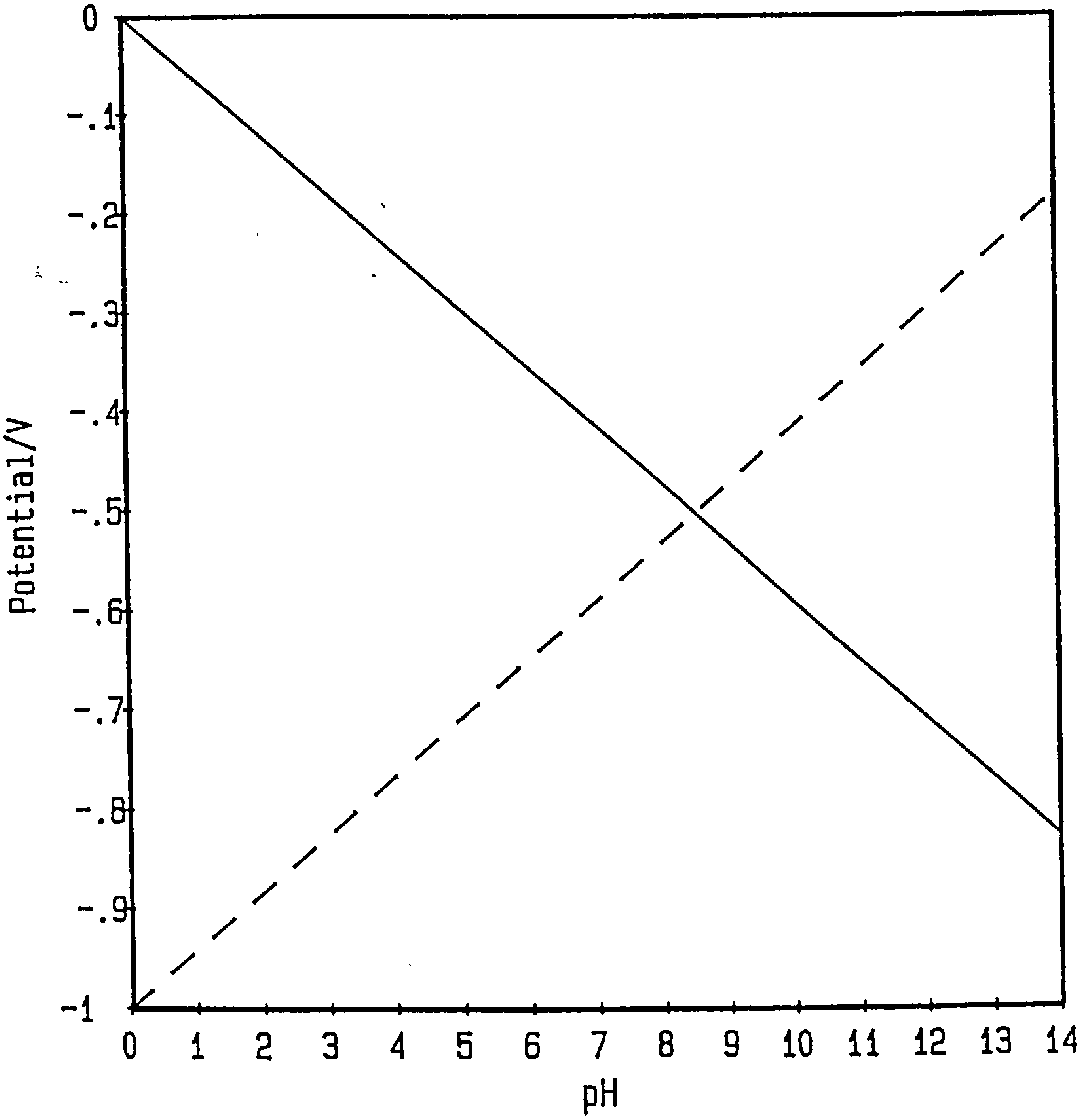

———— = E_{rhe} vs nhe

– – – – – = E_{corr} vs rhe assuming a value of -0.3 V at pH = 12

Fig. 5.14 Change in E_{corr} measured against the reversible hydrogen reference electrode due to pH inside the tube of the rhe, a saturated calomel electrode, sce, was used. This was periodically placed in the cell during a run to record E_{corr} whilst E_{corr} was also continuously recorded using the rhe. The total length of time that the sce was in the sample solution was short and not thought to significantly increase the chloride concentration in the cell. The fact that the change in potential of E_{corr} wrt the sce mirrored that wrt the rhe, figs. 5.13c and 5.13d, indicated that the pH of the solution inside the tube of the rhe was close to the initial pH. This was presumably the result of the poor mixing of the solution inside the narrow rhe tube and that of the solution bulk.

Further experiments were conducted on Magnox held at fixed potentials close to the initial value of E_{corr}. The results in figs. 5.11-5.12 show the same trend as those for the experiments in open circuit conditions, i.e. a decrease in Ψ after several hours to values below that of the bare surface.

In order to obtain further information about the corrosion film, a Magnox coupon that had been immersed in 15 cm^3 of air-saturated 0.01 mol/dm^3 NaOH for 6 hours at open circuit was depth profiled using an argon ion gun and SIMS. The procedure was the same as that described in Chapter Four. From observation of a typical spectrum taken during etching, fig. 5.15, certain features are apparent. There is a strong Mg^+ peak at mass no. 24 with satellites at mass nos. 25 and 26, a weaker Al^+ peak at 27, carbon at 12 and 14 (CH_2^+) with traces of Na^+ at 23 and possibly K^+ at mass no. 39. The latter two ions have a very high relative ion yield in SIMS of 2400 for Na^+ and 2100 for K^+ compared to 260 for Mg^+ and 200 for Al^+ based on Sparrow's formula.[174] This results in traces of these elements being readily observed. In the negative spectra there are strong peaks at mass 16 (O^-) and 17 (OH^-).

The peak heights for Mg remain fairly constant on etching through 500 nm but there are considerable variations in the peak heights of both O^- and OH^- which results in large variations in the Mg/O peak height ratio, fig. 5.16, and makes an accurate determination of the film thickness impossible. A major problem in using SIMS, discussed in Chapter Four, is relating the measured ion currents to concentrations of elements present due to instrumental errors and errors arising from matrix effects, selective sputtering and molecular ion formation.

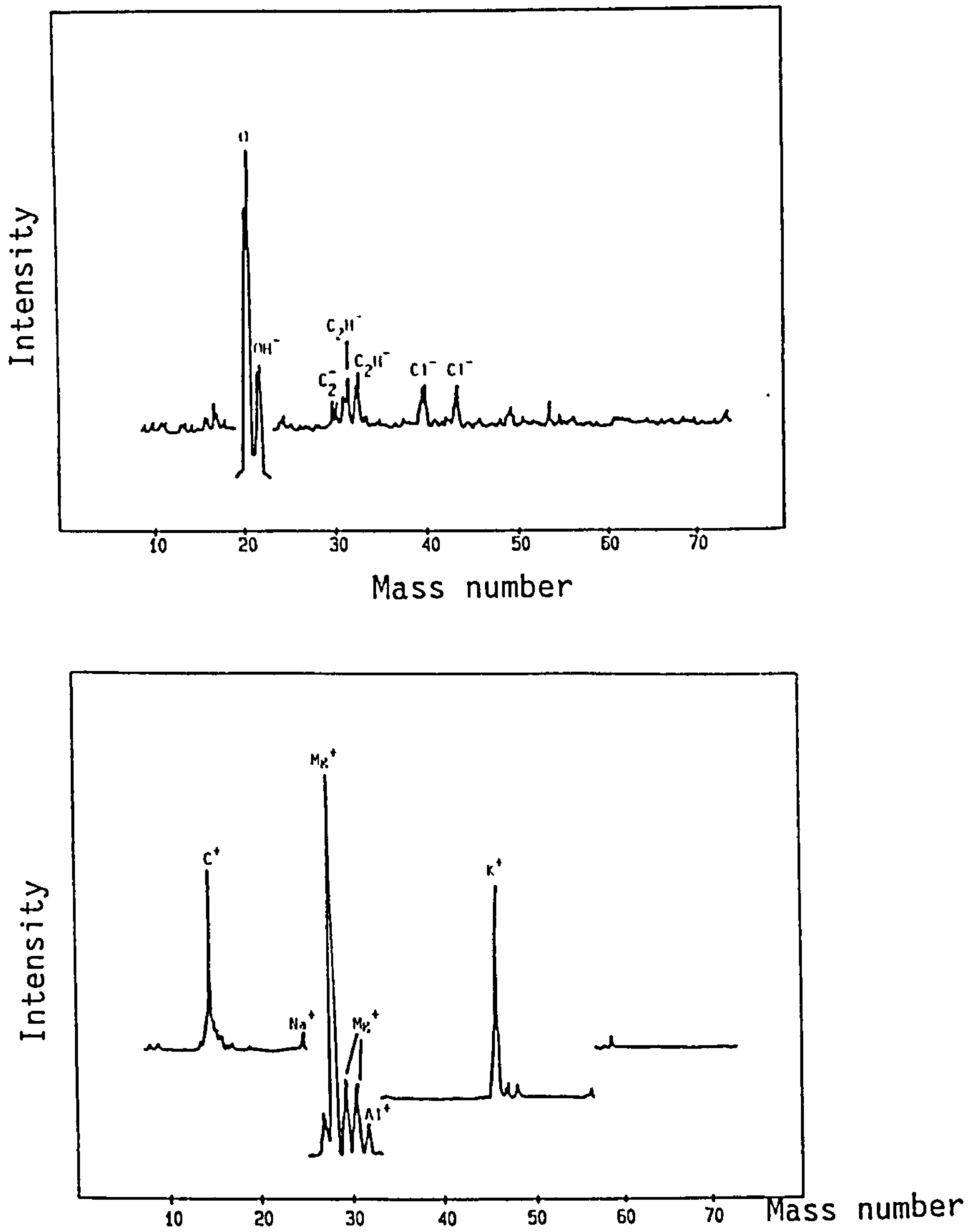

Fig. 5.15 Typical SIMS spectra for Magnox immersed for 6 hours in 0.01 mol/dm^3 NaOH after 15 nm of film has been sputtered

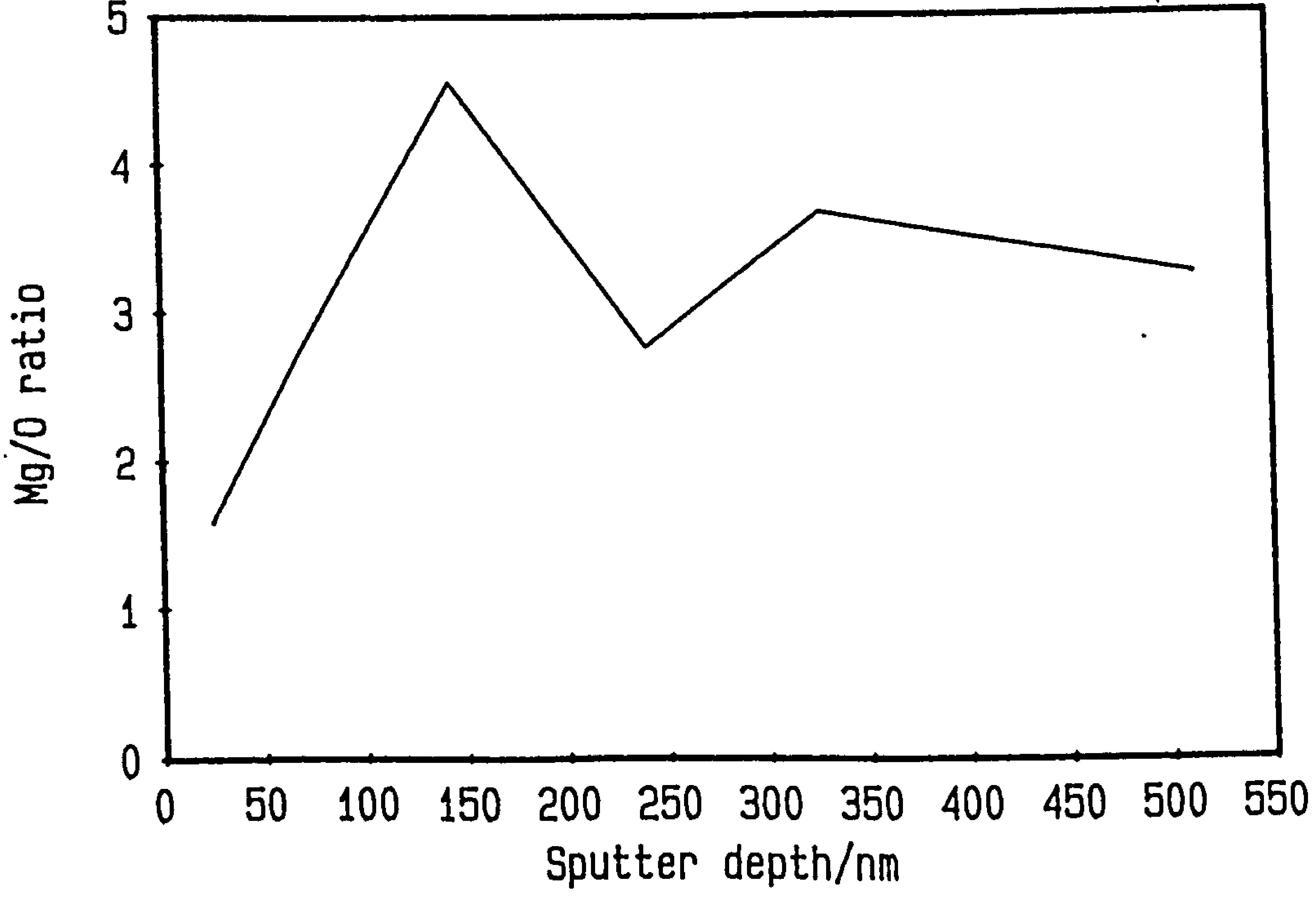

Fig. 5.16 Mg/O ratio from SIMS analysis of a Magnox specimen immersed for 6 hours in 0.01 mol/dm^3 NaOH

If however these variations of the Mg/O peak height ratio are due to actual changes in composition of the film then they suggest that the film is inhomogeneous. One cause of this would be if there was roughening of the film substrate interface.

There is a small amount of sodium present in the outermost layers which falls off rapidly on etching through the film which suggests that it is due to sodium hydroxide solution left on the surface after drying.

Aluminium increases in concentration up to a depth of 50 nm after which it decreases. This may be due to the surface enrichment of aluminium found on annealed and etched Magnox samples[158] and for the polished specimens in Chapter Four. The film formed during the early stages of corrosion will thus have a higher Al content than that formed after the Al enriched layer has been incorporated into the corrosion film.

5.1.3 Magnesium immersed in air-saturated 0.01 mol/dm^3 sodium hydroxide for several hours

The optical and electrochemical results, figs. 5.17-5.19, are broadly similar to those for Magnox under these conditions. There are differences in Δ and Ψ between experiments under the same and slightly different potential conditions but the general trend of a decrease in Ψ after a variable time period is apparent throughout. Again there is also an activation in E_{corr} prior to the decrease in Ψ for the samples at open circuit.

The visible appearance of the samples is similar to those of Magnox at first with small pits on the surface after several hours. In the later stages the magnesium film also becomes patchy, turning a dark grey/black colour, then gradually becoming a uniform jet black after a period of several days immersion. On removal from solution however this dark film lightens considerably and a thick light grey hydroxide film can be seen.

A magnesium sample that had been exposed to 15 cm^3 of 0.01 mol/dm^3 NaOH for 6 hours was depth profiled by SIMS in an identical experiment to that performed on Magnox in the previous section. In the positive spectra, fig. 5.20, strong Mg peaks at mass no. 24 with satellites at mass 25 and 26 can be identified. There are also several compound magnesium ions with peaks at 48 (Mg_2^+) and 64 (Mg_2O^+) with satellites

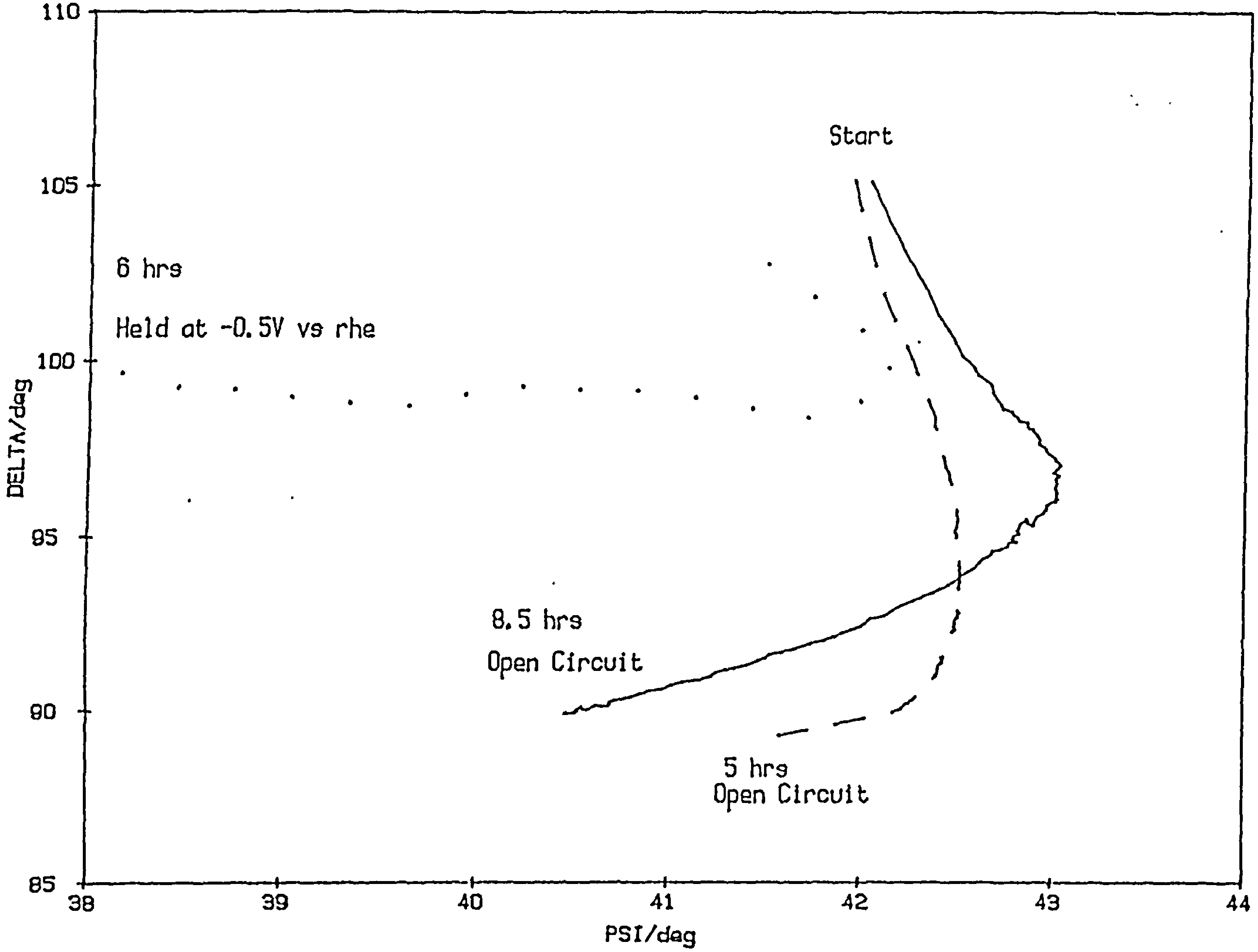

Fig. 5.17 Magnesium in air-saturated 0.01 mol/dm^3 NaOH

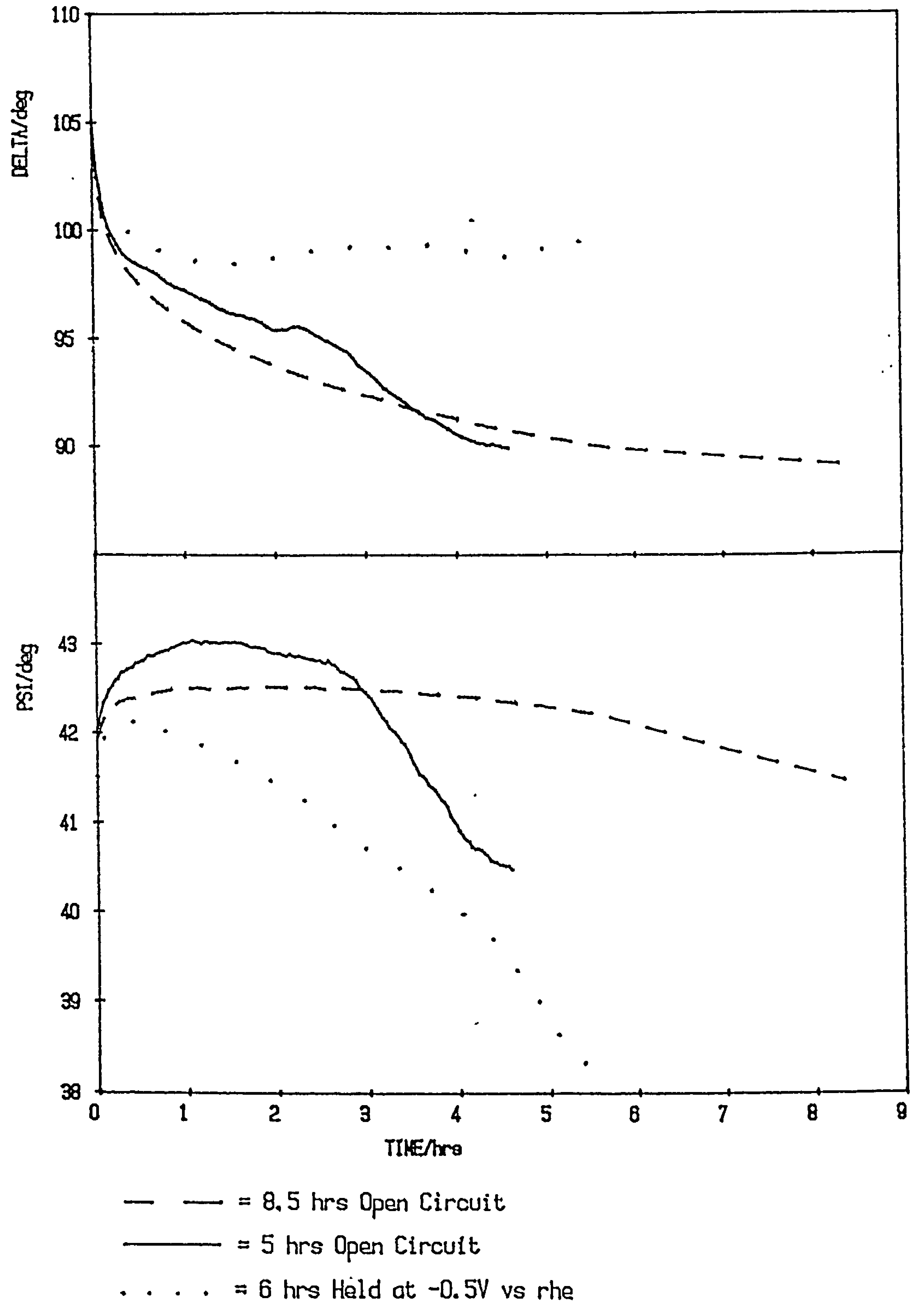

Fig. 5.18 Magnesium in air-saturated 0.01 mol/dm^3 NaOH

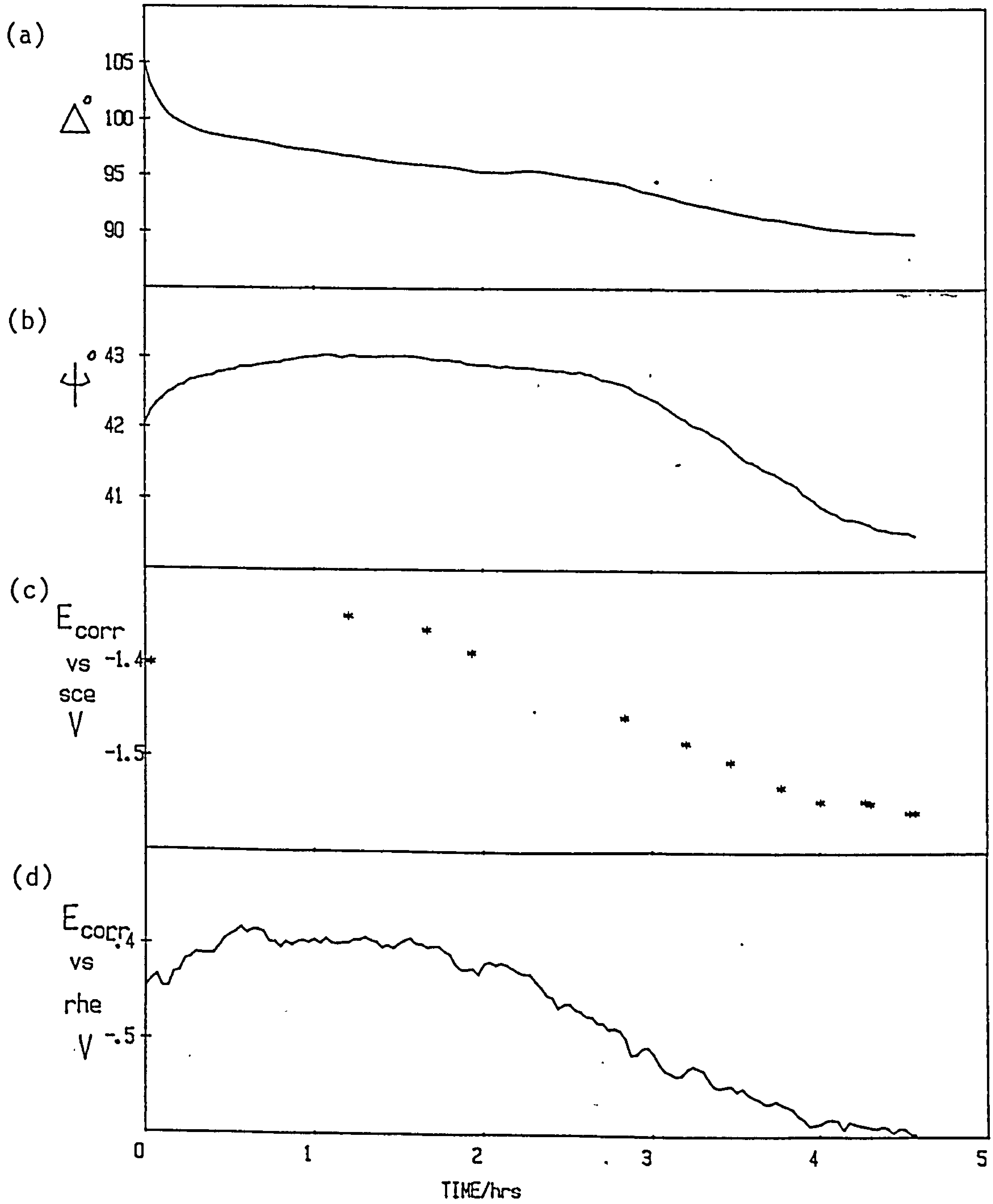

Fig. 5.19 Magnesium at open circuit in air-saturated 0.01 mol/dm^3 NaOH

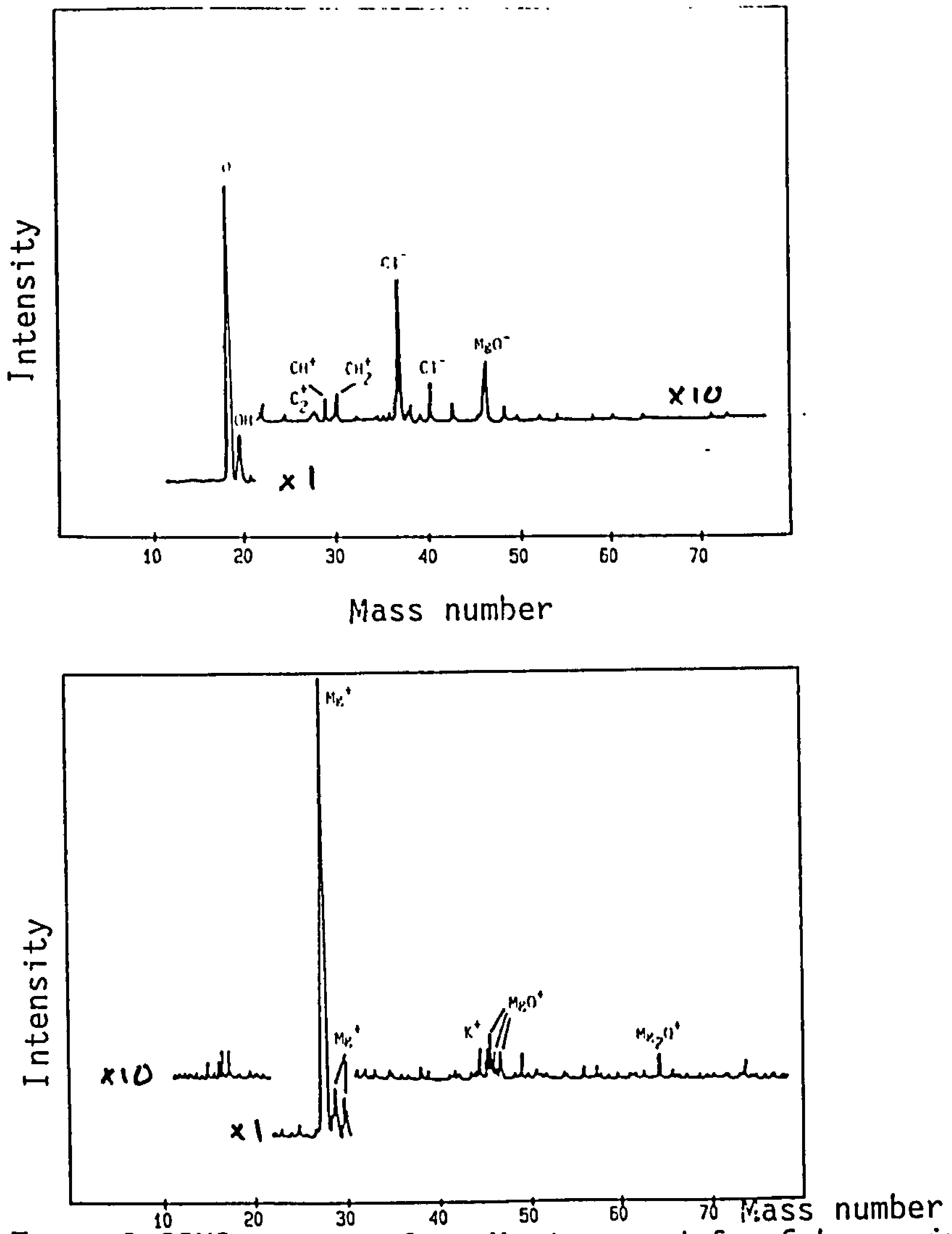

Fig. 5.20 Typical SIMS spectra from Mg immersed for 6 hours in 0.01 mol/dm^3 NaOH after 10.5 nm of film has been sputtered

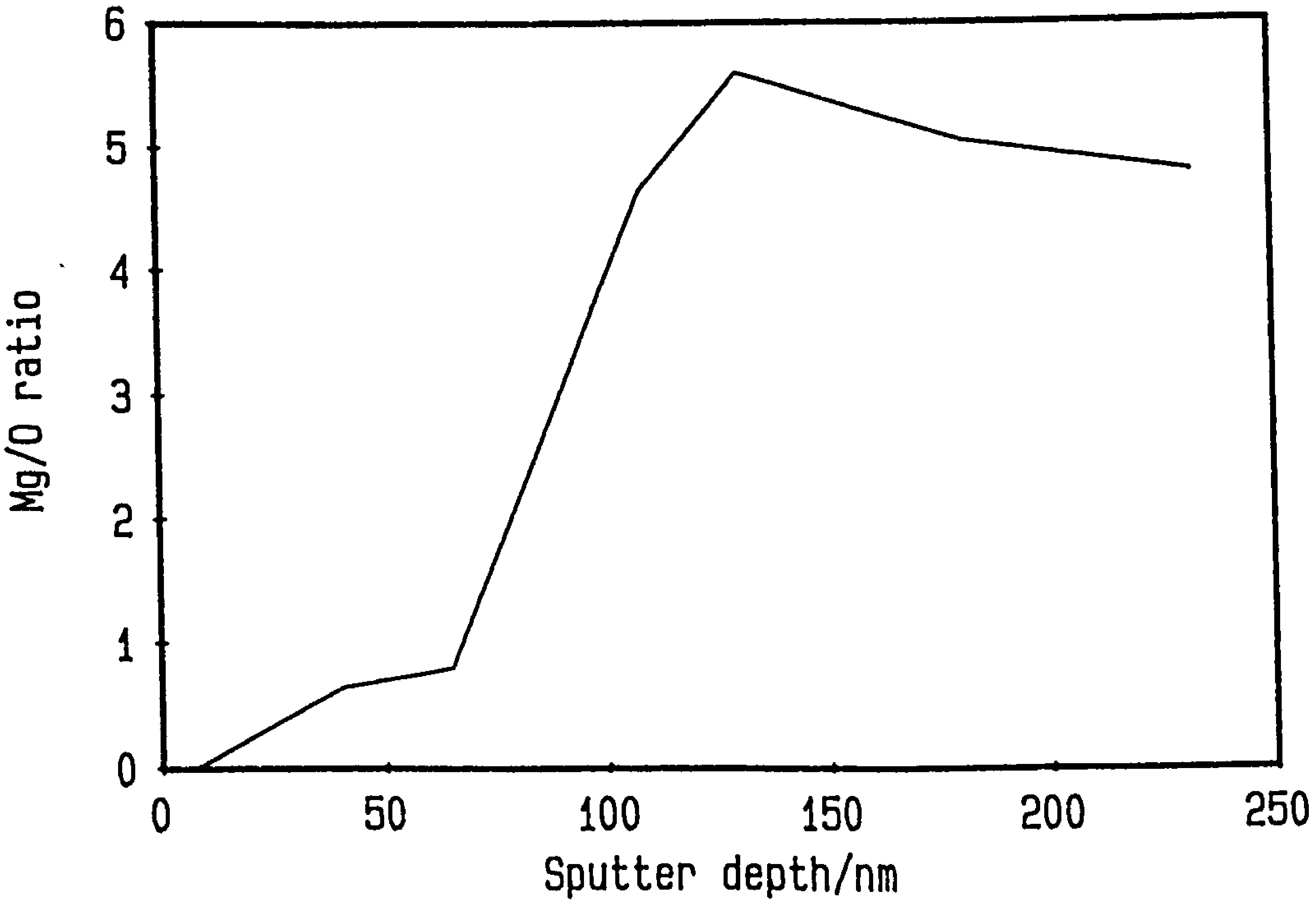

Fig. 5.21 Mg/O ratio from SIMS analysis of a Mg sample immersed in 0.01 mol/dm^3 NaOH

at mass numbers +1 and +2 to these stronger peaks. The peaks at mass numbers 40 to 43 also indicate the presence of compound Mg ions, probably MgO^+ and $MgOH^+$. The peak at mass 39 may be due to K^+ due to the sensitivity of SIMS to this element. Carbon is also present with a weak peak visible at mass 12 in all the positive spectra.

In the negative spectra there are strong O^- and OH^- peaks at mass 16 and 17 with traces of Cl^- being evident from the characteristic peaks at mass 35 and 37, the latter being roughly 1/3 that of the peak at mass 35. Evidence of carbon can be seen from the peaks at mass 12 (C^-) and 24 (C_2^-).

There is a fairly sharp transition in the Mg/O ratio, fig. 5.21, between ca. 60 nm and 130 nm, in contrast to the results for Magnox. An estimate of the film thickness can be made of roughly 105 ± 20 nm. The O/OH ratio shows a slight increase above 160 nm but this can not really be taken as evidence for an MgO layer beneath a $Mg(OH)_2$ film due to the uncertainties inherent in the technique.

Another magnesium sample which had been immersed in 15 cm^3 of 0.01 mol/dm^3 NaOH for 3 days and had turned black was also depth profiled by SIMS. The corrosion film was apparently relatively thick with only an extremely weak Mg peak observed after 700 nm of film had been sputtered.

5.1.4 Discussion of the results for magnesium and Magnox in air-saturated 0.01 mol/dm³ sodium hydroxide

The activation of E_{corr} and subsequent pitting indicate the breakdown of the passive film formed within the first 15 minutes. The reduction in pH and the presence of significant quantities of carbon in the corrosion films suggest that this may be due to the absorption of carbon dioxide from the air.

In solutions with a pH above 10 there is a direct reaction between CO_2 and OH^-:[175]

$$CO_2 + OH^- \rightarrow HCO_3^- \qquad .....(5.1)$$

$$HCO_3^- + OH^- \rightarrow CO_3^{2-} + H_2O \qquad .....(5.2)$$

(instantaneous)

$$\frac{-d(CO_2)}{dt} = K_{OH^-}\,(OH^-)CO_2 \qquad .....(5.3)$$

$$K_{OH^-} = 8500\ \mathrm{sec}^{-1}\ (\mathrm{mol/dm}^3)^{-1}$$

which is a much faster reaction than in solutions with a $pH < 8$ in which the predominant mechanism is via direct hydration:

$$CO_2 + H_2O \rightarrow H_2CO_3 \qquad .....(5.4a)$$

$$H_2CO_3 + 2OH^- \rightarrow CO_3^{2-} + 2H_2O \qquad .....(5.4b)$$

(instantaneous)

$$\frac{-d(CO_2)}{dt} = K_{CO_2}\,(CO_2) \qquad .....(5.5)$$

$$K_{CO_2} = 0.03\ \mathrm{sec}^{-1}$$

This is known to be a problem for Magnox stored in sodium hydroxide for several months[176] but was not initially thought to significantly affect the results over short time periods. Its effect is twofold, firstly it lowers the pH below the critical value of ca. 11.5 sec on the Pourbaix diagram, fig. 1.2, into a region where the corrosion film formed is less protective, and secondly it results in the formation of carbonates which can increase the solubility of the corrosion film.[176]

If the film formed becomes less protective and the substrate dissolution rate increases, it is conceivable that the attack will be channelled through weak points in the film. Substrate roughening would then be likely to occur. The decrease in Ψ can not be reproduced by any simple optical model based on a transparent corrosion film growing on a smooth substrate, but if there is assumed to be a metallic type film situated between the substrate and overlying film then this decrease in Ψ is indeed predicted.[57] One way in which this can occur is if the substrate becomes rough. This is considered in detail in the next chapter.

The changes in pH for various volumes of 0.01 mol/dm^3 sodium hydroxide solution left exposed to the air for 26 hours are given in table 5.1. This indicates that the reason behind the unexpected fall in pH is due to the small volume of the solution in the sample cell and the high surface area of solution exposed to the air compared to the solution volume.

To enable ellipsometric observation of the passive film over longer time periods than one hour the reduction in pH and consequent breakdown of the film must be prevented. There are several methods by which this may be achieved:

1. Use a larger volume of solution.
2. Constantly replenish the solution or replace after each hour.
3. Use a buffered solution.
4. Use a blanket of an inert gas such as nitrogen to prevent carbon dioxide adsorption.

The latter two methods were investigated and the results are given in table 5.2 for the changes in pH over a 26 hour period for a solution buffered using a phosphate solution (50 cm^3 of 0.05 mol/dm^3 Na_2HPO_4 and 26.4 cm^3 of 0.1 mol/dm^3 NaOH[147]) and for a solution with a nitrogen blanket. The change in pH is less for the buffered solutions than it had been for those unbuffered but a significant decrease was still observable. In addition the presence of phosphate ions can inhibit the corrosion of magnesium in neutral solutions[177] and whilst another buffer solution composition could be utilized the additional ionic species present may still affect the corrosion rate.

Increasing the volume of the sample solution is impractical without redesigning the sample cell and to constantly replenish the system with a peristaltic pump is possible but may increase the noise level in the ellipsometric signal. The use of a nitrogen blanket however would appear to offer a satisfactory method for preventing the adsorption of carbon dioxide.

Table 5.1

The change in pH for various volumes of sodium hydroxide solution exposed to the air for 26 hours

Solution	Volume cm^3	Initial pH	Final pH	Change in pH
0.01 mol/dm^3 NaOH	10	11.917	8.023	3.894
0.01 mol/dm^3 NaOH	15	"	8.265	3.652
0.01 mol/dm^3 NaOH	20	"	9.583	2.334
0.01 mol/dm^3 NaOH + Mg (½ g disc)	10	"	9.915	2.002
0.01 mol/dm^3 NaOH + Magnox (½ g disc)	10	"	9.020	2.097

Table 5.2

The effect of a phosphate buffer and a nitrogen blanket on the reduction in pH

Solution	Initial pH	Final pH	Change in pH
10 cm^3 pH 12 buffer	12	9.812	2.188
20 cm^3 pH 12 buffer	12	10.677	1.333
10 cm^3 .01 mol/dm^3 NaOH under an N_2 blanket	11.958	11.903	0.053

5.2 Experiments conducted on magnesium and Magnox in air-saturated 0.01 mol/dm^3 sodium hydroxide under a nitrogen blanket.

5.2.1 The effect of a nitrogen blanket and its removal on Magnox in air-saturated 0.01 mol/dm^3 sodium hydroxide solution

The ability of a nitrogen blanket to prevent carbon dioxide adsorption and the effect of this on Δ and Ψ was examined by sealing the cell with polythene bags, as described in Chapter Four, and maintaining a nitrogen blanket above the sample solution. After 6.2 hours air was admitted and Δ and Ψ monitored for a further 6 hours.

The results, figs. 5.22 and 5.23, show that the behaviour during the first 10 hours is similar to that in fig. 5.7, i.e. indicative of a non-absorbing film growing on a smooth metallic substrate. There is a reduction in Ψ noticeable after about 10½ hours from the start of the experiment and about 4½ hours after the admission of air into the cell. After 12.5 hours small black pits are visible on the surface indicating the breakdown of passivity.

This experiment illustrates the effectiveness of a nitrogen blanket in preventing the breakdown of the passive film formed on Magnox and also the link between the decrease in Ψ and this breakdown.

5.2.2 Magnox held at -0.5 V vs rhe in air-saturated 0.01 mol/dm^3 sodium hydroxide under a nitrogen blanket

On admission of the solution to the cell there is an initial sharp decrease in Δ of several degrees accompanied by an increase of Ψ of ~1° followed by a more gradual increase in both Δ and Ψ, figs. 5.24a,b,c. The electrode appears bright under these conditions with no visible film.

A trial and error method was used to obtain the best possible fit between theory and experiment using a single film model, fig. 5.25, which although it poorly predicts the later behaviour gives information on the rate of growth of the corrosion film, its changes with time, and an idea of its porosity. The departure from the theoretical curve may be due to surface roughness of either the film/substrate or film solution interfaces, inhomogeneities in the film such as the presence of voids or a variation in refractive index through the film.

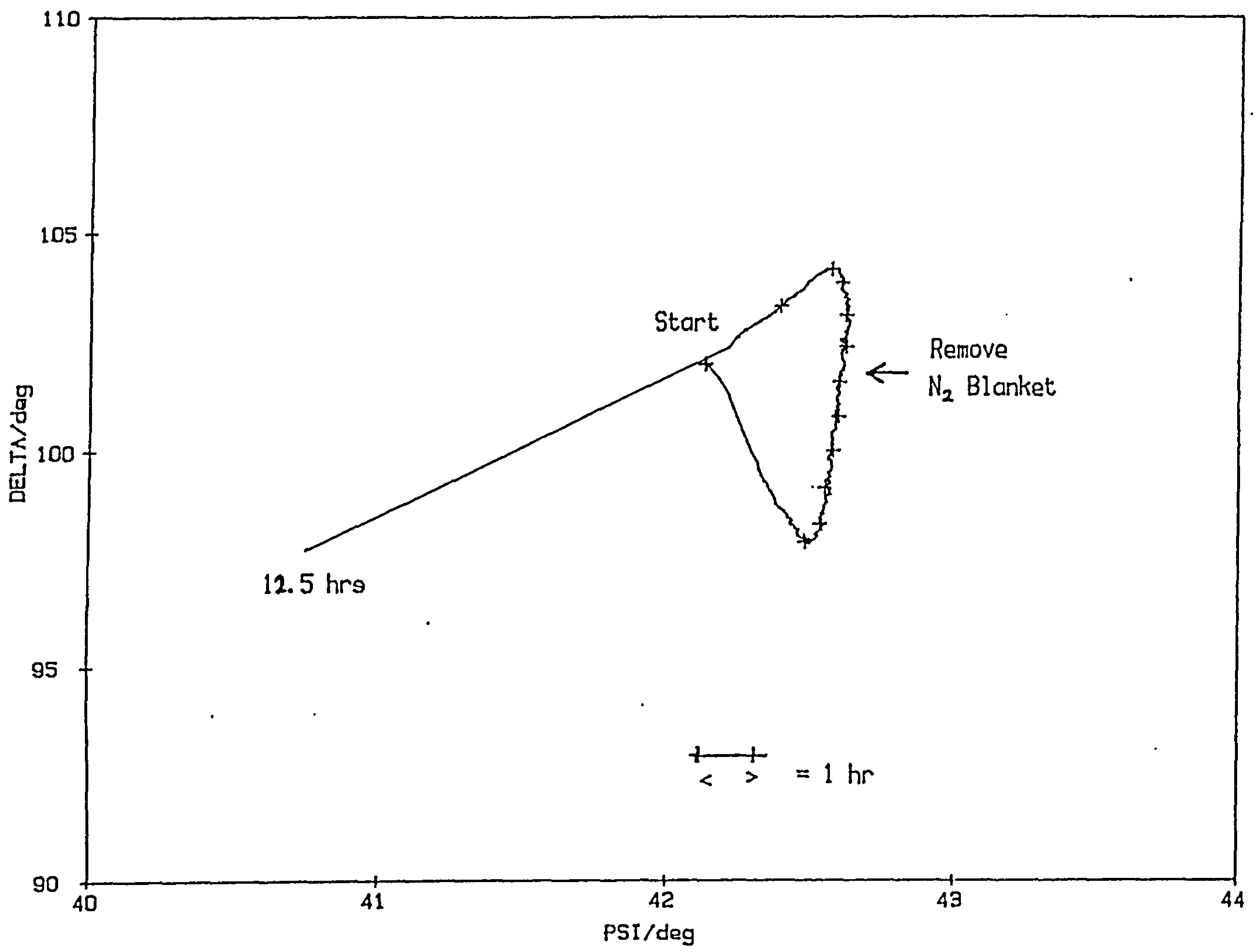

Fig. 5.22 The effect of a nitrogen blanket and its removal on Magnox in air-saturated 0.01 mol/dm3 NaOH

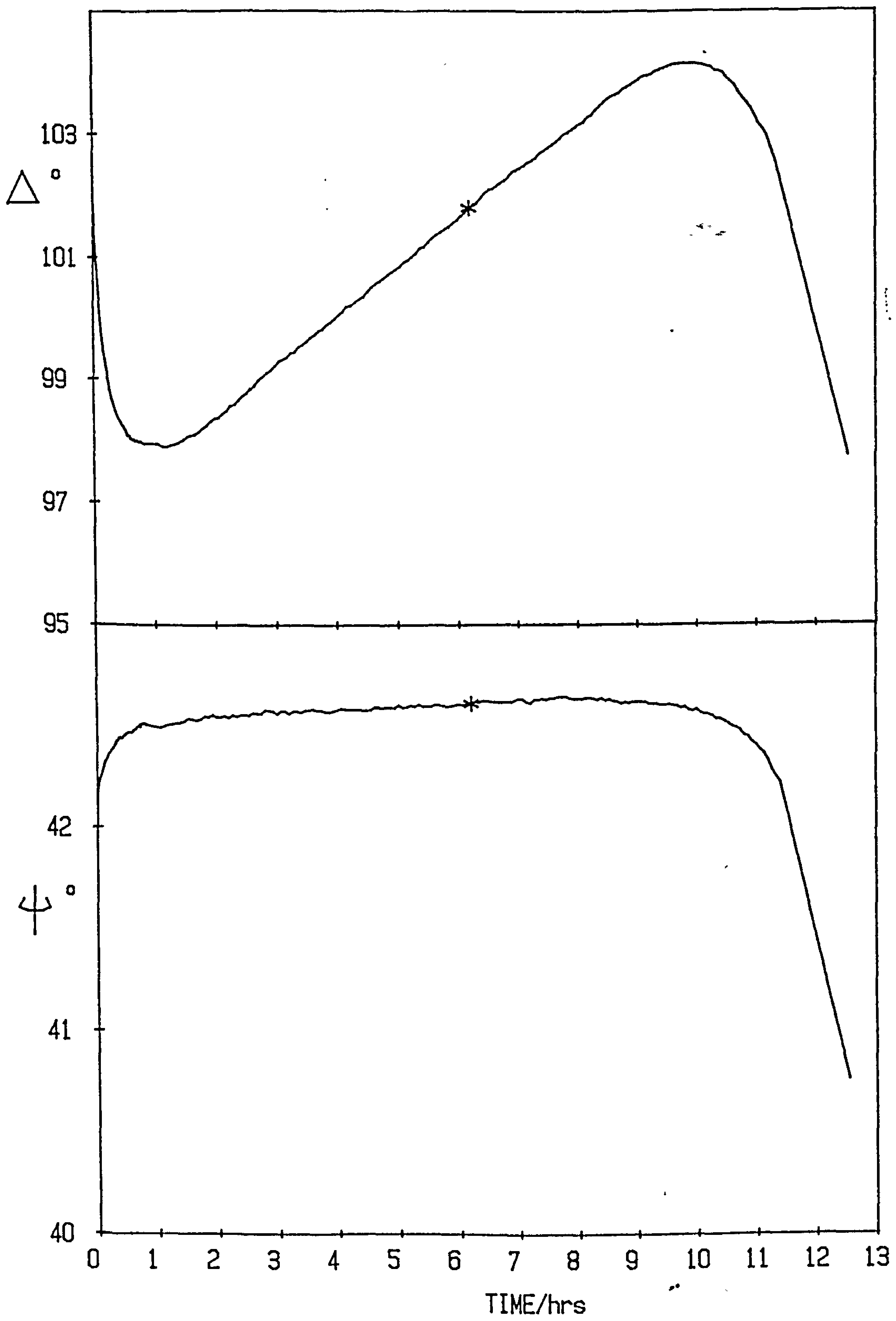

* = removal of nitrogen blanket

Fig. 5.23 The effect of removal of a nitrogen blanket on Magnox held at -0.5 V vs rhe in 0.01 mol/dm^3 NaOH

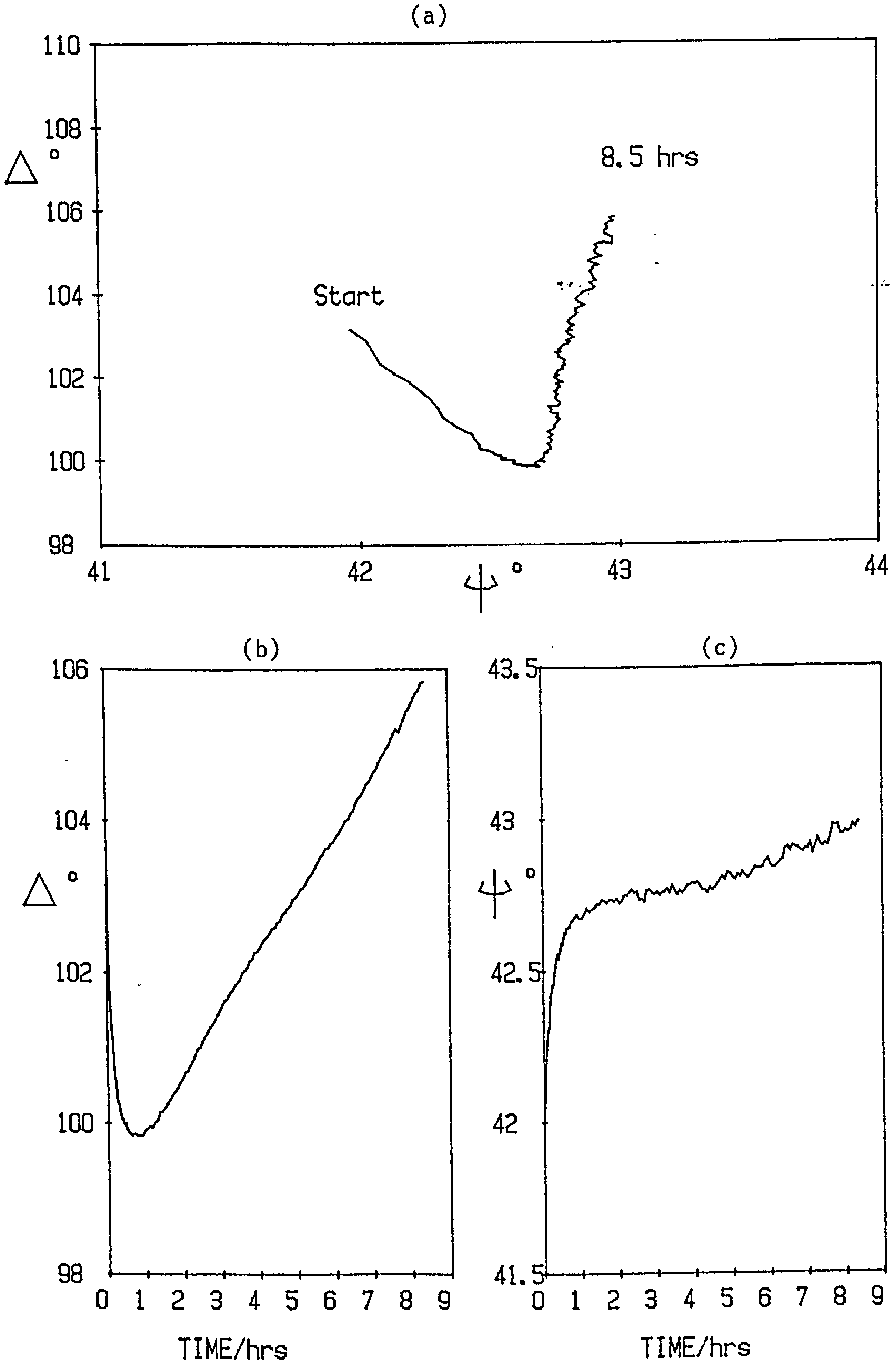

Fig. 5.24 Magnox held at -0.5 V vs rhe in air-saturated 0.01 mol/dm^3 NaOH under a nitrogen blanket

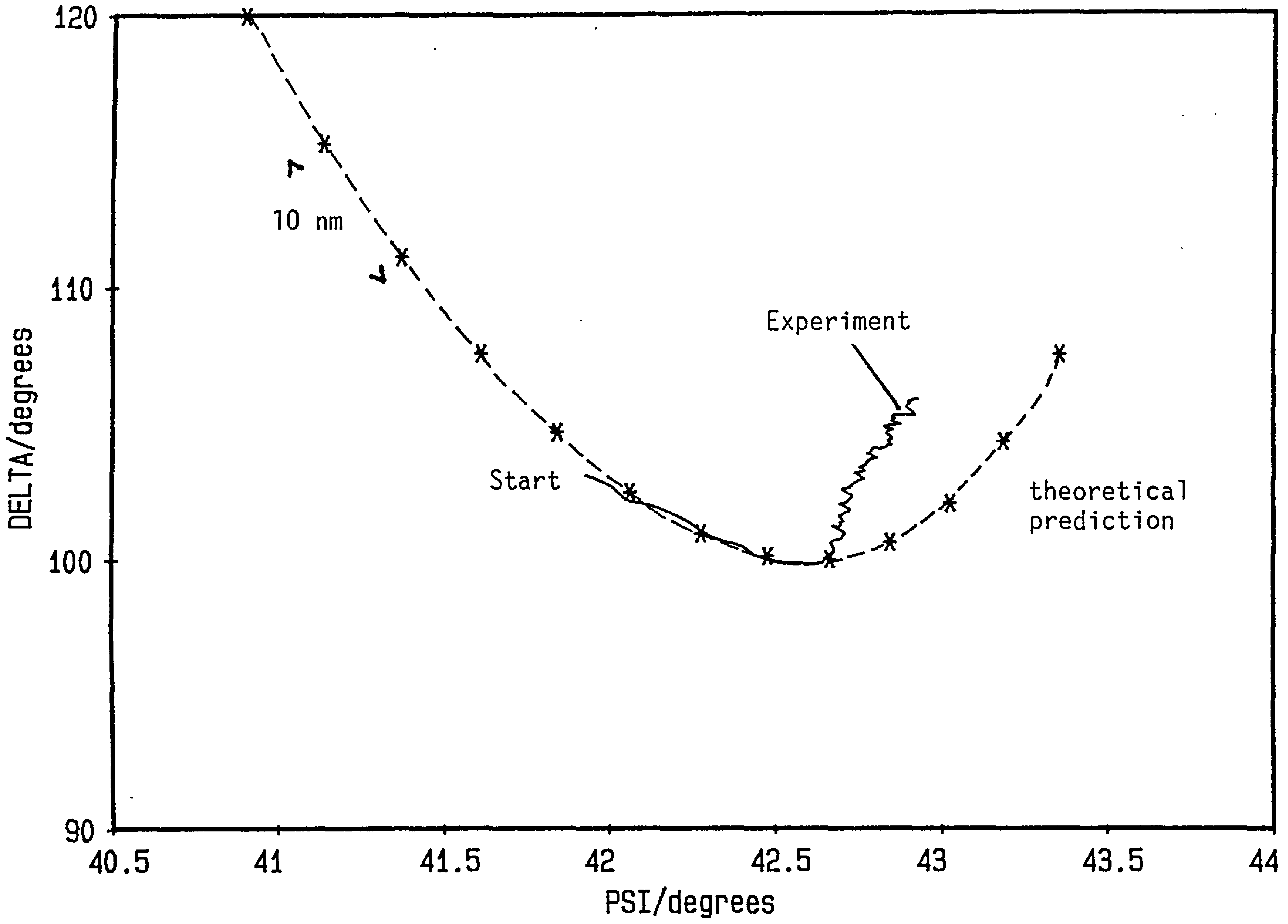

Fig. 5.25 Theoretical prediction using a single film model for a non-absorbing film (n = 1.47) growing on Magnox (n = 0.995, k = 5.71)

There would appear to be about 45 nm of film present when the first experimental point is taken assuming that the bulk of the film had a refractive index, n, of 1.47. This film grows rapidly to ca. 85 nm during the first hour and a half after which the rate slows down, becomes more irregular and departs from the prediction based on a single film model. This departure from the theoretical prediction makes an accurate estimation of film thickness at the end of the experiment impossible. However, a rough estimate of thickness of 100-120 nm can be surmised from a comparison with the theoretical plot in fig. 5.25.

An idea of the porosity of the film can be obtained if it is assumed that the bulk of the film is $Mg(OH)_2$. Taking the optical constants of brucite, Bruggeman's effective medium approximation (see Chapter Two) can be utilized to calculate the effect of voids in the film. This has been done for both solution-free and solution-filled voids, fig. 5.26. A film with a refractive index of 1.47 can then be seen to contain about 16% voids if they were solution-free or ca. 40% voids if they were solution-filled. This treatment is based on a homogeneous distribution of voids however and makes no allowance for inhomogeneities such as increased porosity near the surface of the film. The presence of a porous film does support the proposal made by other workers[49] that water permeates the film in the liquid phase rather than by transport of ions such as H_3O^+ or OH^- through the film.

The theoretical effect on the ellipsometric parameters, Δ and Ψ, of a barrier layer underneath this porous layer can be investigated by using a multi-film model, figs. 5.27 and 5.28, in which films of two different porosities have been grown on various thicknesses of an MgO layer. It has been observed experimentally that the minimum for Δ in the Δ,Ψ curve lies between 98 and 100° which indicates that for a bulk refractive index of 1.47 for the top film the thickness of the MgO layer has a maximum limit of ca. 5 nm whereas if the refractive index of the top film is taken as being 1.5 then this limit is increased to ca. 10 nm. This limit is considerably lower than that given by previous workers using ion beam techniques.[49]

A Magnox specimen, immersed in 0.01 mol/dm^3 NaOH for 6 hours, was analysed by SIMS and a sample under similar conditions for 10 hours was analysed using Auger electron spectroscopy by B.N.L., fig. 5.29.

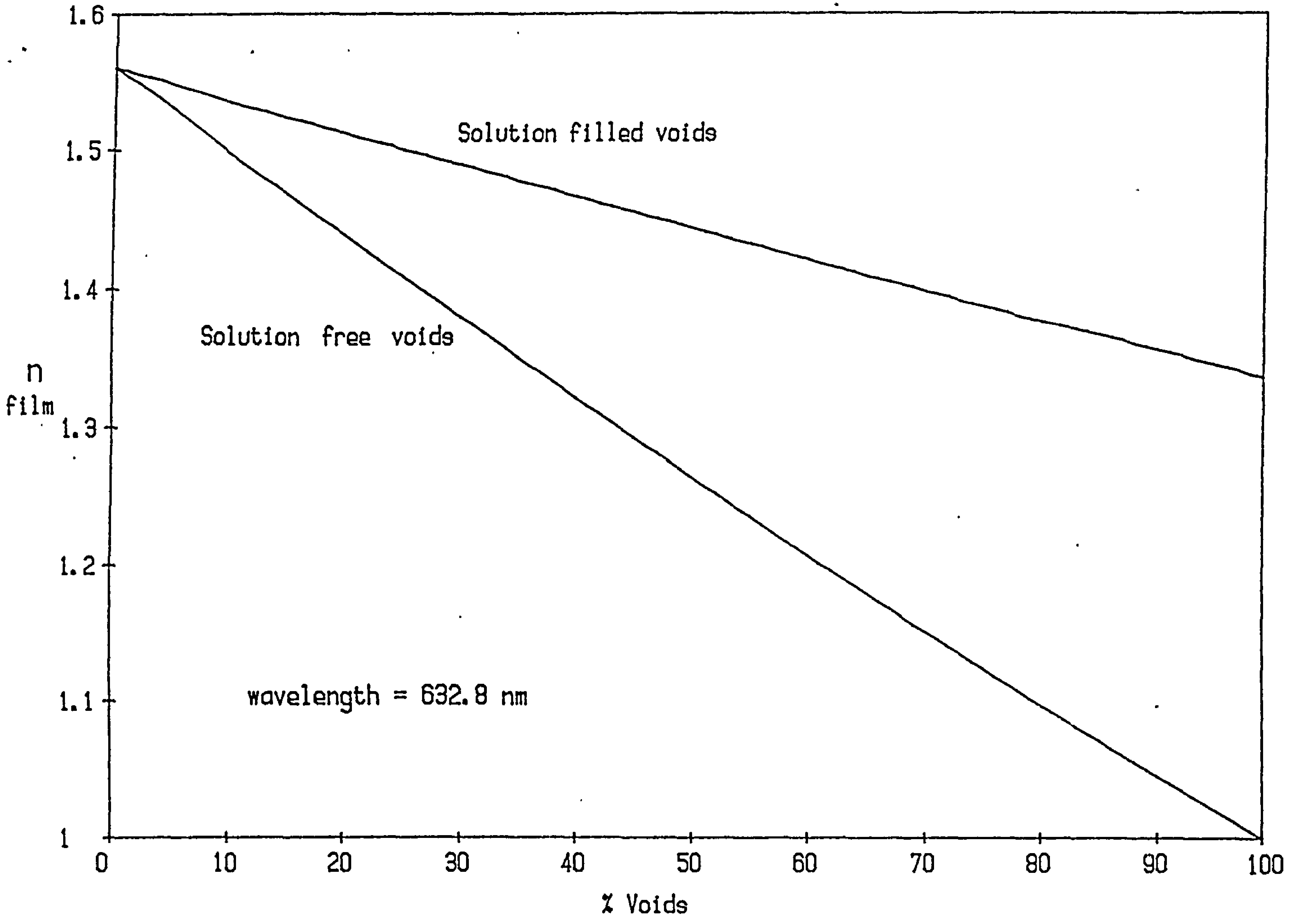

Fig. 5.26 The effect on refractive index of increasing the porosity of an $Mg(OH)_2$ film

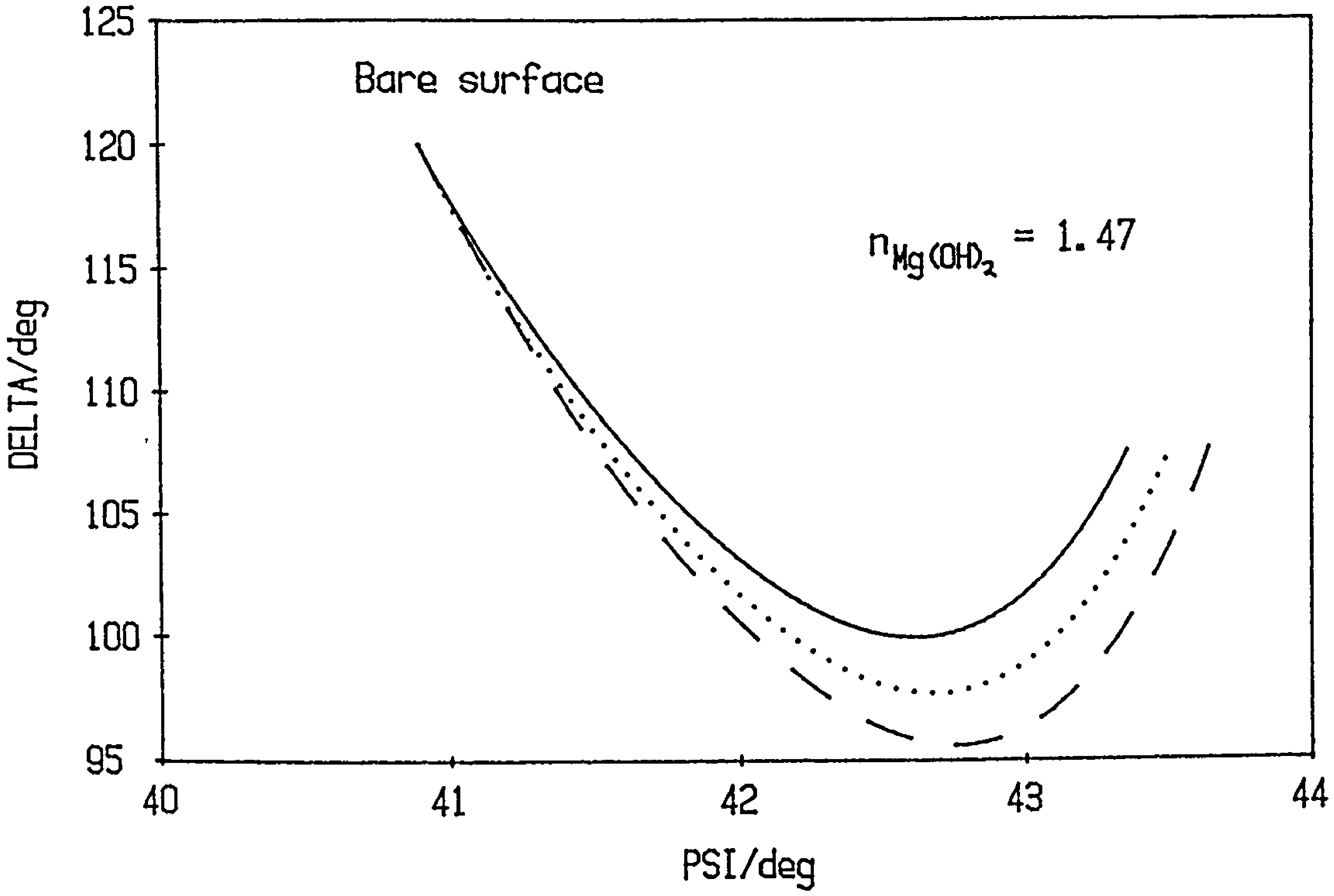

Fig. 5.27 The effect on delta and psi of an MgO layer between the $Mg(OH)_2$ film (n = 1.47) and the underlying substrate

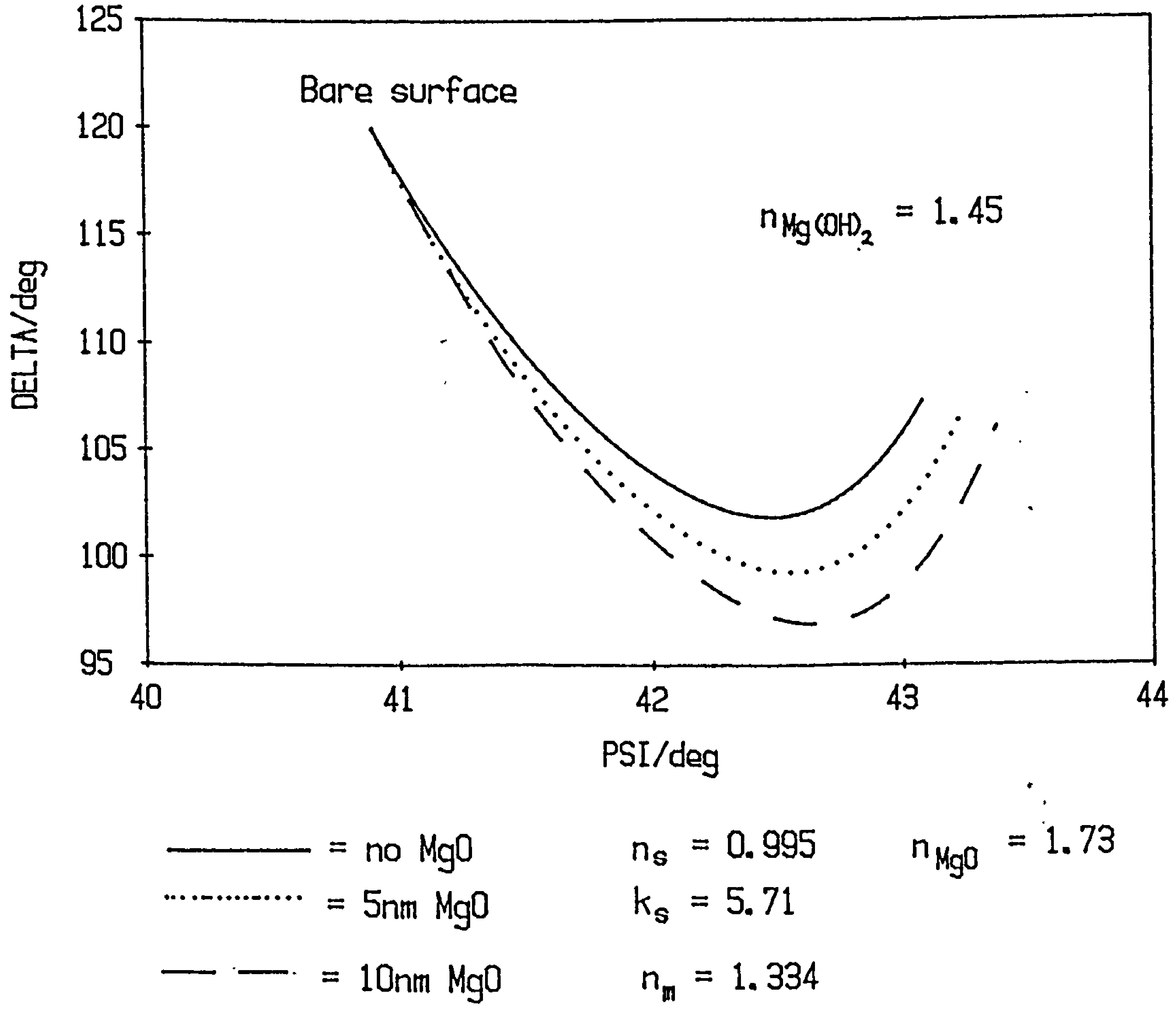

Fig. 5.28 The effect on delta and psi of an MgO layer between the $Mg(OH)_2$ film (n = 1.45) and the underlying substrate

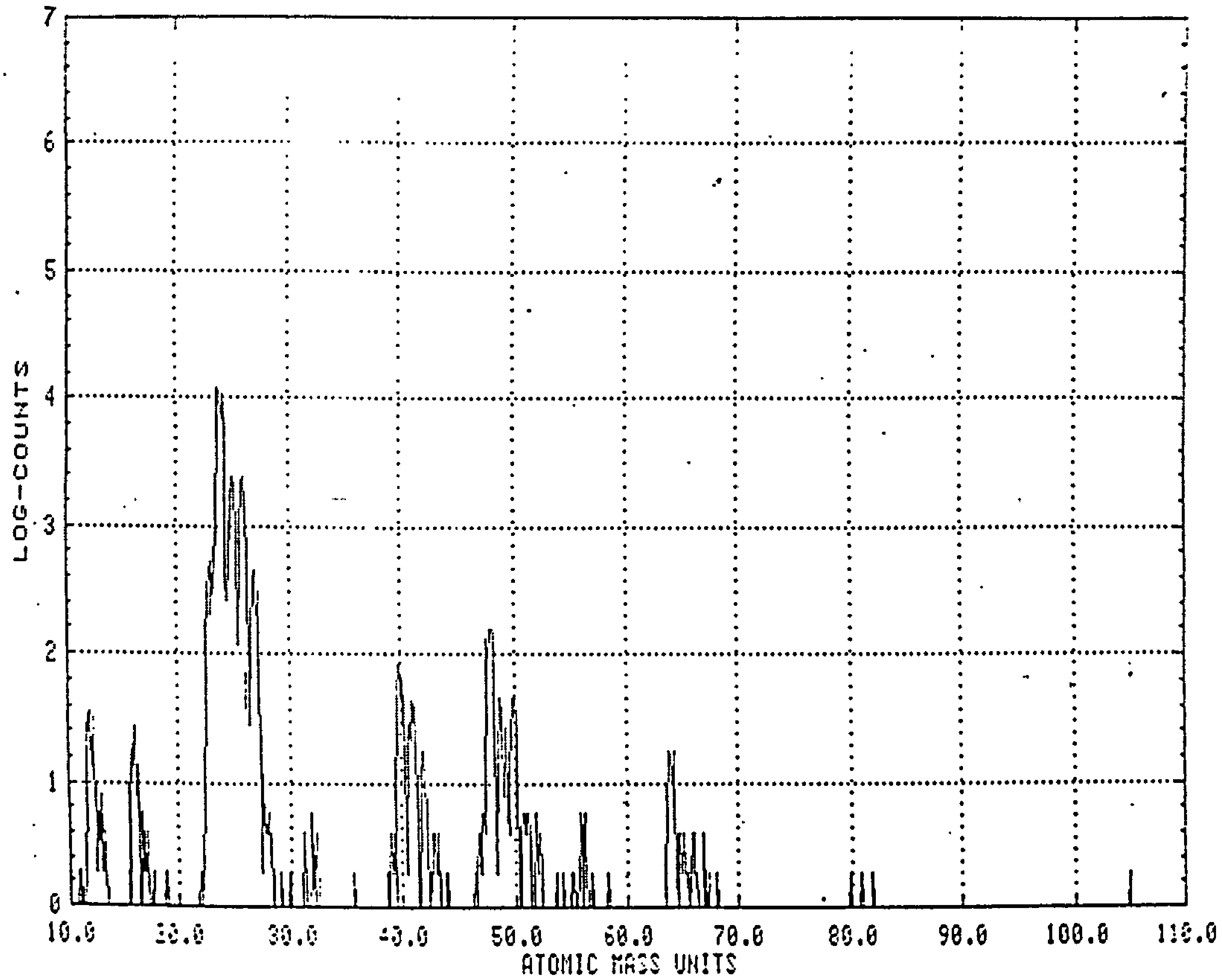

Fig. 5.29 Auger spectrum for Magnox immersed for 6 hours in 0.01 mol/dm^3 NaOH under a nitrogen blanket

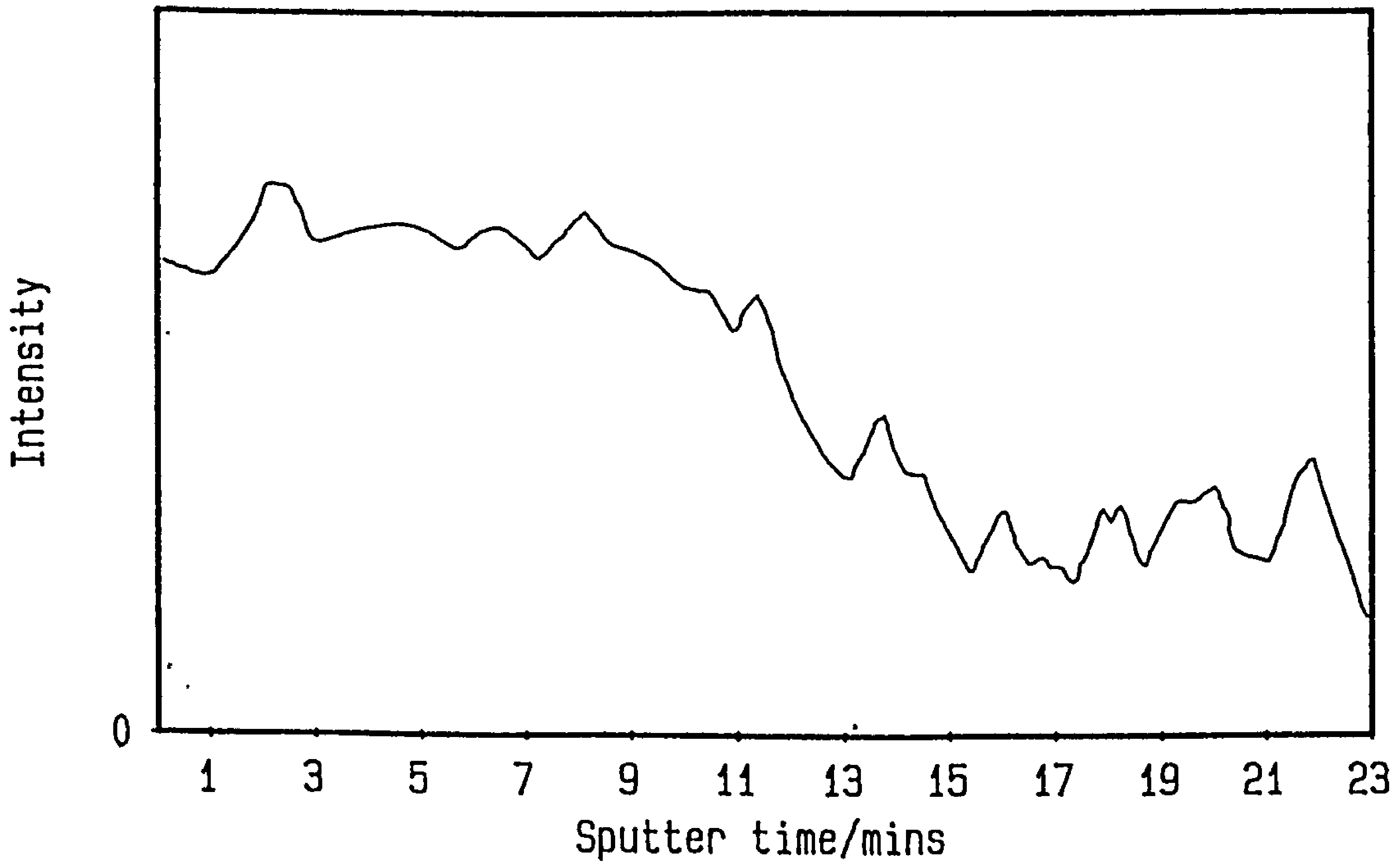

Fig. 5.30 Variation of Auger oxygen peak with depth for Magnox immersed for 6 hours in 0.01 mol/dm^3 NaOH under a nitrogen blanket

The latter technique yielded a value for the film thickness of ~ 113 ± 9 nm based on the sputter time at which the oxygen Auger peak had fallen to half its initial value, fig. 5.30. The SIMS analysis gave a film thickness of 150 nm ± 30 nm based on the Mg/O peak height ratio (fig. 5.31) which is higher than both the estimate from the A.E.S. analysis and from the SIMS analysis for Mg in section 5.1.3. It is possible that this just reflects random variation between samples however, and there was insufficient time available on the SIMS instrument to analyse more than one sample for each set of conditions.

A factor that may have also affected the SIMS results was the long period the sample remained in the UHV chamber under vacuum before analysis. This is reflected in the apparent partial dehydration of the film indicated by the sharply increasing OH^-/O^- ratio in the initial stages of sputtering. It may also explain the high concentration of carbon seen in the spectra as it is well known[178] that surfaces can become contaminated with carbon in UHV chambers due to the presence of carbon monoxide and carbon dioxide impurities within the chamber. This effect will be exacerbated by long periods within the chamber. Although it would be expected that the carbon layer would be concentrated in the surface layers of the surface, errors due to re-sampling and re-implanting could cause significant concentrations of carbon to be present in the mass spectra throughout the depth profile.

Apart from giving an indication of the film depth, the fairly sharp transition in the Mg/O peak height ratio, and the plateau after the sharp rise, indicates a better defined interface between the substrate and the film than was the case for Magnox in section 5.1.2. The resolution of the instrument was insufficient however to detect whether or not there is a layer of MgO beneath the corrosion film.

Aluminium is concentrated in the top layers of the film, with its concentration showing a marked decrease with sputtering time, fig. 5.32. This again probably reflects the surface enhancement of aluminium found for the polished and etched samples in Chapter Four.

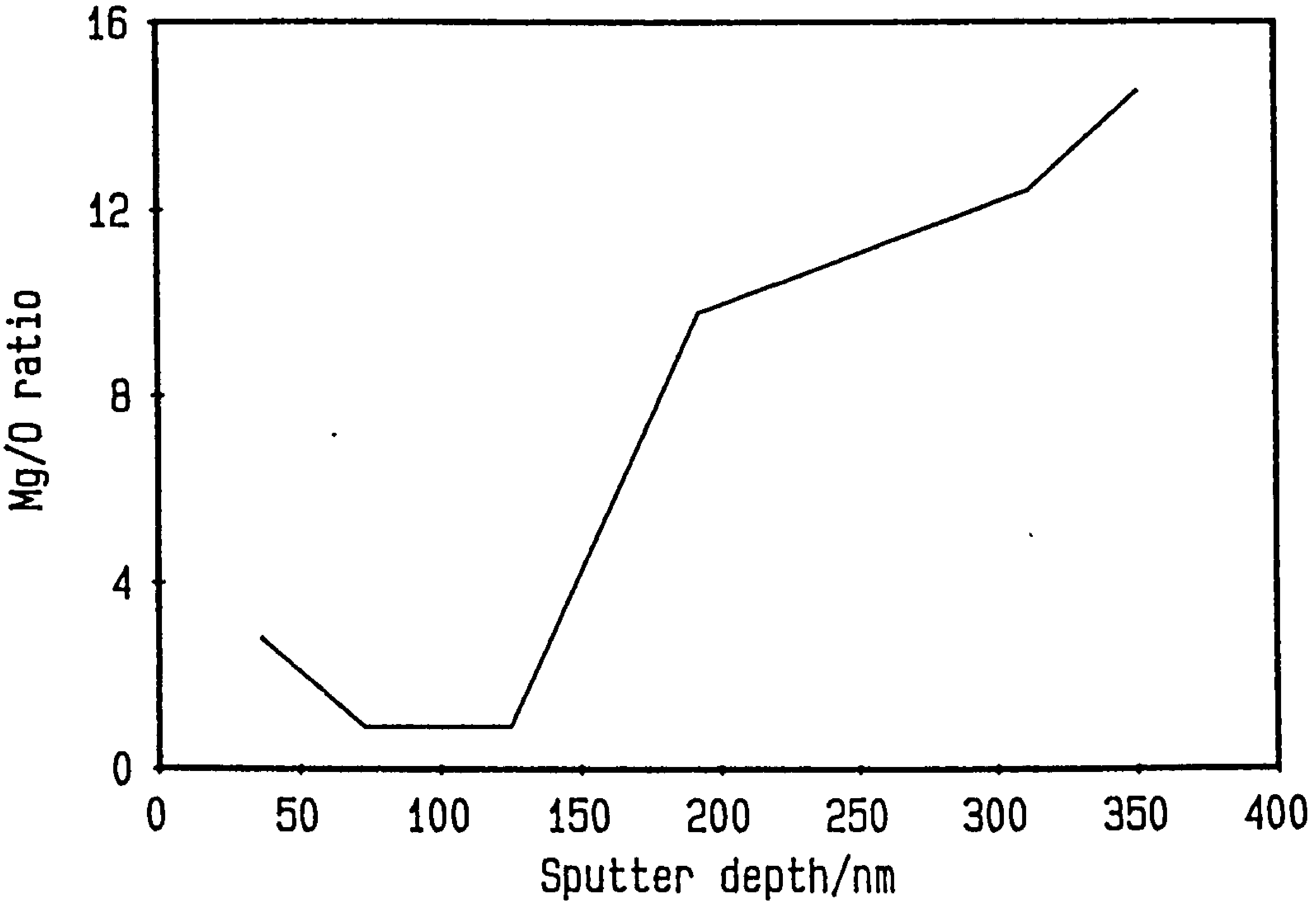

Fig. 5.31 Variation of Mg/O ratio with depth for a Magnox specimen immersed in 0.01 mol/dm^3 NaOH under a nitrogen blanket

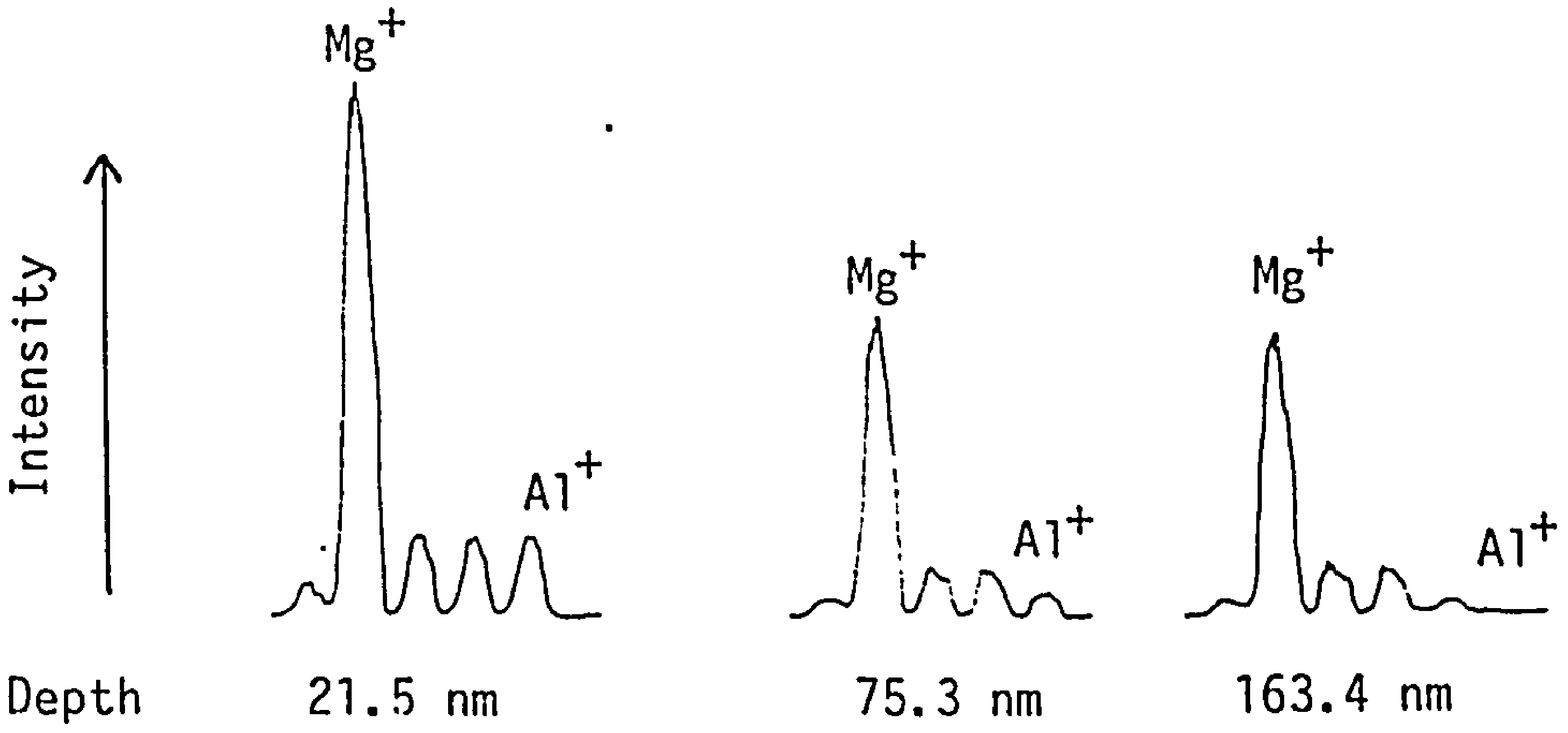

Fig. 5.32 Reduction with aluminium peak with depth sputtered for a Magnox specimen immersed in 0.01 mol/dm^3 NaOH under a nitrogen blanket

5.2.3 Magnesium in air-saturated 0.01 mol/dm^3 sodium hydroxide under a nitrogen blanket

An identical experiment was performed on magnesium as described for Magnox in the last section, figs. 5.33 and 5.34. That the nitrogen blanket was effective in maintaining the pH above 11.5 was confirmed by the value for the pH of 11.93 found at the end of the experiment i.e. after 5½ hours. The appearance of the electrode was dull with a white film visible on removal from the solution and subsequent drying.

The SIMS results, figs. 5.35 and 5.36, for a sample under the same conditions for 6 hours again show the presence of carbon throughout the film at similar concentrations to that found for Mg specimens in solutions open to the air. This may arise from carbon dioxide present in the air-saturated solutions or from carbon contamination in the UHV chamber.

The Mg/O peak height ratio, fig. 5.36, indicates a gradual transition from the oxygen rich environment of the outer film to the metal rich environment near the base of the film, which makes the estimate of the film thickness difficult. The film would appear to be of the order of 70 ± 20 nm thick however, which is less than that for the magnesium specimen for which the solution pH had fallen to below 11.5. It must be stressed that only the early stages of corrosion are being investigated here, as it has been reported[158] that initial oxidation proceeds more rapidly in Magnox alloys than in pure Mg.

In the light of the fact that passivity appears to have been maintained, (in contrast to the situation described in section 5.1.3), then the behaviour of Ψ needs explanation. Previously it has been stated that a decrease in Ψ can be expected on the basis of substrate roughening, a process which would seem feasible if conditions were such that local corrosion could occur. Such a mechanism, i.e. local corrosion leading to a pitting type attack, would seem less likely when passivity has been maintained however.

It is known that hexagonal close packed metals such as Be,[179,180] Ti[180] and Cd[180] display different interference colours on various surface grains and it has been suggested that this is due to epitaxy between the grain and the oxide resulting in oxide films of different orientations and growth rates. As magnesium is also on h.c.p. metal a similar effect may be postulated with differential growth rates on

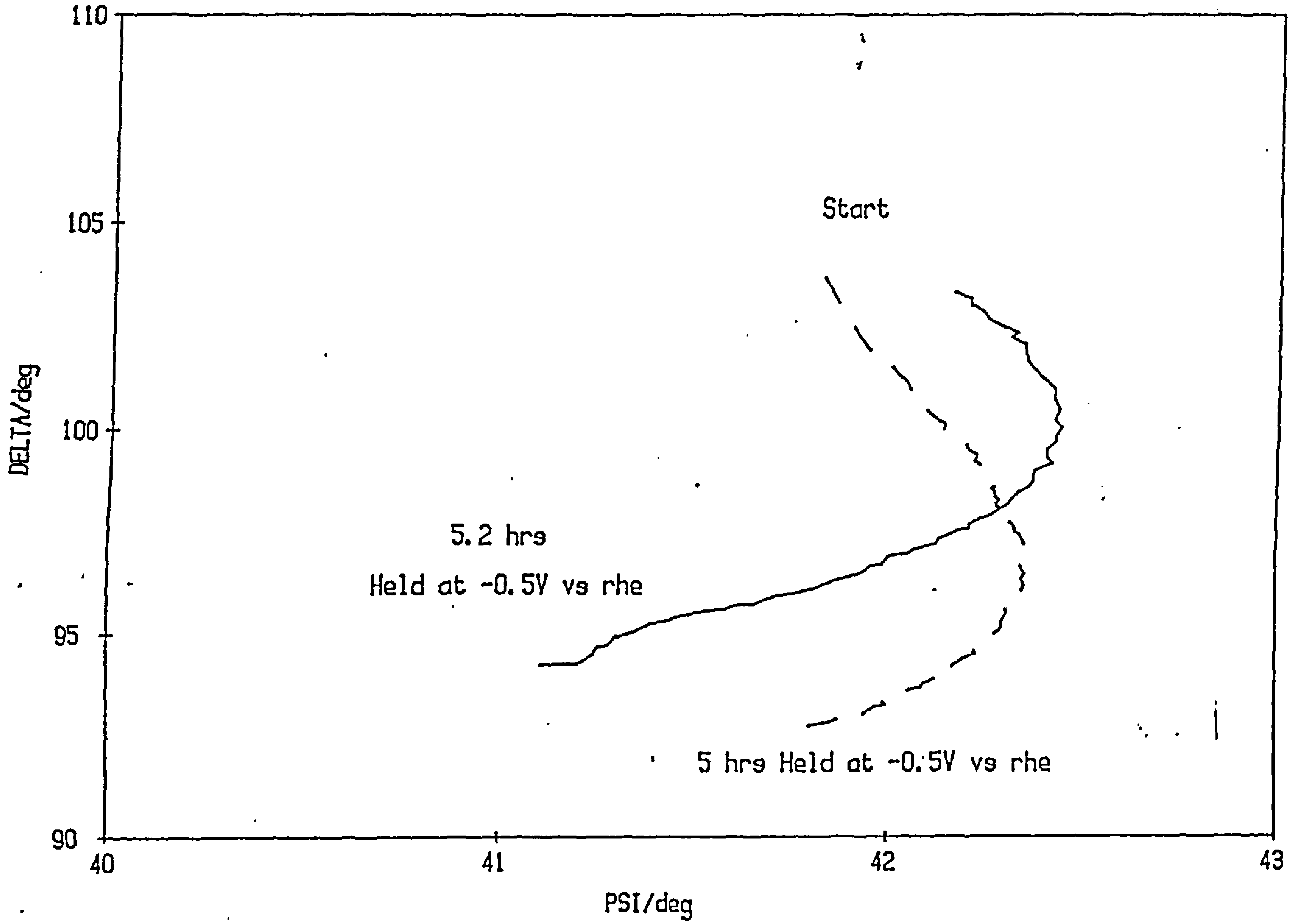

Fig. 5.33 The effect of a nitrogen blanket on magnesium in air-saturated 0.01 mol/dm^3 NaOH

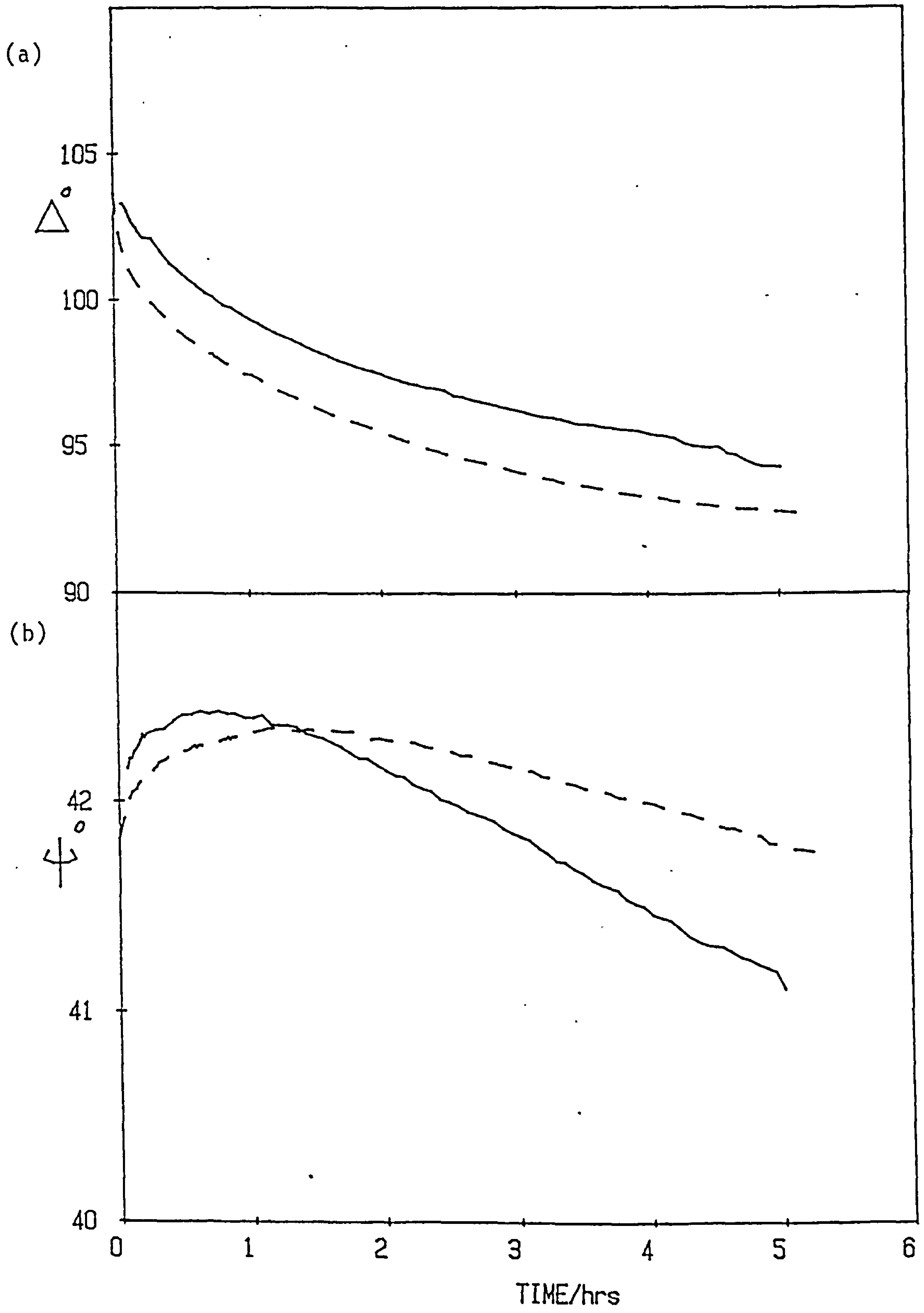

Fig. 5.34 The effect of a nitrogen blanket on Magnesium in air-saturated 0.01 mol/dm^3 NaOH

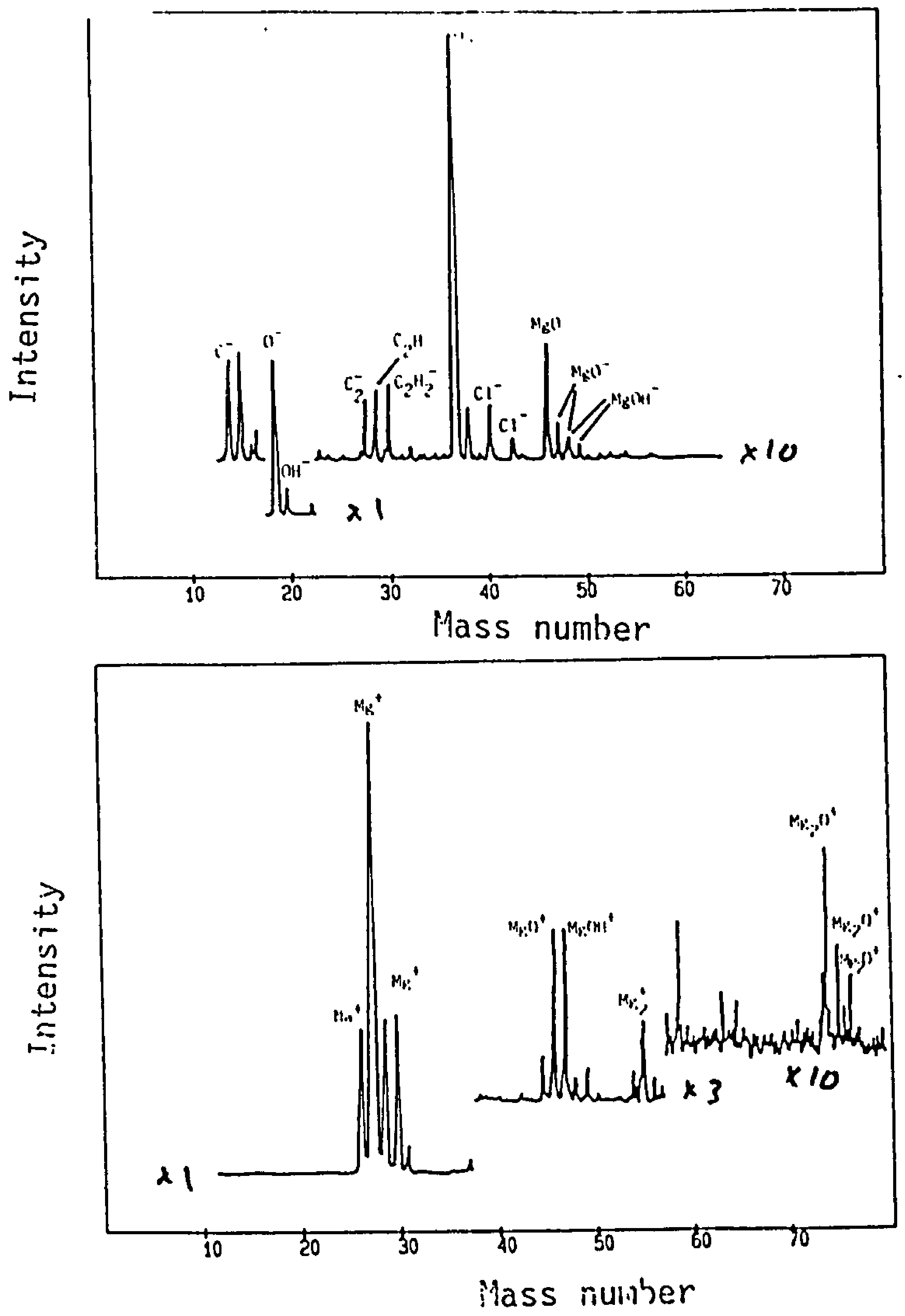

Fig. 5.35 Typical SIMS spectra for Mg after 6 hours immersion in 0.01 mol/dm^3 NaOH under a nitrogen blanket. Spectra taken after 17 nm of film has been sputtered.

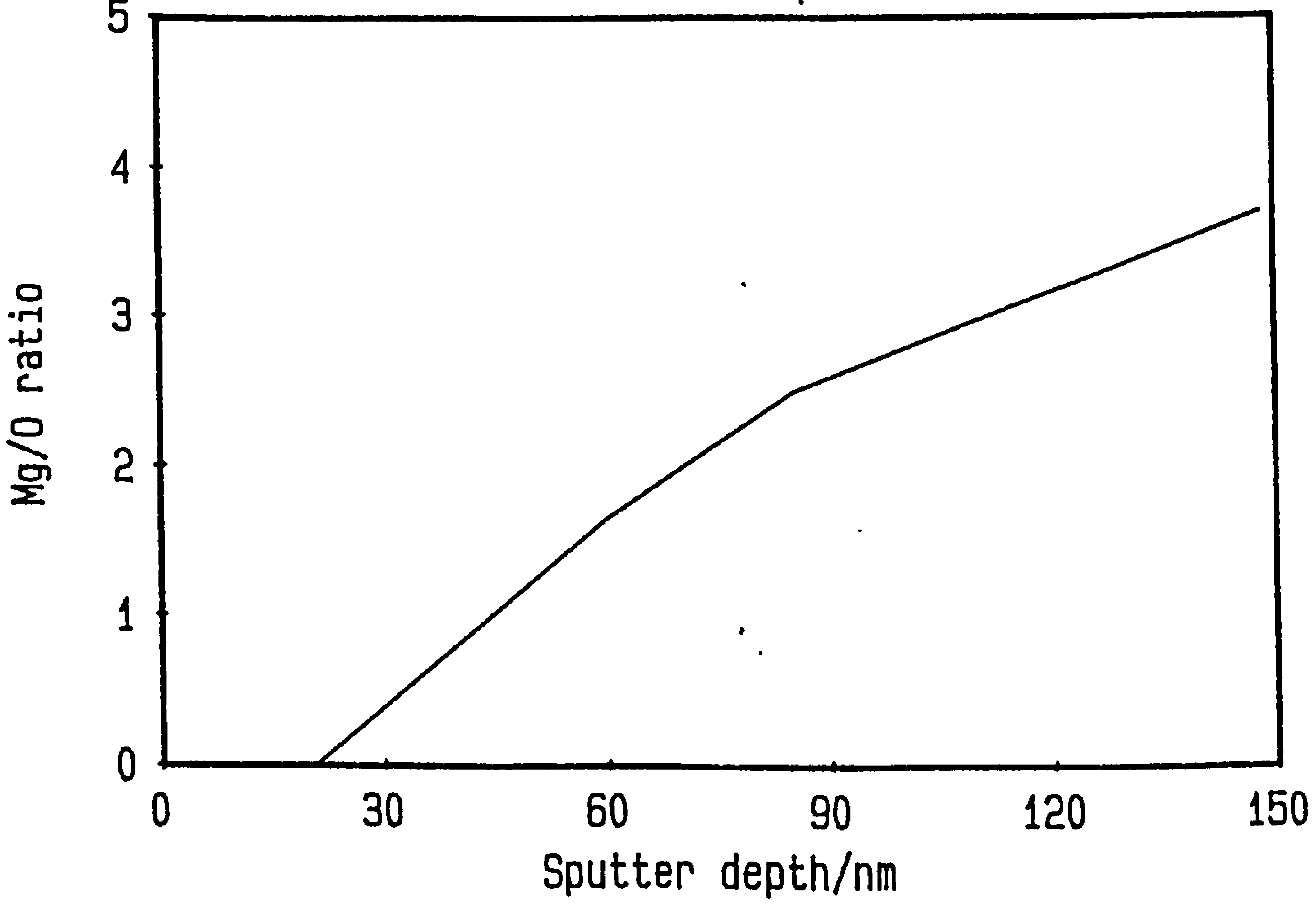

Fig. 5.36 Mg/O ratio from SIMS analysis of Mg after 6 hours immersion in 0.01 mol/dm^3 NaOH under a nitrogen blanket

adjacent grains giving rise to a rough surface. The correlation length of this roughness and hence the effect on Δ and Ψ will then depend upon the crystal grain size found in each metal. As Magnox has a larger grain size than Mg this may explain the different behaviour seen for Mg compared to Magnox.

The grain boundaries in Mg and Magnox were revealed by etching in 1½% citric acid at 60°C for 5 minutes and then examined under an optical microscope to reveal average grain sizes for Mg and Magnox of 15μ and 60μ respectively. Although the average grain size for Mg is only ¼ that for Magnox it is still large compared to the wavelength of the laser beam, 0.63μ, but it is possible that the smaller correlation length of a rough film formed on Mg due to epitaxial film growth would affect Ψ whereas the same film growth on Magnox would not.

The grain size in Mg can be increased by a factor of 2 to 30μ by annealing in argon at 500°C for 1½ hours but this is still less than the grain size in Magnox. It was decided that a better method would be to use a single crystal of Mg to test the hypothesis of a relationship between grain size and the effect of possible epitaxial film growth on the anomalous changes seen in Ψ.

5.2.4 Single crystal of magnesium in 0.01 mol/dm^3 sodium hydroxide solution under a nitrogen blanket

A single crystal of magnesium was obtained from Goodfellow Metals. The orientation of this crystal was unknown. However, it is differences in corrosion rates in differently orientated, adjacent grains that is being investigated rather than absolute corrosion rates on grains of a particular orientation. The crystal was polished and etched as before and immersed in 0.01 mol/dm^3 sodium hydroxide for 3 hours at -0.3 V vs rhe. The results in fig. 5.37 show a marked deviation in Ψ of about 1° after the first hour and a further 1° the next two hours. The significance of this result is discussed in the next section.

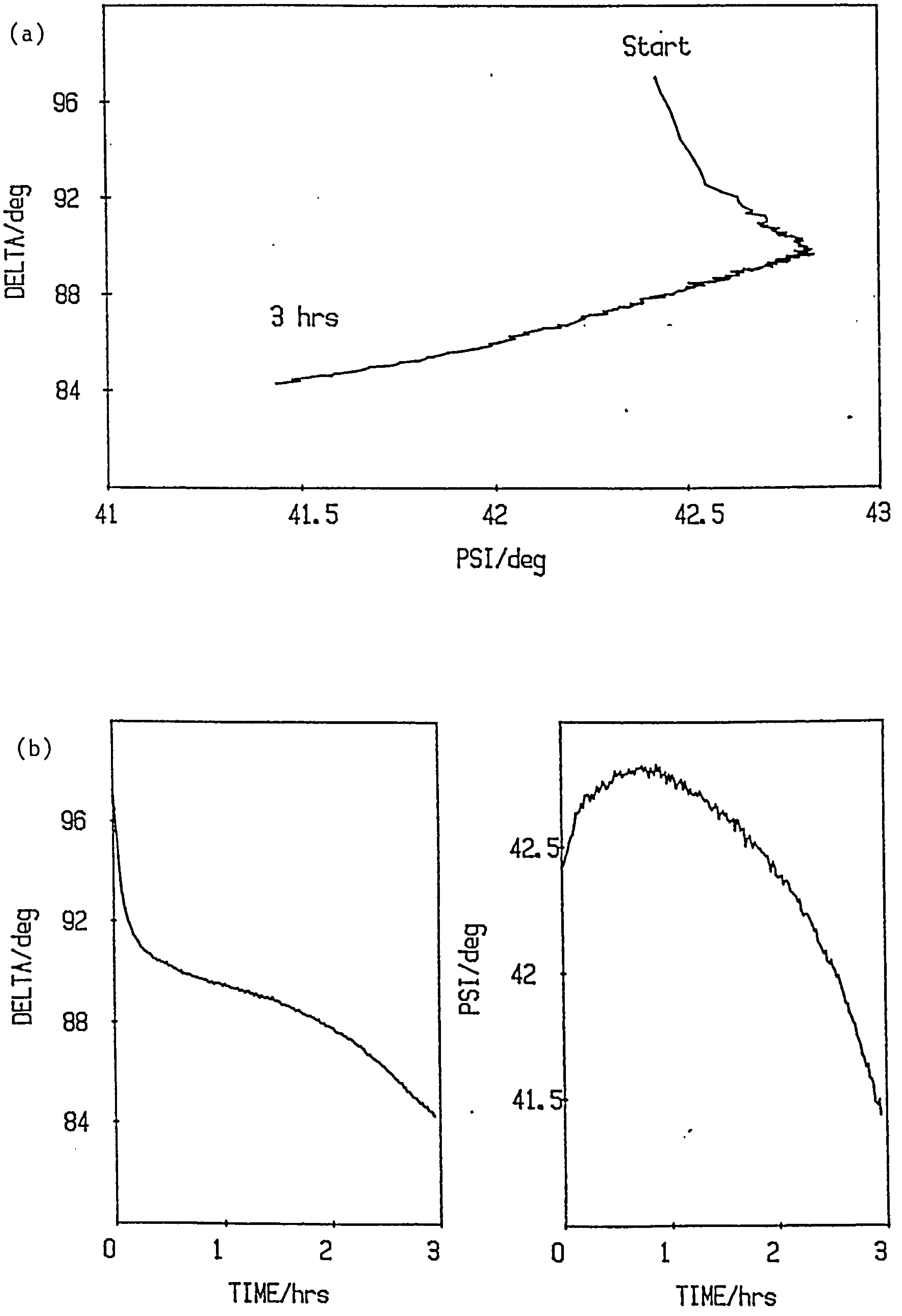

<u>Fig. 5.37</u> Single crystal of magnesium held at -0.3 V vs rhe in air-saturated 0.01 mol/dm^3 NaOH under a nitrogen blanket

5.2.5 Discussion of results for magnesium and Magnox specimens immersed in 0.01 mol/dm^3 NaOH under a nitrogen blanket

The use of a nitrogen blanket seems effective in preventing the breakdown of passivity of both Magnox and Mg as the pitting attack, evident on the surface of samples immersed in solutions where the pH has fallen below ~11, is absent. For Magnox this results in ellipsometric changes more characteristic of film growth than that seen previously but Mg still exhibits a combined drop in both Δ and Ψ with Ψ falling to values less than for the bare substrate.

This can be explained by a metallic type layer between the substrate and the overlying film as discussed previously, but none of the likely corrosion films, $Mg(OH)_2$, MgO and MgH_2, satisfy this criterion. A rough surface would also produce a fall in Ψ to below the value for a bare surface (fig. 2.17b) but the results in sections 5.7 and 5.8 indicate that this is not due to either a pitting type attack arising from a reduction in pH or from epitaxial film growth on differently orientated crystal grains. If roughening of the Mg substrate is affecting Ψ then the mechanism by which this is produced is unclear.

In view of the fact that the film formed during the oxidation of Magnox is more protective than that formed on Mg then a tentative suggestion is that corrosion is channelled through weak points in the corrosion film formed on Mg, and this leads to a roughening of the substrate.

5.3 Further experiments on Magnox and magnesium at open circuit and fixed potential in 0.01 mol/dm^3 sodium hydroxide

Further experiments were conducted at open circuit and fixed potential on these substrates in order to elucidate the effect of various inhibiting and depassivating ions, and also the effect of solution deoxygenation on the corrosion rate. These experiments were primarily aimed at studying the effect of these ions on the early stages of film growth using ellipsometry, but it was also hoped that further information could be obtained as regards the postulated rough substrate under certain conditions.

5.3.1 The effect of carbonate ions on the passive film formed on Magnox in sodium hydroxide solutions at pH > 11.5

The adsorption of carbon dioxide in alkaline solution causes both a reduction in pH through the removal of OH^- ions and the formation of carbonate ions. Although a lowering of the pH below about 11.5 can increase the corrosion rate of Magnox, it has also been reported[176] that the presence of CO_2 results in the formation of basic magnesium carbonates which have a higher solubility than magnesium hydroxide. If it is assumed that the passivity of Magnox is due to an insoluble film of $Mg(OH)_2$ then increasing the solubility of this film will result in a higher corrosion rate. The adsorption of carbon dioxide may play a more direct role in depassivation.

Which of these two mechanisms was primarily responsible for a loss of passivity was investigated by immersing a polished and etched Magnox specimen in 0.1 mol/dm^3 NaOH containing 0.05 mol/dm^3 of sodium hydrogen carbonate under a nitrogen blanket. A more concentrated solution of sodium hydroxide was used to maintain the pH above 11.5 due to the neutralizing effect of the bicarbonate ions:

$$HCO_3^- + OH^- \rightarrow CO_3^{2-} + H_2O \qquad \text{.....(5.2)}$$

From visual examination of the surface and the ellipsometric results, fig. 5.38, it would appear that passivity has been maintained which suggests that carbon dioxide causes depassivation by a reduction in pH rather than by the formation of carbonates in the film.

5.3.2 The effect of fluoride on the corrosion of Magnox in 0.01 mol/dm^3 NaOH

As discussed in Chapter One, dosing an aqueous solution with fluoride inhibits the long term corrosion of Magnox[49] possibly by incorporation of fluoride into the proposed barried layer in the form of a sub-micron oxy-fluoride layer. The effect of the addition of 1000 ppm F^- in the form of NaF on the corrosion of Magnox during the first few hours in air-saturated 0.01 mol/dm^3 NaOH under a nitrogen blanket was investigated ellipsometrically. The results in fig. 5.39 for the optical results indicate broadly similar behaviour to non-F^--dosed solutions, with a minimum in Δ of 98° suggesting that the fluoride

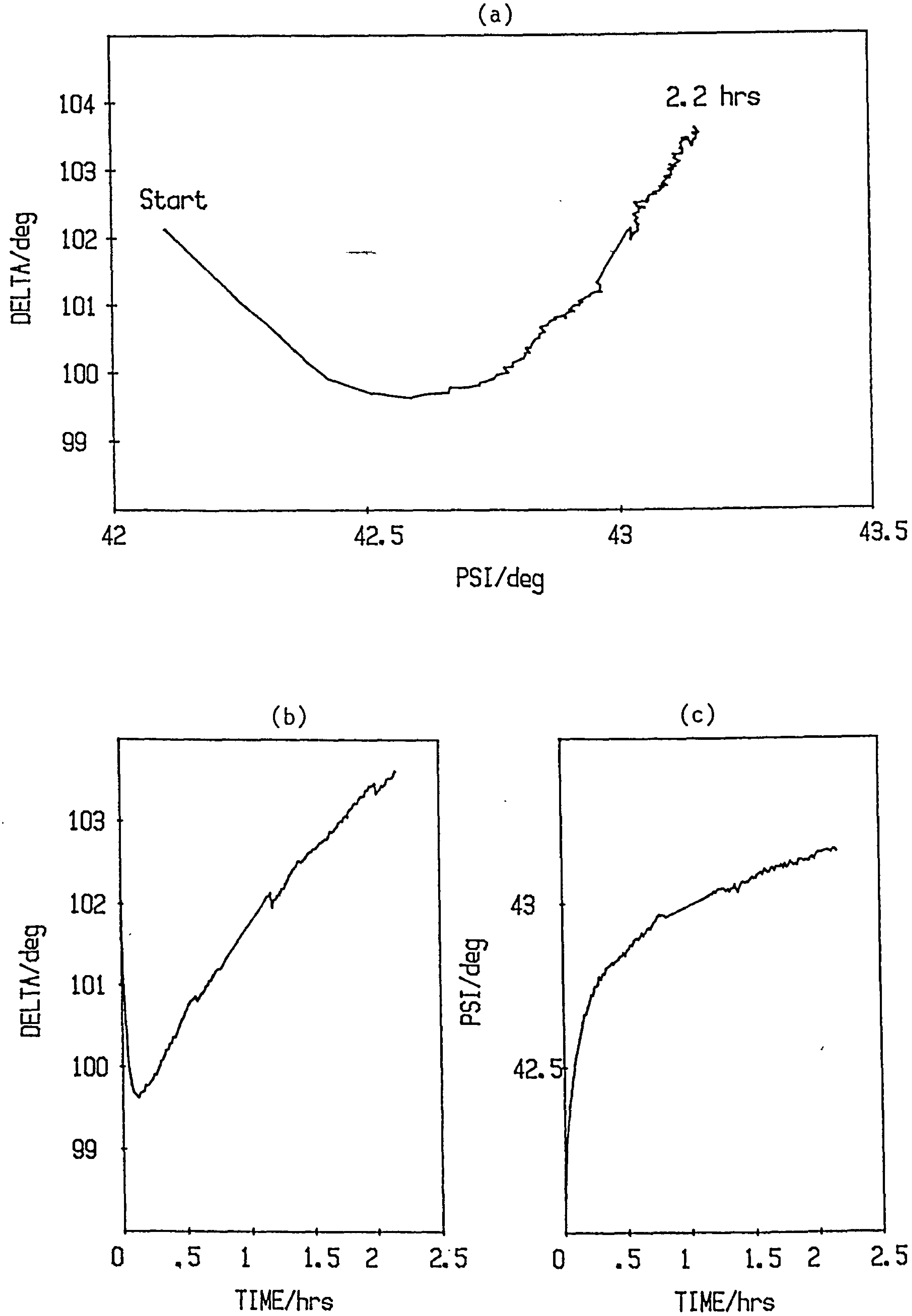

Fig. 5.38 Magnox in air-saturated 0.1 mol/dm^3 NaOH + 0.05 mol/dm^3 Na_2HCO_3 at open circuit under a nitrogen blanket

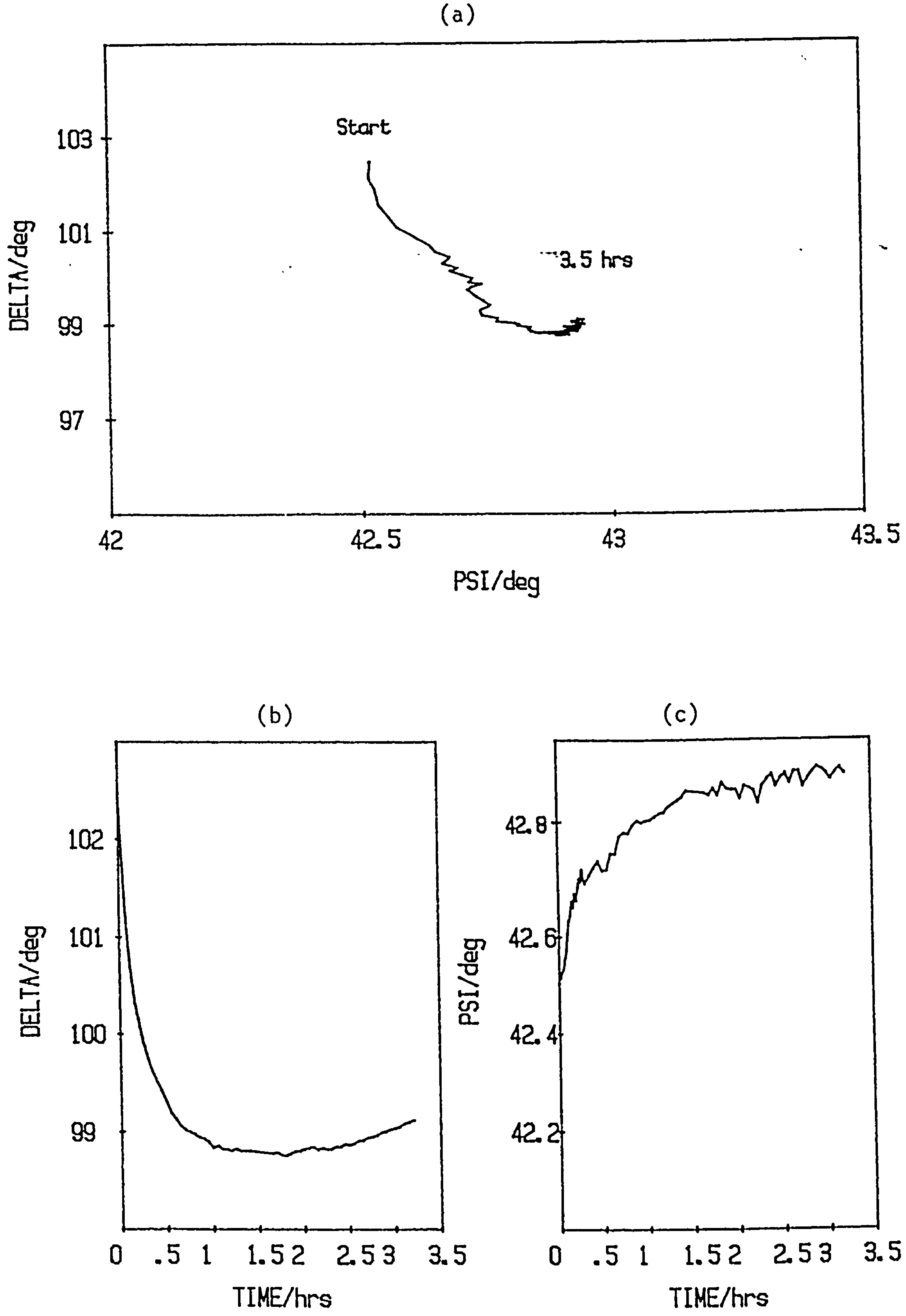

Fig. 5.39 The effect of fluoride (1000 ppm) on Magnox held at -0.5 V vs rhe in air-saturated 0.01 mol/dm^3 NaOH under a nitrogen blanket

has not modified the optical constants for the bulk corrosion film. This agrees with the proposal by Case et al.[49]

Although the initial corrosion rates are similar in both fluoride-dosed and fluoride-free solutions it would appear from the changes observed in Δ and Ψ that the corrosion rate is slower in the fluoride dosed solutions after the first half hour. In view of the similar bulk optical constants of the films, this supports the suggestion that fluoride may be incorporated into a thin film near the metal/oxide surface, with slow transport of ions through this controlling the corrosion rate.

5.3.3 The effect of solution deoxygenation on Magnox and magnesium in 0.01 mol/dm^3 sodium hydroxide

The effect of oxygen on the corrosion of both magnesium and Magnox has also been discussed in Chapter One. Although it has been stated that oxygen can strongly modify the reactions of the magnesium anode,[39] Blanchet[54] and Khalaf[56] have found that Magnox and Mg can still corrode in deoxygenated solutions.

A Magnox and magnesium sample were prepared as normal and briefly etched in a nitrogen atmosphere in situ. The previously N_2-saturated solution was admitted to the cell from a reservoir above, and a nitrogen blanket was maintained above the solution to reduce oxygen ingress. It was not possible to continually sparge the solution during the experiment as the bubbles would have scattered the light beam.

The results in figs. 5.40 and 5.41 indicate that there is little difference in behaviour for both Mg and Magnox, indicating that the reduction of oxygen to levels possible in the experimental arrangement used has not resulted in any apparent modification of the electrode processes.

5.3.4 Magnox in 0.01 mol/dm^3 sodium hydroxide solution with the addition of 1000 ppm chloride

The susceptibility of both magnesium and Magnox to severe localized corrosion in the presence of chloride ions has been widely reported as discussed in Chapter One. Ellipsometry is not an ideal method for

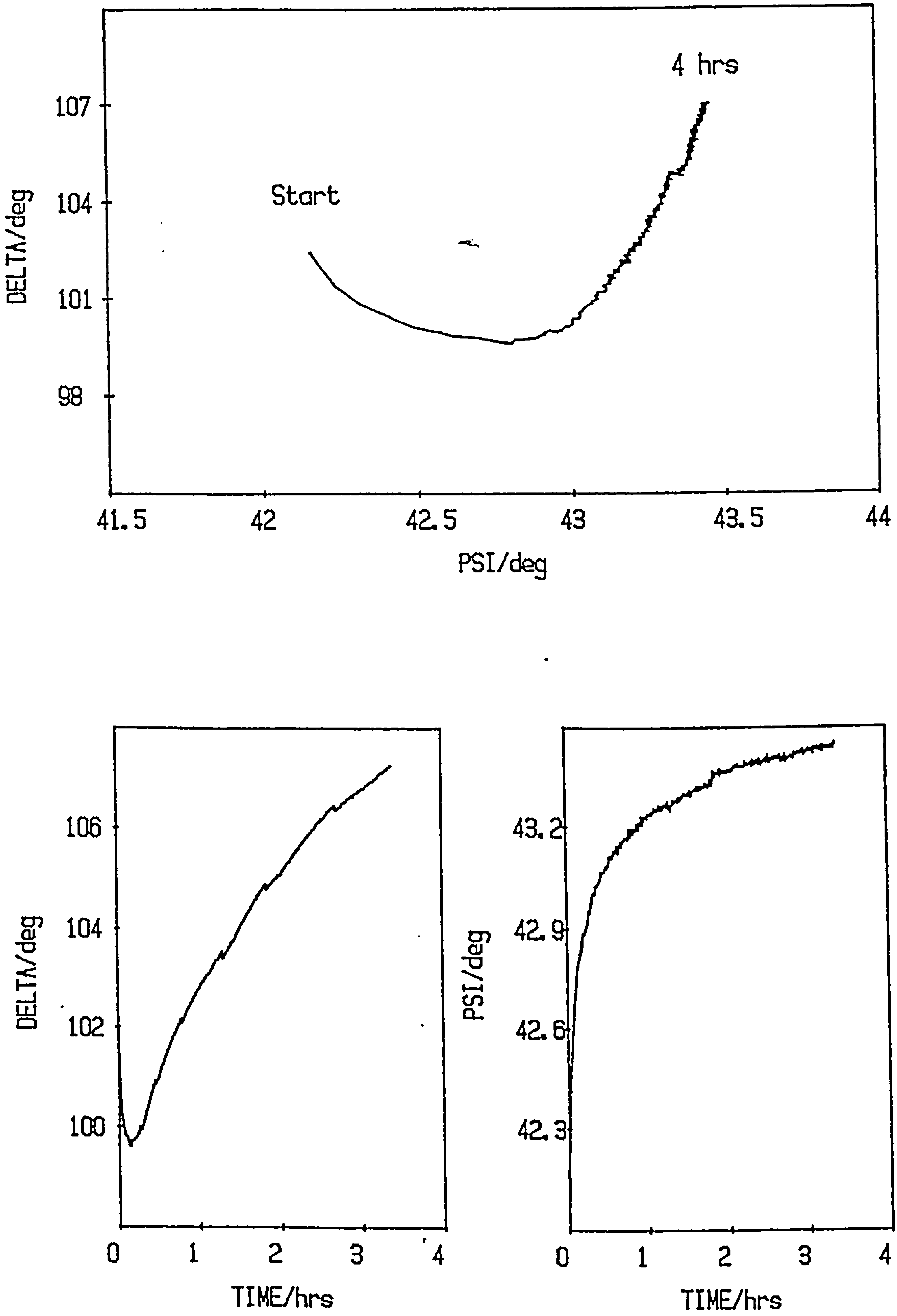

Fig. 5.40 Magnox at open circuit in nitrogen saturated $0.01\ \mathrm{mol/dm^3}$ NaOH

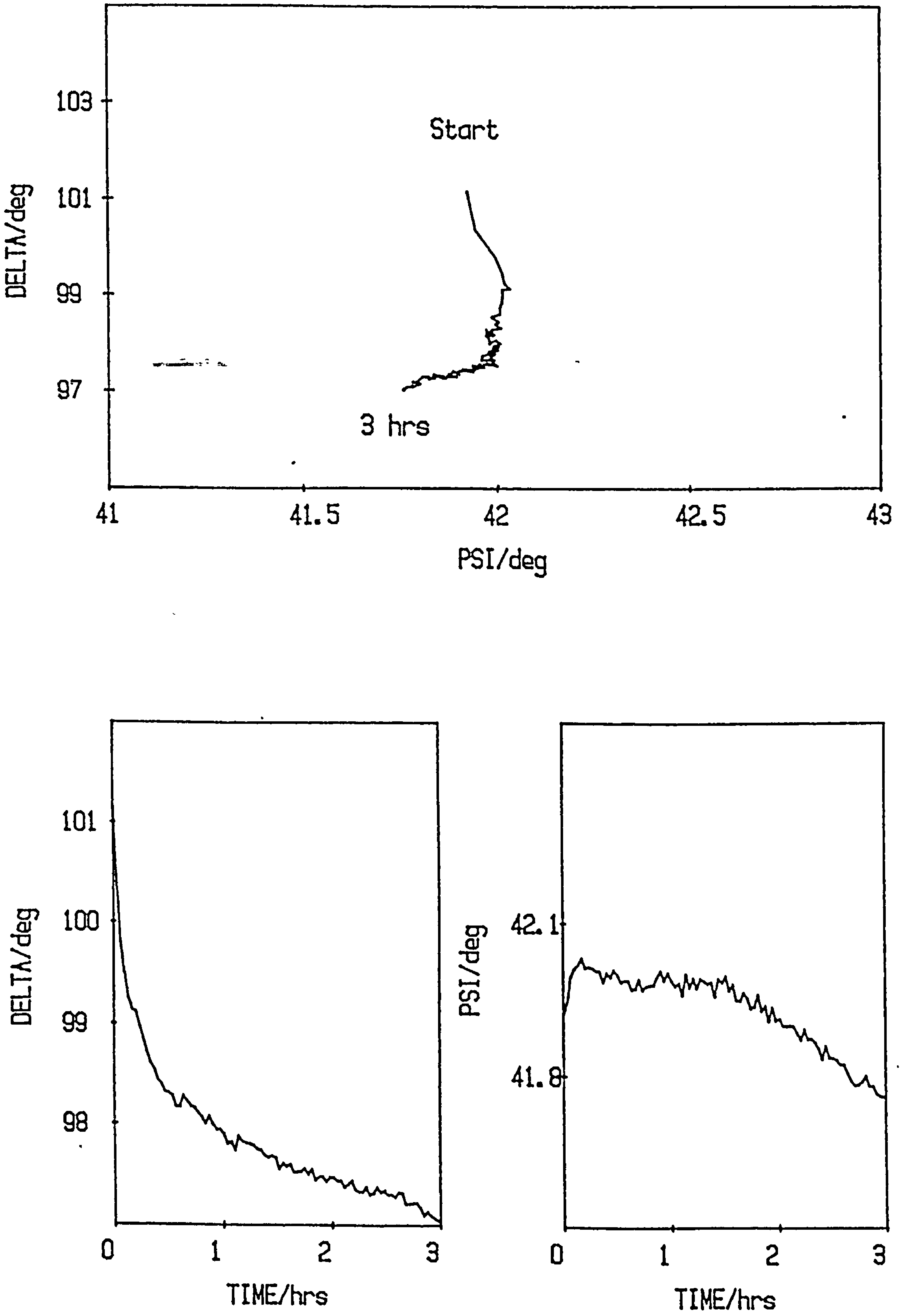

Fig. 5.41 Magnesium held at -0.5 V vs rhe in nitrogen saturated 0.01 mol/dm^3 NaOH

studying metal surfaces after pitting has been initiated, as corrosion may depend upon processes occurring within the pit,[181] with only slight changes to the bulk of the surface film. Substrate roughening may also occur which can cause problems in interpretation. It can however be a valuable tool for studying the initial stages of pit nucleation[73,74,77] which are not fully understood at present.[182,183] These experiments were undertaken to investigate whether there is any overall degradation of the film or whether it is purely local corrosion as it would be with bare metal.

A Magnox sample, polished and etched as before, was immersed in a 0.01 mol/dm^3 sodium hydroxide solution containing 1000 ppm Cl^- (2.25 g/dm^3 KCl), a level of Cl^- sufficient to cause spontaneous breakdown at the open circuit potential, and the ellipsometric parameters Δ and Ψ were recorded. Pitting was observed visually after an induction period of about 20 minutes in a region located away from the incident beam, and after a further 40 minutes had elapsed a white film was visible on the substrate near the epoxy mounting.

The results in fig. 5.42 indicate overall film growth was occurring in the region of the beam with the minimum for Δ in the Δ,Ψ curve being similar to previous values found in non-chloride dosed solutions. This indicates that the bulk optical constants and film thickness after 2 hours are similar for films grown under those differing conditions. Visible pitting however took place away from the region of the beam and when at the end of the experiment the beam was relocated near a pit the optical signal was lost due to scattering of the beam.

The random fluctuations of Ψ are particularly interesting and may be related to the potential fluctuations seen by several authors[183,184,185] and attributed to crack-heal processes. It is known[110] that Ψ is particularly sensitive to film roughness compared to Δ, and it may be postulated that these fluctuations are due to bare metal being transiently exposed at the base of flaws or defects which is in accord with modern theories of pitting.[182] The fluctuations occur immediately on immersion in the presence of 1000 ppm Cl^-, a feature also observed on other metals using noise analysis[182] and supporting the hypothesis of continuous crack healing processes.[186] The induction time before pitting has been measured by other techniques and is considered to be due to the time taken before a pit has survived long enough to become

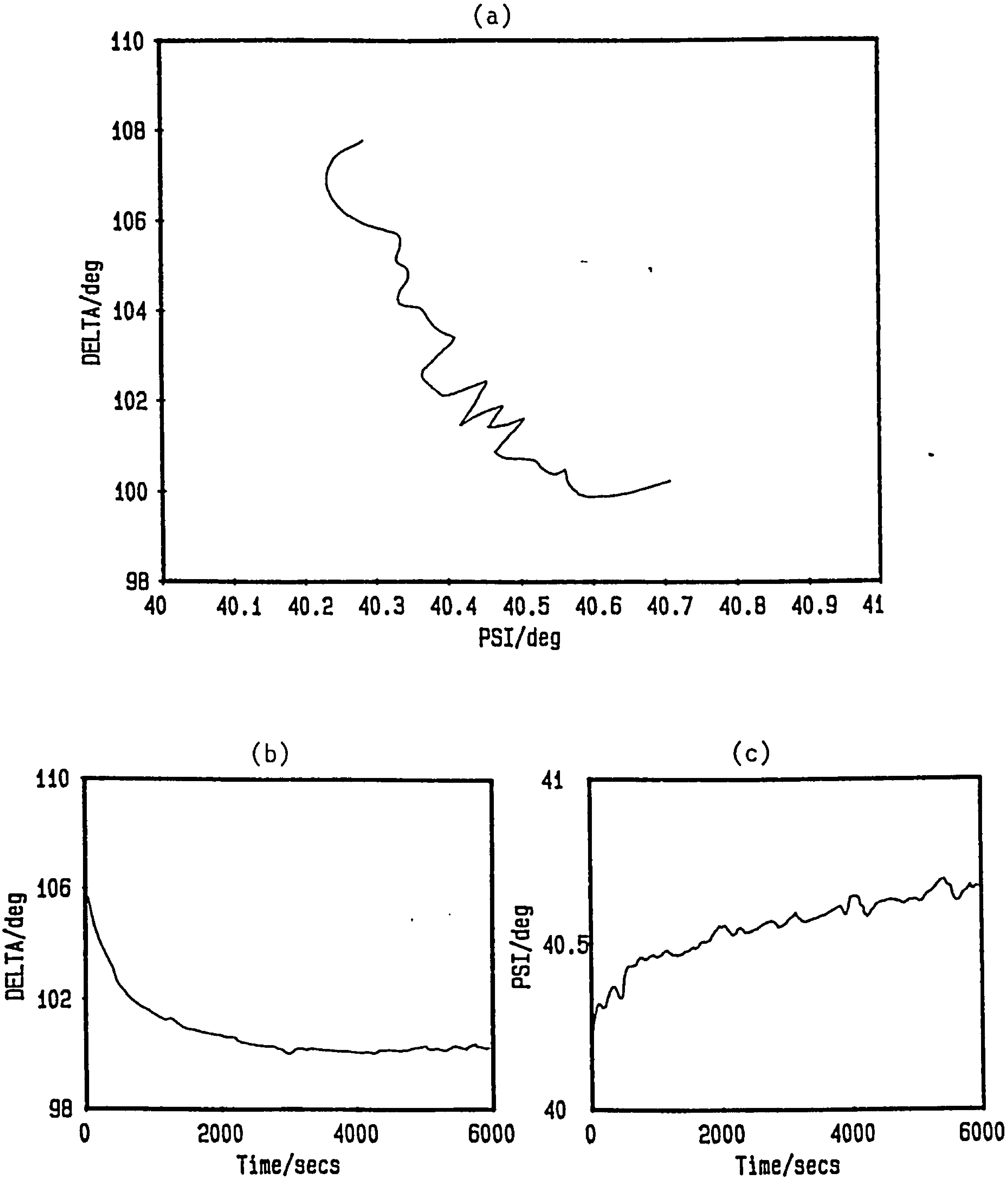

<u>Fig. 5.42</u> Magnox immersed in 0.01 mol/dm^3 NaOH containing 1000 ppm Cl$^-$

self-sustaining. It can then be measured by other means such as visually or by the rise in current.

In the region of the beam the cracks in the film are repaired before they can become established leading to overall film growth being observed, whereas at the edge of the film where there is more surface damage from mechanical polishing the pits become established, leading to severe localized attack.

A useful experiment would have been to have scanned the laser beam across the surface of the sample so that changes happening in regions of film near a pit could be observed, but the facilities for this were not available at the time.

5.4 Potential sweep experiments undertaken on Mg and Magnox in 0.01 mol/dm^3 sodium hydroxide

In order to provide additional information on the electrochemical characteristics of the films formed on Mg and Magnox in the previous sections further experiments were conducted using potential sweeps.

5.4.1 Anodic ramp results for magnesium and Magnox

If a potential ramp is applied to either a Magnox or magnesium specimen immersed in 0.01 mol/dm^3 sodium hydroxide at open circuit in the absence of aggressive anions then a characteristic current voltage response is obtained. There is an immediate rise in the anodic current on sweeping from E_{corr} quickly followed by a plateau with a current density of ca. 0.14 A/m^2. At potentials above about 3 V vs r.h.e. there is a sharp rise in the anodic current by several orders of magnitude with corresponding severe local attack and oxygen evolution from discrete areas on the surface. If the voltage is maintained at these levels then the current continues to rise and a gradual darkening of the surface is seen, eventually leading to a marked roughening with small black pits being visible on optical examination.

Associated with the anodic current on sweeping from E_{corr} there are corresponding changes in Δ and Ψ, a decrease in Δ of a few degrees and an increase in Ψ of a few tenths of a degree. Reproducibility is poor however and above 3.2 V vs r.h.e. gas evolution makes ellipsometric observation of the surface impossible with the electrochemical cell used.

This electrochemical and optical behaviour is seen in both air-saturated and nitrogen-saturated solutions regardless of whether E_{corr} and the changes in Δ and Ψ have been allowed to stabilize over the first half-hour. If however the sweep is undertaken immediately after immersion the effects of the sweep are complicated due to the rapid changes in Δ and Ψ which occur in the absence of any applied potential. Typical results obtained 30 minutes after immersion are shown in figs. 5.43 and 5.44 for Mg and Magnox samples subject to an anodic ramp of 1 mV s^{-1} from E_{corr} in air-saturated 0.01 mol/dm^3 sodium hydroxide solution under a nitrogen blanket.

5.4.2 Discussion of the anodic ramp results

Magnesium is already protected by a passive film in alkaline solutions,[12,29,34,44] hence on sweeping anodically from its open circuit potential no current peak characteristic of an active passive transition is seen but rather a flat plateau with the anode current being independent of potential. In fact a corrosion current can be measured at potentials considerably cathodic to E_{corr} in alkaline environments[51] at which potentials rapid hydrogen evolution occurs. King[29] has postulated an anodic polarization curve for Mg in 1 M NaOH based on current voltage curves and weight gain measurements of the type shown in fig. 5.45 with an active passive transition of ca. -2.4 V vs NHE. More recently Cowan and Harrison[51] using a rotating disc electrode and impedance measurements for Mg in 1 mol/dm^3 KOH have stated that this transition occurs at -2600 mV sce, with a reduction in the corrosion current from a maximum of ~1 A/m^2 at $E \sim -2800$ mV sce to 0.2 A/m^2 at $E > -1400$ mV sce.

Although Young[187] states that Mg can behave as a valve metal under certain conditions these results suggest that the passive film formed under these conditions is not a highly insulating film. This is indicated by the weak field that can be maintained across the film before the transpassive region is reached. In contrast the films formed by more typical valve metals such as that formed on aluminium in neutral solution[188] are able to support a much higher voltage before breakdown. The premise that the film is a poor electronic conductor may be proposed. If the film is a good conductor then oxygen evolution might be expected across the whole oxide surface at potentials

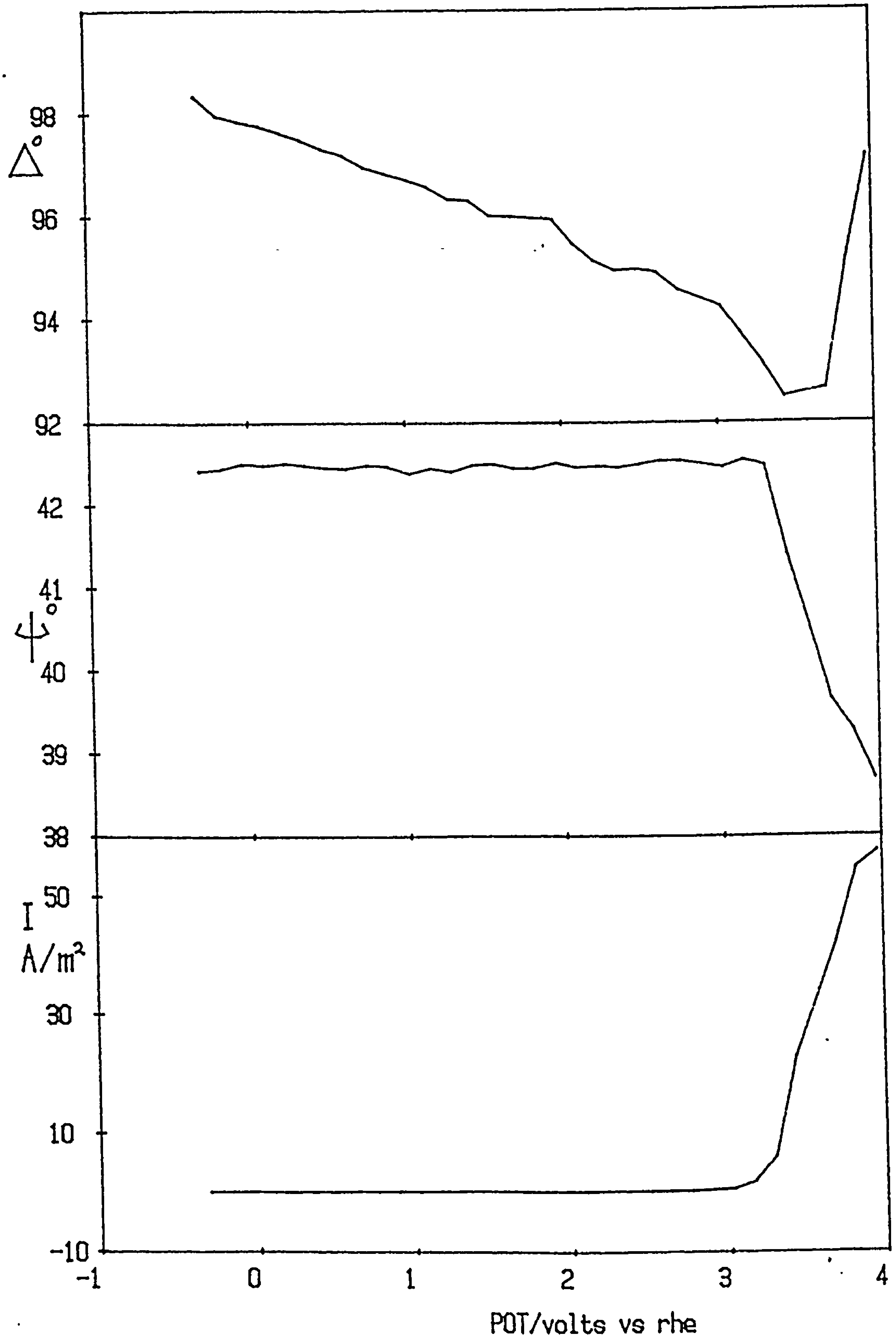

Fig. 5.43 The effect of an anodic potential ramp (1 mV/s) on magnesium in 0.01 mol/dm^3 NaOH

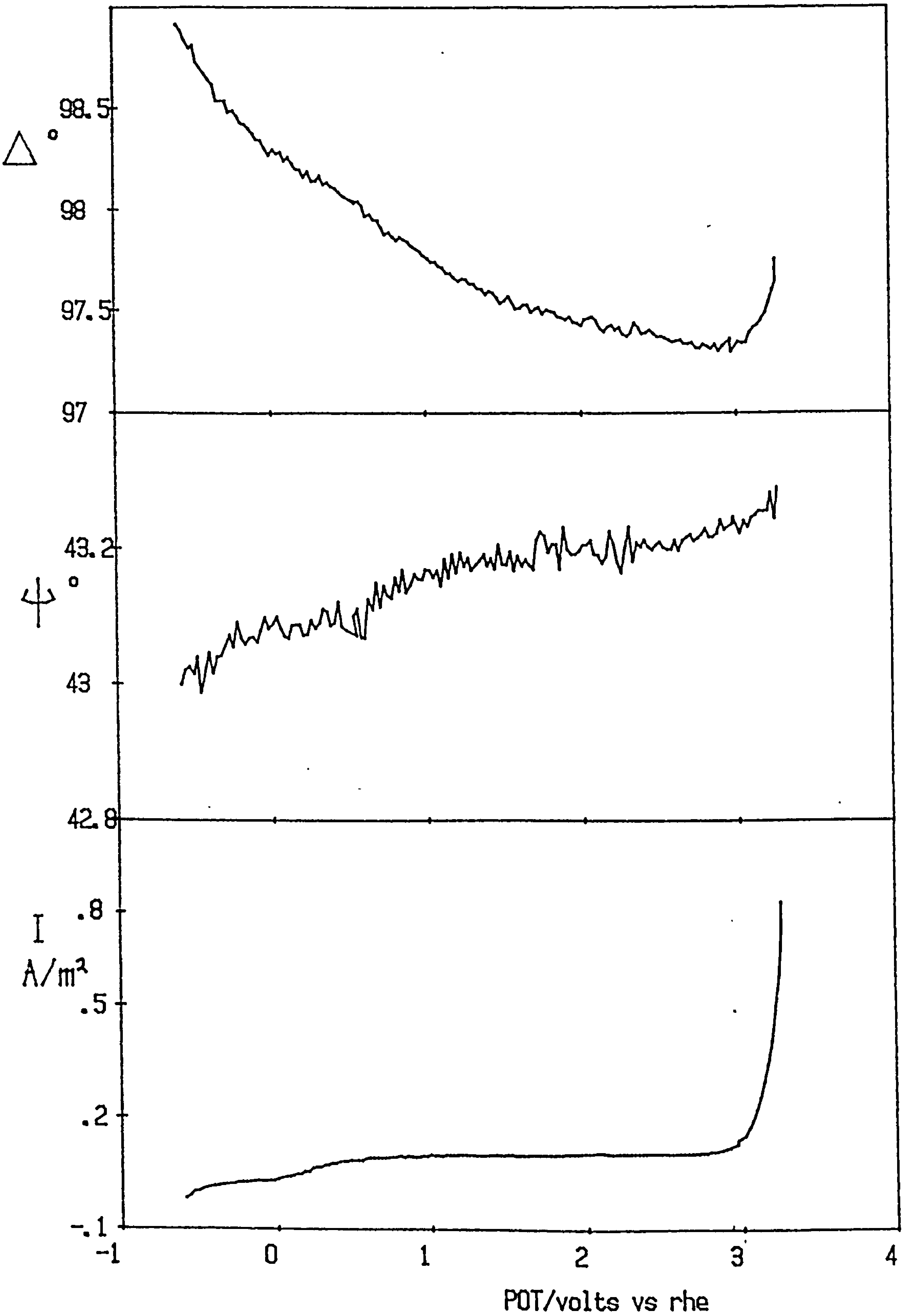

Fig. 5.44 The effect of an anodic potential ramp (1 mV/s) on Magnox in 0.01 mol/dm^3 NaOH

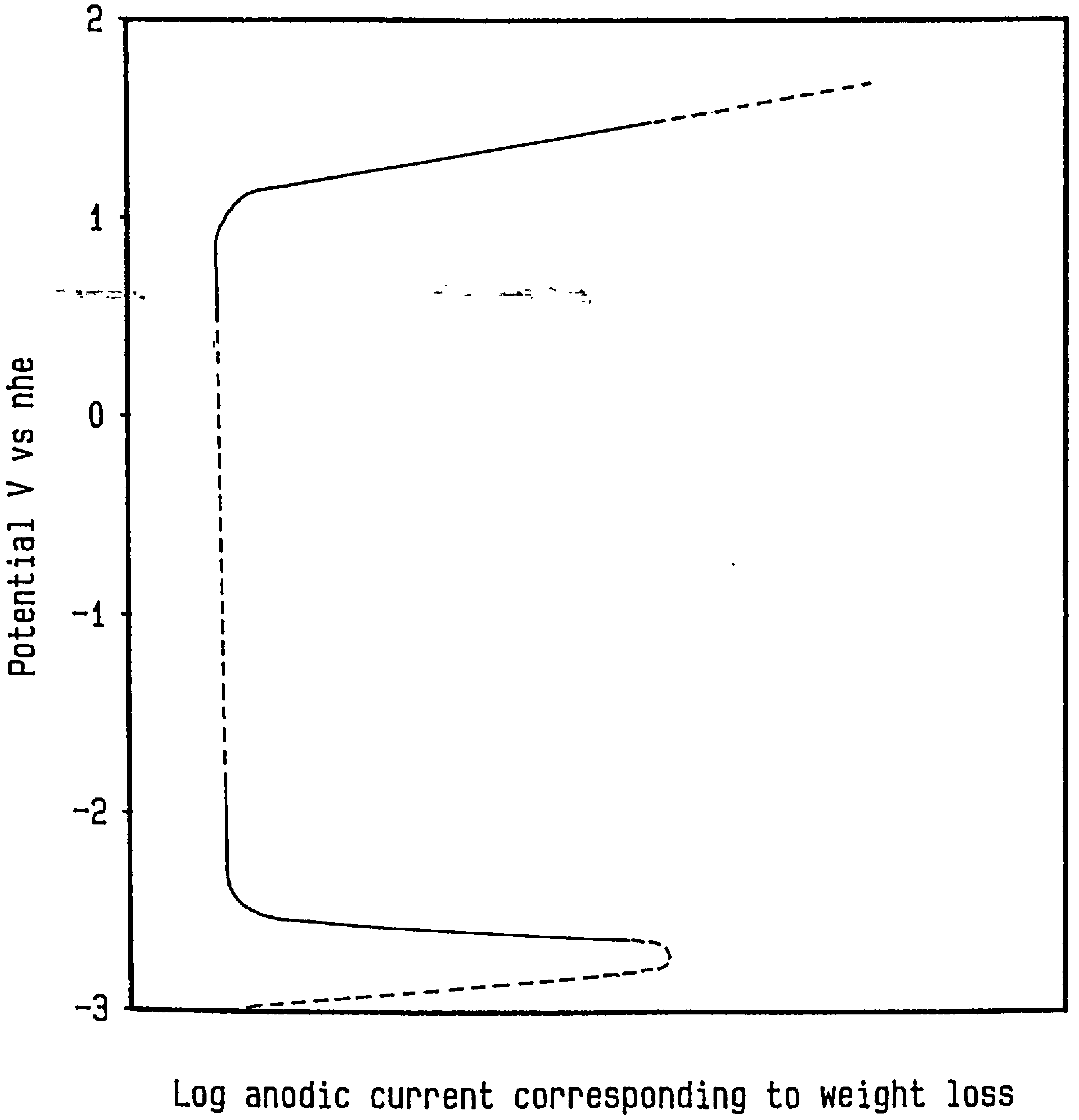

Fig. 5.45 Anodic polarization curve for Mg in 1 mol/dm^3 NaOH[29]

only slightly anodic to 1.2 V vs rhe rather than the localized attack seen at potentials in excess of 3 V vs rhe.

If in keeping with the previous discussion a thin film of MgO is located underneath a more porous top layer of $Mg(OH)_2$ with the kinetics of the corrosion reaction being controlled by diffusion through this MgO layer, then the electrical properties of this film are of interest. Mitoff[189] has discussed the electrical conduction of MgO and states that it is a mixed electronic and ionic conductor, the relative importance of each being a function of temperature, partial pressure of oxygen and impurity content. Mitoff reports that widely different results have been reported by different investigators however and states that transport phenomena in MgO are complex.

Magnesium hydroxide is described as being a poor electronic conductor.[32,34,44,46] However, if the solution permeates through a porous film of $Mg(OH)_2$ with corrosion being controlled by slow ion transport through e.g. an MgO layer, then this obviously is of little importance. No information could be found in the literature concerning the electrical properties of MgH_2.

5.4.3 Cyclic voltammetry of Mg and Magnox in 0.01 mol/dm^3 sodium hydroxide solution

Further experiments were undertaken under fast sweep (200 mV s^{-1}) conditions to enable more information to be gained on the electrochemical and optical behaviour in 0.01 mol/dm^3 NaOH. The sweep was begun anodically from a potential slightly cathodic to E_{corr} and reversed at a potential cathodic to the transpassive region, usually at about 2.5 V vs rhe. The cycle was then repeated once the starting potential had been reached on the cathodic sweep. The voltage applied, resulting current, Δ and Ψ and the time were all logged on the microcomputer using the fast data acquisition program, GETPLT3, described in section 3.5.2. The initial results were obtained in the absence of any inhibiting or aggressive anions but later experiments were carried out in fluorided solutions and also in the presence of varying concentrations of chloride ions.

5.4.4 Mg and Magnox in 0.01 mol/dm^3 sodium hydroxide

The results for both Mg and Magnox are again broadly similar, figs. 5.46-5.50. Starting in the hydrogen evolution region, fig. 5.46, the cathodic current quickly falls as E_{corr} is approached after which an anodic current is seen rising to a plateau of ca. 2-3 A/m^2. On reversing the sweep the anodic current falls immediately to zero with no hysterisis or visible pitting and no measurable cathodic current until hydrogen evolution is reached. On the second and subsequent anodic sweeps there is initially no resultant current once the potential is anodic to E_{corr} until a further over potential of about 1 volt has been applied, when a small potential dependent anodic current occurs rising to a value roughly half that of the plateau current on the first sweep. On the second and subsequent cathodic sweeps the current is again zero until the hydrogen evolution region is reached. It is also noticeable that the peak cathodic current due to hydrogen evolution and also the peak anodic current decrease with time i.e. with increasing the number of sweeps, figs. 5.51 and 5.46.

Corresponding changes in Δ and Ψ to the above anodic currents are seen, figs. 5.47-5.50, with a large decrease of ca. 2° in Δ on the first anodic sweep and an increase in Ψ of a few tenths of a degree. Much smaller changes occur on the second and subsequent anodic sweep in line with the much smaller anodic current. There are no changes in Δ and Ψ on any of the cathodic sweeps. The changes give rise to a 'staircase' type plot if Δ and Ψ are plotted against time (figs. 5.48 and 5.50).

A Magnox specimen that had been immersed for 9 hours under a nitrogen blanket was also subject to a potential sweep to see whether similar behaviour would be observed for the much thicker corrosion film existing after this time. This was indeed the case although the changes in Δ and Ψ were markedly less and Δ showed an increase with increasing anodic current rather than a decrease. This is as expected on the basis of theoretical predictions for film growth from the point on the Δ,Ψ curve from which the potential sweep was begun.

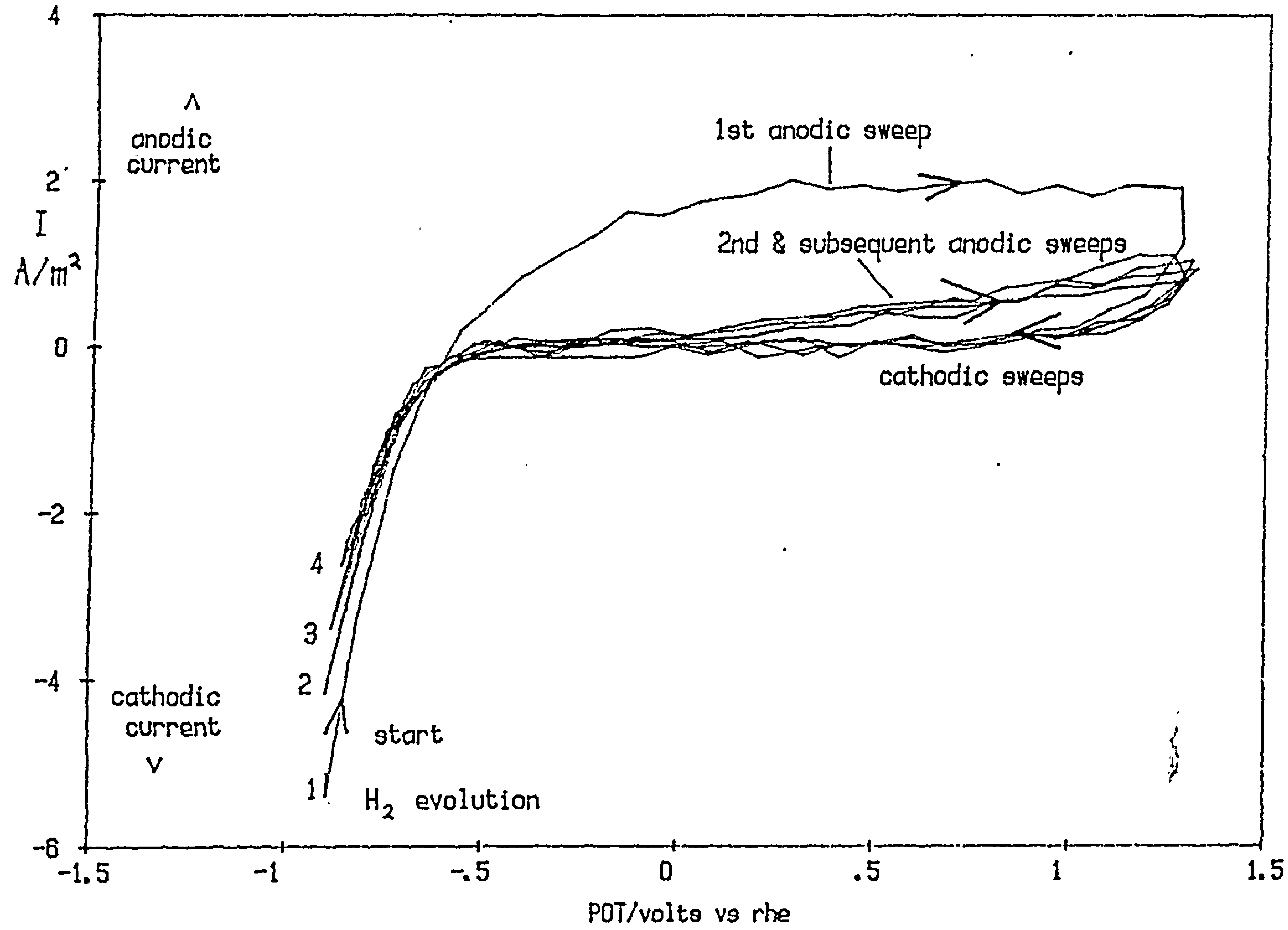

Fig. 5.46 Typical cyclic voltammagram for magnesium in 0.01 mol/dm^3 NaOH in the absence of aggressive anions

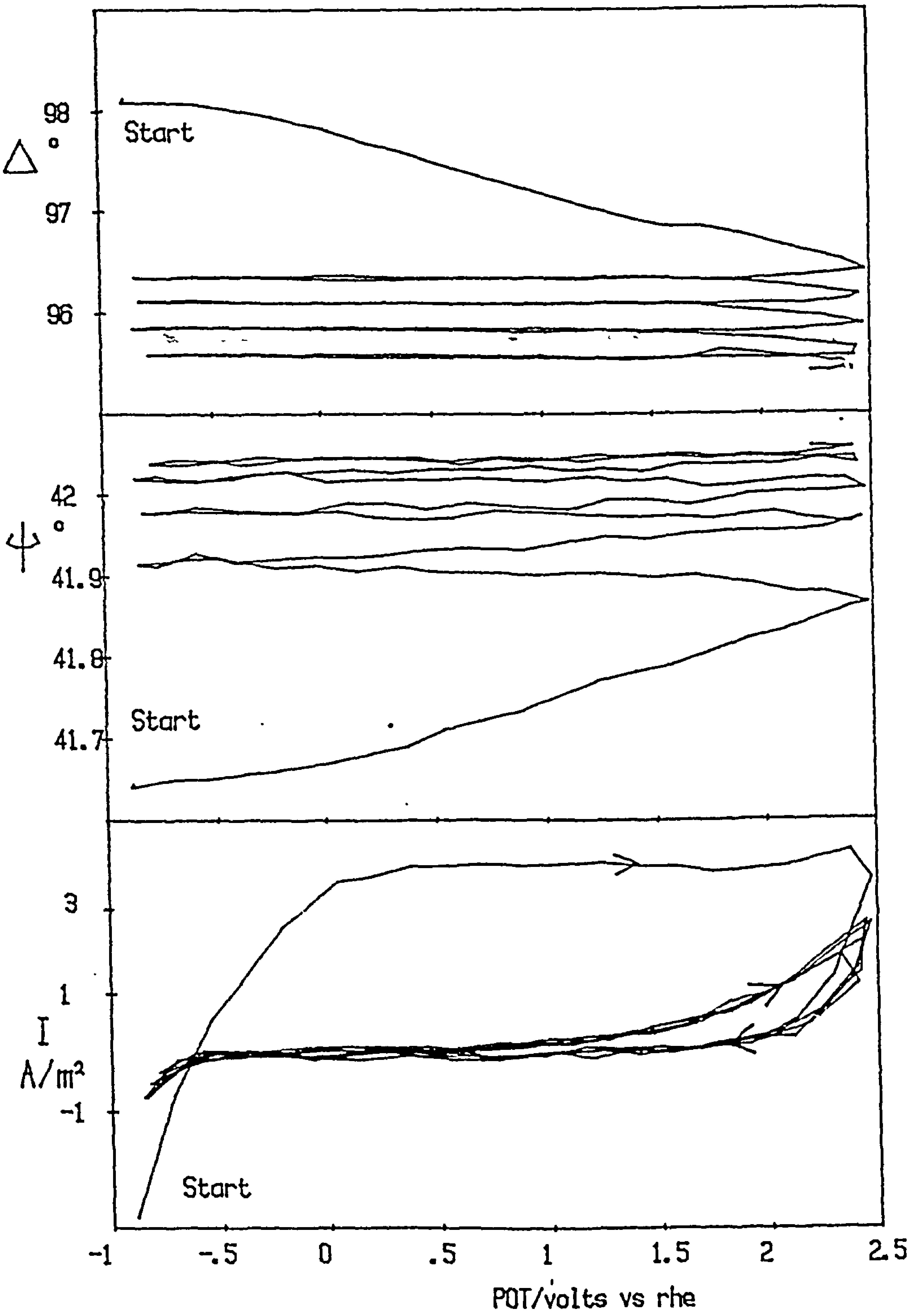

Fig. 5.47 The effect of a potential sweep (200 mV/s) on magnesium in 0.01 mol/dm^3 NaOH

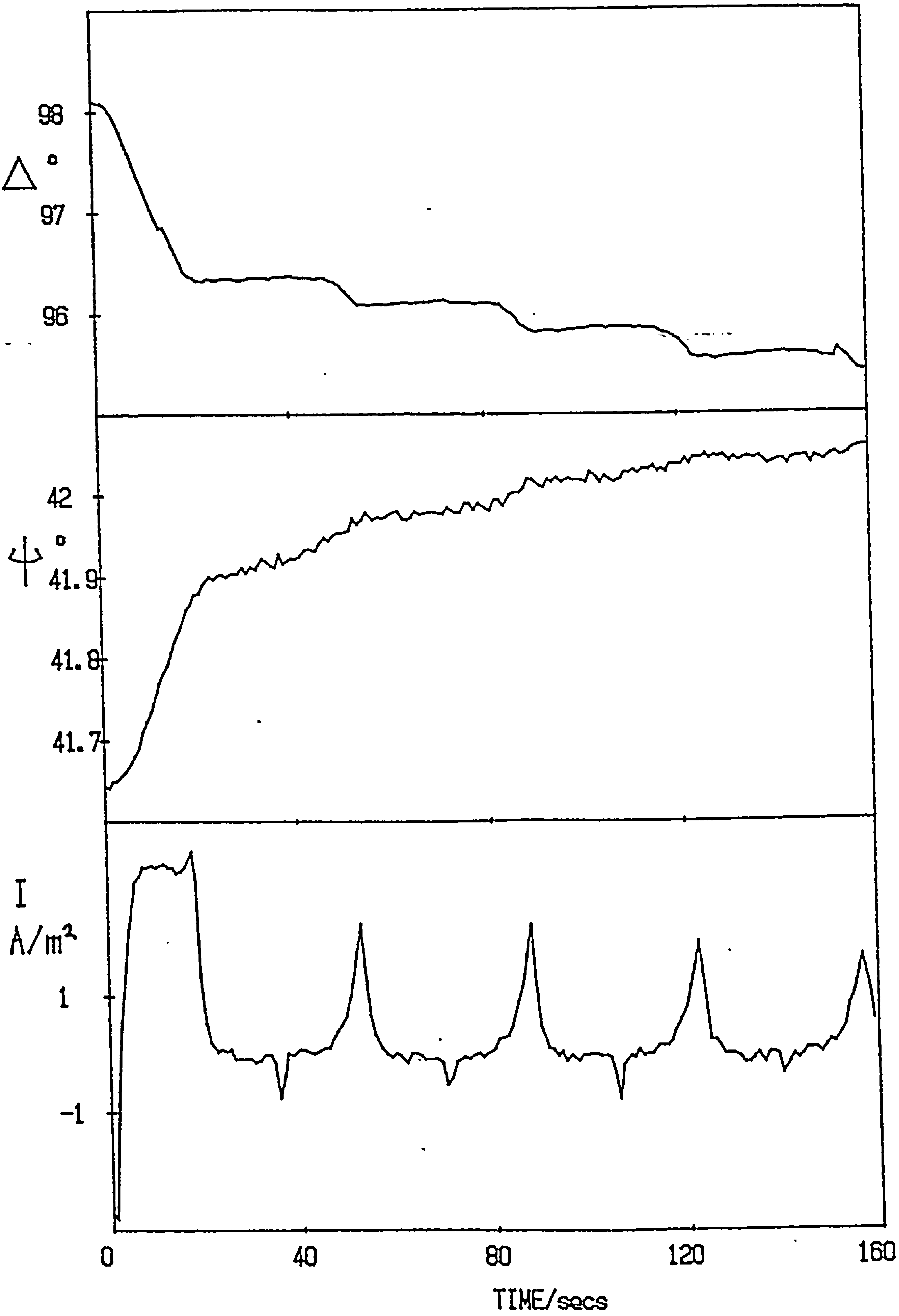

Fig. 5.48 The effect of a potential sweep (200 mV/s) on magnesium in 0.01 mol/dm^3 NaOH

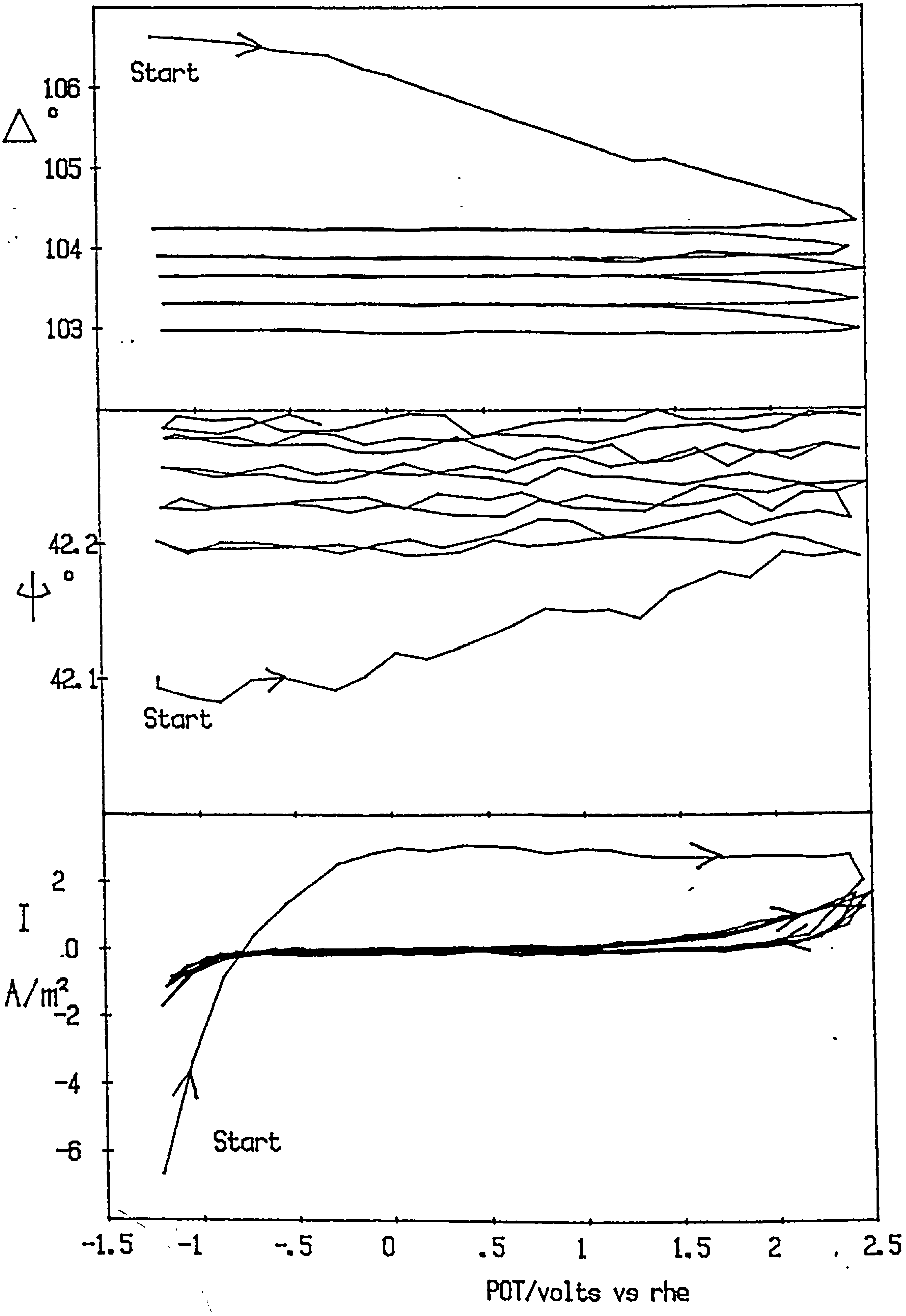

Fig. 5.49 The effect of a potential sweep (200 mV/s) on Magnox in 0.01 mol/dm^3 NaOH

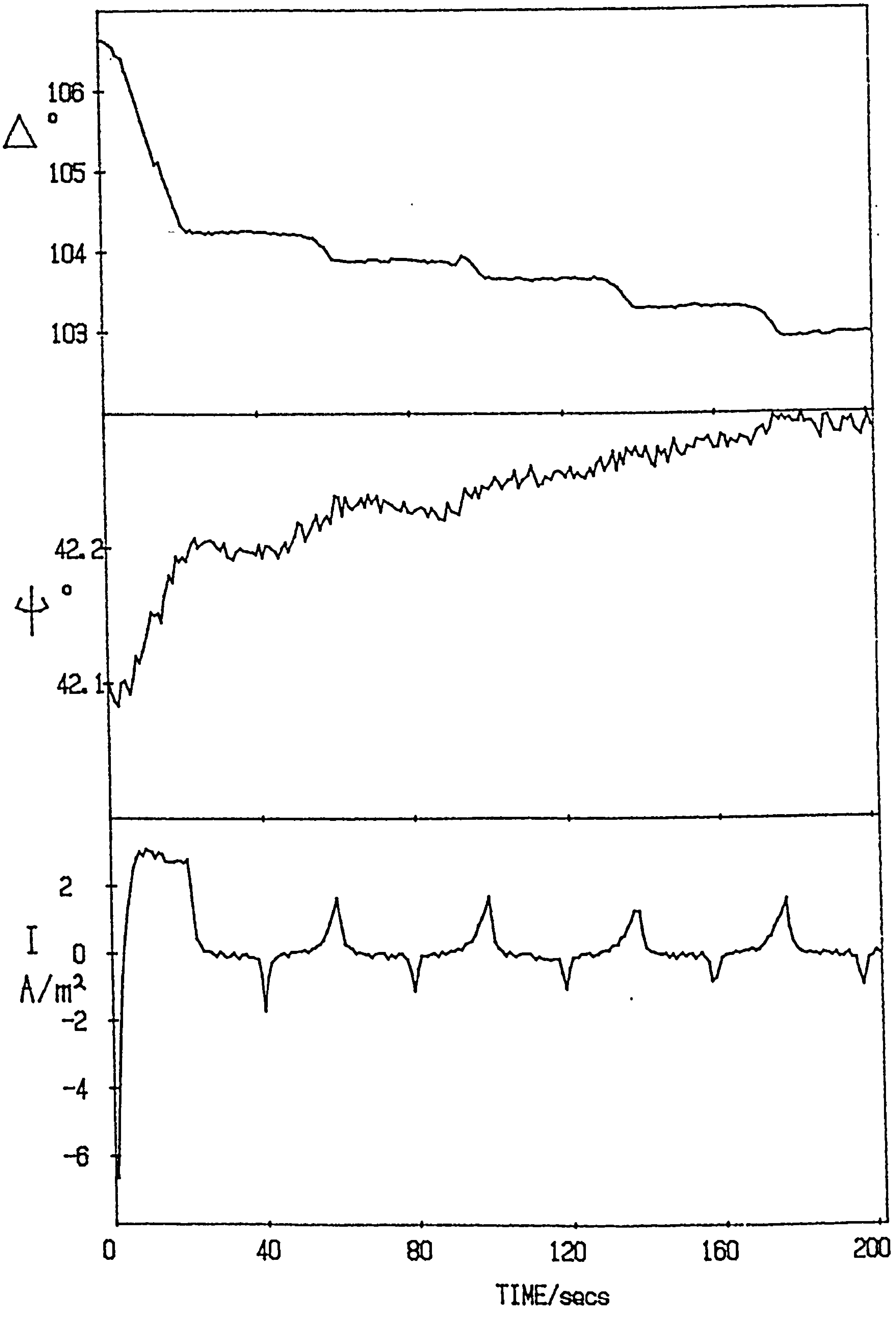

Fig. 5.50 The effect of a potential sweep (200 mV/s) on Magnox in 0.01 mol/dm^3 NaOH

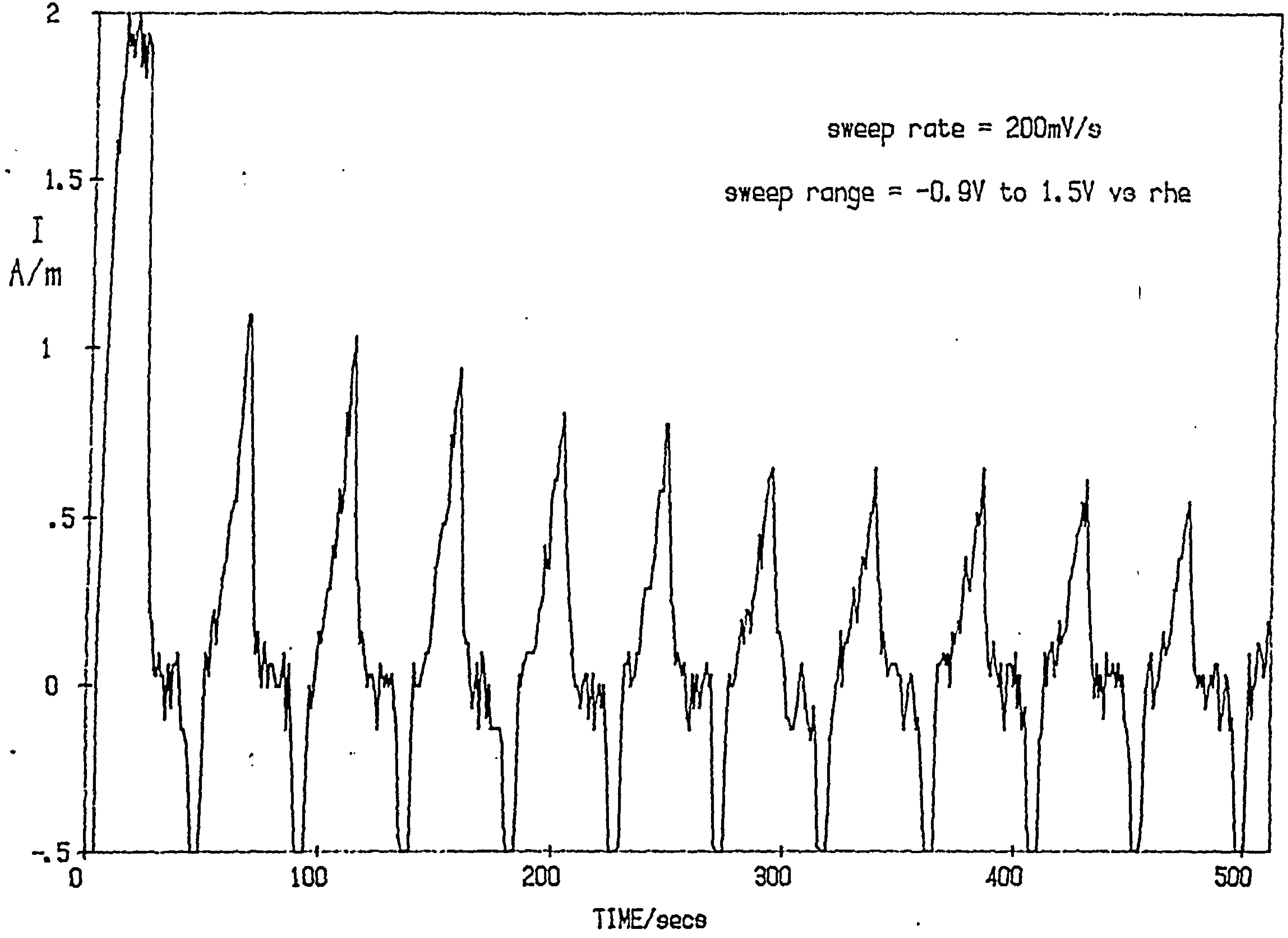

Fig. 5.51 The reduction in the anodic peak with successive potential sweeps for magnesium in 0.01 mol/dm^3 NaOH

5.4.5 Discussion of cyclic voltammagrams in 0.01 mol/dm^3 sodium hydroxide

It is apparent from these results that uniform film growth is occurring mainly on the first anodic sweep but also to a lesser extent on the second and subsequent anodic sweeps. No removal of the film is seen on the cathodic sweep. Reduction would not of course be expected given the very electronegative potential for the reaction:

$$Mg(OH)_2 + 2e = Mg + 2OH^- \qquad .....(1.2)$$

$$E° = -2.7 \text{ V vs NHE}, \ -3.4 \text{ V vs RHE}$$

Neither is there any chemical dissolution of the films formed at high potentials.

It may be surmised that the film being formed on the anodic sweeps is of fairly low conductivity. This can be inferred from the marked reduction in the anodic current and the reduced changes in Δ and Ψ between the first and second anodic sweep, and also by the gradual reduction in I_{max} for both the hydrogen evolution current and the anodic current with the increasing number of potential sweeps.

The current on the second and subsequent anodic sweep is then due to a leakage current[190] through weak points in the film such as flows, micro-fissures, micro-cracks, invisible blisters, incorporated impurities and other surface defects. This leakage current is fairly high and again indicates the relatively poor dielectric properties of the film formed on magnesium and Magnox under these conditions compared with more typical valve metals. The imperfect nature of the passive film formed on the anodic sweep is also indicated by the fact that the corrosion film continues to grow if the substrate is left at open circuit after an anodic sweep as evinced by the changes in Δ and Ψ.

5.4.6 Magnox in 0.01 mol/dm^3 sodium hydroxide with the addition of 1000 ppm fluoride

It has been suggested[49] and discussed previously that fluoride may be incorporated into the proposed barrier layer in the form of a sub-micron oxy-fluoride layer and that transport of ions through this layer may control the corrosion kinetics. If this is the case then the effect of fluoride ions may be to make the corrosion film less 'leaky'. This proposal was investigated by recording the cyclic voltammagram of Magnox in 0.01 mol/dm^3 NaOH dosed with 1000 ppm fluoride. The results in figs. 5.52 and 5.53 however show that again there is little difference in the electrochemical and optical response in fluoride dosed and fluoride free solutions in the short term.

5.4.7 Magnox and magnesium in 0.01 mol/dm^3 NaOH with the addition of 10, 100 and 1000 ppm Cl$^-$

The results for the cyclic voltammetry of both Mg and Magnox in the absence of and in the presence of 10, 100 and 1000 ppm chloride ions are shown in figs. 5.54-5.59. No attempt has been made in these experiments to measure the breakdown and repassivation potentials which are sweep rate dependent[191] and require slower potential sweep rates than were used in these experiments. They were undertaken to get an idea of the electrochemical and optical properties of surface films in the presence of varying concentrations of chloride ions.

Little difference is seen between solutions containing 10 ppm Cl$^-$ and chloride free solutions but on the addition of 100 ppm Cl$^-$ the leakage current is seen to increase although this is not reflected in the changes in Δ and Ψ. This suggests that pitting may be initiating in a region away from the light beam and indeed small pits could be seen on the surface of the sample on removal from the solution.

In the presence of 1000 ppm Cl$^-$ there is a marked rise in current for both samples at about 1.5 V vs rhe. The current continues to grow on the reverse sweep leading to marked hysteris due to active pit formation. The surface of both electrodes became covered with small pits from which a steady stream of hydrogen was evolved. Similar behaviour has been observed for Mg in solutions containing high concentrations of chloride ions[44] for sweep rates of 300 mV s^{-1}. On the successive anodic sweeps film breakdown occurs at lower and lower potentials indicating that there is either incomplete passivation of the pits on sweeping cathodically to the hydrogen evolution region or hydrolysis has resulted in lowering the pH in the pit to a value where breakdown of the passive film is easier.

The ellipsometric results are inconclusive as they only represent what takes place in the region of the beam whereas pitting is a highly localized process. Film growth does appear to occur normally up to the

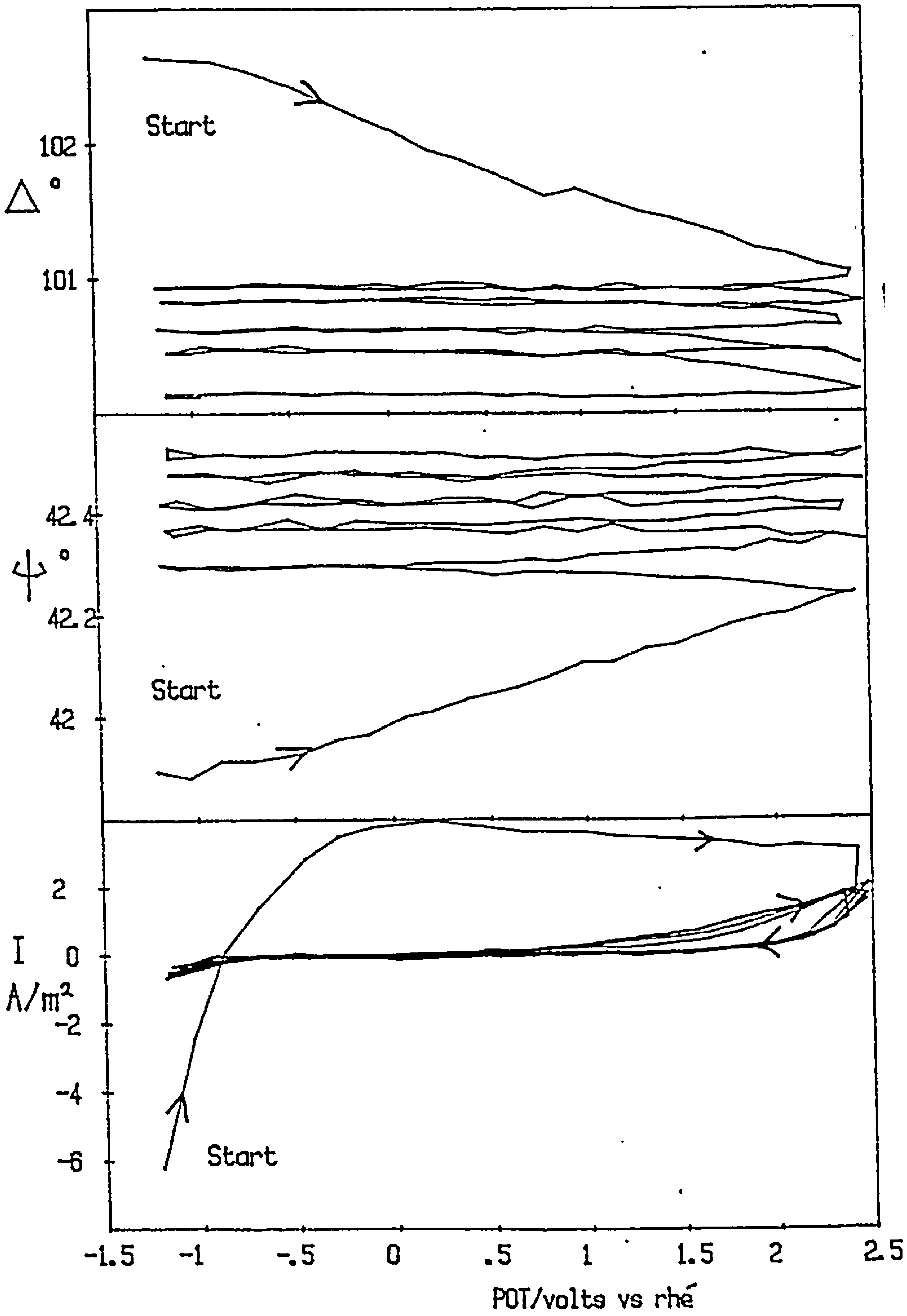

Fig. 5.52 The effect of a potential sweep (200 mV/s) on Magnox in 0.01 mol/dm^3 NaOH + 1000 ppm fluoride

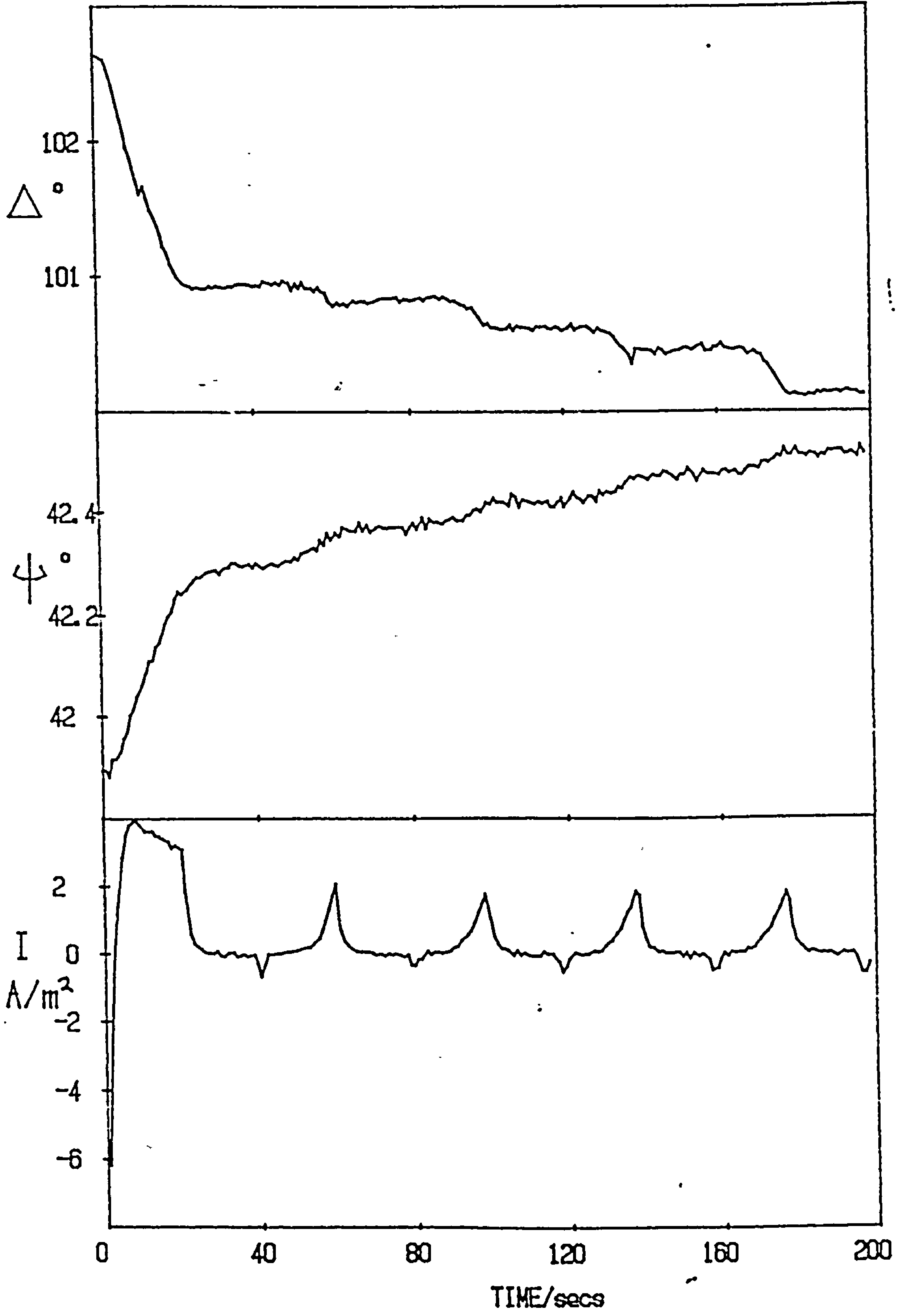

Fig. 5.53 The effect of a potential sweep (200 mV/s) on Magnox in 0.01 mol/dm^3 NaOH + 1000 ppm fluoride

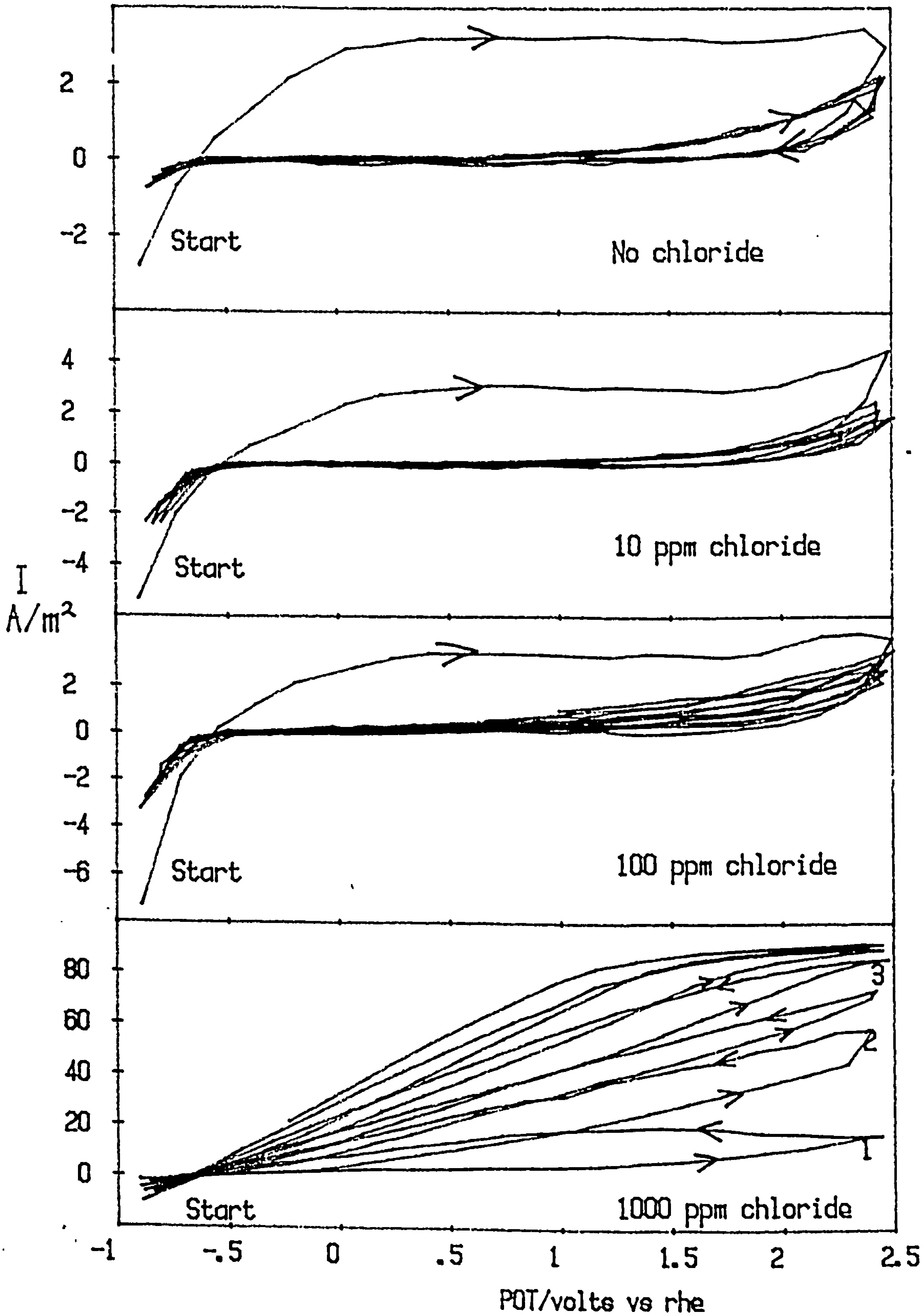

Fig. 5.54 The effect of a potential sweep (200 mV/s) on magnesium in the absence of chloride and in the presence of 10, 100, and 1000 ppm chloride in 0.01 mol/dm^3 NaOH

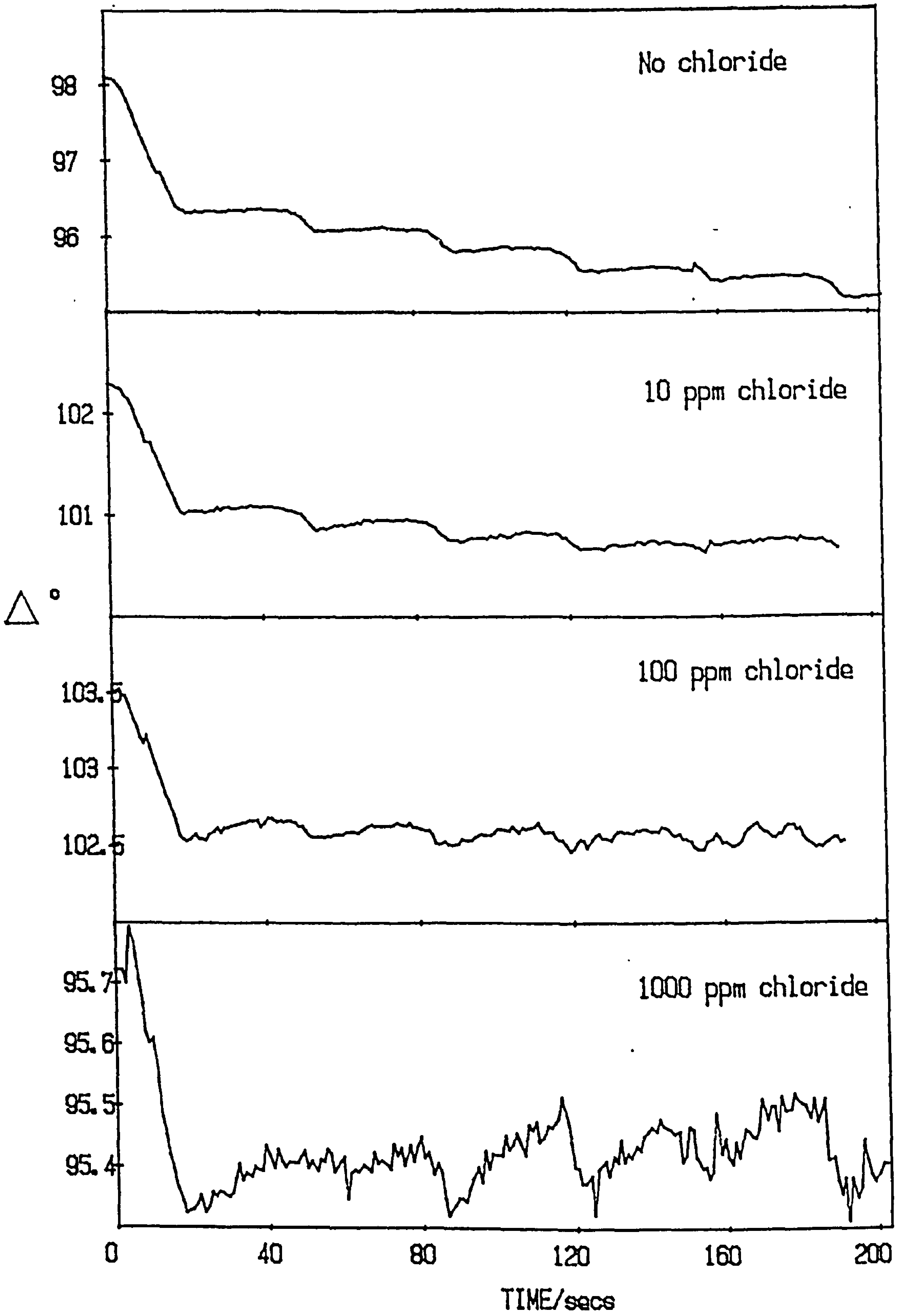

Fig. 5.55 The effect of a potential sweep (200 mV/s) on magnesium in the absence of chloride and in the presence of 10, 100, and 1000 ppm chloride in 0.01 mol/dm^3 NaOH

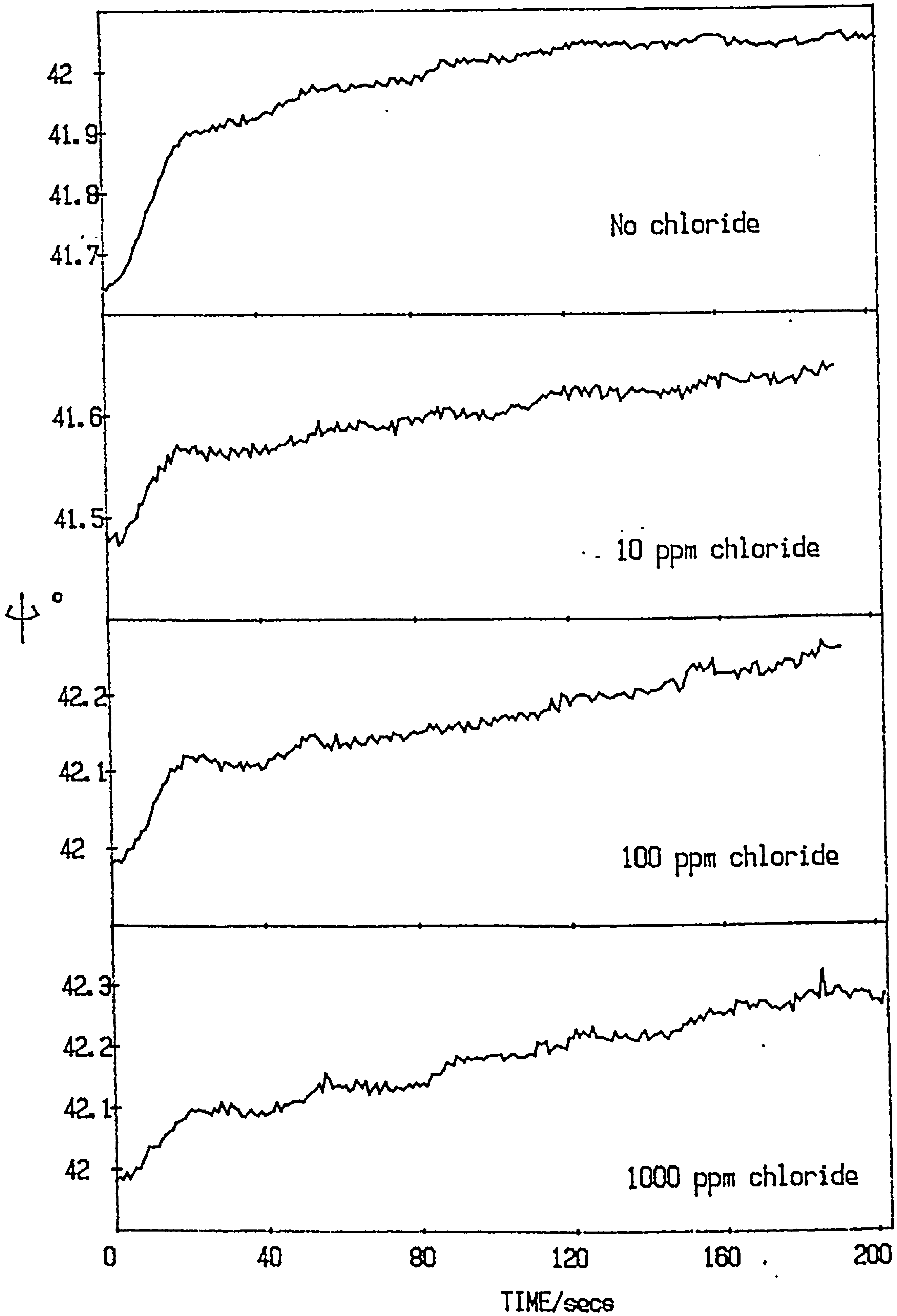

Fig. 5.56 The effect of a potential sweep (200 mV/s) on magnesium in the absence of chloride and in the presence of 10, 100, and 1000 ppm chloride in 0.01 mol/dm^3 NaOH

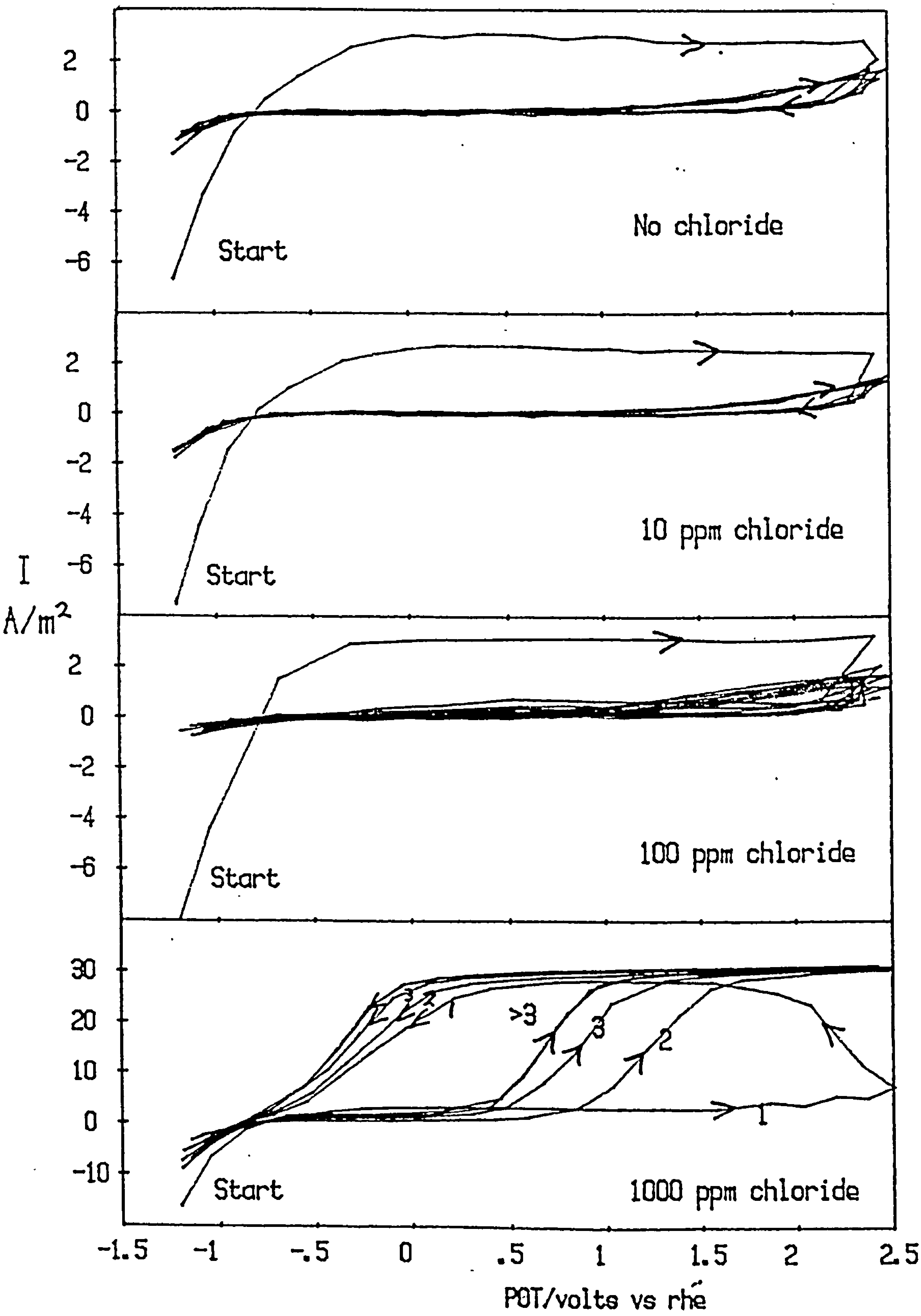

Fig. 5.57 The effect of a potential sweep (200 mV/s) on Magnox in the absence of chloride and in the presence of 10, 100, and 1000 ppm chloride in 0.01 mol/dm^3 NaOH

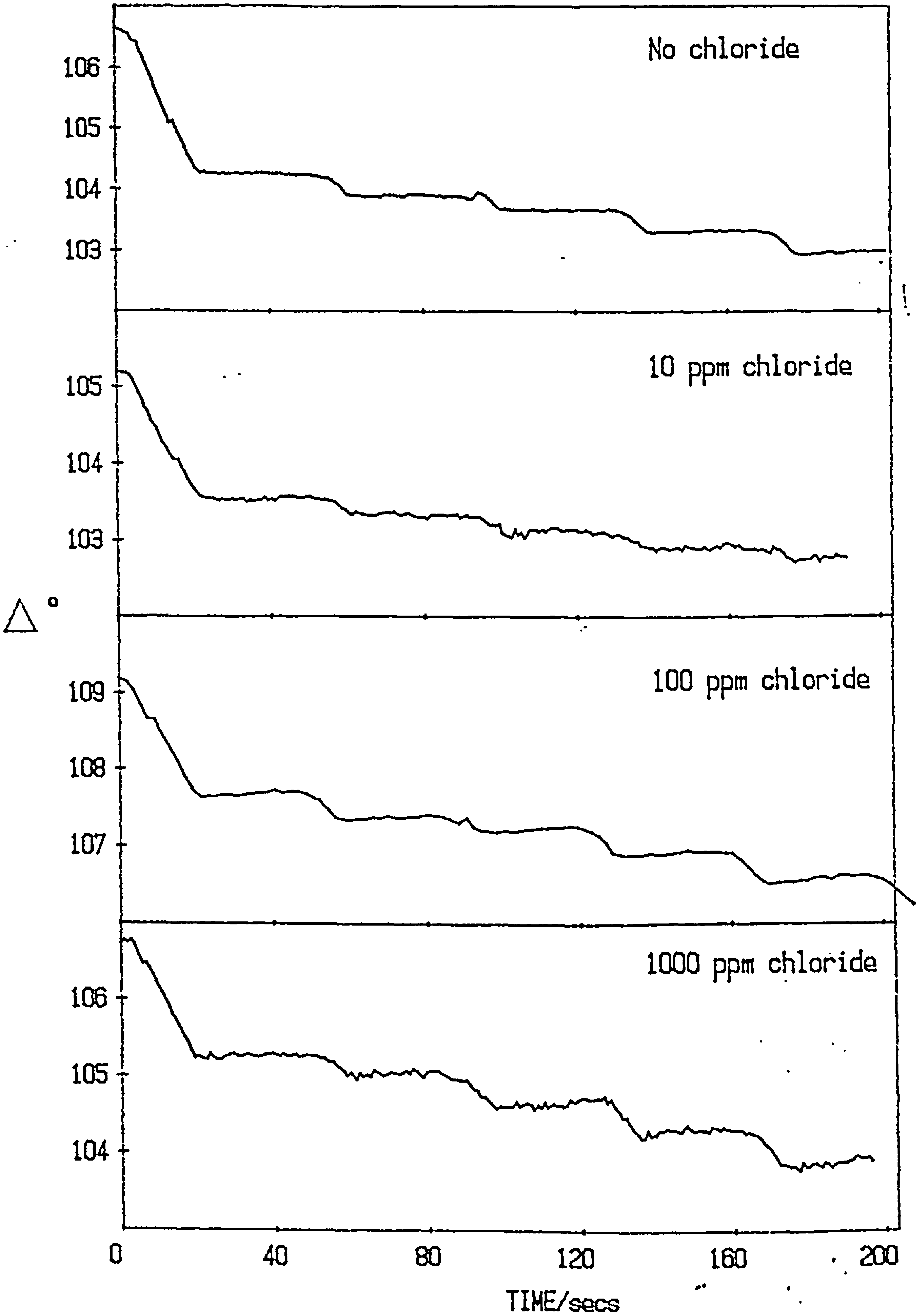

Fig. 5.58 The effect of a potential sweep (200 mV/s) on Magnox in the absence of chloride and in the presence of 10, 100, and 1000 ppm chloride in 0.01 mol/dm NaOH

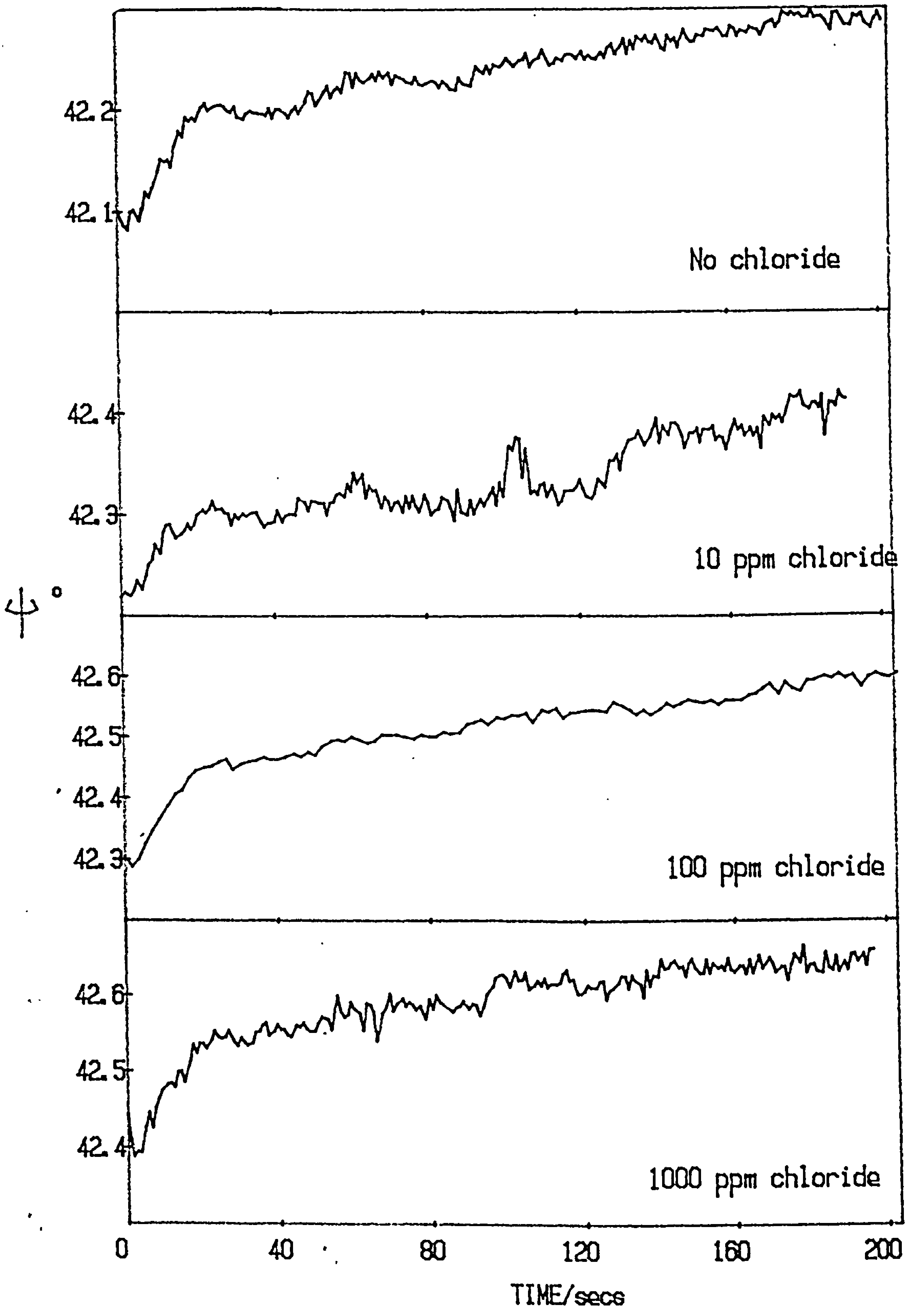

Fig. 5.59 The effect of a potential sweep (200 mV/s) on Magnox in the absence of chloride and in the presence of 10, 100, and 1000 ppm chloride in 0.01 mol/dm^3 NaOH

potentials at which breakdown of the film takes place, but after this the signal for Mg becomes very noisy, probably due to the hydrogen evolution in the surface. The ellipsometric results for Magnox indicate normal film growth as seen in non-chloride containing solutions but again this may not reflect accurately what is happening across the whole surface.

CHAPTER 6

6. Introduction

This chapter describes the additional experiments which were conducted in order to obtain a deeper insight into the processes occurring on Mg and Magnox when the solution pH falls below 11.5.

6.1 Experiments on Mg and Magnox in neutral solutions and 1 mol/dm^3 sodium hydroxide

6.1.1 Magnesium in distilled water

A Mg sample was polished and etched in 0.2% citric acid, as described in Chapter 5, then immersed in distilled water at open circuit for 9 hours. Soon after immersion hydrogen bubbles were visible on the surface of the Mg and were removed periodically by pipette. On removal from solution a white film was visible on the Mg surface which darkened over a period of 24 hours to give interference colours of brown, purple, green and yellow. Fig. 6.1 indicates the rapid changes in Δ and Ψ during the first thirty minutes. Although the rate of change slowed down after this initial period there was a much larger overall change in Δ and Ψ than was the case in more alkaline solutions. The changes in Ψ under these conditions are significantly different to results obtained in solutions in which the pH was changing from 12 to values below 11.5. The initial decrease in Ψ occurs earlier than is the case at higher pH values (~10 minutes compared to about 1-2 hours) and is followed by an increase after 2 hours which gives rise to the 'loop' seen in fig. 6.1. This trend of an early reduction in Ψ followed by an increase after several hours is reproducible.

The ellipsometric result in fig. 6.1 can not be modelled theoretically using a single film but a very rough estimate of the film thickness can be obtained by this method. A closed Δ,Ψ curve or 'egg' is produced, (fig. 6.2), for a film of $Mg(OH)_2$ ($n = 1.56$, $k = 0$) on Mg ($n = 0.85$, $k = 5.85$) when the film has grown to ~340 nm. If it is assumed that the changes in Δ and Ψ in fig. 6.1 correspond to the traversal of three-quarters of the closed curve then the film thickness would be about 250 nm. This value is in reasonable agreement with a film depth of 200 ± 50 nm obtained from changes in the Mg/O ratio with depth using SIMS for a Mg sample immersed in distilled water.

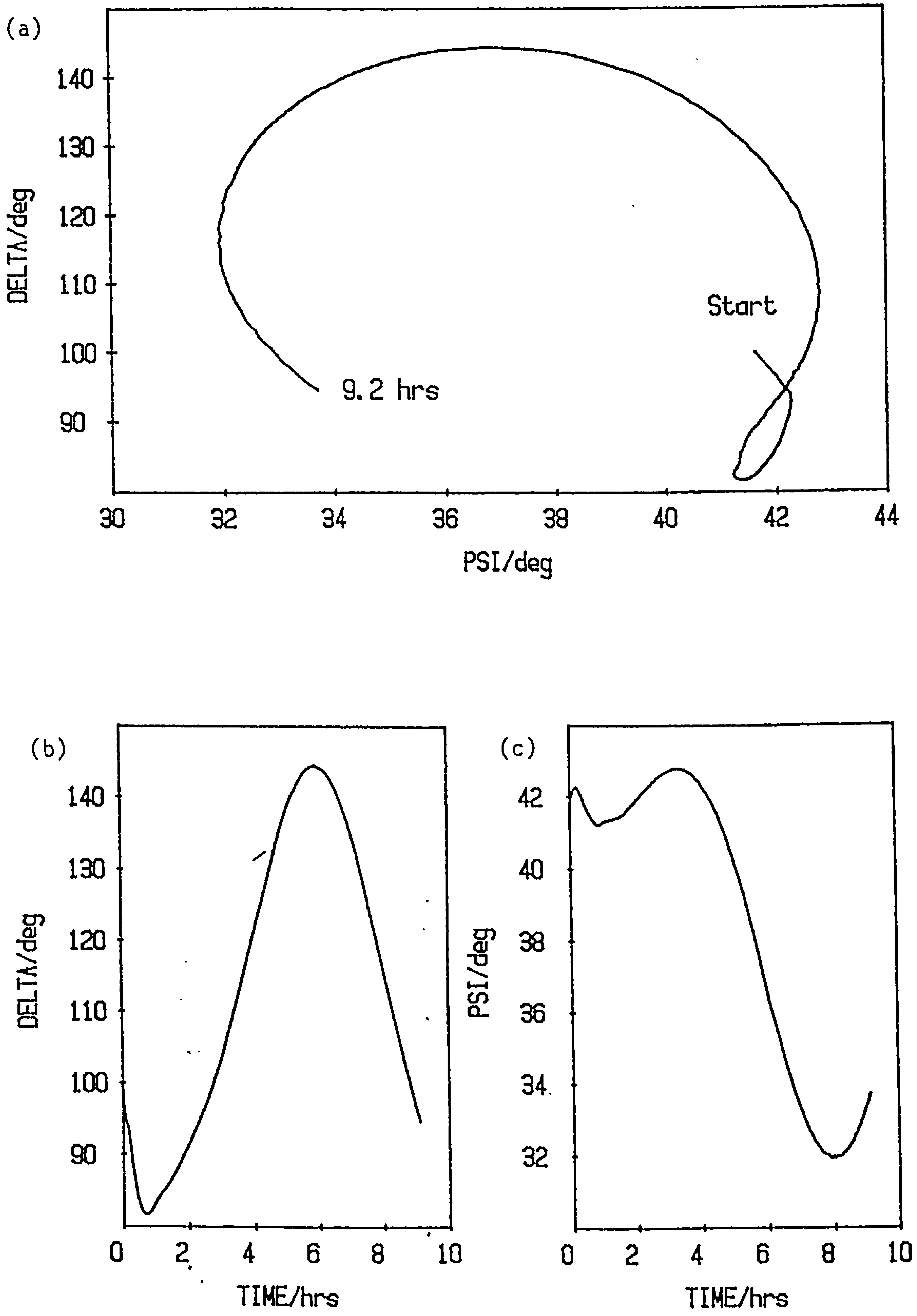

Fig. 6.1 Magnesium at open circuit in distilled water

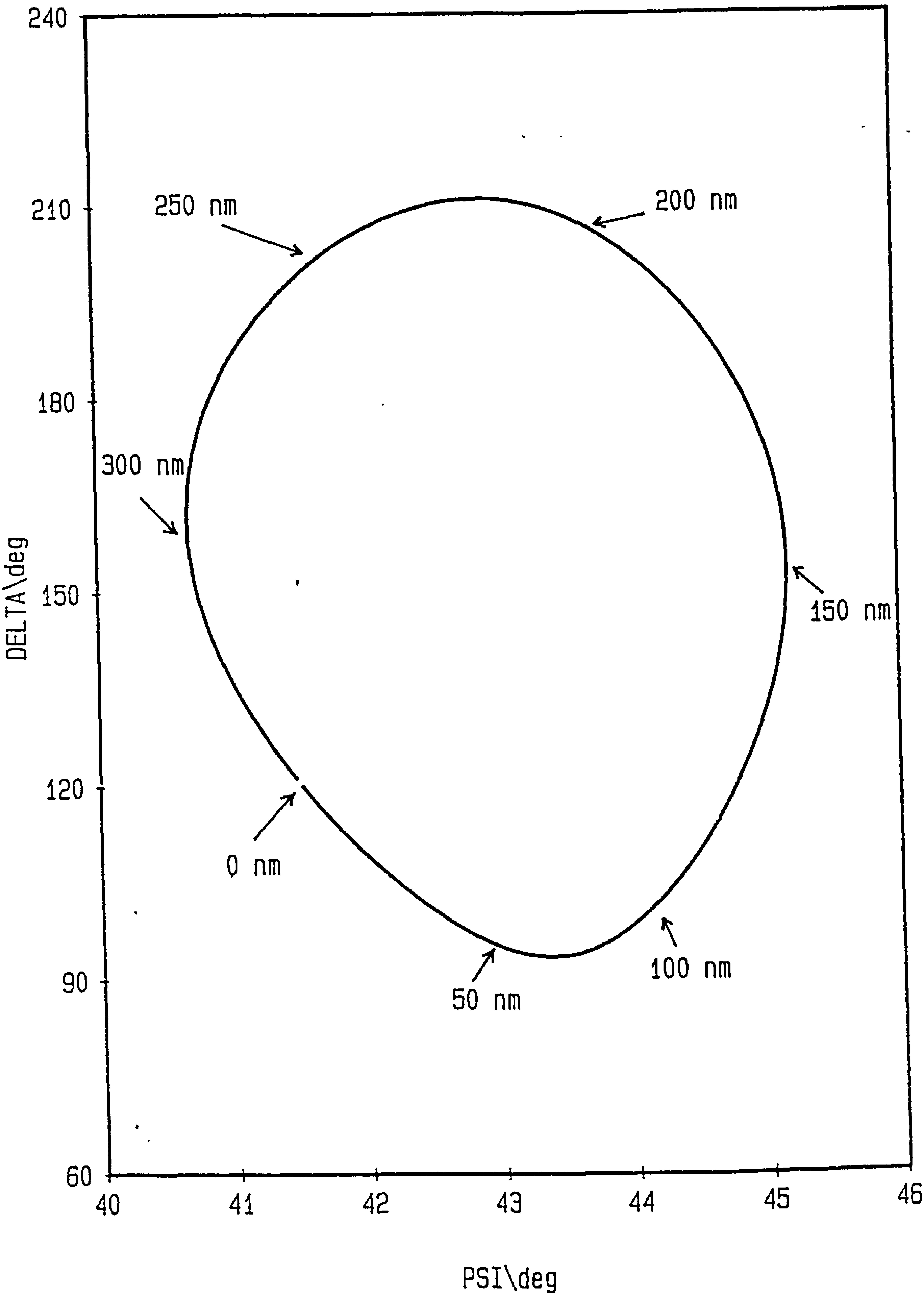

Fig. 6.2 Single film prediction for 340 nm of a non-absorbing film (n = 1.56, k = 0) grown on a Mg substrate (n = 0.85, k = 5.85)

6.1.2 Magnox in distilled water

A Magnox sample was polished and etched in 0.2% citric acid and immersed in distilled water for 6 hours. Hydrogen bubbles were visible on the surface soon after immersion and were removed by pipette. The appearance of the sample was very similar to that of the Mg in the previous section - a white film visible on removal which slowly changed on drying in air to give interference colours of purple and green.

Much larger changes were seen for Δ and Ψ; (fig. 6.3) than was the case for Magnox in alkaline solutions but no reduction in Ψ was observed, unlike the changes in Δ and Ψ recorded for Mg immersed in distilled water. Using the theoretical curve in fig. 6.2 a very rough estimate of ~150 nm for the film thickness was calculated. This value is rather less than the figure of 300 nm obtained from SIMS using the variation of the Mg/O ratio with depth.

6.1.3 Magnesium in 1 mol/dm^3 sodium hydroxide

The ellipsometric results for a Mg specimen polished and etched then immersed in air-saturated 1 mol/dm^3 NaOH, fig. 6.4, are broadly similar to those in 0.01 mol/dm^3 NaOH. There is an initial rapid decrease in Δ accompanied by a slight increase in Ψ. After about 20 minutes the rate of change of Δ slows down and after about 30 minutes Ψ begins to decrease. The appearance of the electrode after 6 hours immersion was in marked contrast to that observed in distilled water with no visible film present on the electrode.

This result indicates that increasing the pH of the solution beyond about 11.5 has little effect on the corrosion of Mg which is in marked contrast to the result obtained for Magnox in the following section.

6.1.4 Magnox in 1 mol/dm^3 sodium hydroxide

When a polished and etched Magnox sample is immersed in air-saturated 1 mol/dm^3 NaOH a characteristic Δ,Ψ curve is observed. Over a period of about 30 minutes Ψ at first increases, then decreases and increases again. Although slight changes in Δ and Ψ were noted on repeating the experiment the trend in Ψ was reproducible as evinced by the two results in fig. 6.5. These results are different from any of

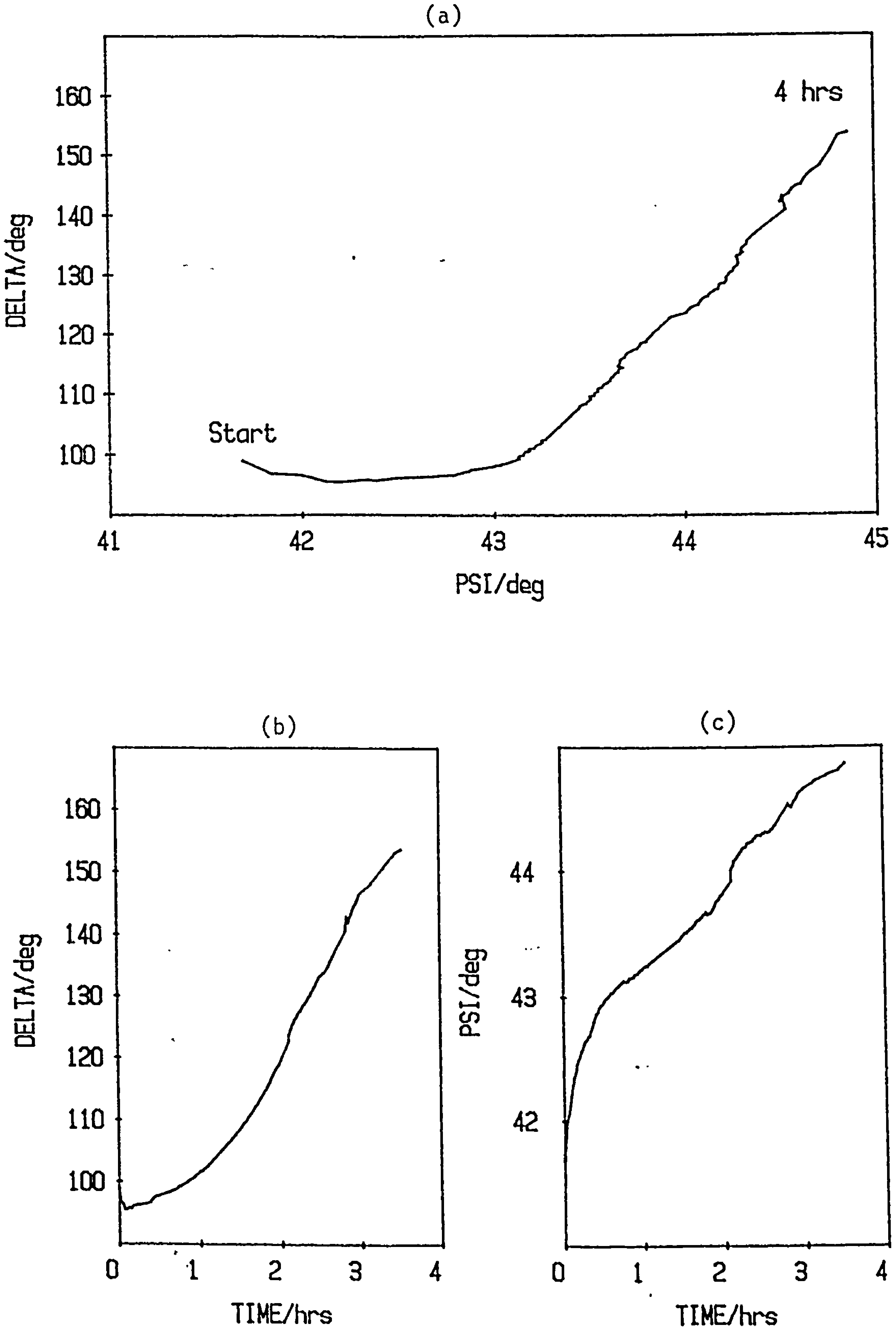

Fig. 6.3 Magnox immersed in distilled water

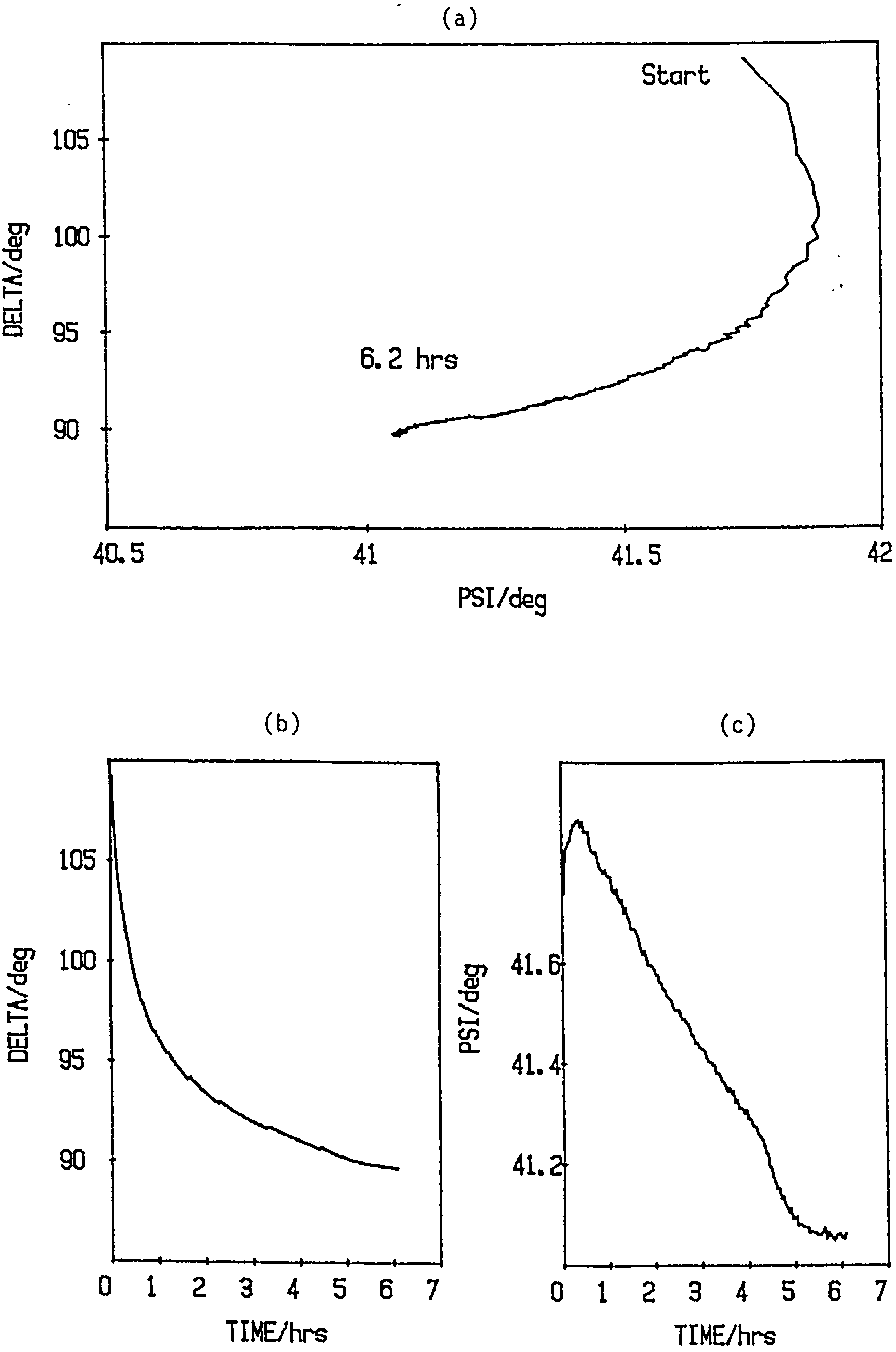

Fig. 6.4 Magnesium in 1 mol/dm^3 NaOH

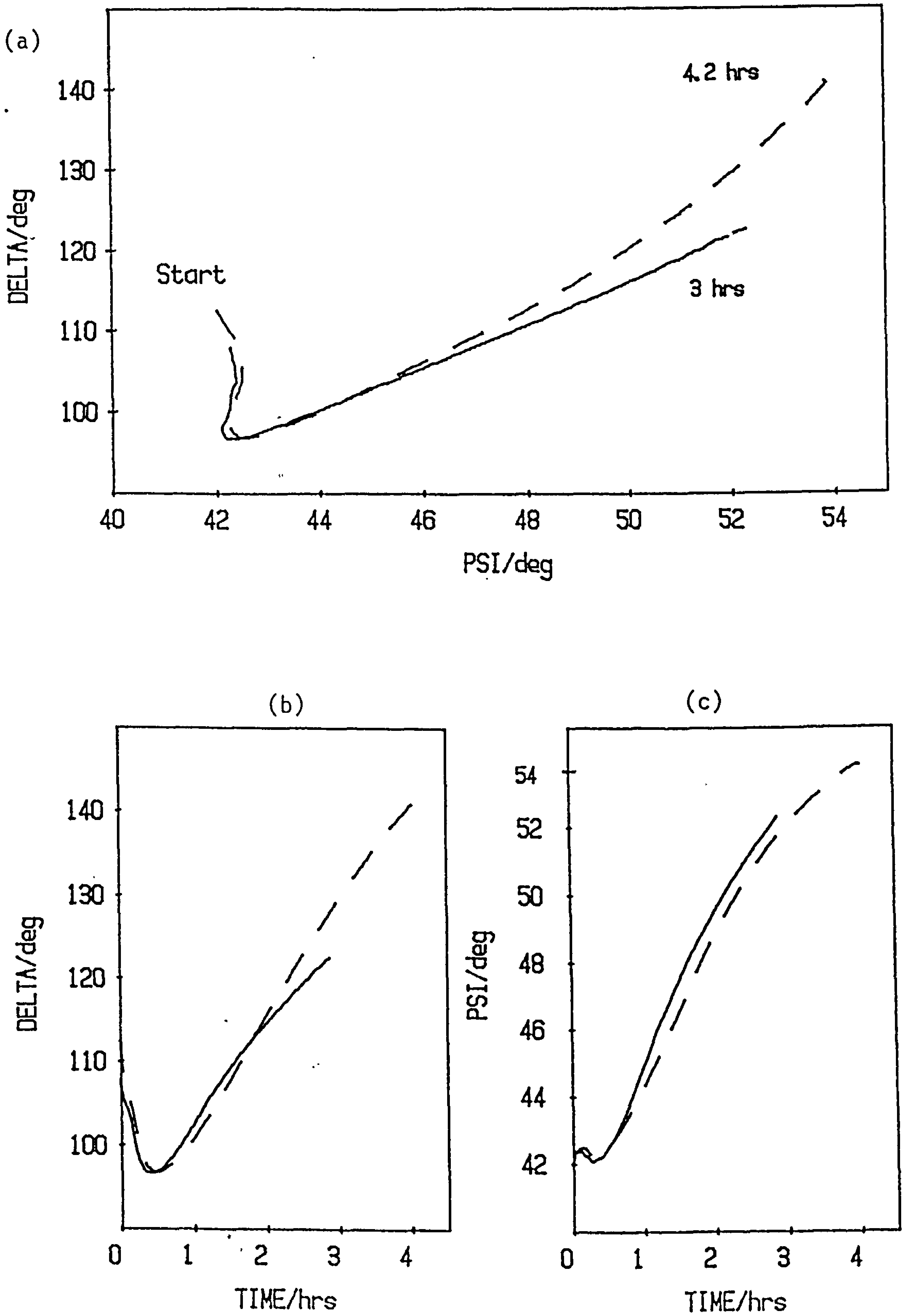

Fig. 6.5 Magnox at open circuit in air-saturated 1 mol/dm^3 NaOH

those seen previously for either Magnox or Mg and again can not be explained by a single non-absorbing film model. However, the much larger changes in Δ and Ψ in 1 mol/dm^3 NaOH compared to 0.01 mol/dm^3 NaOH indicate that there is greater film growth in the more alkaline solution.

6.2 Computer modelling of rough films

6.2.1 Determining Δ and Ψ for a rough surface

Many of the ellipsometric results in this thesis can not be explained by the model of a single non-absorbing film growing on a smooth homogeneous substrate. However, marked deviations from this model are predicted if substrate roughening is taken into account. This proposal of a rough substrate was investigated by computer simulations using multi-film models.

The various theories used to describe reflection from rough surfaces have been discussed in section 2.6. The theories relevant to microscopic roughness fall into two groups - those representing an undulating surface with a correlation length very much larger than the wavelength of light, and effective medium theories which are applicable to roughness with a correlation length less than the wavelength of light. It would seem reasonable to assume that substrate roughening of Magnox and Mg arises from localized corrosion processes such as pitting and will not be well represented by a smoothly undulating surface. The scattering type theories are thus not applicable.

Effective medium theories treat the roughness as a separate layer having its own optical identity which is dependent on the optical constants of the inclusions (fig. 6.6). The rough layer can be treated as a single film or subdivided into a series of 'slices' each with different optical constants. Evaluating the values of Δ and Ψ due to reflection from such films involves several steps:

1. Calculate the volume fraction of each component in the rough layer(s).
2. Using the volume fractions obtained above, and the optical constants of the individual components in each fraction, evaluate the optical constants of the combined phase(s).
3. Determine the values of Δ and Ψ due to reflection from the multi-layered film from the optical constants of each layer.

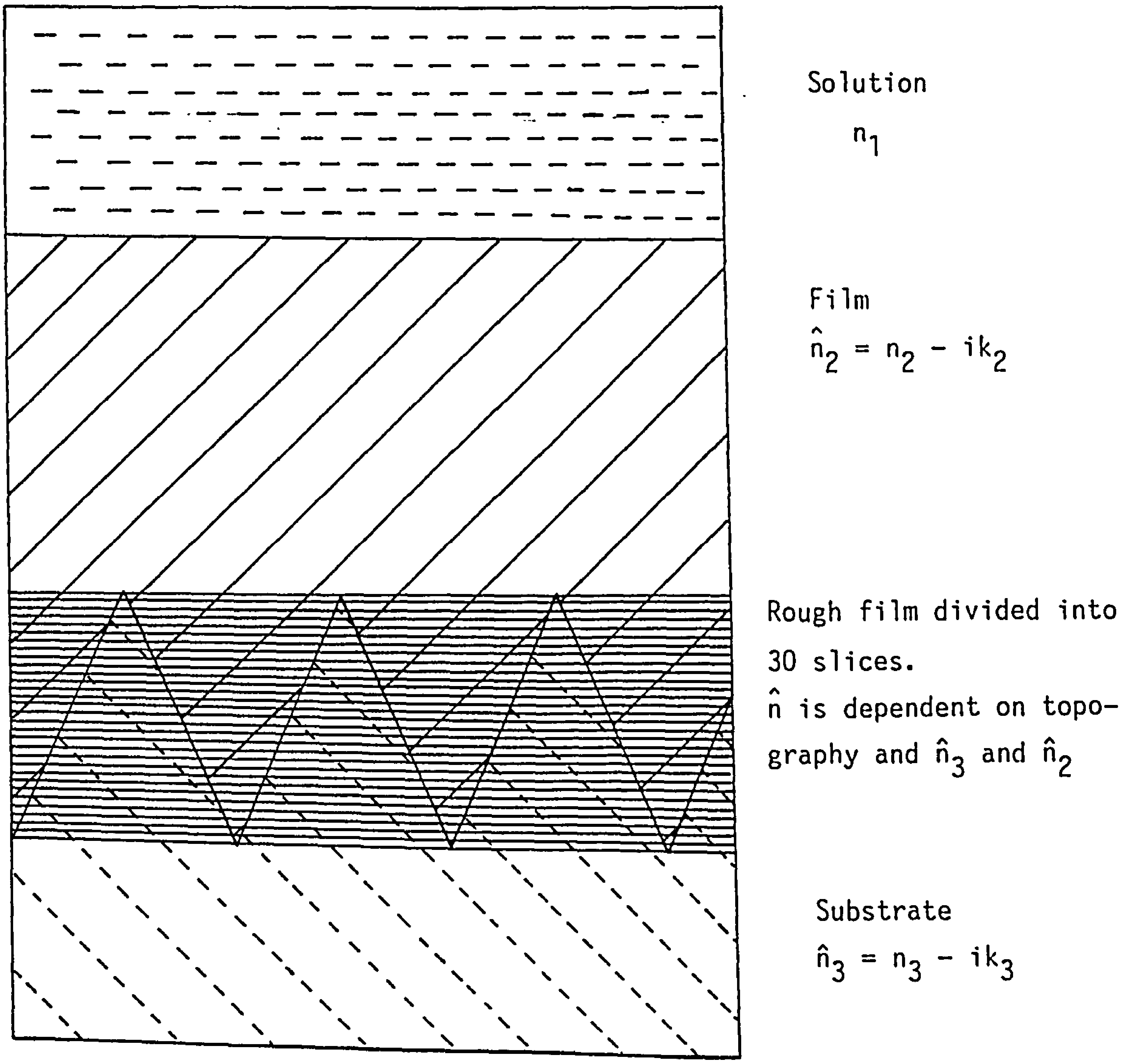

Fig. 6.6 Multi-film model used in modelling rough surfaces

The first step requires an assumption as to the form of the surface topography. In the absence of any information as to the density profile of the rough layer various geometric models which have been used by other authors were chosen.[116,131] These were triangular ridges, hemispheres, cones, inverse hemispheres and inverse cones (fig. 6.7). The volume fraction of substrate, V_f, lying between heights $0 \leq z_1/h \leq z_2/h \leq 1$ above the basal plane for these topographies is given by:

triangular ridges

$$V_f^{tr} = 1 - (z_1 + z_2)/2h \qquad .....(6.1)$$

hemispheres

$$F_f^h = \left| 1 - \frac{z_1^2 + z_1z_2 + z_2^2}{3h^2} \right| \cdot \frac{\pi}{4} \qquad .....(6.2)$$

close packed cones

$$V_f^c = \left| 1 - \frac{z_1 + z_2}{h} + \frac{z_1^2 + z_1z_2 + z_2^2}{3h^2} \right| \cdot \frac{\pi}{4} \qquad .....(6.3)$$

inverse hemispheres

$$V_f^{ih} = 1 - V_f^h \qquad .....(6.4)$$

inverse cones

$$V_f^{ic} = 1 - V_f^c \qquad .....(6.5)$$

Each of these geometric models has a different density profile (fig. 6.8). The close packed cones have the least proportion of substrate in the mixed phase and the inverse cones model the most. The other geometries fall between these two extremes. All these models are highly structured and are unlikely to represent a true rough surface but were chosen to give an idea of the effect of different topographies on Δ and Ψ.

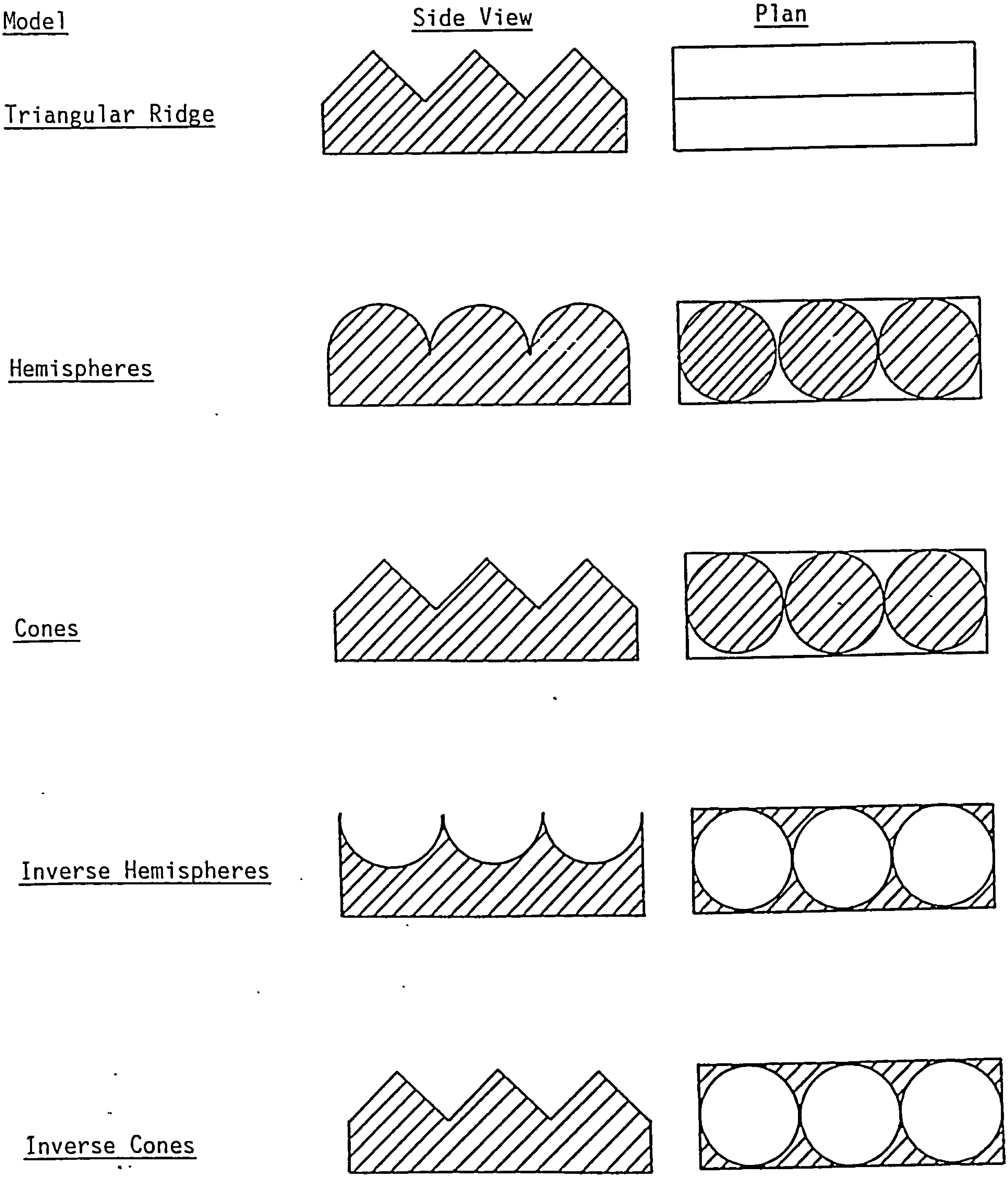

Fig. 6.7 Geometric models used in modelling rough surfaces

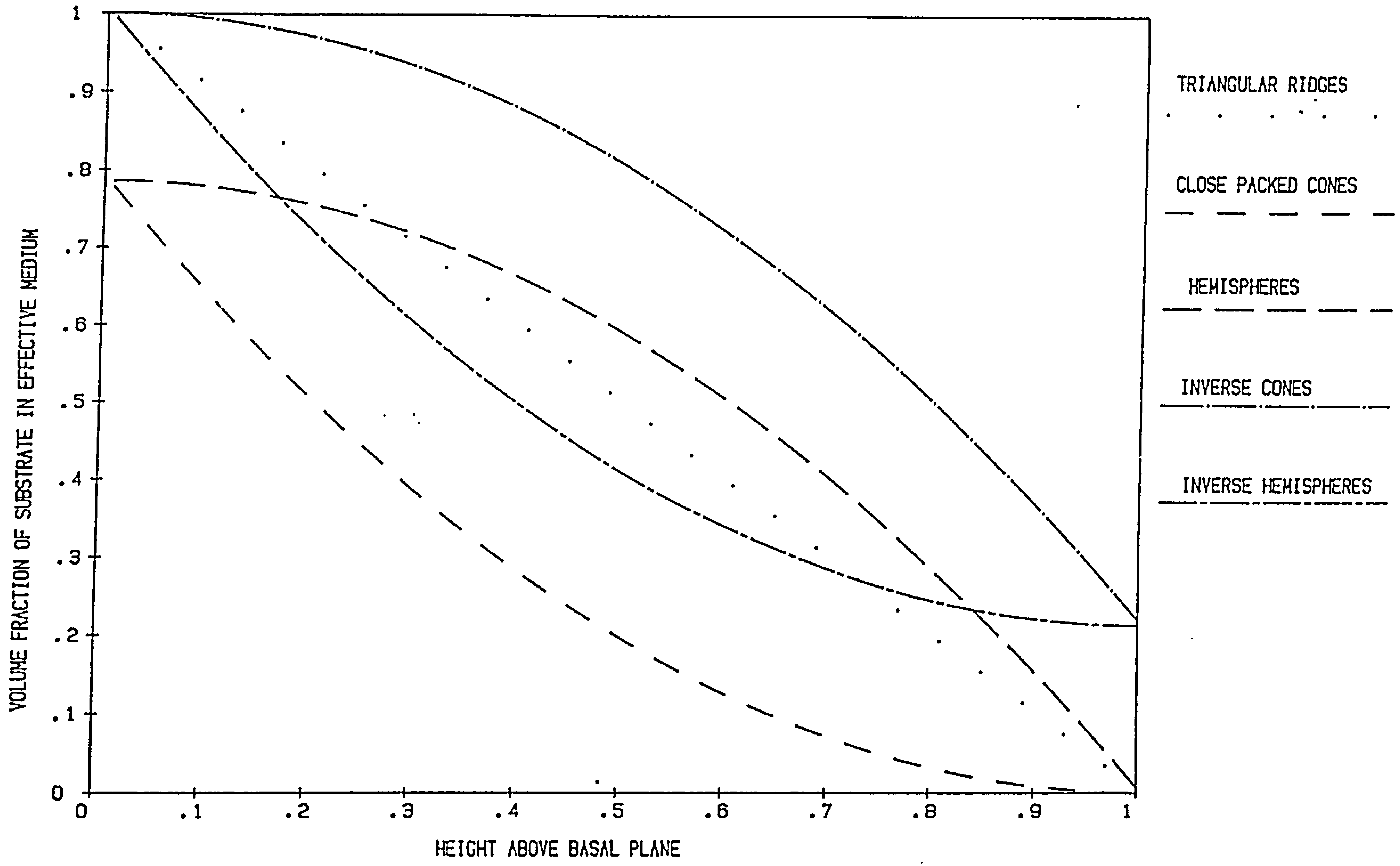

Fig. 6.8 Density profile for different topographies used for rough models

Once the volume fraction of the individual components of the mixed phase has been obtained then the optical constants of the mixed phase can be evaluated. The most suitable theory for this calculation is Bruggeman's effective medium approximation which is self-consistent and does not differentiate between the two phases. Bruggeman's EMA equation has been given in Chapter 2:

$$f_a\left[\frac{\varepsilon_a-\varepsilon}{\varepsilon_a+2\varepsilon}\right] + f_b\left[\frac{\varepsilon_b-\varepsilon}{\varepsilon_b+2\varepsilon}\right] = 0 \qquad .....(2.72)$$

where ε, ε_a and ε_b are the (complex) dielectric constants of the mixed phase, and the phases a and b respectively, f_a and f_b are the volume fractions of a and b in the mixed phase.

Expanding equation (2.72) and using the identity, $f_b = 1-f_a$, the following equation is obtained:

$$-2\varepsilon^2 + \varepsilon[3f_b\varepsilon_b - 3f_b\varepsilon_a + 2\varepsilon_a-\varepsilon_b] + \varepsilon_a\varepsilon_b = 0 \qquad ...(6.6)$$

This is a quadratic equation of the form:

$$a\varepsilon^2 + b\varepsilon + c = 0 \qquad .....(6.7)$$

where $a = -2$, $b = 3f_b\varepsilon_b - 3f_b\varepsilon_a + 2\varepsilon_a - \varepsilon_b$ and $c = \varepsilon_a\varepsilon_b$. It can easily be solved by using the general solution for a quadratic equation:

$$\varepsilon = \frac{-b \pm \sqrt{b^2 - 4ac}}{2a} \qquad .....(6.8)$$

Two values for ε are obtained from equation (6.8). One of these will have a negative value for ε'' and is rejected.

ε' and ε'' can be related to n and k using equations given in Chapter 2:

$$\varepsilon' = n^2 - k^2 \qquad .....(2.29)$$

$$\varepsilon'' = 2nk \qquad .....(2.30)$$

Substituting for n in equation (2.29) and rearranging gives:

$$4k^4 + 4\varepsilon' k^2 - \varepsilon''^2 = 0 \qquad .....(6.9)$$

This is another quadratic and can again be solved using equation (6.8) to give:

$$k = [-0.5\varepsilon' + 0.5\sqrt{\varepsilon'^2 + k\varepsilon''^2}]^{\frac{1}{2}} \qquad .....(6.10)$$

If k is finite then from equation (2.29):

$$n = [\varepsilon' + k^2]^{\frac{1}{2}} \qquad .....(6.11)$$

otherwise

$$n = \varepsilon'^{\frac{1}{2}} \qquad .....(6.12)$$

When the optical constants for each of the films representing the rough layer and the surrounding media are known then Δ and Ψ can be calculated e.g. by using McCrackin's program described in section 4.12.3. This program was adopted to perform the previous calculations. On input of the optical constants of the top film and the required surface topography it calculated Δ and Ψ for various thicknesses of top film and rough layer. This program is appended in A4.

6.2.2 The effect of varying the number of films used to model the rough layer

The effect of subdividing the rough film into several 'slices' was investigated for all five geometries by comparing results calculated by:

(a) treating the rough layer as a single film,
(b) dividing the rough layer into 30 slices,
(c) dividing the rough layer into 80 slices.

Differences in Δ and Ψ between these three approaches were compared for rough films of 0-40 nm on a Mg substrate (n = 0.345, k = 5.85) under a non-absorbing (n = 1.48, k = 0) top film varying from 0 to 140 nm in thickness for an angle of incidence of 70°. Significant differences were seen between (a) and (b) e.g. for 100 nm of top film and a 30 nm rough layer the single film model gave values of $\Delta = 86°$ and $\Psi = 41.2°$ compared to values of $\Delta = 89°$ and $\Psi = 42°$ for the 30 slice rough layer. The fit between (a) and (c) becomes progressively worse as the thickness of both the top layer and rough film increases. Large differences of several degrees in Δ and Ψ are observed for rough films greater than 30 nm and top films thicker than 100 nm. The fit between (a) and (c) is also dependent on the surface topography of the rough layer. The order of best fit is:

<u>Best</u> <u>Worst</u>

inverse hemispheres: hemispheres: triangular ridges: cones: inverse cones

No differences were seen between (b) and (c) i.e. on increasing the number of slices in the rough layer from 30 to 80.

It is apparent from these results that it is not acceptable for this application to model the rough film as a single layer, and computer modelling of the experimental results was therefore undertaken using a 30 slice film.

6.2.3 <u>Comparison between the various geometries used to represent rough layer</u>

A comparison was made of the various geometries described in section 6.2.1. The values of Δ and Ψ were plotted for 120 nm of a non-absorbing film ($n = 1.5$, $k = 0$) grown on rough layers of varying thickness from 0 to 30 nm on a Mg substrate ($n = 0.395$, $k = 5.85$) and are shown in fig. 6.9. All the geometries result in a reduction in Δ and Ψ from the smooth substrate values. This reduction increases in magnitude as the rough film becomes thicker and as the top film becomes thinner.

Three of the geometries - triangular ridges (fig. 6.9a), hemispheres (fig. 6.9b) and cones (fig. 6.9c) give very similar results. The inverse cones (fig. 6.9e) model gives slightly less changes in Δ and Ψ compared to the other models. The other geometry, inverse hemispheres (fig. 6.9d) gives a much greater change in Δ and Ψ for a

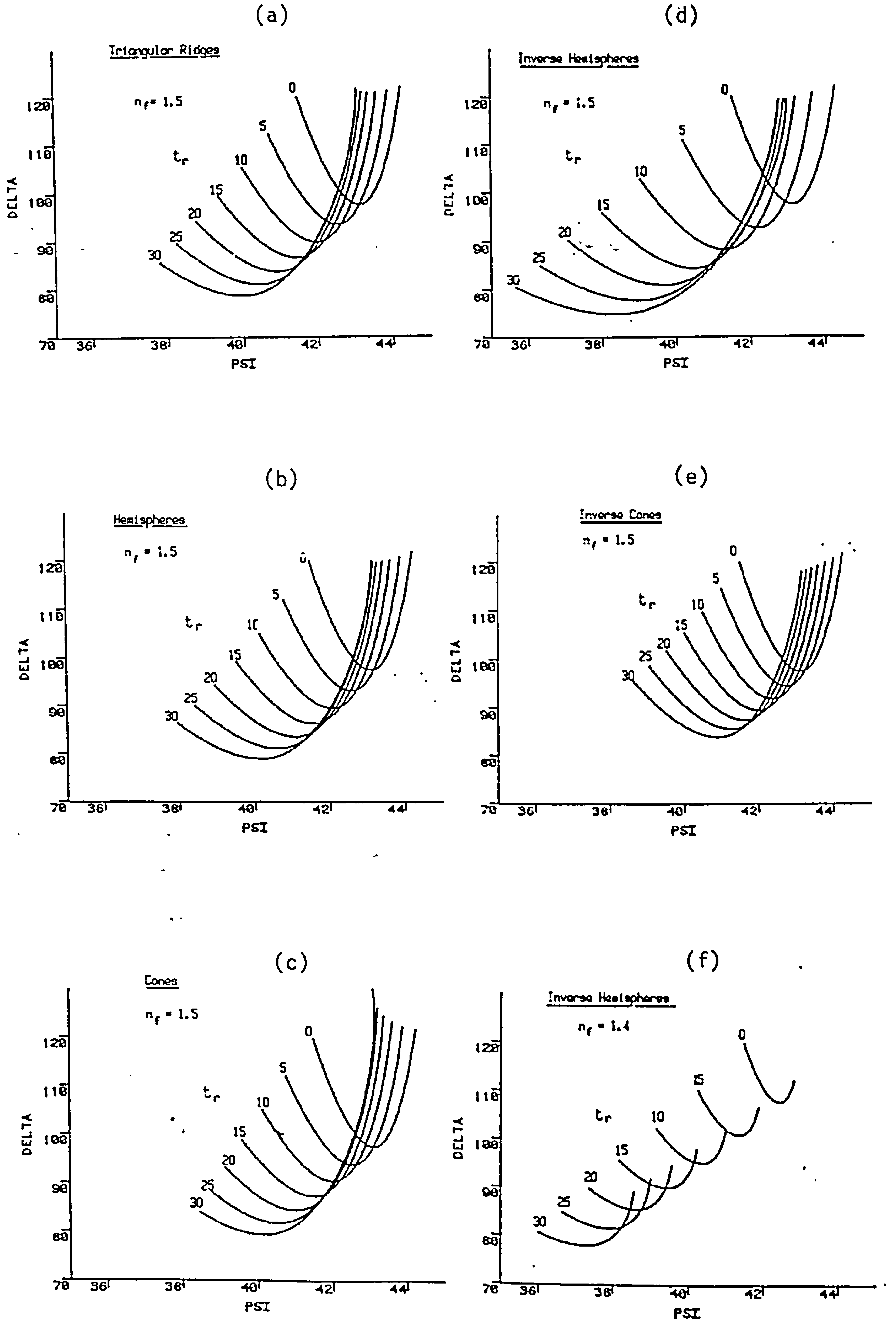

t_r = thickness of rough film (nm) n_f = refractive index of film

Fig. 6.9 Δ,Ψ curves for the different geometries of the rough models given thickness of rough layer. Reducing the refractive index of the top film, fig. 6.9f, from 1.5 to 1.4 also results in an increase in the changes of Δ and Ψ from the smooth substrate values.

6.2.4 Computer modelling of experimental results

Modelling of a rough surface underneath a film using the procedure described in section 6.2.1 involves several variables:

1. n and k of the substrate
2. n and k for the top film
3. surface topography
4. thickness of the top film
5. thickness of the rough layer

The changes of the variables (2)-(5) above with time also has to be considered e.g. does the rough film grow at the same rate as the top film, does the surface topography of the rough surface and the refractive index of the top film remain constant. The trial and error method of modelling experimental results used in section 5.1 is unlikely to give satisfactory results for such complicated models.

The procedure used was to generate a Δ,Ψ 'map' for each of the five surface topographies for various thicknesses of top film and rough layer (fig. 6.10). This process was repeated for several values of n for the top film and the effect of slightly altering n and k for the substrate was also considered. The experimental result was then overlaid over these 'maps' and if possible a fit was obtained between the experimental result and the theoretical predictions. The use of this technique is discussed in the next section.

6.3 Computer simulations of experimental results using rough films

6.3.1 Magnox in 0.01 mol/dm^3 sodium hydroxide

The procedure described in the previous section was applied to the ellipsometric results obtained for Magnox in air-saturated 0.01 mol/dm^3 NaOH (figs. 5.11-5.13). Part of the experimental results could be modelled by first growing a non-absorbing film on a smooth substrate and then roughening the substrate. Fig. 6.11 illustrates the result for a rough film based on triangular ridges compared to an experimental result. A non-absorbing film ($n = 1.48$, $k = 0$) is grown to a thickness

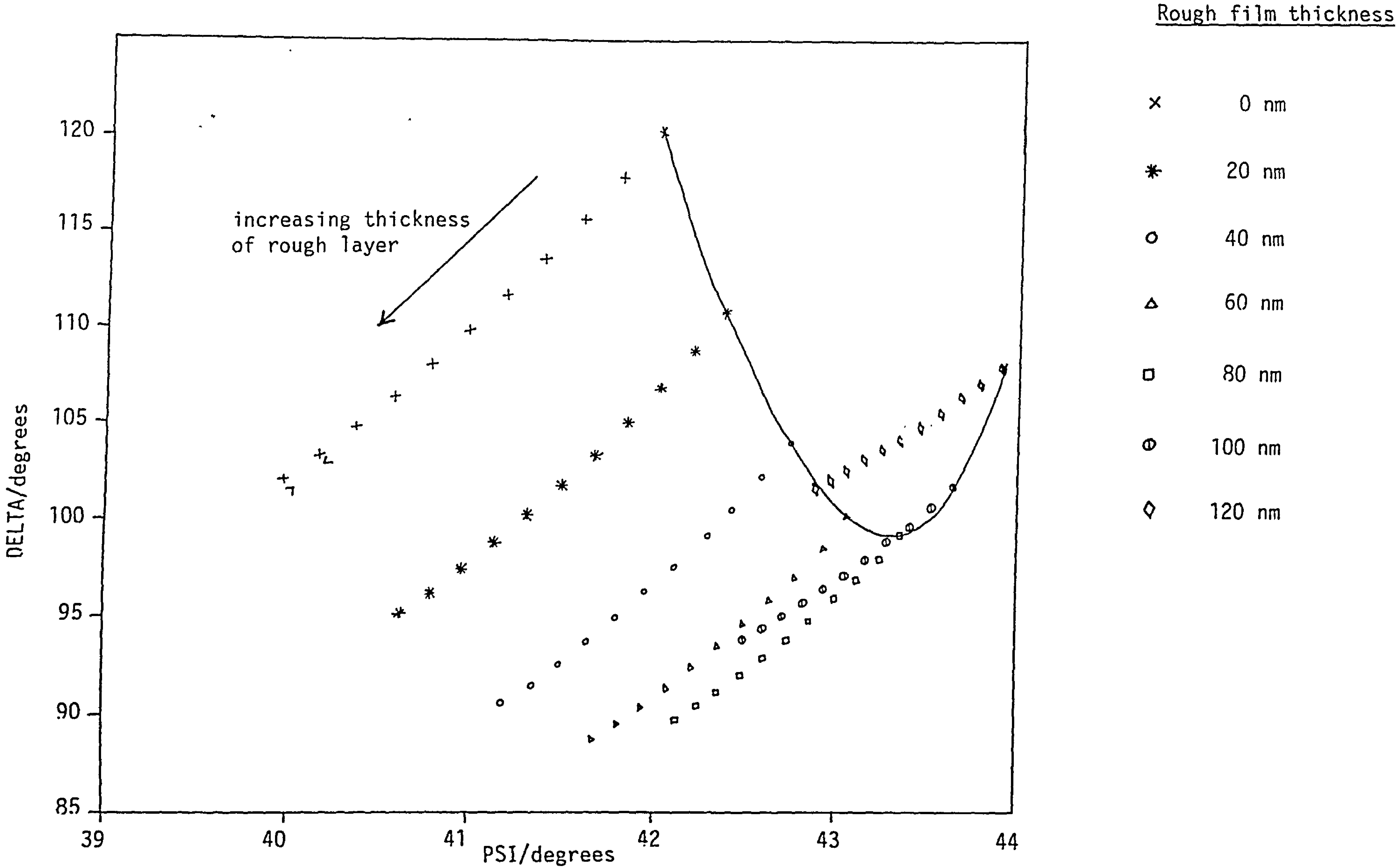

Fig. 6.10 Δ,Ψ 'map' using inverse cones to model rough layer

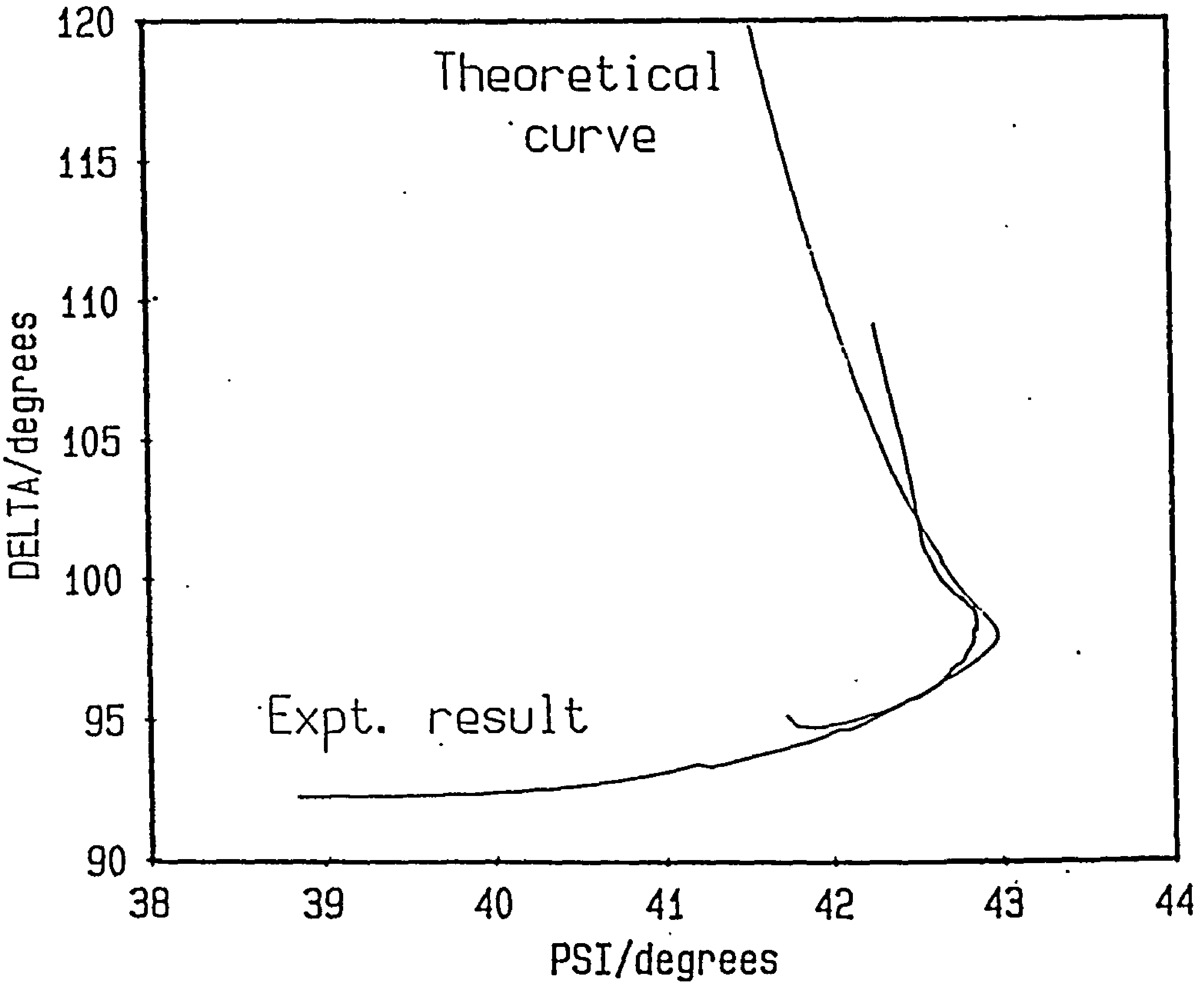

Fig. 6.11 Modelling of Magnox in air-saturated 0.01 mol/dm^3 NaOH using a rough film based on triangular ridges

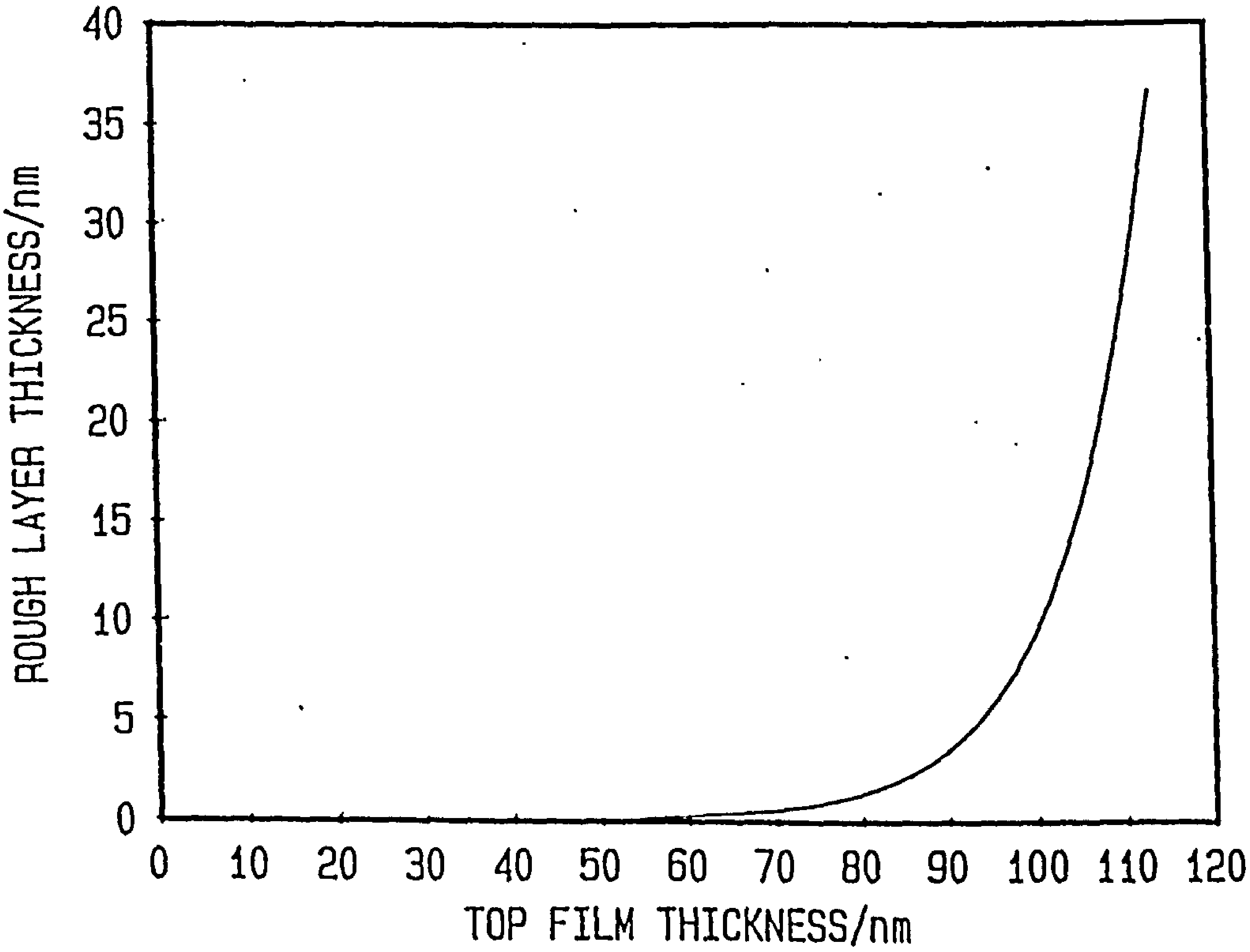

Fig. 6.12 Variation of rough layer thickness with top film in fig. 6.11

of 55 nm then the rough layer begins to grow at an exponential rate with respect to the top layer, (fig. 6.12).

This model is applicable to the period when Ψ begins to decrease and is consistent with the proposal of localized corrosion arising from a reduction in pH and consequent loss of passivity. However, there are marked deviations between the theoretical predictions and the experimental result if both the rough film and the top film continue to increase in thickness. The theoretical model predicts an increase in Ψ after a decrease of several degrees whereas Ψ in the experiments continues to decrease. At longer immersion times the reflected beam becomes more diffuse which indicates that a larger proportion of light is being scattered. The differences between the theoretical prediction and experimental result may therefore arise from errors in the theoretical model which is applicable for specular reflection and microscopic roughness.

A better fit between the experiment and the theoretical prediction was attempted by the use of more sophisticated models. It was found that a continued decrease in Ψ is predicted if the refractive index of the film incorporated into the rough layer decreases. Fig. 6.13 indicates the predicted values of Δ and Ψ for a duplex film composed of a porous top film ($n = 1.46$, $k = 0$) overlying a more dense film ($n = 1.56$, $k = 0$) with a rough substrate underneath. When the combined thickness of the top two layers has reached 100 nm it remains constant and the rough layer begins to thicken. In addition the refractive index of the film incorporated in the rough layer decreases gradually from 1.56 to 1.37, (fig. 6.14). The correlation between this more sophisticated model and the experimental result is much better than that obtained with the previous model. However, an exploration as to why the refractive index of the film incorporated into the rough layers should decrease is required.

An explanation for this decrease would be if a gas was produced at the metal/film interface resulting in the production of voids. The blistering of steels due to the accumulation of molecular hydrogen in voids as a result of corrosion is a well-known phenomenon.[192] As the cathodic reaction in the corrosion of Mg is hydrogen evolution then it is reasonable to assume that there is a possibility of molecular hydrogen being present at the interface.

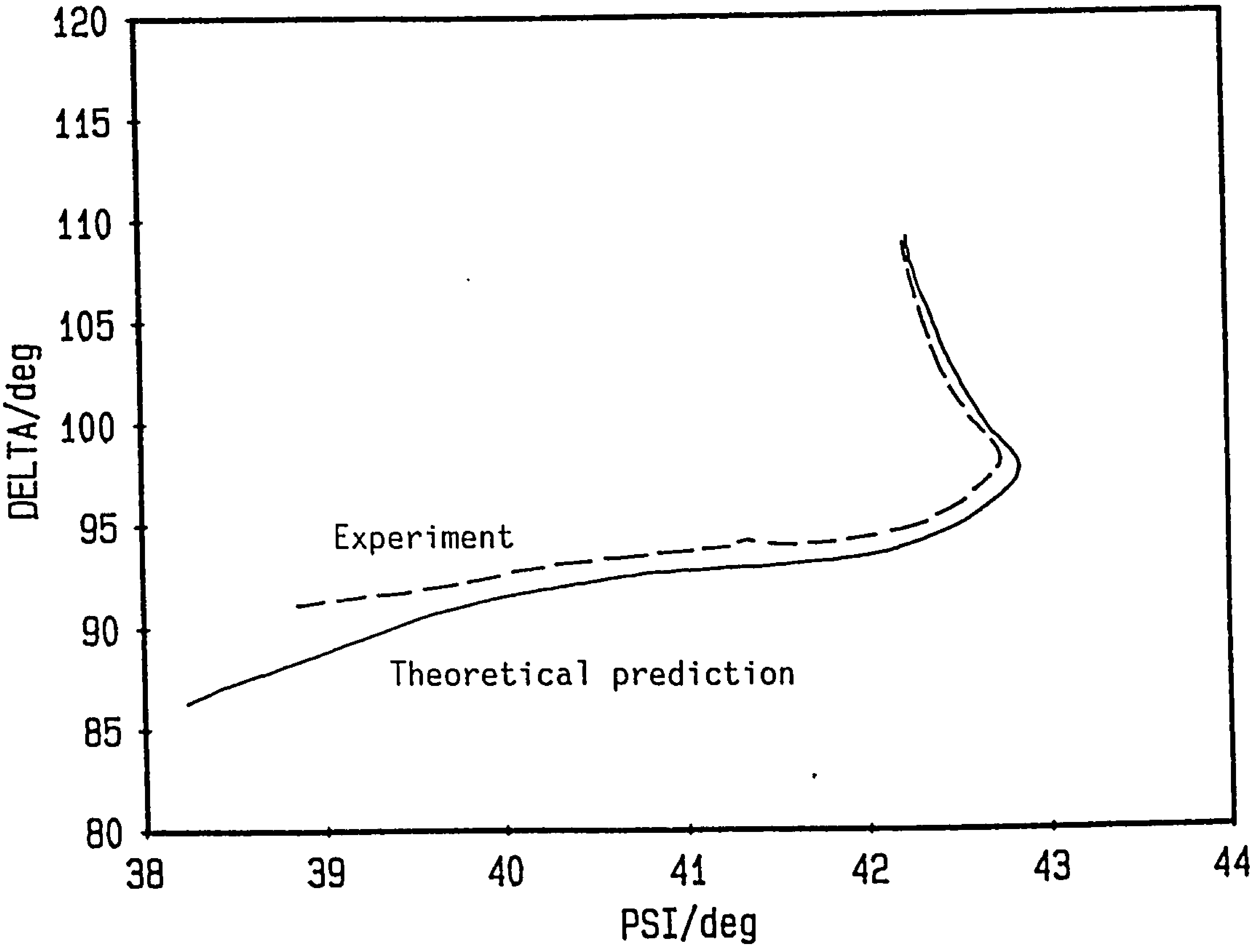

Fig. 6.13 Modelling of Magnox in 0.01 mol/dm^3 NaOH using duplex film and variation of the refractive index of n(film) in the rough layer

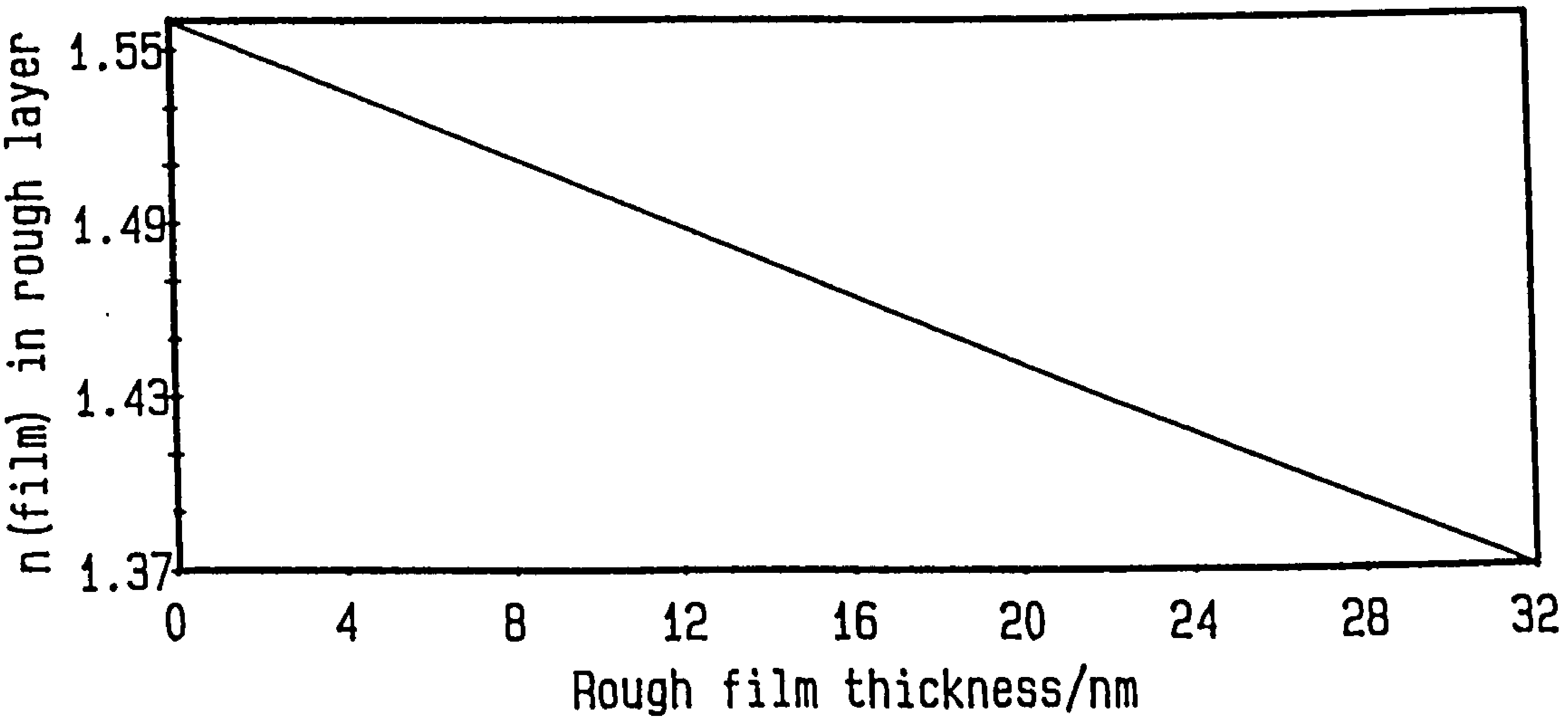

Fig. 6.14 Variation of n(film) with rough film thickness in Fig. 6.13

6.3.2 Magnesium in distilled water

The experimental results in fig. 6.1 for magnesium in distilled water was compared to the theoretical Δ,Ψ values predicted using rough substrate models. It was impossible to obtain a good fit between experiment and theoretical predictions for a model similar to that used for Magnox in section 6.3.1. This resulted in modifications in the computer program to allow for variation in a surface coverage of the rough layer. Fig. 6.15 indicates the results obtained using cones to represent the rough layer for non-absorbing films of $n = 1.56$, $n = 1.48$ and $n = 1.42$. The rough film grows at a constant rate 1/7 that of the top film and the area of coverage of the rough film increases by 1% per 2 nm increase in thickness of the top film. The changes in thickness and surface coverage of the layers is given in fig. 6.16.

The variation in surface coverage of the rough layer from 0 to 100% can be explained by a pitting type mechanism. Small pits are initiated on the surface which grow laterally and vertically. If the pits continue to grow laterally and more pits are initiated on the surface then after a certain period the whole surface will become rough and will correspond to a 100% surface coverage of the rough layer.

The best fit between the theoretical prediction and the early stages of film growth (figs. 6.1 and 6.15) is obtained for a refractive index of $n = 1.48$ for the film overlying the substrate. In the later stages of film growth a value of $n = 1.42$ gives a better correlation between experiment and theory. This implies that the film is fairly porous initially ($n = 1.48$ compared to $n = 1.56$ for $Mg(OH)_2$) and becomes even more porous in the later stages of film growth. This would occur if the top film slowly dissolves in the solution. The dissolution of $Mg(OH)_2$ is dependent on the pH with the dissolution rate increasing with decreasing pH.[43] An increase in porosity or the film ages would thus appear likely.

6.3.3 Magnox in distilled water and 1 mol/dm^3 sodium hydroxide

It is not possible to model the ellipsometric results for either Magnox in water, or in 1 mol/dm^3 NaOH using rough films as described previously. The values of Δ and Ψ obtained for Magnox in water however, can be modelled if slightly different optical constants are used for the bare surface ($n_s = 1.2$ and $k_s = 5.68$ compared with $n_s = 0.75$ and

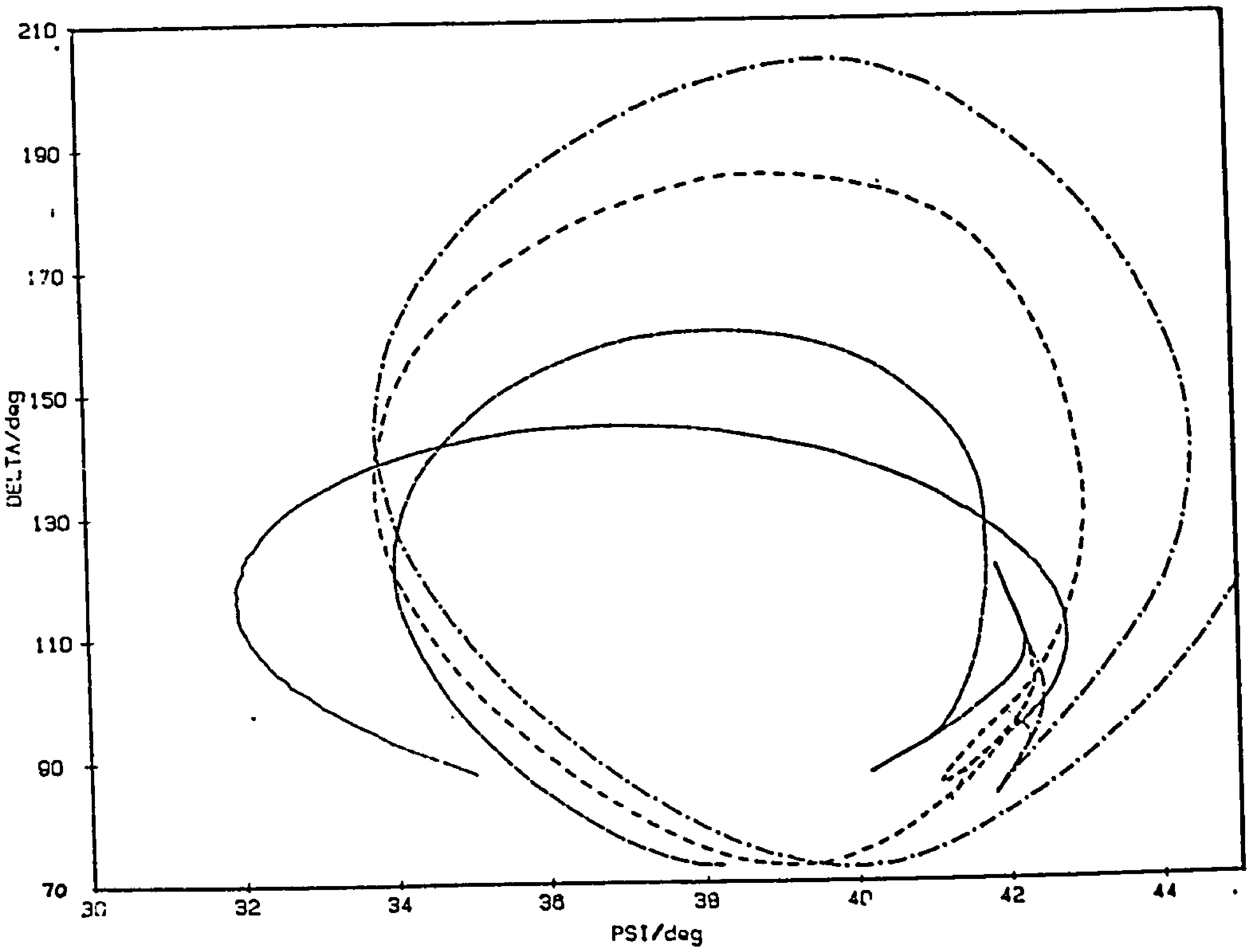

———— Experiment

– – – – – = n(film) = 1.56

—·—·— = n(film) = 1.50

- - - - - - - - = n(film) = 1.44

Total film thickness = 500 nm

Fig. 6.15 Modelling of Mg in distilled water using a rough film based on a cones model

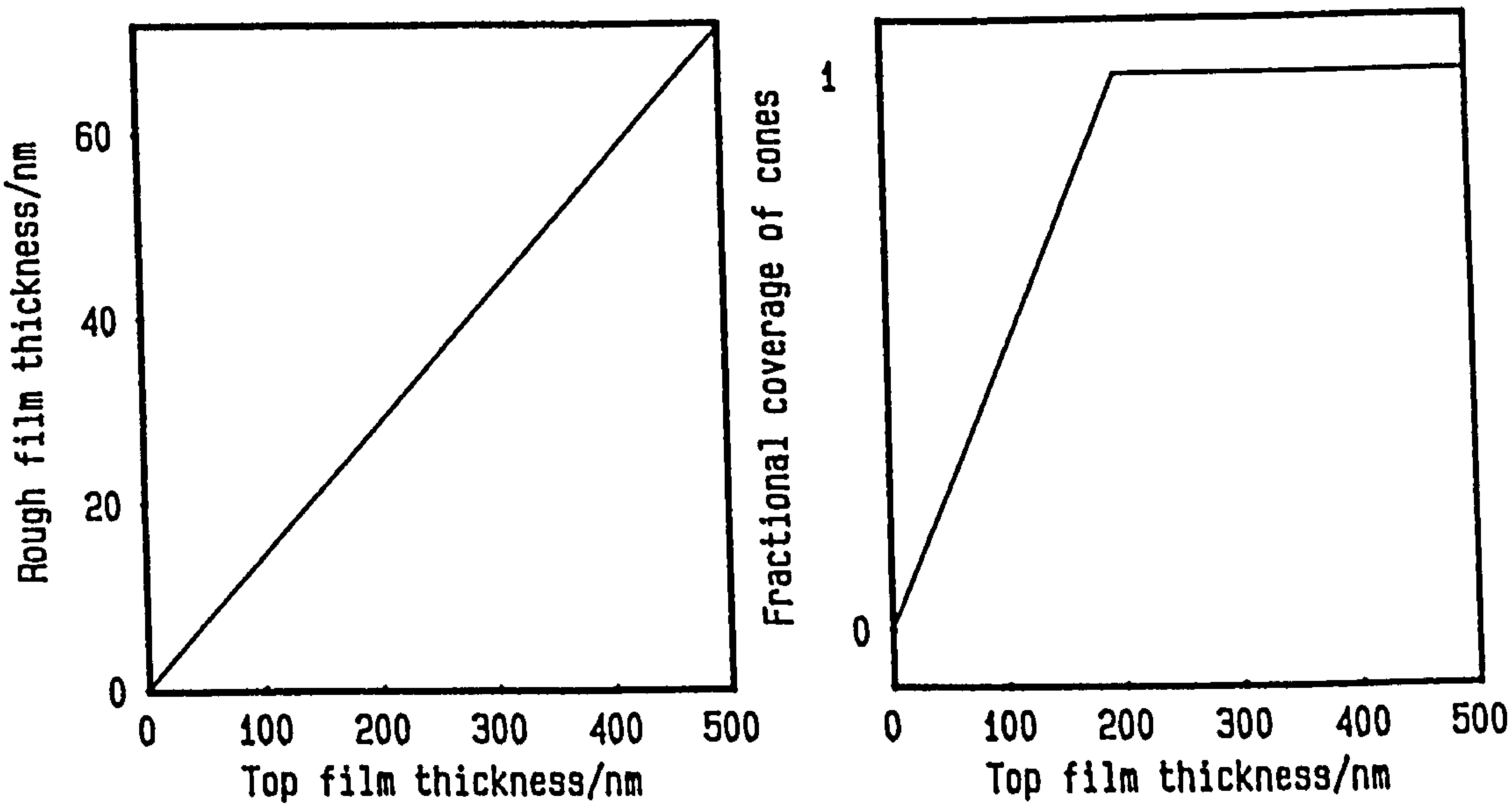

Fig. 6.16 Variation of rough film thickness and fractional surface coverage of cones with top film thickness

k_s = 5.85). The results in fig. 6.17 then indicate that a fairly porous film (n_s = 1.56, k_s = 0) of about 160 nm has formed on Magnox after 4 hours immersion in water.

The result 'in NaOH is much more difficult to model, particularly with respect to the behaviour of Δ.Ψ The results can be modelled roughly by using a single metallic film growing in the Magnox surface (n_f = 1.56, k_f = 5.75) fig. 6.18. This is quite different to the rough films considered previously which had optical constants intermediate between a rough film and Mg or Magnox.

The mechanism by which the optical constants of the metal surface may change is unclear but the observation that it does not occur on Mg suggests it may be due to the presence of one of the alloy constituents such as aluminium. If selective leaching of one of the alloy components occurred, as is the case for e.g. brass in seawater,[193] then it is possible that the surface layers of the metal may become enriched with the remaining components. This would then have the effect of changing the optical constants of the underlying substrate.

6.3.4 Discussion of theoretical modelling of experimental results for films grown on Mg and Magnox using rough layers

The results in sections 6.3.1 and 6.3.2 illustrate the success that can be achieved in modelling complicated results using models which take account of surface roughening. The major problem in calculations of this nature using multi-parameter computer simulations is the lack of experimental parameters measured. The experimental results do not permit all the variables such as thickness of each layer, optical constants of the films etc., to be determined with any degree of accuracy. Confirmation of these predictions was therefore sought by further experiments.

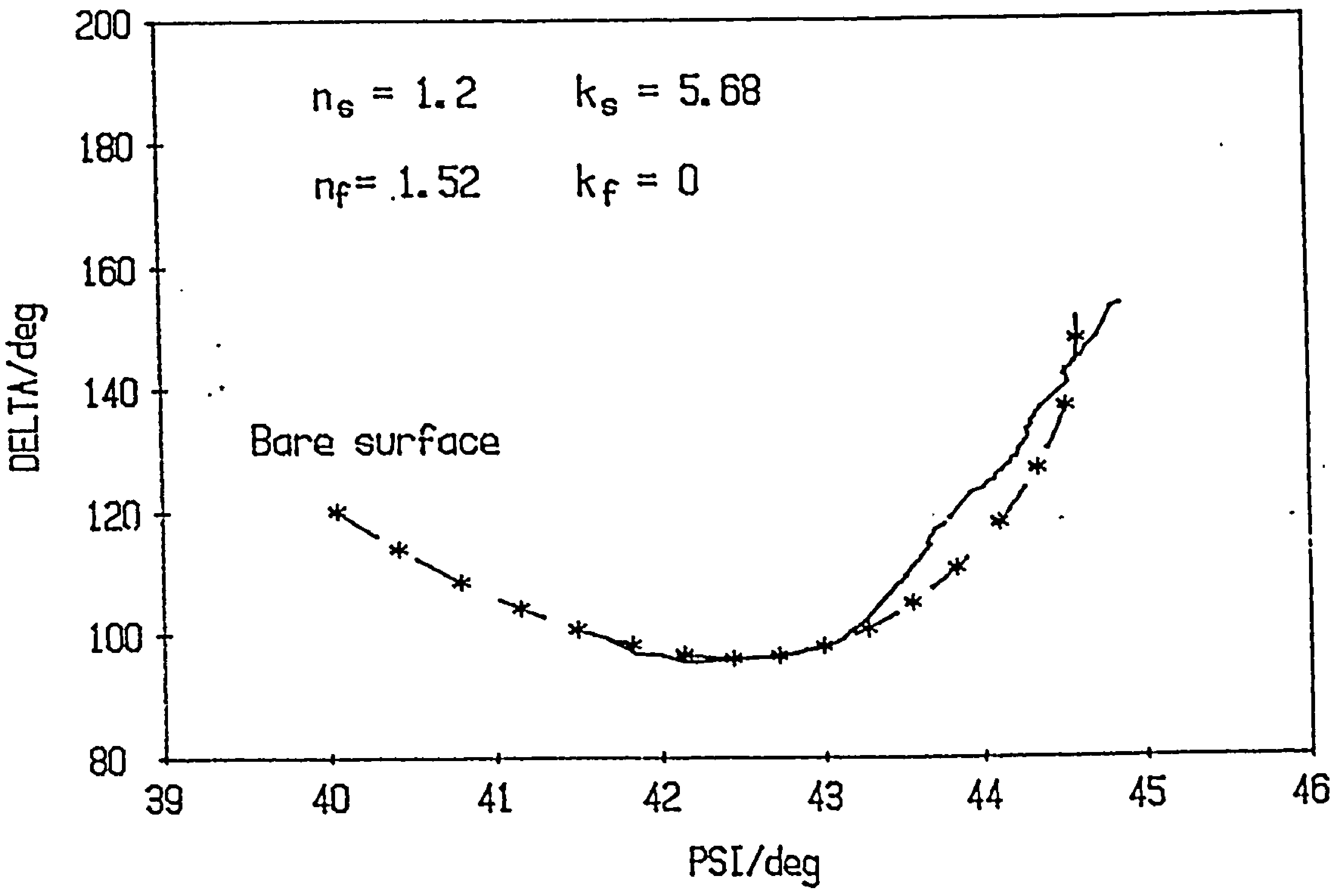

Fig. 6.17 Theoretical modelling of Magnox in distilled water

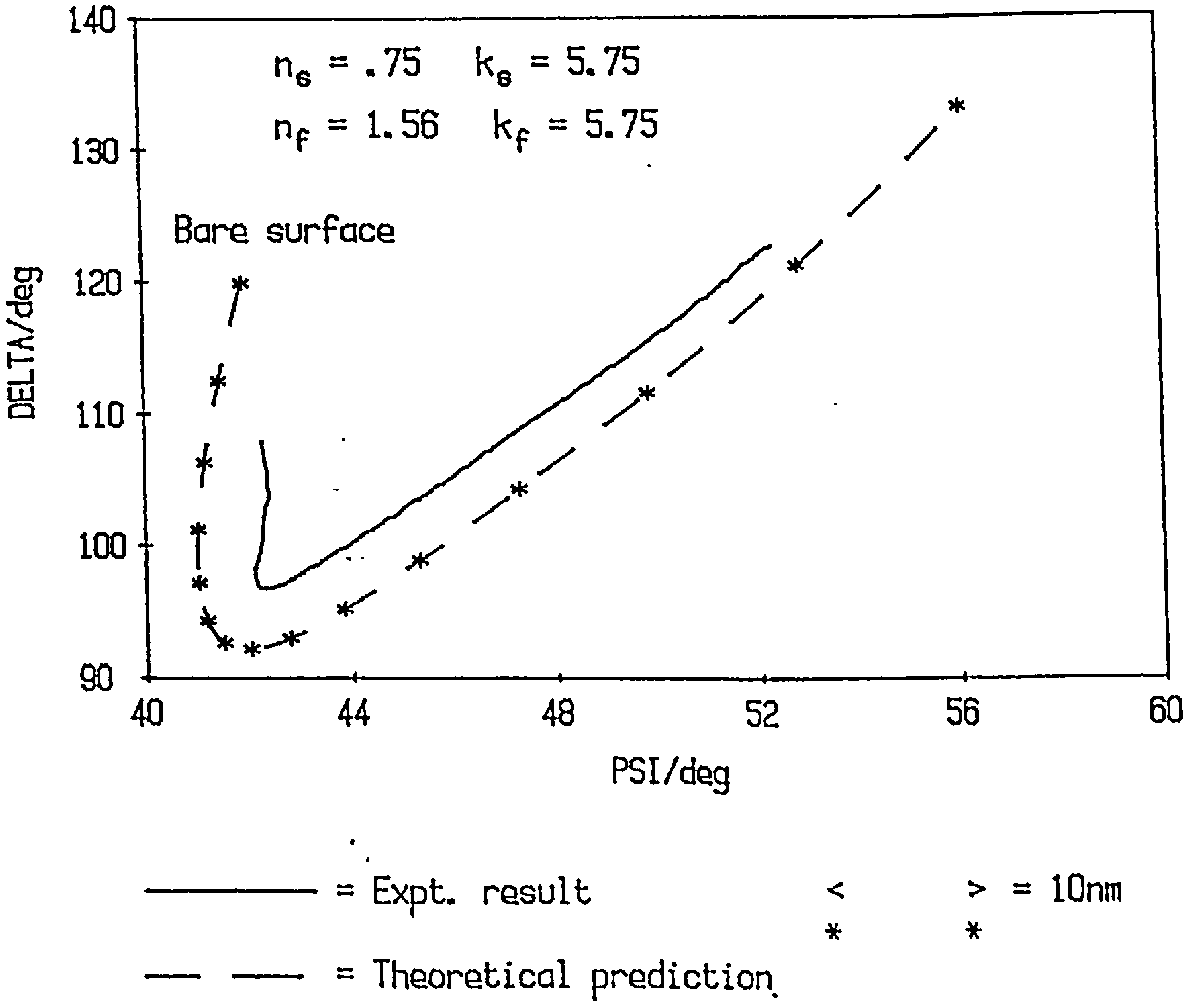

Fig. 6.18 Theoretical modelling of Magnox in 1 mol/dm^3 NaOH

6.4 Further experiments to investigate the proposal of substrate roughening

6.4.1 Ellipsometric investigations

One way in which the number of experimentally determined parameters can be increased is to vary the angle of incidence or the wavelength of light used. Snyder et al.[194] have recently published work describing the use of this technique. They determined the thickness and composition of multiple layer semiconductor heterostructures and found good agreement between theoretical predictions and experimental results.

The effect of varying both the angle of incidence and the wavelength of light for a rough model similar to that in section 6.3.2 is shown in figs. 6.19 and 6.20. The ideal result would be for a large change between the predictions for the rough model on changing either the wavelength or the angle of incidence. It is also a requirement that there should be significant differences between the result based on a rough substrate and one based on a smooth film/substrate interface. Changing the wavelength of light from 632.8 nm to 400 nm does not result in large differences in the predicted result for this model. Changing the wavelength to 400 nm would also necessitate the use of the xenon arc lamp which gives a less intense incident beam compared to the He/Ne laser. It was thought that this would be a problem in monitoring film growth on Mg in distilled water due to the appreciable scattering of the light beam by the fairly thick film which forms.

Changing the angle of incidence does have a marked effect on the results predicted by the theoretical models. It was decided to use an angle of incidence of 50° to record the film growth on Mg in distilled water as this angle of incidence produced a quite different result to that at 70°. Although the result in fig. 6.21 does not correspond to the prediction in fig. 6.20, the behaviour of Ψ does suggest that substrate roughening does occur. The differences between figs. 6.20 and 6.21 may thus be due to variations in topography of the roughened substrate between the samples in the two experiments. This problem of reproducibility could have been resolved by obtaining values of Δ and Ψ at various angles of incidence throughout an experiment. This was not done however due to lack of time.

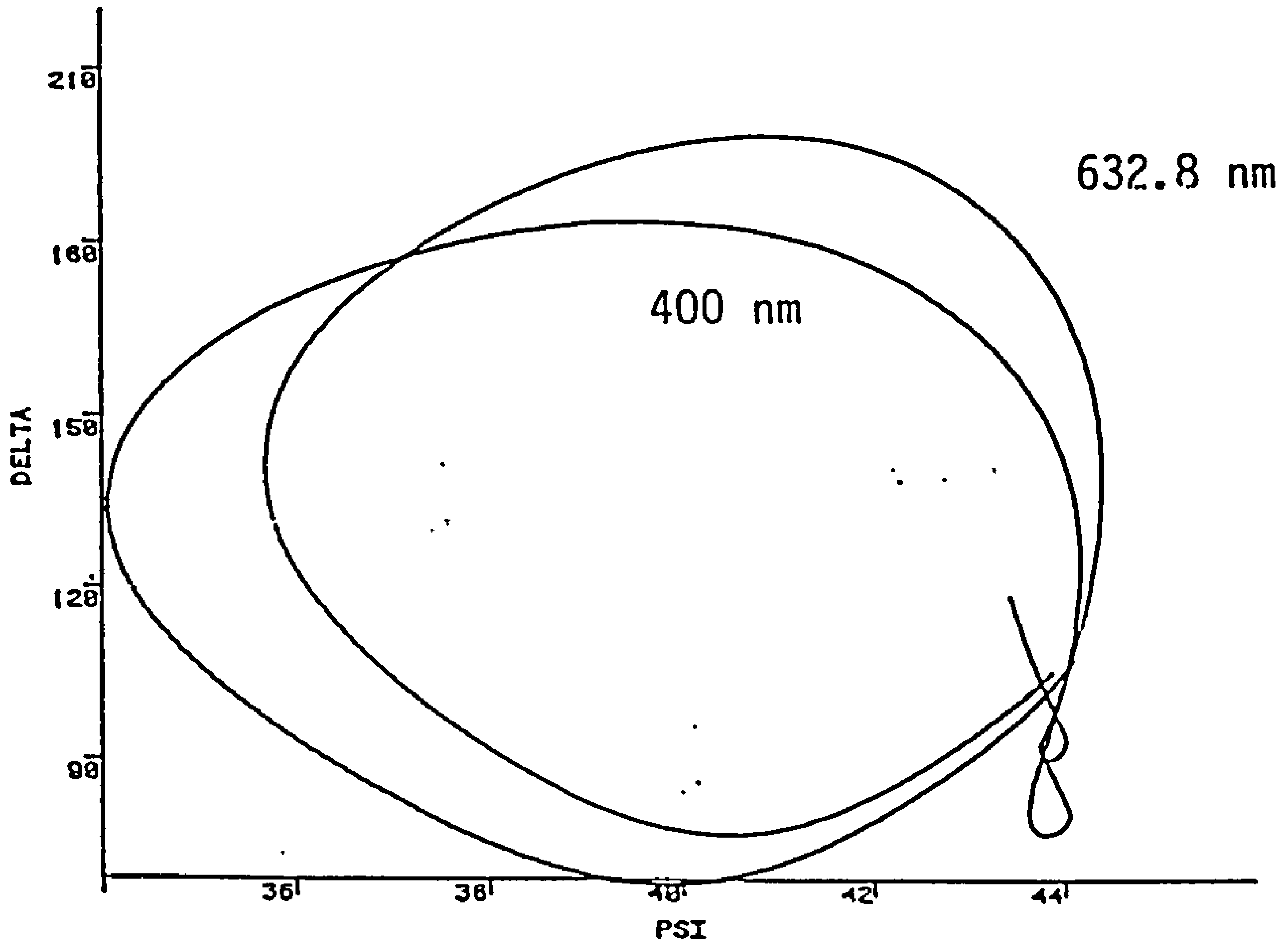

Fig. 6.19 Variation of Δ,Ψ curves with wavelength for roughness model based on an inverse cones model

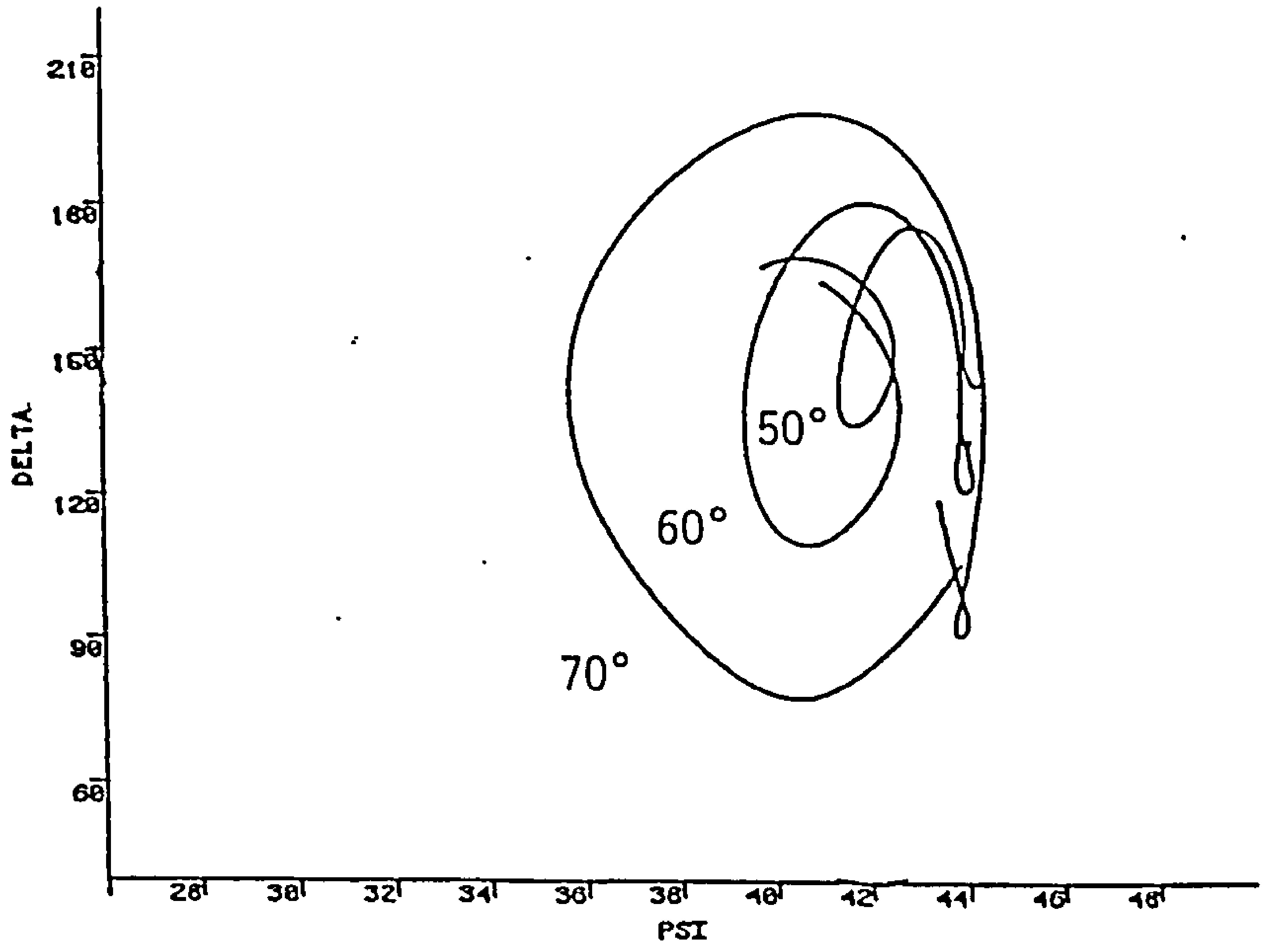

Fig. 6.20 Variation of Δ,Ψ curve with angle of incidence for roughness model based on an inverse cones model

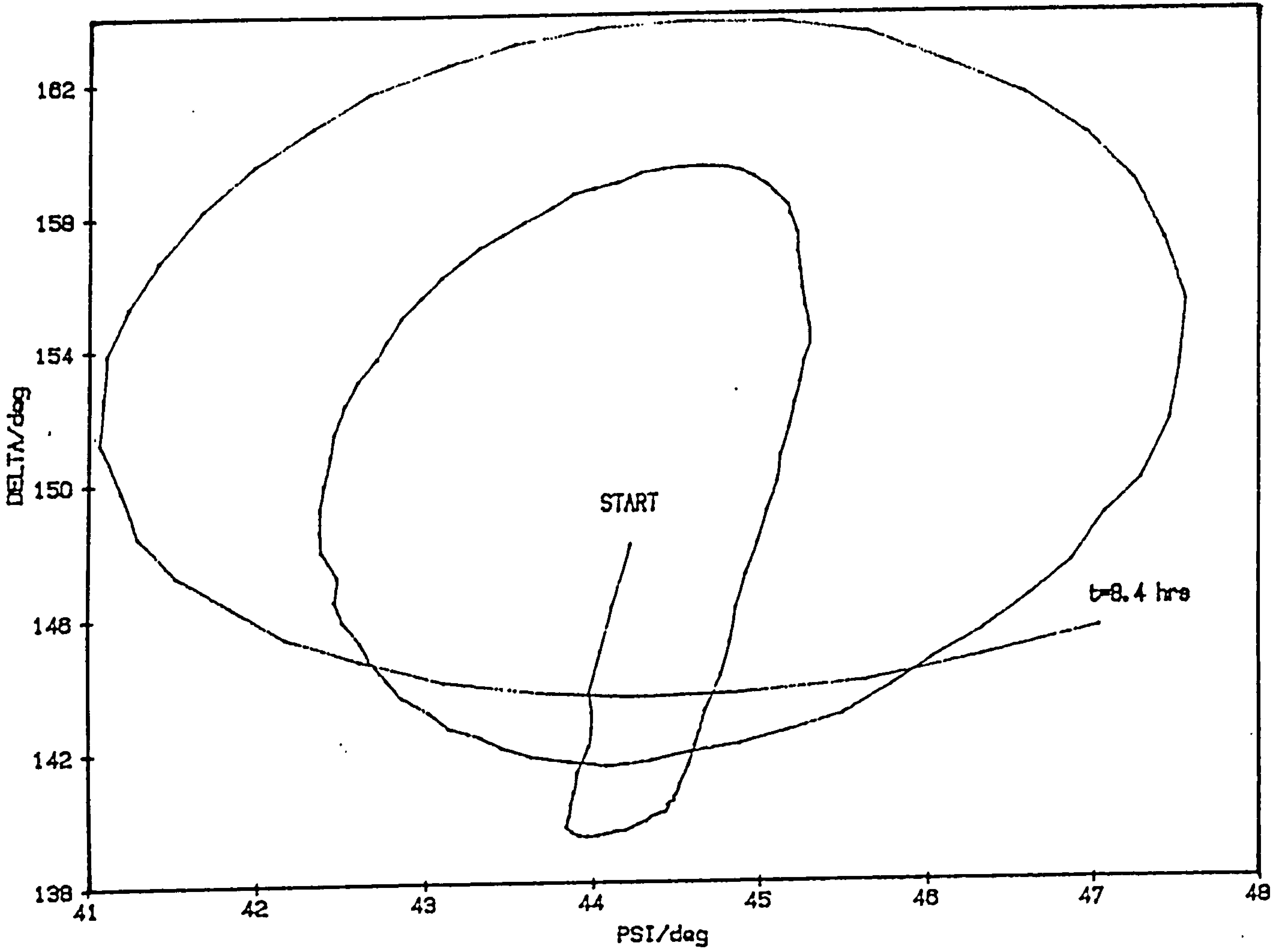

Fig. 6.21 Magnesium in distilled water at an angle of incidence of 50°

6.4.2 Other methods of investigation

There are various techniques available for examining the topography of rough surfaces, by scanning electron microscopy (SEM), transmission electron microscopy (TEM) and stylus measurements. All of these techniques have been used to study rough surfaces in conjunction with ellipsometric analysis.[121,130,131] Evaluating the topography of a bare surface or the film/air interface however, requires the removal of either the film or the substrate whilst retaining the original topography. A common technique is to obtain a thin slice or cross section of a filmed surface using an ultramicrotome and then examining this section by TEM.[195] Alternatively carbon replicas of fracture sections can be prepared and analysed by TEM or SEM.

TEM has much higher resolution than SEM but the preparation of the very thin samples necessary for TEM requires a high degree of skill and the use of, e.g., an ultramicrotome or ion beam thinning. For these reasons SEM was chosen to study the topography of the Mg substrate underneath corrosion films grown in various environments.

Thin magnesium foil was polished and etched in 0.2% citric acid then immersed in demineralized water or 0.01 mol/dm^3 NaOH, with and without a nitrogen blanket. The samples were then placed in liquid nitrogen for about 1 minute and then bent into a 'V' shape using tweezers (fig. 6.22). On removal from the liquid nitrogen the samples were air-dried and sputtered with gold before examining in the SEM. It was hoped that this technique would produce cracks in the oxide film through which the film/substrate interface could be observed. This method has proved successful in investigation of substrate roughening under anodic films grown on aluminium.[196]

Initial experiments indicated that the cracks produced by this treatment were too narrow to permit observation deep within the crack. Increasing the angle through which the samples were bent widened the cracks and did permit observation of the base of the cracks. Unfortunately there still appeared to be a film present at the base of the crack as well as considerable debris and surface damage presumably arising from the preparation of the fracture. The debris could be removed by ultrasonic cleaning in an inert solvent but this would not resolve the problem of surface damage due to the preparation of the fracture. In hindsight it would seem that an alternative technique is needed such as TEM analysis. Unfortunately lack of time and the necessary equipment precluded this.

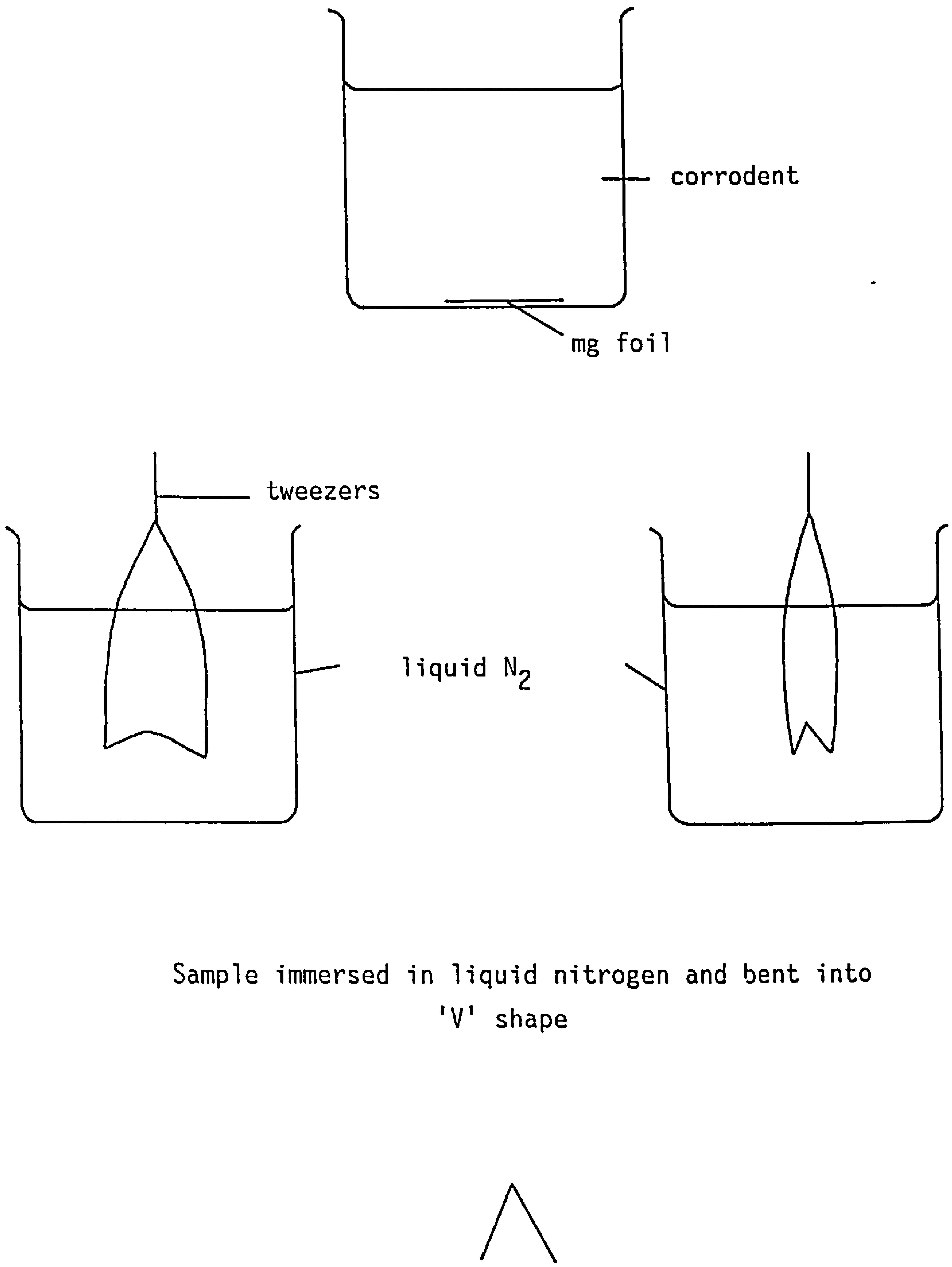

Sample immersed in liquid nitrogen and bent into 'V' shape

Sample sputtered with Pt

Region of crack examined by SEM

Fig. 6.22 Preparation of sample for SEM investigation

CHAPTER 7 SUMMARIZING REMARKS

This thesis is a report of an investigation into the early stages of corrosion of Magnox and Mg in alkaline environments. Most of the work was undertaken in situ using an automatic nulling ellipsometer in conjunction with an electrochemical cell. In vacuo surface analysis using SIMS and Auger spectroscopy with ion beam sputtering has been used, where possible, to provide additional information and to confirm the ellipsometric results. Although none of the experimental data conformed to an ideal model of a single homogeneous film growing on a smooth substrate, considerable information was obtained from the use of ellipsometry.

The rate of corrosion of Magnox in air-saturated 0.01 mol/dm^3 NaOH, in the absence of aggressive ions, is initially rapid, with the film growing from 45 nm to 85 nm in the first 90 minutes. The corrosion rate decreases thereafter to a roughly linear increase in film thickness with time. After 7 hours immersion at 20°C the film thickness is about 100-120 nm. This value is in good agreement with results obtained by ex-situ analysis using AES (113 ± 9 nm for a sample immersed under identical conditions for 6 hours). SIMS analysis of a sample under these conditions gave a slightly larger film thickness (150 nm after 6 hours immersion). These differences may arise from experimental variation between samples, or in the case of SIMS, from matrix effects.

The initial rapid fall in the rate of corrosion of Magnox in air-saturated 0.01 mol/dm^3 NaOH indicates that the film formed during the first 30 minutes is protective. However, although film growth continues throughout the experiment, as evinced by the changes in Δ and Ψ, the corrosion rate remains fairly constant after the first 90 minutes. This suggests that the film formed after the first 90 minutes may not be protective which in turn implies a bi-layer film may exist such as that proposed by Bradford et al.[49] They put forward the idea of a permeable top film through which water molecules could permeate. The corrosion rate is then dependent on the thickness and transport processes occurring across the underlying protective or 'barrier' layer. The model of a bi-layer film and the proposal of a porous top film were examined by computer simulations. The bulk corrosion film was found to be very porous. No evidence of an underlying film was found but a limit of 5 nm was given for the thickness of this film on the basis that it is composed of MgO. This limit is considerably less than the previous value of 100 nm obtained by ion beam studies. If the 'barrier' film is composed of $Mg(OH)_2$ then this limit is reduced even further. In addition to being fairly thin, potential sweep results indicate that the underlying protective layer is 'leaky' and not highly insulating.

Reducing the oxygen content of the corrodent from saturation to fairly low levels has no effect on the corrosion of both Mg and Magnox in 0.01 mol/dm^3 NaOH. This is in accord with results obtained by Blanchet[54] and Khalaf.[56] It is possible though that very low levels of oxygen may modify the electrode reactions but facilities for investigating this were not available.

The addition of 1000 ppm fluoride does not modify the bulk optical constants of the corrosion film on either Mg or Magnox in 0.01 mol/dm^3 NaOH. However, the corrosion rates are less after the first half-hour in fluoride dosed solutions compared to solutions in which fluoride is absent. This does support the suggestion[49] that fluoride may be incorporated into a thin film near the metal/oxide surface, with slow transport of ions through this controlling the corrosion rate. On investigation of Mg and Magnox in fluoride dosed solutions by potential sweep experiments however it was found that the fluoride had not improved the poor insulating properties of the protective film.

The deleterious effect of chloride was due to purely localized corrosion processes such as pitting as would be the case with bare metal. No modification of the bulk film was observed as might be the case if anion entry into the film resulted in a greatly increased ion conduction in the 'contaminated' oxide film[183]. A deeper investigation of these processes would be useful but requires the use of an ellipsometer able to scan the electrode surface.

Magnesium immersed in neutral and alkaline solutions gave anomalous results - a decrease in Ψ, on immersion, to values below that for the bare metal. This was attributed to substrate roughening. The mechanism by which this roughening takes place in 0.01 mol/dm^3 NaOH is unclear as it does not occur on Magnox under similar conditions. It was tentatively suggested as being due to channelling of the corrosion attack through weak points and fissures in the film present on Mg. This film is more porous than that on Magnox and hence may explain the differences seen between Mg and Magnox. Substrate roughening also complicates the ellipsometric result for Magnox immersed in 0.01 mol/dm^3 NaOH for which the pH subsequently falls below 11.5.

Computer simulations have been used to model these theoretical results by treating the rough layer as a separate film having optical constants dependent on the inclusions in this film. Some of the results could be modelled by such means but the fit between theory and experiment was not particularly good. Attempts to confirm the substrate roughening by ellipsometry and SEM were unsuccessful. The model of a rough film could not explain the results obtained for Magnox immersed in either water or 1 mol/dm^3 NaOH. Under these conditions it appeared that there was a change in the optical constants of the underlying substrate. This implied that there may be selective leaching of one of the alloying components in Magnox.

The above comments indicate the complicated nature of the corrosion processes which occur on Mg and Magnox in neutral and alkaline media. They also illustrate the sensitivity of ellipsometry in measuring such processes. Although the results for Magnox corroding in 0.01 mol/dm^3 NaOH are consistent with a bi-layered model there are still several outstanding questions concerning the exact nature of the protective film. The application of current 'state of the art' rough models to complex real systems shows the gulf that exists between theory and experiment. Considerable additional work would have been undertaken given more time. This would have involved the inclusion of more than two components in the rough film, to take into account the presence of voids, and also the effect of inhomogeneous films. Additional experimental data would have been obtained by varying the angle of incidence and wavelength scanning. The recent interest shown in substrate roughening by using such techniques and the experimental response of more 'ideal' rough surfaces would also prove beneficial in modelling the results for Mg and Magnox.

REFERENCES

1. A.B. McIntosh, K.Q. Bagley, J.Inst.Met., 84, 1955, 251.

2. S.F. Pugh, J.E. Harris, L.E. Raraty, J. Wareing, G.A. Burras, J.E. Anthill, B.W. Mort, R.S. Busk, J.Brit.Nuc.Energy Soc., 11, 1972, 313.

3. 'The Guardian', 3/13/86, p.1.

4. R.A.U. Huddle, L.M. Wyatt, J.Brit.Nuc.Energy Soc., 1957, 110.

5. 'Nuclear Power Technology', Ed. W. Marshall, Vol.2, 1983, p.221.

6. H.G. Masterson, J.T. Harrison, Proc.First Int.Congress Met. Corrosion, London, 1961, (Butterworths, 1962), p.451.

7. L.E. Pucher, J.Electrochem.Soc., 99, 1952, 2036.

8. R.C. Kirk, P.F. George, A.B. Fry, ibid., 99, 1952, 323.

9. R. Glicksman, ibid., 106, 1959, 457.

10. I.C. Blake, ibid., 99, 1952, 2020.

11. S. Gilman, P. Bramhall, ibid., 125, 1978, 1924.

12. W. Schneider, K. Wiesener, Bull.de la Soc.Chim.Beograd, 48, 1983, S241.

13. Ch. Fabjan, Kh. El-Khalaf, Int.Soc.Electrochem., 35th Meeting, Berkeley, A2-21, Aug. 1984, 99.

14. F. Barz, W. Vielstich, Bull.de la Soc.Chim.Beograd, 48, 1983, S37.

15. H.A. Robinson, Corrosion, 2, 1946, 199.

16. H.A. Robinson, Trans.Electrochem.Soc., 90, 1946, 485.

17. H.A. Robinson, P.F. George, Corrosion, 10, 1954, 182.

18. O. Osborne, H.A. Robinson, Corrosion, 8, 1952, 114.

19. R.B. Mears, C.D. Brown, Corrosion, 1, 1945, 113.

20. J.H. Greenblatt, Corrosion, 18, 1962, 125.

21. W.E. Higgins, J.Electrochem.Soc., 105, 1958, 757.

22. G.R. Hoey, M. Cohen, ibid., 105, 1958, 245.

23. G.R. Hoey, M. Cohen, ibid., 106, 1959, 776.

24. W.J. James, M.E. Straumanis, B.K. Bhatia, W.J. Johnson, ibid., 110, 1963, 1117.

25. W.J. James, M.E. Straumanis, W.J. Daniels, Corrosion, 7, 1967, 151.

26. W.J. James, 'Advances in Corrosion Science and Technology', Vol.4, M.G. Fontana, R.W. Staehle, Eds., (Plenum Press, N.Y. (1974)), p.128.

27. J.W. Johnson, C.K. Chi, W.J. James, Corrosion, 7, 1967, 204.

28. P.F. King, J.Electrochem.Soc., 113, 1966, 536.

29. P.F. King, ibid., 110, 1963, 1113.

30. R.L. Petty, A.W. Davidson, J. Kleinberg, J.Amer.Chem.Soc., 76, 1954, 363.

31. G.C. Perrault, Bull.de la Soc.Chim.Beograd, 48, 1983, S155.

32. B. Roald, W. Beck, J.Electrochem.Soc., 98, 1951, 277.

33. J.L. Robinson, P.F. King, ibid., 108, 1961, 36.

34. R. Tunold, H. Holtan, M.H. Berge, A. Lasson, R. Steen-Hansen, Corr.Sci., 17, 1977, 353.

35. S. Sathyanarayana, J.App.Electrochem., 11, 1981, 33.

36. T. Przyluski, E. Palka, Electrochim.Acta, 15, 1970, 853.

37. G.C. Perrault, C.R.Acad.Sci., Ser.C, 275, 1972, 1157.

38. G.C. Perrault, ibid., 276, 1973, 1437.

39. G.C. Perrault, 'Encyclopaedia of the Electrochemistry of the Elements', A.J. Bard (Ed.), Vol.7, 1975, p.263.

40. 'The Oxidation States of the Elements and their Potentials in Aqueous Solutions', W.M. Latimer (Ed.), (Prentice-Hall, N.Y., 1952).

41. I.R. Bellobono, F. Mazza, M.T. Cataldi, Gaz.Chim.Ital., 106, 1976, 259.

42. L. Whitby, Trans.Faraday Soc., 29, 1933, 1318.

43. M. Pourbaix, 'Atlas of Electrochemical Equilibria in Aqueous Solutions', (Nat.Assoc.Corr.Eng., 1974), p.139.

44. K.G. Cowan, J.A. Harrison, Electrochim.Acta, 24, 1979, 301.

45. K. Huber, J.Electrochem.Soc., 100, 1953, 376.

46. C. Sheldon Roberts, 'Magnesium and its Alloys', (John Wiley & Sons, 1974).

47. D. Vermilyea, J.Electrochem.Soc., 116, 1969, 1179.

48. D. Vermilyea, C.F. Kirk, ibid., 116, 1969, 1487.

49. P.M. Bradford, B. Case, G. Dearnaley, J.F. Turner, I.S. Woolsey, Corr.Sci., 16, 1976, 747.

50. Proc. Conf. 'Gas-Cooled Reactors Today', C.A. Friskney, R.J. Pearce, I.H. Robbins, K.H. Simpson, A.B.J. Cutler, C.J. Grant, B. Case, P.M. Bradford, B.N.E.S., Sept. 1982, Vol.1, p.77.

51. K.G. Cowan, J.A. Harrison, Electrochim.Acta, 25, 1980, 899.

52. G.C. Perrault, J.Electroanal.Chem., 51, 1974, 107.

53. G.C. Perrault, ibid., 27, 1970, 47.

54. J. Blanchet, H. Coriou, L. Grall, M. Pelras, G. Plante, M. Salesse, J.Nuc.Mat., 7, 1962, 311.

55. G. Wranglen, 'An Introduction to Corrosion and Protection of Metals', (Butler and Tanner Ltd., 1972).

56. Ch. Fabjan, Kh. El-Khalaf, M. Jaskula, Bull. de la Soc.Chim. Beograd, 48, 1983, S83.

57. R. Greef, P.R. Harvey, S.P. Tyfield, 'Electrochemical Methods in Corrosion Research', M. Duprat (Ed.), Materials Science Forum, Vol.8, 1986, 395.

58. T.P. Hoar, Corr.Sci., 7, 1967, 341.

59. J.A. Richardson, G.C. Wood, ibid., 10, 1970, 313.

60. T.R. Beck, S.G. Chan, J.Electrochem.Soc., 130, 1983, 1289.

61. B. Case, P.M. Bradford, K. Garbett, Nature, 268, 1977, 223.

62. D.T. Larson, Corr.Sci., 14, 657, 1979.

63. J. Kruger, P.C.S. Hayfield, 'Handbook on Corrosion Testing and Evaluation', W.H. Ailor, Ed., (Wiley, N.Y. 1971), p.783.

64. J. O'M. Bockris, A.K.N. Reddy, B. Rao, J.Electrochem.Soc., 113, 1966, 1133.

65. N. Sato, M. Cohen, ibid., 109, 781, 1962.

66. M. Cohen, K. Hashimoto, ibid., 121, 42, 1974.

67. G.M. Bulman, A.C.C. Tseung, Corr.Sci., 13, 1973, 531.

68. M. Okuyama, S. Haruyama, ibid., 14, 1974, 1.

69. J.L. Ord, J.C. Clayton, W.P. Wang, J.Electrochem.Soc., 124, 1977, 1671.

70. J.L. Ord, Surf.Sci., 56, 1976, 413.

71. Z.-Sklarska Smialowska, Corr.Sci., 15, 1975, 741.

72. J.J. Ritter, J. Kruger, Surf.Sci., 96, 1980, 364.

73. J. Kruger, 'Adv. in Electrochemistry and Electrochemical Engineering', Vol.9, P. Delahay, C.W. Tobias, Eds., (Wiley, N.Y., 1973), p.227.

74. P.C.S. Hayfield, Surf.Sci., 56, 1976, 488.

75. W.E.J. Neal, App.Surf.Sci., 2, 1979, 445.

76. K. Vedam, P.J. McMara, T. Narayan, App.Phys.Lett.; 47, 339, 1985.

77. J.A. Petit, F. Dabosi, Corr.Sci., 20, 1980, 745.

78. J. Kruger, J.R. Ambrose, Surf.Sci., 56, 1976, 394.

79. E. Passaglia, R.R. Stromberg, J. Kruger, Eds., 'Ellipsometry in the Measurement of Surfaces and Thin Films', Natl.Bur.Stand. Misc.Pub., 256, (U.S. Govt. Printing Office, Washington D.C. 1964).

80. N.M. Bashara, A.P. Buckman, A.C. Hall, Eds., 'Proc. of the Symp. on Recent Development in Ellipsometry', Pub. as Surf.Sci., 16, 1969.

81. N.M. Bashara, R.M.A. Azzam, Eds., 'Proceedings of the Third International Conference on Ellipsometry', Pub. as Surf.Sci., 56, 1976.

82. R.H. Muller, R.M.A. Azzam, D.E. Aspnes, Eds., 'Proceedings of the Fourth International Conference on Ellipsometry', Pub. as Surf.Sci., 96, 1980.

83. Journal Des Physique, Colloque, C10, Supplement No.12. 'Ellipsometry and Other Optical Methods for Surface and Thin Film Analysis', Printed in 1983.

84. R.H. Muller, in ref.73, p.167.

85. R.M.A. Azzam, N.M. Bashara, 'Ellipsometry and Polarised Light', (North Holland Pub. Company, 1977).

86. R. Greef, 'Ellipsometry' in 'Comprehensive Treatise of Electrochemistry', Vol.8, R.E. White, J. O'M. Bockris, B.E. Conway, E. Yeager, Eds., Plenum Press, (1984), pp.339-371.

87. F.S. Crawford Jr., 'Waves', (McGraw Hill, 1968) p.400.

88. R.H. Muller, Surface Sci., 16, 1969, 14.

89. W.A. Shurcliff, 'Polarized Light, Production and Use', (O.U.P. 1962).

90. J.E. Nestell, Jr., R.W. Christy, Amer.J.Phys., 39, 1971, 313.

91. J. Bennett, M.E. Bennett, 'Handbook of Optics', Opt.Soc.Am., 1978.

92. E. Hecht, A. Zajac, 'Optics', Addison Wesley Pub. Co. Inc., 1974, p.85.

93. R.W. Ditchburn, J.Opt.Soc.Am., 45, 1955, 743.

94. W. Koenig, Hanbuch der Physik, Vol.XX, M. Cruger, K. Scheel, Eds., Springer-Verlag, Berlin, 1928, p.141.

95. P. Drude, 'Theory of Optics'.

96. H.J. Hageman, W. Gudat, C. Kunz, D.E.S.Y., SR-74/7, Hamburg, 1974.

97. H.E. Bennett, M. Silver, E.J. Asley, J.Opt.Soc.Am., 53, 1963, 1089.

98. G. Hass, J.E. Waglonis, ibid., 51, 1961, 719.

99. J.D.E. McIntyre, in ref.73, p.61.

100. R. Kronig, J.Opt.Soc.Am., 12, 1926, 547.

101. J.D.E. McIntyre, D.E. Aspnes, Surf.Sci., 24, 1971, 417.

102. D.W. Berreman, J.Opt.Soc.Am., 62, 1972, 502.

103. A.A. Maradudin, D.C. Mills, Phys.Rev.(B), 11, 1975, 1392.

104. D. Beaglehole, O. Hunderi, ibid., 2, 1970, 309.

105. D. Hunderi, Surface Sci., 96, 1980, 1.

106. P. Bousquet, P. Roche, F. Florey, J.Opt.Soc.Am., 71, 1981, 1115.

107. R.H. Muller, C.C. Smith, Surf.Sci., 96, 1980, 375.

108. D.E. Aspnes, Phys.Rev.(P), 26, 1983, 5313.

109. D.E. Aspnes, ibid., 25, 1982, 1358.

110. T. Smith, Surface Sci., 56, 1976, 252.

111. D.E. Aspnes, E. Kingsbron, D.D. Bacon, Phys.Rev.(B), 21, 1980, 3290.

112. T. Smith, G. Lindberg, Surf.Tech., 8, 1979, 1.

113. J. Kruger, J.P. Calvert, J.Electrochem.Soc., 114, 1967, 43.

114. V. Brusic, J. O'M. Bockris, M.A. Genshaw, Surface Sci., 29, 1972, 653.

115. R. Greef, Ber.Buns.Phys.Chem., 88, 1984, 150.

116. C.A. Fenstermaker, F.C. McCrackin, Surf.Sci., 16, 1969, 85.

117. I. Ohlidal, F. Lukes, ibid., 55, 1976, 467.

118. I. Ohlidal, F. Lukes, Opt.Acta, 19, 1972, 817.

119. I. Ohlidal, F. Lukes, Opt.Comm., 7, 1973, 76.

120. R.M.A. Azzam, N.M. Bashara, Phys.Rev.(B), 58, 1972, 4721.

121. T.V. Vorburger, K.C. Ludema, App.Opt., 19, 1980, 561.

122. M.M. Wind, J. Vlieger, to be published in Physica A.

123. M.M. Wind, J. Vlieger, Physica A, 125A, 1984, 549.

124. E.L. Church, J.M. Zavada, App.Opt., 14, 1975, 1788.

125. M.Y. Abyaneh, W. Vischer, E. Barendrecht, Electrochim.Acta, 28, 1983, 285.

126. See for example, J.D. Jackson, 'Classical Electrodynamics', Wiley, N.Y., 1962, pp.98-131.

127. D.E. Aspnes, Thin Solid Films, 89, 1982, 249.

128. D.A.G. Bruggeman, Ann.Phys., Leipzig, 24, 1935, 636.

129. W.R. Tinga, W.A.G. Voss, J.App.Phys., 44, 1973, 3897.

130. G.A. Niklasson, G.G. Granqvist, O. Hundesi, App.Optics, 20, 1981, 26.

131. D.E. Aspnes, J.B. Theeton, F. Hottier, Phys.Rev.(B), 20, 1979, 3292.

132. T. Smith, J.Electroanal.Chem., 150, 1983, 227.

133. P.S. Hauge, Surface Sci., 96, 1980, 108.

134. K. Sugimoto, S. Motsuda, J.Electrochem.Soc., 130, 1983, 2323.

135. K. Sugimoto, S. Matsuda, Y. Ogiwara, K. Kitamura, J.Electrochem. Soc., 132, 1985, 1791.

136. V.M. Bermudez, Surf.Sci., 94, 1980, 24.

137. R.M.A. Azzam, R.M. Kemp, ibid., 135, 1983, 261.

138. A.B. Winterbottom in ref.79, p.97.

139. H.D. Leyer, Surface Sci., 16, 1969, 177.

140. P.J. Pearson, Ph.D. Thesis, University of Southampton, 1983.

141. A.C. Lowe, Surface Sci., 56, 1976, 134.

142. J.R. Partington, 'An Advanced Treatise of Physical Chemistry', Vol.IV, p.592.

143. P.B. Clapham, M.J. Downs, R.J. King, App.Optics, 8, 1969, 1971.

144. 'Tables of Physical and Chemical Constants', 14th Ed., G.W.C. Kaye, T.H. Laby, (Longman, 1982)

145. See for example, F.A. Jenkins, H.E. White, 'Fundamentals of Physical Optics', (McGraw-Hill, 1937), p.266.

146. 'Handbook of Chemistry', 6th Ed., N.A. Lange, (Handbook Publishers, Ohio, 1946).

147. 'C.R.C. Handbook of Chemistry and Physics', 64th Edition, Ed. C. Weast, 1983.

148. F.H. Ellinger, C.E. Holley Jr., B.B. McInteer, D. Pavone, R.M. Potter, E. Staritzky, W.H. Zachariasen, J.Amer.Chem.Soc., 77, 1955, 2647.

149. G.B. Sabine, Phys.Rev., 55, 1939, 1064.

150. R. Boch, ibid., 68, 1945, 210.

151. M. Priol, A. Daude, S. Robin, Compt.Rend., 264B, 1967, 1489.

152. M. Priol, A. Daude, S. Robin, ibid., 264B, 1967, 935.

153. C. Reale, Thin Solid Films, 9, 1972, 395.

154. T. Gesell, E.T. Arakawa, M.W. Williams, R.N. Mann, Phys.Rev.B, 7, 1973, 5141.

155. D. Hacman, W. Heitmann, App.Optics, 12, 1973, 895.

156. P. Drude, Ann.Phys., 39, 1890, 529.

157. H.M. O'Bryan, J.Opt.Soc.Am., 26, 1936, 122.

158. G.C. Allen, Metal Science, 18, 1984, 295.

159. W.D. Biggs, 'Physical Metallurgy', R.W. Cahn (Ed.), (North Holland Pub., 1965), p.541.

160. K. Vedam, W. Knausenberger, F. Lukes, J.Opt.Soc.Am., 59, 1969, 64.

161. S.P. Tyfield, Personal Communication, 1982.

162. D.J. Arrowsmith, 'Corrosion', Vol.2, L.L. Shreir (Ed.), (Newnes Butterworths, 1976), p.12:24.

163. S. Hofmann, Surface and Interface Anal., 2, 1980, 148.

164. D.T. Larson, Corr.Sci., 19, 1979, 657.

165. H.W. Werner, Surface and Interface Anal., 2, 1980, 56.

166. M.P. Seah, C.P. Hunt, ibid., 5, 1983, 33.

167. R.M.A. Azzam, N.M. Bashara, J.Opt.Soc.Am., 61, 1971, 600.

168. R.M.A. Azzam, N.M. Bashara, ibid., 61, 1971, 1236.

169. R.M.A. Azzam, N.M. Bashara, ibid., 61, 1971, 1380.

170. F.L. McCrackin, J.P. Colson, 'A FORTRAN Program for Analysis of Ellipsometer Measurements', Natl.Bur.Stands., Tech.Note 479, (U.S. Govt. Printing Office, Washington D.C., 1969).

171. J.C. Scully, 'The Fundamentals of Corrosion', 2nd Ed., (Pergamon Press, 1975), p.127.

172. N. Sato, Passivity Met., Proc.4th Int.Symp., 1977, (Pub.1978), R.P. Frankenthal, J. Kruger (Eds.), p.29.

173. N.D. Tomashov, G.P. Chernova, Yu.S. Ruskol, G.A. Ayuyan, 'Proc.5th ICMC - Yokyo', (NACE, Houston, 1975), p.245.

174. G.R. Sparrow, Proc.Pittsburgh Meeting on 'Analytical Chemistry', Ohio, 1977, Paper No.348.

175. D.M. Kern, 'CO_2 Corrosion in Oil and Gas Production', NACE task group T-1-3 (Eds.) (Pub. NACE, 1984), p.75.

176. B. Case, D.M. Hilton, Proc.Conf. 'Water Chemistry of Nuclear Reactor Systems', B.N.E.S., 1978, p.429.

177. N.A.J. Van Muylder, M. Pourbaix, 'Electrochemical Behaviour of Magnesium, pH-Voltage Equilibrium $Mg-H_3PO_4-H_2O$ at 25°C, Centre belge etude corrosion, Tech.Rept. No.39, 1956.

178. D. Briggs, M.P. Seah, 'Practical Surface Analysis', (John Wiley and Sons, 1984), p.143.

179. L. Young, Trans.Faraday Soc., 53, 1957, 229.

180. A.N. Piggot, L.L. Shreir, Corr.Sci., 5, 1965, 165.

181. A. Turnbull, Corr.Sci., 23, 1983, 833.

182. J. Uruchurtu, J.L. Dawson, in ref. 57, p.113.

183. M. Janik-Czachor, A. Szummer, Z. Szklarska-Smialowska, Corr.Sci., 15, 1975, 975.

184. C. Bataillon, C. Fiaud, ibid., p.141.

185. D.E. Williams, M. Fleischmann, J. Stewart, T. Brooks, ibid., p.151.

186. U. Bertocci, J. Krugur, Surf.Sci., 101, 1980, 600.

187. L. Young, 'Anodic Oxide Films', (Academic Press, 1961).

188. H. Takahashi, M. Nagayama, Electrochim.Acta, 23, 1978, 279.

189. S.D. Mitoff, J.Chem.Phys., 36, 1962, 1838.

190. A.K. Vijh, Surf.Tech., 4, 1976, 7.

191. H.C. Man, D.R. Gabe, Corr.Sci., 21, 1981, 627.

192. J.O'M. Bockris, A.K.N. Reddy, 'Modern Electrochemistry', Vol.2, (Plenum, 1977), p.1328.

193. See for example ref. 171, p.209.

194. P.G. Snyder, M.C. Rost, G.H. Bu-Abbud, J.A. Wollam, S.A. Alterovitz, J.App.Phys., 60, 1986, 3293.

195. B. Bethune, R.C. Furneaux, G.C. Wood, J.Mat.Sci., 12, 1977, 1764.

196. C.F.W. Norman, Ph.D. Thesis, University of Southampton, 1986.

Appendix A1 Data Acquisition Program - GETPLT

```
100 REM ***** GETONE CONVERTED TO 6809 *****
105 DIGITS 9,4
110 PRINT "THIS PROG. GETS,PLOTS & FILES AN INFINITE NO."
120 PRINT "OF POINTS WITH VARYING TIME INTERVALS"
130 F1=2.4417E-3 : REM *** ADC DIGITS * F1 = VOLTS ***
131 F2=F1/10 : REM *** ALTERED FOR GAIN OF 10 ON CH2 ***
132 F3=2320 : REM *** P DEG = ADC DIGITS / F3 ***
134 F4=2412 : REM *** A DEG = ADC DIGITS / F4 ***
136 REM ***** F6=FILE RESULTS FLAG *****
137 REM ***** F7=PLOTTER FLAG *****
138 REM ***** F8=PRINTER FLAG *****
140 DIM N2(7)
145 DIM N(12)
150 REM***** GOTO MAIN PROG *****
160 GOTO 3000
200 REM ***** PLOTTER S/R *****
220 REM ***** PLOTTER INIT. *****
230 U$=CHR$(27);A$=U$+".Y": J$=U$+".Z"
240 E$=CHR$(3)
250 PRINT A$+"INSP1'+U$+".N10;27:"+U$+".I40;;27:"
260 PRINT "IP700,500,8653,6500";J$
270 INPUT "SCALE VALUES X1,X2,XSTEP,Y1,Y2,YSTEP",J1,J2,J3,K1,K2,K3
280 PRINT A$+"SC";J1;J2;K1;K2
290 REM ***** END OF INIT. *****
300 REM ***** PLOT & LABEL AXES *****
310 PRINT "PU";J1;K1;"PD";J2;K1;J2;K2;J1;K2;J1;K1;"PU"
320 FOR A=J1 TO J2 STEP J3
330 PRINT "PA";A;K1;"XT"
340 PRINT "CP-2,-1;LB";A;E$
350 NEXT A
360 PRINT "PA";J1;K1;"CP40,-2.25;LBPSI/deg";E$
370 FOR B=K1 TO K2 STEP K3
380 PRINT "PA";J1;B;"YT"
390 IF B<100 THEN PRINT "CP-4,-0.25;LB";B;E$
400 IF B>99 THEN PRINT "CP-5,-0.25;LB";B;E$
410 NEXT B
420 PRINT "PA";J1;K1;"DI0,1;CP30,2.5;LBDEL/deg";E$
425 PRINT "DI1,0";J$
430 INPUT "LABEL HEADING & DATE",H1$
440 IF H1$="N" THEN 480
450 INPUT "HEADING",H2$
460 PRINT A$+"SP2;PA";J1;K2;"CP5,1;LB";H2$;E$;J$
470 GOSUB 600 : REM***** GET DATE *****
480 PRINT A$+"CP10,0;LB";D1$;E$;J$
490 PRINT A$+"SM+";J$
500 RETURN
600 REM ***** S/R TO GET DATE *****
610 AD=DPEEK(HEX("CC2B"))
620 H=HEX("F7F8")
640 D$="SUNMONTUEWEDTHUFRISATSUN"
650 M$="JANFEBMARAPRMAYJUNJULAUGSEPOCTNOVDEC"
660 S$=" "
670 DPOKE(AD-2),HEX("F0AC")
680 X=USR(0)
690 FOR J=1 TO 12
700 N(J)=PEEK(H-12+J)
710 NEXT J
```

```
720 S$=S$+MID$(D$,3*(N(10)-1)+1,3)+" "
730 S$=S$+MID$(M$,3*(10*N(12)+N(11)-1)+1,3)+" "
740 S$=S$+STR$(10*N(9)+N(8))
750 S$=S$+" 1985 AT "
760 S$=S$+STR$(10*N(7)+N(6))+":"
770 S$=S$+STR$(10*N(5)+N(4))
780 D1$=S$
790 RETURN
800 REM ***** S/R FOR TIMER *****
802 H=HEX("F7FB")
810 DPOKE(AD-2),HEX("F0AC")
820 X=USR(0)
830 FOR J=1 TO 7
840 N2(J)=PEEK(H-12+J)
850 NEXT J
860 S1=10*N2(7)+N2(6)
870 S2=60*S1+10*N2(5)+N2(4)
880 S3=60*S2+10*N2(3)+N2(2)+N2(1)/10
890 RETURN
900 REM ***** TIMER LOOP *****
910 DPOKE HEX("F7E1"),T2
920 DPOKE(AD-2),HEX("F17D")
930 X=USR(0) : REM *** TINT S/R ***
940 RETURN
1000 D0=PEEK(AC)+256*PEEK(AC-1) : REM *** REFORMAT ADC ***
1010 AC=AC-2
1020 IF D0>=61440 THEN D0=-(65536-D0)
1030 RETURN
1200 REM ***** CALCULATE DELTA & PSI FROM P1,A1 *****
1210 P2=P1+D3/F3 : REM *** APPLY FARADAY CORRECTION ***
1220 A2=A1+D4/F4
1230 IF P2<0 THEN P2=P2+180
1240 IF A2<0 THEN A2=A2+180
1250 IF P2>360 THEN P2=P2-360
1260 IF A2>360 THEN A2=A2-360
1270 IF P2>180 THEN P2=P2-180
1280 IF A2>180 THEN A2=A2-180
1290 IF A2<=90 THEN 1360 : REM *** SPLIT INTO 2 GROUPS WRT A2 VALUE ***
1300 P=180-A2 : REM ***** FIRST A GROUP *****
1310 IF Q=135 THEN 1340
1320 IF P2<=45 THEN D=90-2*P2 : RETURN
1330 D=450-2*P2 : RETURN
1340 IF P2<=45 THEN D=630-2*P2 : RETURN
1350 D=2*P2-90 : RETURN
1360 P=A2 : REM ***** SECOND A GROUP *****
1370 IF Q=135 THEN 1400
1380 IF P2>=135 THEN D=630-2*P2 : RETURN
1390 D=270-2*P2 : RETURN
1400 IF P2>=135 THEN D=2*P2-270 : RETURN
1410 D=90+2*P2 : RETURN
3000 REM ***** MAIN PROGRAM *****
3010 REM ***** INIT ROUTINE *****
3020 AD=DPEEK(HEX("CC2B"))
3030 HU=HEX("F7FF")
3035 DE=HU-1
3040 MI=HU-2
3045 SE=HU-3
3050 DPOKE(AD-2),HEX("F000")
3060 X=USR(0) : REM***DO THE INIT***
3070 REM ***** END OF INIT ******
3100 PRINT"PLOT RESULTS (Y OR N)":Q1$=INCH$(0)
```

```
3105 PRINT" "
3110 IF Q1$="Y" THEN GOSUB 200 : F7=1
3120 INPUT "TIME INTERVAL BETWEEN POINTS (IN SECS)",T1
3125 T2=(T1-0.9)*100
3130 REM *****POKE T1 INTO TIX*****
3140 DPOKE HEX("F7E1"),T2
3150 PRINT "FILE RESULTS ?  Y OR N ":Q2$=INCH$(0)
3155 PRINT" "
3160 IF Q2$="Y" THEN F6=1
3170 IF F6<>1 THEN 3202
3180 INPUT "FILENAME",F$
3190 OPEN NEW F$ AS 1
3195 GOSUB 600 : REM ***** GET DATE *****
3200 PRINT#1,"DATE=";D1$
3202 Q3$="N":REM ***** SET PRINT RESULTS FLAG TO NO *****
3204 IF Q3$="N" THEN 3206
3205 F8=1
3206 PRINT "DO YOU WANT TO AVERAGE CH2 (CURRENT) OVER 50 PTS?"
3207 PRINT "TIME FOR AVERAGING=10 SECS": Q4$=INCH$(0)
3208 IF Q4$="N" THEN 3215
3209 F9=1 : T2=T2-900 : REM SET FLAG & ALLOW FOR AVERAGING TIME
3210 DPOKE HEX("F7E1"),T2
3215 REM ***** GET (Q) VALUE *****
3220 DPOKE(AD-2),HEX("F045")
3230 X=USR(3) : REM ***** CIRC S/R *****
3240 Q=100*PEEK(HU)+PEEK(DE)+PEEK(MI)/60+PEEK(SE)/3600
3242 PRINT " "
3245 PRINT "Q=";Q
3248 Q0=INT(Q+0.01)
3250 IF ((Q-45)*(Q-45))<1E-6 THEN 3290
3260 PRINT "ERROR IN Q, RESET & PRESS ANY KEY & RETURN"
3270 Q$=INCH$(0)
3275 PRINT" "
3280 GOTO 3210
3290 REM ***** (Q) VALUE OBTAINED*****
3295 PRINT "TYPE ANY KEY TO START":Q3$=INCH$(0)
3298 PRINT" "
3300 REM ***** GET TIME *****
3310 GOSUB 800 :REM **GET TIME**
3320 S4=S3
3330 S6=0
3340 REM ***** GET CIRCLE DATA *****
3345 I=0 : D5=0
3350 DPOKE(AD-2),HEX("F045")
3360 J=1
3370 X=USR(J) : REM *** CIRC S/R ***
3380 A1=100*PEEK(HU)+PEEK(DE)+PEEK(MI)/60+PEEK(SE)/3600
3390 X=USR(2) : REM *** CIRC S/R ***
3400 P1=100*PEEK(HU)+PEEK(DE)+PEEK(MI)/60+PEEK(SE)/3600
3410 REM ***** GET ADC4CH *****
3415 I=I+1
3420 DPOKE(AD-2),HEX("F0FF")
3430 X=USR(0) : REM *** GETADC S/R ***
3440 AC=HEX("F7EE")
3450 GOSUB 1000 : D1=D0 :GOSUB 1000 : D2=D0
3460 GOSUB 1000 : D3=D0 : GOSUB 1000 : D4=D0
3470 GOSUB 1200 : REM *** CALCULATE DEL & PSI ***
3480 D1=D1*F1 : D2=D2*F2
3482 IF F9<>1 THEN 3490
3484 D5=D5+D2
3486 IF I<50 THEN 3415
```

```
3480 D2=D5/50 : D5=0
3490 PRINT S6;D;P;D1;D2
3500 IF F6<>1 THEN 3520
3510 PRINT#1,S6;",";D;",";P;",";D1;",";D2
3520 IF F7<>1 THEN 3540
3530 PRINT A$+"SM+;PU";P;D;J$
3540 IF F8<>1 THEN 3560
3550 PRINT#0,S6;D;P;D1;D2
3560 GOSUB 900 : REM *** CALL TIME DELAY ***
3570 GOSUB 800 : REM *** GET CHANGE IN TIME ***
3580 S6=S3-S4
3590 GOTO 3340
```

Appendix A2 Machine Code Program - FASTI-BIN

```
                        **** S/R TO INITIALISE PIAS ****
F000                                ORG     $F000
              E00A  HICIRC  EQU     $E00A
              E008  LOCIRC  EQU     $E008
              E010  MOTORS  EQU     $E010
              E012  ADDBUS  EQU     $E012
              E020  VIA     EQU     $E020
)F000 7E   F015                 JMP     INIT
>F003 7E   F045                 JMP     CIRC
 F006 7E   F0AC                 JMP     TINIT
 F009 7E   F0FF                 JMP     ANALOG
 F00C 7E   F159                 JMP     TINT
 F00F 7E   F17A                 JMP     SCANT
 F012 7E   F138                 JMP     STEPIT
                        **** STORE LOCATIONS FOR ALL S/R'S****
F7FF                                ORG     $F7FF
              F7FF  HUNDEG  EQU     *
              F7FE  DEG     EQU     *-1
              F7FD  MINS    EQU     *-2
              F7FC  SEC     EQU     *-3
              F7FB  DAT12   EQU     *-4
              F7FA  DAT11   EQU     *-5
              F7F9  DAT10   EQU     *-6
              F7F8  DAT9    EQU     *-7
              F7F7  DAT8    EQU     *-8
              F7F6  DAT7    EQU     *-9
              F7F5  DAT6    EQU     *-10
              F7F4  DAT5    EQU     *-11
              F7F3  DAT4    EQU     *-12
              F7F2  DAT3    EQU     *-13
              F7F1  DAT2    EQU     *-14
              F7F0  DAT1    EQU     *-15
              F7EF  XTEMP   EQU     *-16
              F7ED  CHAN1   EQU     *-18
              F7EB  CHAN2   EQU     *-20
              F7E9  CHAN3   EQU     *-22
              F7E7  CHAN4   EQU     *-24
              F7E5  CNTRL   EQU     *-26
              F7E3  NSTEPS  EQU     *-28
              F7E1  TIX     EQU     *-30
              CC2B  MEMIND  EQU     $CC2B
F015                                ORG     $F015
F015 7F    E009         INIT    CLR     HICIRC+1  CIRCLES ARE INPUTS
F018 7F    E009                 CLR     LOCIRC+1
F01B 7F    E00A                 CLR     HICIRC
F01E 7F    E008                 CLR     LOCIRC
F021 86    04                   LDA     #04
F023 B7    E00B                 STA     HICIRC+1
F026 B7    E009                 STA     LOCIRC+1
F029 86    22                   LDA     #$22
F02B B7    E011                 STA     MOTORS+1  MOTORS, ADDBUS ARE OUTPUTS
F02E B7    E013                 STA     ADDBUS+1
F031 4F                         CLRA
F032 43                         COMA
F033 B7    E010                 STA     MOTORS
F036 B7    E012                 STA     ADDBUS
F039 86    36                   LDA     #$36
```

```
F03B B7   E011            STA   MOTORS+1
F03E B7   E013            STA   ADDBUS+1
F041 7F   E010            CLR   MOTORS
F044 39                   RTS
                **** S/R TO GET A CIRCLE AND STORE AS DEG,MIN,SEC ****
                * ASSUMES PIAS HAVE BEEN INITIALISED
F045 34   10      CIRC    PSHS  X
F047 BE   CC2B            LDX   MEMIND
F04A A6   1D              LDA   -3,X
F04C 4A                   DECA
F04D 48                   ASLA
F04E B7   E012            STA   ADDBUS    PUT 0,2, OR 4 IN MUX
F051 86   0F              LDA   #$0F
F053 B4   E00A            ANDA  HICIRC    KILL MS BITS
F056 B7   F7FF            STA   HUNDEG
F059 C6   F0              LDB   #$F0
F05B F4   E008            ANDB  LOCIRC    SELECT MS DIGIT
F05E 54                   LSRB
F05F 54                   LSRB
F060 54                   LSRB
F061 54                   LSRB
F062 86   0A              LDA   #10       MULTIPLIER
F064 3D                   MUL
F065 B6   E008            LDA   LOCIRC    WHOLE NO. IS IN B
F068 84   0F              ANDA  #$0F      KILL MS BITS
F06A 34   04 ABE0         ABA
F06E B7   F7FE            STA   DEG
F071 A6   1D              LDA   -3,X
F073 4A                   DECA
F074 48                   ASLA
F075 4C                   INCA
F076 B7   E012            STA   ADDBUS    PUT 1,3 OR 5 IN MUX
F079 F6   E00A            LDB   HICIRC
F07C C4   F0              ANDB  #$F0
F07E 54                   LSRB
F07F 54                   LSRB
F080 54                   LSRB
F081 54                   LSRB
F082 86   0A              LDA   #10       MULTIPLIER
F084 3D                   MUL
F085 B6   E00A            LDA   HICIRC
F088 84   0F              ANDA  #$0F
F08A 34   04 ABE0         ABA
F08E B7   F7FD            STA   MINS
F091 C6   F0              LDB   #$F0
F093 F4   E008            ANDB  LOCIRC
F096 54                   LSRB
F097 54                   LSRB
F098 54                   LSRB
F099 54                   LSRB
F09A 86   0A              LDA   #10       MULTIPLIER
F09C 3D                   MUL
F09D B6   E008            LDA   LOCIRC
F0A0 84   0F              ANDA  #$0F
F0A2 34   04 ABE0         ABA
F0A6 B7   F7FC            STA   SEC
F0A9 35   10              PULS  X
F0AB 39                   RTS
```

```
                   **** S/R TO GET DATE AND TIME****
              E01E TADDR    EQU    $E01E     PRINTER PIA B SIDE
              E01C DADDR    EQU    $E01C     PRINTER PIA A SIDE
                   **** S/R INITIALISE PIA ****
F0AC 7F   E01F     TINIT    CLR    TADDR+1   SELECT DDR
F0AF 7F   E01D              CLR    DADDR+1
F0B2 7F   E01C              CLR    DADDR
F0B5 7F   E01E              CLR    TADDR
F0B8 73   E01E              COM    TADDR     ALL OUTPUTS
F0BB 86   04                LDA    #04       SELECT DATA REG
F0BD B7   E01F              STA    TADDR+1
F0C0 B7   E01D              STA    DADDR+1
                   **** S/R SET COUNT
F0C3 BF   F7EF              STX    XTEMP
F0C6 C6   0C                LDB    #12
F0C8 8E   F7F8              LDX    #DAT12
                   **** S/R CONTROL PULSES TO PIA OUTPUTS ****
F0CB 86   70       GET      LDA    #112
F0CD 34   04 ABE0           ABA
F0D1 B7   E01E              STA    TADDR
F0D4 86   30                LDA    #48
F0D6 34   04 ABE0           ABA
F0DA B7   E01E              STA    TADDR
F0DD 86   10                LDA    #16
F0DF 34   04 ABE0           ABA
F0E3 B7   E01E              STA    TADDR
F0E6 B6   E01C              LDA    DADDR
F0E9 84   0F                ANDA   #$0F
F0EB 81   0F                CMPA   #$0F      CHECK DATA VALIDITY
F0ED 27   DC                BEQ    GET       READ AGAIN IF NOT
F0EF A7   84                STA    0,X
F0F1 30   1F                DEX
F0F3 86   70                LDA    #112
F0F5 B7   E01E              STA    TADDR
F0F8 5A                     DECB
F0F9 26   D0                BNE    GET
F0FB BE   F7EF              LDX    XTEMP
F0FE 39                     RTS




                   * THIS READS THE FIRST FOUR ANALOG CHANNELS**
                   * ASSUMES INIT HAS BEEN CALLED*
                   *STORE FOR DATA*
                   * OBTAIN DATA AND STORE IN CHANNELS(1 TO 4)*
F0FF BF   F7EF     ANALOG  STX    XTEMP
F102 8E   F7ED             LDX    #CHAN1
F105 C6   04               LDB    #04       CYCLE COUNTER
F107 86   0C       CALCAD  LDA    #12       8 IS FIRST MUX ADDR
F109 34   04 A0E0          SBA              CALC FIRST MUX ADDR
F10D B7   E012     GETADC  STA    $E012
F110 12                    NOP
F111 12                    NOP
F112 12                    NOP
F113 86   3E               LDA    #$3E
F115 B7   E013             STA    ADDBUS+1  CB2 IS HIGH
```

```
F118 86    36                 LDA    #$36
F11A B7    E013               STA    ADDBUS+1  CB2 IS LOW

F11D B6    E013     NRDY      LDA    ADDBUS+1  READ CONTROL REG.
F120 48                       ASLA             WAIT FOR CB1 TO GO HIGH
F121 24    FA                 BCC    NRDY
F123 B6    E009               LDA    LOCIRC    LSB OF ADC
F126 A7    01                 STA    1,X       STORE LSB IN TOP CHAN1
F128 B6    E00A               LDA    HICIRC    MSB+SIGN OF ADC
F12B A7    84                 STA    0,X       STORE MSB+SIGN IN BOT CHAN1
F12D 30    1F                 DEX
F12F 30    1F                 DEX
F131 5A                       DECB
F132 26    D3                 BNE    CALCAD    NEXT VALUE
F134 BE    F7EF               LDX    XTEMP
F137 39                       RTS
```

```
                   ** THIS S/R DRIVES THE MONOCHROMATOR**
                   ** AT 400 STEPS/SEC. USE FROM BASIC **
                   ** BY POKEING CONTROL BYTE AND NO'   **
                   ** OF STEPS AS SHOWN.                **
                   ** FIRST SAVE X REG **
F138 BF   F7EF     STEPIT  STX    XTEMP
F13B BE   F7E3             LDX    NSTEPS
F13E 27   15               BEQ    RETN      RETURN IF ZERO STEPS
F140 B6   F7E5             LDA    CNTRL
F143 5F                    CLRB
F144 B7   E010     PULS    STA    $E010     RAISE PULSE IN PIAA
F147 7F   E010             CLR    $E010
F14A 30   1F               DEX
F14C 27   07               BEQ    RETN      END OF PULSES?
F14E 5A            LOOP    DECB             10 CYCLELOOP, 256 TIMES
F14F 12                    NOP
F150 12                    NOP
F151 26   FB               BNE    LOOP
F153 20   EF               BRA    PULS      NEXT PULSE
F155 BE   F7EF     RETN    LDX    XTEMP     RESTORE X
F158 39                    RTS
```

```
* THIS USES TIMER 1 & TIMER 2 OF THE (6840) CHIP
* AT PORT 3. THEY OPERATE IN TANDEM, CONTINUOUS MODE
* TO GENERATE INTR. REQUESTS. THE FIRST TIMER USES A
* 1200 BAUD CLOCK (19200 HZ) AS INPUT TO GIVE 10MS TICKS,
* WHICH ARE COUNTED DOWN BY THE SECOND CHIP ACCORDING TO
* A DIVISOR SET IN TIX BEFORE ENTRY.
* TIMER ADDRESES ARE $E00C,D,E,F & $E40C,D,E,F.
```

```
 F159 BF   F7EF    TINT   STX    XTEMP
 F15C 8E   005F           LDX    #$5F       $5F NEEDED FOR 19200 HZ CLOCK
 F15F BF   E00E           STX    $E00E      INTO T#1 LATCHES
 F162 BE   F7E1           LDX    TIX        GET NO. TICKS (2 BYTES)
 F165 BF   E40C           STX    $E40C      INTO T#2 LATCHES
 F168 86   81             LDA    #$81       NO IRQ RESET
 F16A B7   E00D           STA    $E00D      WRITE TO CR2
 F16D 86   81             LDA    #$81       NO IRQ RESET
 F16F B7   E00C           STA    $E00C      STORE IN CR1
 F172 4A                  DECA              REMOVE RESET BIT
 F173 B7   E00C           STA    $E00C      START TIMERS
 F176 BE   F7EF           LDX    XTEMP
 F179 39                  RTS
                   * POLLING TIMER FOR ONE SCAN
                   * ENTER WITH TIX($BFE1), SET TO INTERVAL REQU.
                   * VALUE OF TIX+1 EQUALS TIME IN SEC FOR 1 SCAN
 F17A BD   F015    SCANT  JSR    INIT       JUMP TO INIT S/R
 F17D BD   F159           JSR    TINT
 F180 B6   E00D    WAIZ   LDA    $E00D      READ STATUS
 F183 84   02             ANDA   #02        LOOK FOR TIMER 2 FLAG
 F185 27   F9             BEQ    WAIZ       WAIT FOR NON-ZERO
 F187 B6   E00D           LDA    $E00D      THESE TWO INSTRUCTIONS
 F18A B6   E40C           LDA    $E40C      RESET FLAGS
 F18D 39                  RTS
                          END

0 ERROR(S) DETECTED

SYMBOL TABLE:
```

Appendix A3 Plotting Program - PLOTV

```
100 REM ***** PLOT PROG FOR HP 7470A PLOTTER *****
105 REM ***** RAEDS 3 OR 5 COLUMN FILE *****
110 REM ***** PLOTS VERTICALLY *****
115 REM ***** LINE TYPE STATEMENT IS AT 1530 *****
120 REM ***** IP VALUES ARE AT 1115 *****
125 DIGITS 8,3
130 DIM F(180,5),X(180),Y(180)
132 DIM P(5)
135 CC=0
140 GOTO 3000: REM GOTO MAIN PROG
200 REM ***** PLOTTER INIT. *****
210 U$=CHR$(27):A$=U$+".Y":J$=U$+".Z":E$=CHR$(3)
220 PRINT A$+"PU"+U$+".M20;63;13;10:";J$
225 PRINT A$+"PU"+U$+".H80;35;64:";J$
228 PRINT A$+"IN";J$
230 RETURN
300 REM ***** DATREAD *****
305 REM ***** FI$=FILENAME *****
315 REM ***** D$=DATE FROM FILE *****
320 INPUT "INPUT FILENAME",F1$
322 PRINT " "
325 INPUT"NO. OF DATA COLUMNS 3 OR 5",Y
328 PRINT " "
330 OPEN OLD F1$ AS 1
335 I=1
340 ON ERROR GOTO 5000
345 REM
350 IF Y=5 THEN INPUT#1,F(I,1),F(I,2),F(I,3),F(I,4),F(I,5)
352 IF Y=3 THEN INPUT#1,F(I,1),F(I,2),F(I,3)
355 I=I+1
360 GOTO 350
365 CLOSE 1
370 C1=I-1
375 IF Y=3 THEN RETURN
380 INPUT"CURRENT IN mA wrt FSD OF POTENTIOSTAT",B1
390 FOR I=1 TO C1
400 F(I,5)=F(I,5)*5*B1
410 NEXT I
420 RETURN
500 REM ***** DATHILO *****
505 REM ***** CREATES 2 ARRAYS FROM DATA & FINDS HIGH & LOW VALUES.*****
510 REM ***** ASSUMES NO. OF POINTS=C1 & DATA IN FORM F(I,N) WHERE N= OR 5
520 REM ***** B1=CURRENT IN mA *****
525 REM ***** J1,J2,J3,K1,K2,K3=X,Y AXES,START,END,STEP *****
530 REM ***** M,N,=X,Y,AXES *****
535 PRINT"TITLES FOR AXES ARE"
539 PRINT " "
540 PRINT "TIME/secs (1), DELTA/deg (2), PSI/deg (3)"
545 PRINT "POT/volts (4), CURRENT/ma (5), OTHER (6)"
548 PRINT " "
550 INPUT"TITLES X,Y",T1,T2
555 IF T1<>6 THEN 560
558 INPUT"X TITLE",L1$
559 GOTO 562
560 T3=T1 : GOSUB 1365 : L1$=L$
562 IF T2<>6 THEN 566
564 INPUT"Y TITLE",L2$
565 PRINT " " : GOTO 565
566 T3=T2 : GOSUB 1365 : L2$=L$
```

```
567 PRINT " "
568 INPUT"COLUMNS FOR X & Y AXES",M,N
570 FOR I =1 TO C1
575 X(I)=F(I,M)
580 Y(I)=F(I,N)
585 NEXT I
587 IF F2=3 THEN RETURN
590 X1=-1E38:Y1=X1:X2=1E39:Y2=X2
595 FOR I=1 TO C1
600 IF X(I)>X1 THEN X1=X(I)
605 IF Y(I)>Y1 THEN Y1=Y(I)
610 IF X(I)<X2 THEN X2=X(I)
615 IF Y(I)<Y2 THEN Y2=Y(I)
620 NEXT I
622 PRINT " "
625 PRINT"X VALUES RANGE FROM";X2;"TO";X1
630 INPUT"X AXIS START,END,STEP",J1,J2,J3
632 PRINT " "
635 PRINT"Y VALUES RANGE FROM";Y2;"TO";Y1
640 INPUT"Y AXIS START,END,STEP",K1,K2,K3
642 PRINT " "
645 RETURN
800 REM ***** SCALES J&K IF NON INTEGER *****
805 REM ***** S1=1 FOR 1<J1,J2<0.1 S1=2 FOR 0.1<J1,J2<0.01 *****
810 REM ***** S2=1 FOR 1<K1,K2<0.1 S2=1 FOR 0.1<K1,K2<0.01 *****
815 IF S1<>0 THEN 910
825 IF S2<>0 THEN 910
830 IF INT(J1)-J1<>0 THEN S1=1
835 IF INT(J2)-J2<>0 THEN S1=1
840 IF INT(K1)-K1<>0 THEN S2=1
845 IF INT(K2)-K2<>0 THEN S2=1
850 IF S1<>1 THEN 880
855 J1=J1*10:J2=J2*10:J3=J3*10
860 IF INT(J1)-J1<>0 THEN S1=2
865 IF INT(J2)-J2<>0 THEN S1=2
870 IF S1<>2 THEN 880
875 J1=J1*10:J2=J2*10:J3=J3*10
880 IF S2<>1 THEN 910
885 K1=K1*10:K2=K2*10:K3=K3*10
890 IF INT(K1)-K1<>0 THEN S2=2
895 IF INT(K2)-K2<>0 THEN S2=2
900 IF S2<>2 THEN 910
905 K1=K1*10:K2=K2*10:K3=K3*10
910 IF S1<>1 THEN 930
915 FOR I=1 TO C1
920 X(I)=X(I)*10
925 NEXT I
930 IF S1<>2 THEN 950
935 FOR I=1 TO C1
940 X(I)=X(I)*100
945 NEXT I
950 IF S2<>1 THEN 970
955 FOR I=1 TO C1
960 Y(I)=Y(I)*10
965 NEXT I
970 IF S2<>2 THEN 990
975 FOR I=1 TO C1
980 Y(I)=Y(I)*100
985 NEXT I
990 RETURN
```

```
1100 REM ***** DRAWS & LABELS AXES FOR PLOTTER *****
1105 REM ***** ASSUMES PLOTINT HAS BEEN RUN *****
1110 REM ***** ASSUMES SC VALUE HAS BEEN ENTERED *****
1111 X1=J1 : X2=J2 : Y1=K1 : Y2=K2
1112 J1=K2 : J2=K1 : K1=X1 : K2=X2
1115 GOSUB 6400
1118 PRINT "SP1;SI.14,.28"
1120 PRINT "SC";J1;J2;K1;K2
1125 PRINT "PA";J1;K1:"PD;PA";J2;K1;J2;K2;J1;K2;J1;K1;"PU";J$
1130 PRINT A$+"DI0,1";J$
1160 FOR A=X1 TO X2 STEP J3
1164 IF A*A<0.0001 THEN A=0
1165 PRINT A$+"PA";Y1;A;"YT"
1170 IF S1=1 THEN A=A/10
1175 IF S1=2 THEN A=A/100
1180 IF P$<>"B" THEN IF E>2 THEN IF E<6 THEN 1200
1185 IF A<100 THEN PRINT "CP-2,-1"
1190 IF A>99 THEN PRINT "CP-3,-1"
1195 PRINT "LB";A;E$
1200 IF S1=1 THEN A=A*10
1205 IF S1=2 THEN A=A*100
1206 PRINT CHR$(35) : INPUT AD$
1208 PRINT "AP;PU";J$
1210 NEXT A
1212 PRINT A$+"AP"
1213 PRINT CHR$(35) : INPUT AF$
1214 PRINT "AP";J$
1215 IF P$<>"B" THEN IF E>2 THEN IF E<6 THEN 1223
1217 PRINT A$+"PU"
1219 LE=LEN(L1$)/2
1220 PRINT "PA";J2;(K1+K2)/2;"CP";-LE,-2.25;"LB";L1$;E$
1221 PRINT CHR$(35) : INPUT AG$
1222 PRINT "AP";J$
1223 IF E>2 THEN Y1=Y1+K3 : Y2=Y2-K3
1225 FOR B=Y1 TO Y2 STEP K3
1228 PRINT A$+"AP"
1229 IF B*B<0.0001 THEN B=0
1230 PRINT "PA";B;X1;"XT"
1235 IF S2=1 THEN B=B/10
1240 IF S2=2 THEN B=B/100
1245 IF B>0.999 THEN PRINT "CP-5,-0.25"
1250 IF B<1 THEN PRINT "CP-4,-0.25"
1260 PRINT"LB";B;E$
1265 IF S2=1 THEN B=B*10
1270 IF S2=2 THEN B=B*100
1272 PRINT CHR$(35) : INPUT AD$
1273 PRINT "AP;PU";J$
1275 NEXT B
1280 LE=LEN(L$)/2
1283 PRINT A$+"PU"
1285 PRINT "PA";(J1+J2)/2;K1;"DI-1,0;CP";-LE,2.5;"LB";L2$;E$
1290 PRINT "DI1,0";J$
1320 RETURN
1365 ON T3 GOTO 1370,1375,1380,1385,1390
1370 L$="TIME/secs" : GOTO 1395
1375 L$="DELTA/deg":GOTO 1395
1380 L$="PSI/deg" : GOTO 1395
1385 L$="POT/volts" : GOTO 1395
1390 L$="CURRENT/mA": GOTO 1395
1395 M=N : RETURN
```

```
1500 REM ***** PLOTXY *****
1505 REM ***** Y$= L OR S MODE,I2=LT TYPE *****
1510 REM ***** I$=SYMBOL FOR SM,I1$=NORMAL OR OTHER LINE TYPE *****
1515 PRINT "LINE TYPE OR SYMBOL MODE,L OR S":Y$=INCH$(0)
1518 PRINT " "
1520 IF Y$="S" THEN INPUT"SYMBOL",I$
1525 IF Y$="S" THEN PRINT A$+"SM";I$
1530 IF Y$="L" THEN GOSUB 6200
1535 PRINT "PA";Y(1);X(1);"PD";J$
1540 FOR I=1 TO C1
1596 IF X(I)<0.01 THEN IF X(I)>-0.01 THEN X(I)=0
1597 IF Y(I)<0.01 THEN IF Y(I)>-0.01 THEN Y(I)=0
1598 PRINT A$+"AP"
1600 IF Y$="S" THEN PRINT "SM";I$;"PU";Y(I);X(I)
1605 IF Y$="L" THEN PRINT "PA";Y(I);X(I)
1615 PRINT CHR$(35) : INPUT AT$
1619 PRINT "AP";J$
1620 NEXT I
1623 PRINT A$+"PU;SM;";J$
1630 RETURN
2000 REM ***** READS $ SCALES FILES *****
2005 GOSUB 300 : REM DATREAD S/R
2010 FOR I=1 TO C1
2015 X(I)=F(I,M)
2020 Y(I)=F(I,N)
2025 NEXT I
2030 FOR I=1 TO C1
2035 IF S1=1 THEN X(I)=X(I)*10
2040 IF S1=2 THEN X(I)=X(I)*100
2045 IF S2=1 THEN Y(I)=Y(I)*10
2050 IF S2=2 THEN Y(I)=Y(I)*100
2055 NEXT I
2060 GOSUB 1500 : REM PLOTXY S/R
2065 RETURN
2200 REM ***** LABEL ROUTINE *****
2205 PRINT CHR$(31)
2210 PRINT "INPUT DL FOR DELTA/deg IN GREEK ALPHABET, PSI FOR PSI/deg"
2220 INPUT"LABEL",L4$
2225 PRINT "DIRECTION OF LABEL"
2230 PRINT" "
2240 PRINT "L TO R (1), R TO L (2), TOP TO BOTTOM (3), B TO T (4)"
2245 INPUT "DIRECTION",DI
2248 PRINT A$+"PU"
2250 IF DI=1 THEN PRINT "DI0,1"
2255 IF DI=2 THEN PRINT "DI0,-1"
2260 IF DI=3 THEN PRINT "DI1,0"
2265 IF DI=4 THEN PRINT "DI-1,0"
2268 PRINT A$+"PU";J$
2269 IF S5=2 THEN 2278
2270 INPUT"SIZE OF LETTERS IN cm, LENGTH,HEIGHT",S3,S4
2275 PRINT A$+"SI";S3;S4;J$
2278 PRINT "POSITION PEN & PRESS ANY KEY" : Q$=INCH$(0)
2279 PRINT A$+"PU"
2280 IF L4$="DL" THEN 2400
2290 IF L4$="PS" THEN 2450
2300 PRINT "LB";L4$;E$;J$
2310 INPUT"CHANGE LABEL(1),DIRECTION(2),LETTER SIZE(3),REPLOT(4),END(5)",S5
2320 ON S5 GOTO 2330,2240,2270,3100,9999
2330 INPUT"LABEL",L4$
2335 IF L4$="DL" THEN 2400
```

```
2340 IF L4$="PS" THEN 2450
2345 GOTO 2270
2400 PRINT"UC99,4,0,-2,4,-2,-4,PU"
2410 PRINT"CP0,.2;SI.1,.2;LBo";E$;J$
2420 PRINT A$+"SI";S3;S4
2430 GOTO 2310
2450 PRINT"UC.5,2.5,99,-.5,-1,1,-.5,2,0,1,.5,-.5,1,-99,1.5,1.5,99,0,-6,PU"
2455 PRINT"CP.05,.2;SI.1,.2;LBo";E$;J$
2460 PRINT A$+"SI";S3;S4
2465 GOTO 2310
3000 REM XXXXX MAIN PROG XXXXX
3010 GOSUB 200 : REM PLOTINT S/R
3020 GOSUB 300 : REM DATREAD S/R
3030 GOSUB 500 : REM DATHILO S/R
3040 GOSUB 800 : REM SCALE S/R
3050 GOSUB 1100 : REM PLOTLAB S/R
3060 GOSUB 1500 : REM PLOTXY
3100 PRINT"TYPE 1 FOR Y2 PLOT"
3110 PRINT"TYPE 2 FOR SAME FILE ANOTHER GRAPH"
3120 PRINT"TYPE 3 FOR DIFFERENT FILE,SAME AXES & SCALES"
3130 PRINT"TYPE 4 FOR LABEL ROUTINE"
3140 PRINT"TYPE 5 FOR END"
3150 INPUT"NUMBER REQD",F2
3160 IF F2=2 THEN GOSUB 200
3170 IF F2=5 THEN 9999
3190 IF F2=1 THEN PRINT "THIS OPTION NOT AVAILABLE ON THIS PROG."
3200 IF F2=2 THEN S1=0 : IF F2=2 THEN S2=0
3205 IF F2<>2 THEN 3210
3208 IF M=5 THEN F3=1:IF N=5 THEN F3=1
3210 IF F2=2 THEN GOTO 3030
3215 IF F2=3 THEN INPUT"VALUE FOR X AXIS,Y AXIS",M,N
3220 IF F2=3 THEN GOSUB 2000 : REM DIFFILE S/R
3230 IF F2=4 THEN GOSUB 2200 : REM LABEL S/R
3240 GOTO 3100
5000 IF ERR=8 THEN RESUME 365
5002 IF ERR=4 THEN CLOSE 1
5005 IF ERR=22 THEN PRINT "REDUCE DIMENSIONS OF ARRAY,LINE 130"
5006 IF ERR=4 THEN PRINT "FILE NOT FOUND"
5007 IF ERR=4 THEN RESUME 320
5008 IF ERR=77 THEN RESUME 365
5010 IF ERR<>30 THEN ON ERROR GOTO 0
5020 CLOSE 1
5030 OPEN OLD F1$ AS 1
5040 INPUT LINE#1,D$
5050 RESUME 345
6000 GOSUB 200
6010 PRINT A$+"IP300,500,8753,6500;SC";J1;J2;K1;K2;J$
6020 INPUT"NEW Y STEP",K3
6030 PRINT A$+"SP1"
6040 GOTO 1225
6200 REM LINE TYPE S/R
6205 PRINT CHR$(31) : REM CLEAR SCREEN
6208 PRINT CHR$(31)
6210 PRINT "SOLID LINE(L) OR OTHER(O)" : L4$=INCH$(0) : PRINT " "
6220 IF L4$="L" THEN PRINT A$+"LT"  : RETURN
6230 PRINT " "
6240 PRINT "TYPE 0              . . . . . . . . . . . . . ."
6245 PRINT " "
6250 PRINT "TYPE 1              . . . . . . . . . . . . . . . . . . ."
6255 PRINT " "
```

```
6260 PRINT "TYPE 2          __ __ __ __ __ __ __ __ __ _"
6265 PRINT" "
6270 PRINT "TYPE 3          ___ ___ ___ ___ ___ ___ ___ ___ ___ _"
6275 PRINT " "
6280 PRINT "TYPE 4          ___.___.___.___.___.___.___.___.___._"
6285 PRINT " "
6290 PRINT "TYPE 5          ___ _ ___ _ ___ _ ___ _ ___ _ ___ _ _"
6295 PRINT " "
6300 PRINT "TYPE 6          ___ _ _ ___ _ _ ___ _ _ ___ _ _ ___ _"
6305 PRINT " "
6310 INPUT"LINE TYPE",LT
6330 REM GET P1 & P2 VALUES FROM PLOTTER
6340 PRINT A$+"PU" : INPUT"OP",P(1),P(2),P(3),P(4): PRINT "PU";J$
6350 REM FIND DIAGONAL DISTANCE BETWEEN P1 & P2
6360 PL=SQR((P(3)-P(1))*(P(3)-P(1))+(P(4)-P(2))*(P(4)-P(2)))
6365 PRINT "PATTERN LENGTH IS",PL*0.04*0.0025;"cm"
6370 PRINT " "
6375 PRINT "CHANGE PATTERN LENGTH" : Q$=INCH$(0)
6378 PRINT " "
6380 IF Q$="N" THEN PRINT A$+"LT";LT : RETURN
6385 INPUT"PATTERN LENGTH IN cm",PC
6390 PL=(PC/(PL*0.0025))*100
6395 PRINT A$+"LT";LT,PL : RETURN
6400 REM SET UP IP VALUES FOR PLOTTER
6405 PRINT "OPTIONS ARE"
6410 PRINT "SINGLE PLOT (1)"
6415 PRINT " "
6420 PRINT "2 SEPARATE PLOTS (2)"
6425 PRINT " "
6430 PRINT "2 PLOTS COMMON X AXIS (3)"
6435 PRINT " "
6440 PRINT "3 PLOTS COMMON X AXIS (4)"
6445 PRINT " "
6450 PRINT "4 PLOTS COMMON X AXIS (5)"
6455 PRINT " "
6456 PRINT "3 SEPARATE PLOTS (6) "
6458 PRINT " "
6460 INPUT"OPTION REQUIRED",E
6465 ON E GOTO 6470,6480,6500,6540,6580,6620
6470 PRINT A$+"IP1000.2000,9800,7000" : RETURN
6480 REM 2 SEPERATE PLOTS
6485 PRINT "TOP(T) OR BOTTOM(B) PLOT" : P$=INCH$(0)
6490 IF P$="T" THEN PRINT A$+"IP900,2000,4100,7000" : RETURN
6495 IF P$="B" THEN PRINT A$+"IP5600,2000,8800,7000" : RETURN
6500 REM 2 PLOTS COMMON X AXIS
6510 PRINT "TOP(T) OR BOTTOM(B) PLOT" : P$=INCH$(0)
6520 IF P$="T" THEN PRINT A$+"IP1000,2000,4900,7000" : RETURN
6530 IF P$="B" THEN PRINT A$+"IP4900,2000,8800,7000":RETURN
6540 REM 3 PLOTS COMMON X AXIS
6550 PRINT "TOP(T),MIDDLE(M) OR BOTTOM(B) PLOT" : P$=INCH$(0)
6560 IF P$="T" THEN PRINT A$+"IP1000,2000,3600,7000" : RETURN
6565 IF P$="M" THEN PRINT A$+"IP3600,2000,6200,7000" : RETURN
6570 IF P$="B" THEN PRINT A$+"IP6200,2000,8800,7000" : RETURN
6580 PRINT "TOP(T),MIDDLE UPPER(U),LOWER(L) OR BOTTOM(B) " : P$=INCH$(0)
6590 IF P$="T" THEN PRINT A$+"IP1000,2000,2950,7000" : RETURN
6595 IF P$="U" THEN PRINT A$+"IP2950,2000,4900,7000" : RETURN
6600 IF P$="L" THEN PRINT A$+"IP4900,2000,6850,7000" : RETURN
6610 IF P$="B" THEN PRINT A$+"IP6850,2000,8800,7000" : RETURN
6620 REM 3 SEPARATE PLOTS
6630 PRINT "TOP(T),BOTTOM LEFT(L),OR BOTTOM RIGHT(R)" : P$=INCH$(0)
```

```
6640 IF P$="T" THEN PRINT A$+"IP1000,2000,4100,7000" : RETURN
6650 IF P$="L" THEN PRINT A$+"IP5600,2000,8600,4100" : RETURN
6660 IF P$="R" THEN PRINT A$+"IP5600,4900,8900,7000" : RETURN
7000 REM TIME DELAY FOR PLOTTER BUFFER TO EMPTY
7010 FOR K=1 TO 25
7020 FOR J=1 TO 100
7030 NEXT J
7040 NEXT K
7050 PRINT A$+"PU";B1$;J$
7060 INPUT#0,B1
7070 IF B1>100 THEN RETURN
7080 GOTO 7010
9999 END
```

Appendix A4 Computer program for modelling substrate roughening - RUFFILM

```
C        CALCS DELTA & PSI FOR FOUR FILM MODEL
C        USES K NOT KAPPA
C       SUBSRATE IS MAGNESIUM
         DIMENSION FNSI(2),DFNS(2),FNSE(2),FNSX(2),TN(8),TD(8)
         DIMENSION VFRAC(30)
         INTEGER*1 FILE(40)
         REAL MODEL,VFRACT
         REAL RF1,RF2,RF3,RF4,NTH1,NTH2
         REAL EPS1MD,EPS2MD
         COMPLEX C2,C3,CI,CIP1,CN,CNM1,CRN,CRN21,CRN32,CRP,CRP21,CRP32
         COMPLEX FN2,FNX,FNS,RHO,RN,RN21,RP,RP21,RC,SRC
         COMPLEX T1,T2,T3,T4,RHOC,RHO1,RHO2,CAT,ALP1,ALP2,BET1,BET2
         COMPLEX GAM1,GAM2,CALC
         COMMON/OPT/FN1,S1,C1,N,FNX(205),D(205),FN2,CRP,CRN,CRP32,CRN32,
      1WL,
      1RP21,RN21,DEL,PSI,C2,C3,FN2I(2),DFN2(2),FN2E(2),FN2X(2),T1,T2,T3,
      1T4,D2,DELDX,PSIDX,ELDEL,ELPSI,DENP,FNP,DEN1,MX,K,IS,RHO
         DIMENSION CALC(205)
C        SIN,COS,ATAN,TAN FOR ANGLES IN DEGREES
         SIND (X)=SIN(X/57.29573)
         COSD (X)=COS(X/57.29578)
         ATAND (X)=ATAN(X)*57.29578
         TAND (X)=SIND(X)/COSD(X)
C        S IS USED FOR CALCULATING SPECIFIC REFRACTION
         S(XN)=(XN*XN-1.)/(XN*XN+2.)
         WRITE(6,13)
 13      FORMAT(1H1,'FILENAME?')
         READ(5,17) FILE
 17      FORMAT(40A1)
         OPEN(3,FILE)
C        GIVE STANDARD VALUES TO VARIABLES
 10      FN1I=1.334
         FN2I(1)=1.334
         FN2I(2)=0.
C        MAKE SUBSTRATE MAGNESIUM
         FNSI(1)=.85
         FNSI(2)=5.75
         EPS1IC=FNSI(1)*FNSI(1)-FNSI(2)*FNSI(2)
         EPS2IC=2.*FNSI(1)*FNSI(2)
         AII=70.
         WLI=6328.
         RHOC=(0.,-1.)
         TC=1.
         DELC=90.
         DEN1=1.
         DENP=1.
         FNP=1.5
         FN=1.
         PI=3.1415926
 1000    CONTINUE
         STEP=20.
         D(2)=0.
         N=32
C        INPUT OF VARIABLES
         WRITE(6,12)
 12      FORMAT(1H1,'TOP FILM THICKNESS?    ')
         READ(5,14)NTH1
 14      FORMAT(F8.3)
         WRITE(6.16)
 16      FORMAT(1H1,'TOP FILM REFRACTIVE INDEX?     ')
        .READ(5,18)RF1,RF2
 18      FORMAT(F8.3)
         WRITE(6,20)
 20      FORMAT(1H1,'MODEL REQD..T.RIDGE(1).CONES(2),HEMISPHERES(3)?    ')
         WRITE(6,21)
 21      FORMAT(1H1,'INVERSE CONES(4),INVERSE HEMISPHERES(5)?     ')
         READ(5,14)MODEL
         WRITE(6,22)
 22      FORMAT(1H1,'RATE OF INCREASE OF ROUGHNESS?     ')
         READ(5,18)RATE
C        SETTING COMPLEX EQN
         FNX(2)=CMPLX(RF1,-RF2)
         NPHASE=1.
```

```
      EPS1MD=RF1*RF1-RF2*RF2
      EPS2MD=2.*RF1*RF2
C     ROUGHNESS MODELLING
C     START OF CALC
      DO 2100 I=1,30
      J=I-1
      IF(MODEL.GT.1.) GOTO 50
      VFRAC(I)=1.-(2.*I-1)/60.
      GOTO 70
 50   IF(MODEL.GT.2.) GOTO 60
      VFRAC(I)=(1.-(I+J)/30.+(J*J+I*J+I*I)/(3.*30.*30.))*(PI/4.)
      GOTO 70
 60   CONTINUE
      IF(MODEL.GT.3.) GOTO 75
      VFRAC(I)=(1.-(I*I+I*J+J*J)/(3.*30.*30.))*(PI/4.)
      GOTO 70
 75   IF(MODEL.GT.4.) GOTO 78
      VFRACT=(1.-(I+J)/30.+(J*J+I*J+I*I)/(3.*30.*30.))*(PI/4.)
      VFRAC(I)=1.-VFRACT
      GOTO 70
 78   VFRACT=(1.-(I*I+I*J+J*J)/(3.*30.*30.))*(PI/4.)
      VFRAC(I)=1.-VFRACT
 70   CONTINUE
      WRITE(6,100) VFRAC(I)
      CALL OPTCON(VFRAC(I),EPS1MD,EPS2MD,EPS11C.EPS21C,EMAN.EMAK)
      IF(MODEL.GT.3.) GOTO 80
      FNX(33-I)=CMPLX(EMAN,-EMAK)
      GOTO 2100
 80   CONTINUE
      FNX(I+2)=CMPLX(EMAN.-EMAK)
 2100 CONTINUE
C     START OF CALC
      D(2)=D(2)-STEP
 2300 CONTINUE
      IF(FLAG.EQ.1) GOTO 1155
      D(2)=D(2)+STEP
 1155 CONTINUE
      RATE=RAT/(EXP(RATED))
      RATED=RATED+.1
      IF(RATE.GT.1) GOTO 1128
      RATE=1
 1128 CONTINUE
      GOTO 1210
 1210 CONTINUE
      DO 2150 I=3,32
      D(I)=0.
 2150 CONTINUE
 2155 CONTINUE
      IF(D(2).LE.NTH1) GOTO 2000
      GOTO 3000
C     PROCEED TO PRINT USING CTABLE
C     THICKNESS OF TOP FILM & ,OPTIONALLY,SETTING OF WAVE PLATE
 2000 CONTINUE
      Q=Z4
C     SET INITIAL VALUES
 310  FN1=FN1I
 311  AI=AII
 312  S1=SIND(AI)
      C1=COSD(AI)
 315  WL=WLI
 320  NP1=N+1
C     SET VALUES FOR REFRACTIVE INDEX OF SUBSTRATE
      FNX(NP1)=CMPLX(FNSI(1),-FNSI(2))
C     COMPUTE REFLECTION COEFF. BETWEEN LAYERS 3 & 4
      IF(N.EQ.2) GOTO 335
      X=SIND(AI)*FN1
      CN=CSQRT(1.-(X/FNX(N+1))**2)
      CNM1=CSQRT(1.-(X/FNX(N))**2)
      CRP=(FNX(N+1)*CNM1-FNX(N)*CN)/(FNX(N+1)*CNM1+FNX(N)*CN
      CRN=(FNX(N)*CNM1-FNX(N+1)*CN)/(FNX(N)*CNM1+FNX(N+1)*CN
      IF(N.EQ.3) GOTO 335
      NX=N-3
      I=N-1
      DO 330 JK=1,NX
      CIP1=CSQRT(1.-(X/FNX(I+1))**2)
      CI=CSQRT(1.-(X/FNX(I))**2)
      RP=(FNX(I+1)*CI-FNX(I)*CIP1)/(FNX(I+1)*CI+FNX(I)*CIP1
      T1=FNX(I+1)*CIP1*D(I+1)/WL
```

```
      RN=(FNX(I)*CI-FNX(I+1)*CIP1)/(FNX(I)*CI+FNX(I+1)*CIP1)
      CRP=RC(RP,CRP,T1)
      CRN=RC(RN,CRN,T1)
 330  I=I-1
 335  CONTINUE
      FN2=FNX(2)
C     CALCULATE REFLECTION COEFF. BETWWEN LAYERS 2 & 3
     CALL SUBROT
C     TABLES OF DEL & PSI FOR CTABLE
 350  CONTINUE
 390  D2=D(2)
 400  CRP21=RC(RP21,CRP32,FN2*C2*D2/WL)
      CRN21=RC(RN21,CRN32.FN2*C2*D2/WL)
      RHO=CRP21/CRN21
      IF(FN.NE.1.) RHO=CEXP(1./FN*CLOG(RHO))
      DEL=ATAN2(AIMAG(RHO),REAL(RHO))*57.29578
      IF(REAL(RHO).LT.0. . AND. ABS(AIMAG(RHO)).LT.1.0E-6) DEL=180.
      PSI=ATAND(CABS(RHO))
      XM1=CABS(CRP21)
      XM12=XM1*XM1
      THETA1=ATAN2(AIMAG(CRP21),REAL(CRP21))*57.29578
      IF(REAL(CRP21).LT.0 . AND. ABS(AIMAG(CRP21)).LT.1.0E-6) THETA1=180.
      XM2=CABS(CRN21)
      XM22=XM2*XM2
      THETA2=ATAN2(AIMAG(CRN21),REAL(CRN21))*57.29578
      IF(REAL(CRN21).LT.0.AND.ABS(AIMAG(CRN21)).LT.1.0E-6)THETA2=180.
      IF(DEL.LT.0.) DEL1=DEL+360
      IF(DEL.LT.0.) DEL=DEL1
      WRITE(6,100) D(2),D(3),PSI,DEL
  100 FORMAT(1X,F7.3,6F10.3)
      GOTO 2300
 3000 CONTINUE
      STOP
      END
      SUBROUTINE SUBROT
C     CALCULATES CRP32 AND CRN32 REFLECTION COEFF. OF MEDIUM 2 & 3
      COMPLEX FNX,FN2,CRP,CRN,CRP32.CRN32,RP21,RN21,C2,C3,T1,T2,T3,T4
      COMPLEX RC,RP32,RN32
      COMMON/OPT/FN1,S1,C1,N.FNX(205).D(205),FN2,CRP,CRN,CRP32,CRN32,
     1WL,
     1RP21,RN21,DEL,PSI,C2,C3,FN2I(2),DFN2(2),FN2E(2),FN2X(2),T1,T2,
     1T3,T4,D2,DELDX,PSIDX,ERDEL.ERPSI.DENP,FNP,DEN1
      X=FN1*S1
      C2=CSQRT(1.-(X/FN2)**2)
      C3=CSQRT(1.-(X/FNX(3))**2)
  100 FORMAT(1X,F7.3,6F10.3)
      RP21=(FN2*C1-FN1*C2)/(FN2*C1+FN1*C2)
      RN21=(FN1*C1-FN2*C2)/(FN1*C1+FN2*C2)
      IF(N.EQ.2) GOTO 10
      RP32=(FNX(3)*C2-FN2*C3)/(FNX(3)*C2+FN2*C3)
      RN32=(FN2*C2-FNX(3)*C3)/(FN2*C2+FNX(3)*C3)
      CRP32=RC(RP32,CRP,FNX(3)*C3*D(3)/WL)
      CRN32=RC(RN32,CRN,FNX(3)*C3*D(3)/WL)
      RETURN
 10   CRP32=(FNX(3)*C2-FN2*C3)/(FNX(3)*C2+FN2+C3)
      CRN32=(FN2*C2-FNX(3)*C3)/(FN2*C2+FNX(3)*C3)
      RETURN
      END
C
C
C
C




      COMPLEX FUNCTION RC(R21,CR32,Q)

      COMPLEX R21,CR32,Q,T
      T=CEXP((0.,-12.56637)*Q)
C     Q=N2*COS(PHI2)*D/WL         (0.,-12.56637)=-4.*PI*J
      RC=(R21+CR32*T)/(1.+R21*CR32*T)
      RETURN
      END
```

```
C
C
C
C
      SUBROUTINE OPTCON(V1,EPS1MD,EPS2MD,EPS1IC,EPS2IC,RN,RK)
C     CALCULATES N&K FOR EFFECTIVE MEDIUM APPROXIMATION USING EMA
C     APPROXIMATION
      COMPLEX EPS1,EPS2,EPSE,A,B,C,EPSE1,EPSE2,TERM2,RESULT
      COMMON/OPT/FN1,S1,C1,N,FNX(205),D(205),FN2,CRP,CRN,CRP32,CRN32,
     1WL,
     1RP21,RN21,DEL,PS1,C2.C3,FN21(2),DFN2(2),FN2E(2),FN2X(2),T1,T2,T3,
     1T4,D2,DELDX,PSIDX,ELDEL,ELPSI,DENP,FNP,DEN1,MX,K,IS,RHO
       EPS1=CMPLX(EPS1IC,EPS2IC)
      EPS2=CMPLX(EPS1MD,EPS2MD)
      A=CMPLX(-2.,0.)
      B=(3.*V1*EPS1-3.*V1*EPS2+2.*EPS2-EPS1)
      C=EPS1*EPS2
      TERM2=CSQRT(B*B-4.*A*C)
      EPSE1=(-B+TERM2)/(2.*A)
      EPSE2=(-B+TERM2)/(2.*A)
      IF (AIMAG(EPSE1).LT.0.) GOTO 300
      IF (AIMAG(EPSE2).LT.0.) GOTO 400
 300  EPSR=REAL(EPSE2)
      EPSI=AIMAG(EPSE2)
      GOTO 500
 400  EPSR=REAL(EPSE1)
      EPSI=AIMAG(EPSE1)
 500  IF(ABS(-0.5*EPSR+0.5*SQRT(EPSR*EPSR+EPSI*EPSI)).GE.1.E-8) GOTO 15
      RK=0.
      RN=SQRT(EPSR)
      GOTO 20
 15   RK=SQRT(-0.5*EPSR+.5*SQRT(EPSR*EPSR+EPSI*EPSI))
      RN=SQRT(EPSR+RK*RK)
 20   CONTINUE
 100  FORMAT(F6.3.6F10.3)
      RETURN
       END
```